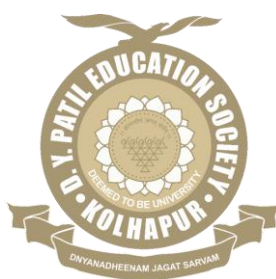


**CHEMICAL SYNTHESIS AND  
SUPERCAPACITIVE PERFORMANCE OF  
NICKEL VANADIUM OXIDE/rGO COMPOSITE  
ELECTRODE**

A THESIS SUBMITTED TO  
**D. Y. PATIL EDUCATION SOCIETY (DEEMED TO BE  
UNIVERSITY), KOLHAPUR**



FOR THE DEGREE OF  
**DOCTOR OF PHILOSOPHY**  
IN  
**PHYSICS**

UNDER THE FACULTY OF  
**INTERDISCIPLINARY STUDIES**

BY  
**Ms. SHRADDHA BANDOPANT BHOSALE**  
M. Sc.

UNDER THE SUPERVISION OF  
**Dr. UMAKANT MAHADEV PATIL**  
M. Sc., Ph. D.

ASSOCIATE PROFESSOR,  
CENTRE FOR INTERDISCIPLINARY RESEARCH,  
D. Y. PATIL EDUCATION SOCIETY (DEEMED TO BE UNIVERSITY),  
KOLHAPUR- 416 006, MAHARASHTRA, (INDIA)

**2024**

# **DECLARATION**

I am Shraddha Bandopant Bhosale, hereby declare that the thesis entitled "CHEMICAL SYNTHESIS AND SUPERCAPACITIVE PERFORMANCE OF NICKEL VANADIUM OXIDE/rGO COMPOSITE ELECTRODE" submitted for the degree of Doctor of Philosophy (Ph.D.) in Physics, Faculty of Interdisciplinary Studies, under the guidance of Dr. Umakant M. Patil, Centre for Interdisciplinary Research (CIR), D. Y. Patil Education Society (Deemed to be University), Kolhapur is completed and written by me, has not before made the basis for the award of any other higher education institute in India or any other country to the best of my knowledge and belief the thesis contains no material previously published or written by another person except where due reference is made. Further, I declare that I have not violated any of the provisions under the Copyright and Piracy/Cyber/IPR Act amended from time to time.

Place: Kolhapur

Research Student



Date: 25/10/2024

Ms. Shraddha Bandopant Bhosale


## **CERTIFICATE OF GUIDE**

This is to certify that the thesis entitled "CHEMICAL SYNTHESIS AND SUPERCAPACITIVE PERFORMANCE OF NICKEL VANADIUM OXIDE/RGO COMPOSITE ELECTRODE" which is being submitted herewith for the award of the Degree of Doctor of Philosophy (Ph.D.) in Physics, Faculty of Interdisciplinary Studies, under the guidance of Dr. Umakant Mahadev Patil, Centre for Interdisciplinary Research (CIR), D. Y. Patil Education Society (Deemed to be University), Kolhapur, is the result of the original research work completed by Ms. Shraddha Bandopant Bhosale under my supervision and guidance and to the best of my knowledge and belief the work embodied in this thesis has not formed earlier the basis for the award of any degree or similar title of this or any other University or examining body.

Place: Kolhapur

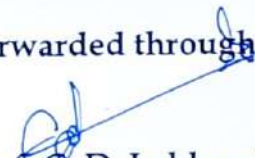
Research Guide

Date: 25/10/2024

  
**Dr. Umakant Mahadev Patil**  
Associate Professor,  
Centre for Interdisciplinary Research,  
D. Y. Patil Education Society,  
(Deemed to be University),  
Kolhapur- 416 006.

**Dr. U.M.Patil**  
Associate Professor  
Centre for Interdisciplinary Research  
DY. Patil Education Society  
(Deemed to be University),  
Kolhapur-416006 (India)

Forwarded through,

  
**Prof. C. D. Lokhande**  
Dean and Research Director,  
Centre for Interdisciplinary Research,  
D. Y. Patil Education Society,  
(Deemed to be University),  
Kolhapur- 416 006.

**Prof. C. D. LOKHANDE**

Research Director  
D. Y. Patil Education Society  
(Institution Deemed to be University)  
869, 'E', Kasaba Bawada  
KOLHAPUR- 416006



# **ACKNOWLEDGEMENT**

*The journey in the pursuit of a doctorate has been beautiful! It's been a quest to expand the horizons of knowledge, a voyage to discover hidden strengths. The beauty of the journey was made better by the amazing people I met along the way. I wish to seize this moment to express gratitude to those wonderful personalities who made this journey truly memorable.*

*I express my heartfelt appreciation to my mentor, **Dr. Umakant M. Patil**, Associate Professor at the Centre for Interdisciplinary Research (CIR), D. Y. Patil Education Society (Deemed to be University), Kolhapur, for his valuable guidance, unwavering support, and countless insightful discussions throughout this endeavor. His boundless passion for science and his adept mentorship always inspires me deeply. I consider myself incredibly fortunate to be a member of the 'Thin Film Electrochemistry Research group'.*

*I extend my heartfelt gratitude to **Prof. C. D. Lokhande**, Dean and Research Director at the CIR, for his valuable advice, and constructive recommendations. His guidance on effective time management significantly propelled the advancement of my doctoral research. I offer my sincere appreciation to Vice-Chancellor **Prof. R. K. Mudgal** and Registrar **Dr. V. V. Bhosale** for their encouragement and support. Furthermore, I am grateful to **Dr. R. S. Patil**, **Dr. J. L. Gunjakar**, **Dr. S. B. Patil**, **Dr. V. M. Khot**, and **Dr. Arpita Pandey-Tiwari** for their collaborative approach and empathetic assistance in result analysis.*

*I am deeply grateful to **Dr. Kishor Gurav** (Devchand College, Arjunnagar) for his encouragement and insightful suggestion to pursue a Ph.D., which has enriched my academic journey immeasurably. Moreover, I recognize the contributions of **Dr. Rahul Salunkhe** (IIT Jammu), and **Dr. Vinayak Parale** (Yonsei University, South Korea), for their vital support in providing sample characterization data throughout my research journey. I would like to extend special thanks to my colleague, **Mr. Sambhaji Kumbhar**, who started this journey with me back in 2020 and made this 'synopsis to thesis' journey much easier. I had the pleasure of working with my seniors, **Dr. P. Katkar**, **Dr. S. Marje**, **Dr. S. Kale**, **Dr. D.***



*Malvekar, Dr. S. Pujari, Dr. S. Sadavar, Dr. R. Shinde, Dr. S. Jadhav, Dr. P. Bagwade, Mr. V. Magdum, Mr. Y. Chitare, and Ms. S. Kulkarni, for their insightful guidance, scientific exchanges, and invaluable recommendations regarding my current research. Many thanks to the upcoming Doctors from CIR, including Ketaki, Sambhaji, Satish, Manohar, Ajinkya, Sumita, Kuldip, Ganesh, Prashant, Shweta, Shraddha, Rakesh, Sohel, Naziya, Nadiya, Dhanashri, Arti, Suhasini, Shivprasad, Suraj, Anil, Mayura, Gouri, Sayali, and Vinay for their wonderful collaboration throughout our research endeavours. I am also thankful to all non-teaching staff of the CIR for their cooperation.*

*I extend my heartfelt appreciation to **Rutuja** and **Akash** for standing by me through both my moments of joy and sorrow during this thesis journey. I want to express my heartfelt thanks to **Rushiraj**, and **Vinod** for always being there for me, offering constant support and assistance in every situation. To the amazing friends **Gayatri, Bhushan, Meghana, Naziya, Namrata and Akshay** thank you to each of you who has played a part in making this moment possible.*

*Words cannot express my gratitude to my dear parents, **Mr. Bandopant and Mrs. Alaka**, whose encouragement has propelled me to exceed my expectations and pursue excellence. I am eternally thankful to my wonderful woman, my aunt **Smt. Vimal**, my sister **Mrs. Padmini**, and sister-in-law **Mrs. Tejaswini** for empowering me to break free from traditional gender roles. I cannot express enough gratitude to my sister and brothers, **Yashshri, Atharv, and Amar** for their invaluable assistance in refining my thesis and manuscripts, elevating them to their best possible versions. Special thanks to my adorable nieces, **Devki** who have been my constant source of joy and relaxation. Thank You all for being a part of this journey. The Journey that all matters.*

*~Shraddha*

*Place: Kolhapur*

# **SUMMARY OF RESEARCH WORK**

## **Granted (03) /Published Patents (02)**

- 1) Nickel vanadate thin film on conducting substrate, preparation method for the same and supercapacitor comprising the same, Dr. J. L. Gunjekar, **Ms. S. B. Bhosale**, Dr. U. M. Patil, Mr. S. S. Kumbhar, Mr. V. V. Patil, Prof. C. D. Lokhande, (Application No: 202221020652).
- 2) Electrochemical Method for Detection of Cancer, Dr. A. Pandey-Tiwari, Dr. U. M. Patil, Ms. Rutuja Gambhir, **Ms. S. B. Bhosale** (Application No: 202321064185)
- 3) Nickel cobalt phosphate thin-film electrodes: chemical method for preparation of the same, application for supercapacitor and electrocatalysis using the same, Dr. U. M. Patil, Mr. V. V. Patil, Mr. S. S. Kumbhar, **Ms. S. B. Bhosale**, Prof. C. D. Lokhande, (Patent No: 432303).
- 4) Chemical method for growing a cobalt vanadium oxide thin film on solid substrate, Dr. U. M. Patil, Mr. S. S. Kumbhar, **Ms. S. B. Bhosale**, Mr. V. V. Patil, Prof. C. D. Lokhande, Dr. P. R. Deshmukh, (Patent No:459219).
- 5) Cobalt vanadium oxide, preparation method for the same, and supercapacitor comprising the same, Dr. U. M. Patil, Mr. S. S. Kumbhar, **Ms. S. B. Bhosale**, Mr. V. V. Patil, Prof. C. D. Lokhande, Dr. R. R. Salunkhe, (Patent No: 529322).

## **Articles in International Journals (11)**

- 1) **S. B. Bhosale**, S. S. Kumbhar, S. S. Patil, A. Ransing, V. G. Parale, C. D. Lokhande, J. L. Gunjekar, H. Park, U. M. Patil\*, Harnessing morphological alteration from microflowers to nanoparticles and cations synergy (Co:Ni) in binder-free cobalt nickel vanadate thin film cathodes synthesized via SILAR method for hybrid supercapacitor devices, Journal of Colloid and Interface Science, 666 (2024) 101-117 (**I.F- 9.4**).
- 2) **S. B. Bhosale**, S. S. Kumbhar, S. S. Pujari, V. V. Patil, N. Kumar, R. R. Salunkhe, C. D. Lokhande, J. L. Gunjekar, U. M. Patil\*, Development of binder-free, amorphous nickel vanadate cathodes by SILAR method for hybrid supercapacitors: Exploiting surface area by monitoring growth rate, Journal Energy Storage, 72 (2023) 108417-108432 (**I.F- 8.9**).
- 3) S. S. Pujari, S. A. Kadam, Y. R. Ma, S. B. Jadhav, S. S. Kumbhar, **S. B. Bhosale**, V. V. Patil, J. L. Gunjekar, C. D. Lokhande, U. M. Patil\*, A binder-free facile synthetic approach for amorphous, hydrous nickel copper phosphate thin film electrode preparation and its application as a highly stable cathode for hybrid asymmetric supercapacitors, Sustainable Energy & Fuels, 6 (2022) 5608-5620 (**I.F- 5**).
- 4) S. S. Pujari, S. A. Kadam, Y. R. Ma, S. B. Jadhav, S. S. Kumbhar, **S. B. Bhosale**, J. L. Gunjekar, C. D. Lokhande, U. M. Patil\*, Hydrothermally synthesized nickel

copper phosphate thin film cathodes for high-performance hybrid supercapacitor devices, Journal of Energy Storage, 52 (2022) 105037 (**I.F- 8.9**).

- 5) V. V. Patil, S. S. Pujari, **S. B. Bhosale**, S. S. Kumbhar, V. G. Parale, J. L. Gunjekar, H. Park, C. D. Lokhande, M. G. Mali, D. S. Mhamane, U. M. Patil\*, Hydrous and amorphous cobalt phosphate thin-film electrodes synthesized by the SILAR method for high-performing flexible hybrid energy storage devices, Energy & Fuels, 36 (2022) 12791-12806 (**I.F- 5.2**).
- 6) S. S. Kumbhar, **S. B. Bhosale**, S. S. Pujari, V. V. Patil, N. Kumar, R. R. Salunkhe, C. D. Lokhande, U. M. Patil\*, Growth dynamics-dependent chemical approach to accomplish nanostructured cobalt vanadium oxide thin film electrodes with controlled surface area for high-performance solid-state hybrid supercapacitor devices, Energy Technology, 11 (2023) 2300400 (**I.F- 3.6**).
- 7) V. V. Patil, S. S. Pujari, **S. B. Bhosale**, S. S. Kumbhar, V. G. Parale, C. D. Lokhande, J. L. Gunjekar, M. G. Mali, D. S. Mhamane, H. Park, U. M. Patil\*, SILAR synthesized binder-free, hydrous cobalt phosphate thin film electrocatalysts for OER application: annealing effect on the electrocatalytic activity, International Journal of Energy Research, 2023 (2023) 1-17 (**I.F- 4.3**).
- 8) R. P. Bhosale, S. S. Kumbhar, **S. B. Bhosale**, R. R. Salunkhe, V. A. Kadam, S. P. Pardhi, S. S. Gholap, C. D. Lokhande, V. S. Jamadade\*, Morphology modulation of  $\text{MnFe}_2\text{O}_4$  thin film electrode for enhanced performance of hybrid supercapacitor, Journal of Energy Storage, 86 (2024) 111146 (**I.F-8.9**).
- 9) S. A. Khalate, S. A. Kadam, Y. R. Ma, S. S. Kumbhar, **S. B. Bhosale**, V. V. Patil, V. G. Parale, S. B. Kulkarni, C. D. Lokhande, H. Park, U. M. Patil\*, Impact of Co:Fe cations composition in amorphous and mesoporous cobalt iron phosphate electrocatalysts synthesized by SILAR method on durable electrochemical water splitting, International Journal of Hydrogen Energy, 61 (2024) 162-172 (**I.F- 8.1**).
- 10) S. S. Kumbhar, **S. B. Bhosale**, S. S. Patil, A. Ransing, V. G. Parale, C. D. Lokhande, H.H. Park\* and U. M. Patil\*, Chemical synthesis of binder-free nanosheet-like cobalt vanadium oxide thin film electrodes for hybrid supercapacitor devices, Sustainable Energy & Fuels, (2024) (**I. F. 5**) .
- 11) N. R. Mulla, N. N. Patel, **S. B. Bhosale**, U. M. Patil\*\*, R. S. Patil\*, Morphologically tuned  $\text{MnO}_2$  thin film electrodes prepared by growth kinetic dependent SILAR approach for high-performance extrinsic pseudocapacitors, Journal of Alloys and Compounds, 1006 (2024) 176261 (**I.F.5.8**).

### **Book Chapter (01)**

- 1) S. S. Kumbhar, S. J. Marje, V. V. Patil, **S. B. Bhosale**, S. S. Pujari, J. L. Gunjekar, C. D. Lokhande, U. M. Patil, 1D, 2D and 3D structured chalcogenides for supercapacitor applications. chemically deposited nanocrystalline metal chalcogenide based carbon composite for versatile applications, Springer Nature, ISBN-13: 9783031234002.



**Attended/ Presented, National/International Conference,  
Workshop and Seminar (06)**

- 1) Poster presentation in the International Conference on “Advanced Materials Synthesis, Characterisation and Application-2023 (AMSCA-2023)” held at Savitribai Phule Pune University, Pune, from 21<sup>st</sup> to 24<sup>th</sup> November 2023.
- 2) Oral presentation at the “International Conference on Nanotechnology Addressing the Convergence of Materials Science, Biotechnology, and Medical Science (IC-NACMBM-2024)” held at D. Y. Patil Education Society, Kolhapur, from 12<sup>th</sup> -14<sup>th</sup> February 2024.
- 3) 2<sup>nd</sup> Prize for poster presentation at the National Conference on “Recent Trends in Functional Materials and Their Applications (RTFMA-2024) held at Shardabai Pawar Mahila Arts, Commerce & Science College Shardanagar, Malegoan, Baramati from 13<sup>th</sup> to 14<sup>th</sup> March 2024.
- 4) Attended DST-STUTI-funded one-week training programme on “Hands-on Training on Sophisticated Instruments for Materials Science” organized by Bundelkhand University, Jhansi from 14<sup>th</sup> to 20<sup>th</sup> September 2022.
- 5) Attended workshop & hands-on training on XRD organized by SAIF-CFC under STRIDE programme in the Shivaji University, Kolhapur held from 11<sup>th</sup> to 12<sup>th</sup> November 2021.
- 6) Attended national seminar on “Emerging Nano Materials for Renewable Energy” organized by Sanjay Ghodawat University, Kolhapur, held on 26<sup>th</sup> December 2022.

## **LIST OF ABBREVIATIONS**

<b>AC</b>	Activated Carbon	<b>JCPDS</b>	Joint Committee on Powder Diffraction Standards
<b>BET</b>	Brunauer-Emmett-Teller	<b>LBL</b>	Layer-by-Layer
<b>BJH</b>	Barrett-Joyner-Halenda	<b>MIBs</b>	Metal-Ion Batteries
<b>CBS</b>	Chemical Bath Synthesis	<b>MOCVD</b>	Metal-Organic Chemical Vapor Deposition
<b>CBD</b>	Chemical Bath Deposition	<b>MWCNT</b>	Multi-Walled Carbon Nanotube
<b>CNT</b>	Carbon Nanotube	<b>NF</b>	Nickel Foam
<b>CPs</b>	Conducting Polymers	<b>NMP</b>	N-Methyl 2-Pyrrolidone
<b>CPE</b>	Constant Phase Element	<b>NVO</b>	Nickel Vanadium Oxides
<b>C<sub>sp</sub></b>	Conducting Polymers	<b>OCP</b>	Open Circuit Potential
<b>CV</b>	Cyclic Voltammetry	<b>OHP</b>	Outer Helmholtz Plane
<b>CVD</b>	Chemical Vapor Deposition	<b>PD</b>	Power density
<b>DC</b>	Direct Current	<b>PVA</b>	Polyvinyl Alcohol
<b>DDW</b>	Double Distilled Water	<b>PVDF</b>	Polyvinylidene Fluoride
<b>ED</b>	Energy Density	<b>RF</b>	Radiofrequency
<b>EDLC</b>	Electrochemical Double-Layer Capacitors	<b>R<sub>ct</sub></b>	Charge Transfer Resistance
<b>EDS</b>	Energy-Dispersive Electron Spectroscopy	<b>rGO</b>	Reduced Graphene Oxide
<b>EIS</b>	Electrochemical Impedance Spectroscopy	<b>R<sub>s</sub></b>	Solution Resistance
<b>ESR</b>	Electrochemical Series Resistance	<b>SAED</b>	Selected Area Electron Diffraction
<b>ESS</b>	Energy Storage System	<b>SCs</b>	Supercapacitors
<b>FE-SEM</b>	Field Emission Scanning Electron Microscopy	<b>SE</b>	Specific Energy
<b>GCD</b>	Galvanostatic Charge-Discharge	<b>SILAR</b>	Successive Ionic Layer Adsorption and Reaction
<b>GO</b>	Graphene Oxide	<b>SP</b>	Specific Power
<b>HEV</b>	Hybrid Electric Vehicle	<b>SS</b>	Stainless Steel
<b>HESD</b>	Hybrid Energy Storage Devices	<b>TG</b>	Thermogravimetric
<b>Hg/HgO</b>	Mercury/Mercury Oxide	<b>TMO</b>	Transition Metal Oxides
<b>HR</b>	High-Resolution	<b>TMVOs</b>	Transition Metal Vanadium Oxides
<b>HR-TEM</b>	High-Resolution Transmission Electron Microscopy	<b>W</b>	Warburg
<b>IHP</b>	Inner Helmholtz Plane	<b>XPS</b>	X-ray Photoelectron Spectroscopy
<b>I<sub>p</sub></b>	Ionic Product	<b>XRD</b>	X-ray Diffraction

# **LIST OF FIGURES**

<b>Figure No.</b>	<b>Figure Name</b>	<b>Page No.</b>
<b>Chapter-I: General Introduction and Overview of Literature</b>		
1.1	Comparison of several ESDs using a Ragone plot	3
1.2	Possible applications of SCs	4
1.3	Development of SCs	5
1.4	SCs market size 2021-2030	6
1.5	Schematic representation of the charge storage mechanism in an electrochemical capacitor	8
1.6	Schematic illustration of different charge storage mechanisms of SC electrodes	10
1.7	Illustration of diverse applications of nickel vanadium oxide	15
1.8	Different structures and phases of NVO	16
1.9	Structures of graphene, GO, and rGO	19
<b>Chapter-II: Basics of CBS and SILAR Methods and Characterization Techniques</b>		
2.1	Photograph of instrument for CBS method	35
2.2	Heterogenous nucleation on the surface of the solid surface	37
2.3	Particle growth by aggregation and coalescence process	38
2.4	A schematic representation of the SILAR setup	41
2.5	The schematic of the adsorption process on the adsorbent	42
2.6	Schematic of Helmholtz double layer during the adsorption step in SILAR method	42
2.7	Schematic of excessive ions removal during first rinsing in the second step of the SILAR method	43
2.8	Schematic of solid compound formation during the reaction process in the third step of SILAR method	44
2.9	Schematic of monolayer formation during the second rinsing after the fourth step of the SILAR method	44
2.10	Photograph of SILAR Instrument	45
2.11	Schematic of (a) half-test cell and (b) Full-test cell for electrochemical performance evaluation	52
2.12	The CV plot with forward and reverse scan	53
2.13	Plot of the charge-discharge curve	54
2.14	Nyquist plot and equivalent Randles circuit	55



### Chapter-III: Synthesis of Nickel Vanadium Oxide/rGO Composite Electrodes by CBS Method: Characterizations and Supercapacitive Performance

3.1	Schematic representation of the CBS process for NVO preparation	62
3.2	Photograph of SILAR synthesized NVO thin films for different urea concentrations	63
3.3	Plot of mass loading for C-NV series samples over SS substrates	65
3.4	XRD patterns of C-NV series samples (a) over SS substrate and (b) powder sample	66
3.5	FT-IR patterns for C-NV series samples	67
3.6	XPS spectra of C-NV3 samples (a) survey spectrum, HR spectra of (b) Ni 2p, (c) V 2p, and (d) O 1s	68
3.7	FE-SEM images of sample (a <sub>1</sub> , a <sub>2</sub> ) C-NV1, (b <sub>1</sub> , b <sub>2</sub> ) C-NV2, (c <sub>1</sub> , c <sub>2</sub> ) C-NV3, and (d <sub>1</sub> , d <sub>2</sub> ) C-NV4 at the magnification of X15K and X70K, respectively, and (a <sub>3</sub> -d <sub>3</sub> ) histograms of particles size distribution	69
3.8	Nitrogen adsorption/desorption isotherm of C-NV series (inset: pore size distribution)	71
3.9	(a) Comparative CV curves at 50 mV s <sup>-1</sup> scan rate, (b-e) CV curves of C-NV series samples at different scan rates of 2-100 mV s <sup>-1</sup>	72
3.10	Plot of log (peak current, A g <sup>-1</sup> ) vs log (scan rate, mV s <sup>-1</sup> )	74
3.11	Charge contribution plots of (a) C-NV1, (b) C-NV2, (c) C-NV3, and (d) C-NV4 electrodes	75
3.12	(a) Comparative GCD plots for C-NV series electrodes at 1 A g <sup>-1</sup> current density, GCD plots at various current densities for (b) C-NV1, (c) C-NV2, (d) C-NV3, (e) C-NV4 electrode, and (f) The plot of C <sub>sp</sub> at various current densities (1-5 A g <sup>-1</sup> ) for C-NV series electrodes	76
3.13	The Nyquist plots of C-NV series samples	77
3.14	Plot of capacitive retention and coulombic efficiency vs number of cycles	78
3.15	XRD patterns for GO and rGO	82
3.16	Raman spectrum of rGO	83
3.17	CV curves at various scan rates from 2 to 100 mV s <sup>-1</sup> of rGO electrode	84
3.18	(a) GCD curves at various current densities from 1 to 5 A g <sup>-1</sup> , and (b) The plot of obtained C <sub>sp</sub> values as a function of current densities for rGO electrode	84
3.19	Nyquist plot of rGO electrode (inset equivalent circuit of the	85

	data)	
3.20	Schematic representation of the synthesis of NVO/rGO composite through the CBS method and electrode preparation	89
3.21	XRD patterns for C-rNV series samples	90
3.22	FT-IR spectra of C-rNV series samples	91
3.23	Raman spectra of C-rNV series samples	92
3.24	XPS spectra of C-rNV0 and C-rNV3 samples (a) survey spectrum, HR spectra of (b) Ni 2p, (c) V 2p, (d) O 1s, and (e) C 1s	93
3.25	TG analysis of C-rNV series samples	95
3.26	FE-SEM images of sample (a <sub>1</sub> , a <sub>2</sub> ) C-rNV1, (b <sub>1</sub> , b <sub>2</sub> ) C-rNV2, (c <sub>1</sub> , c <sub>2</sub> ) C-rNV3, (d <sub>1</sub> -d <sub>2</sub> ) C-rNV4, (e <sub>1</sub> -e <sub>2</sub> ) C-rNV5 at the magnification of X5K and X40K, respectively, and (a <sub>3</sub> -e <sub>3</sub> ) histograms of particles size distribution	96
3.27	EDS mapping images of (a) C-rNV0, (b) C-rNV1, (c) C-rNV2, (d) C-rNV3, and (e) C-rNV4 samples	97
3.28	EDS spectra of (a) C-rNV0, (b) C-rNV1, (c) C-rNV2, (d) C-rNV3, (e) C-rNV4 samples	98
3.29	(a-d) HR-TEM images (e) lattice distortion image and interplanar distance calculation using HR-TEM patterns (f) SAED pattern, and (g) EDS elemental mapping for C-rNV3 sample	99
3.30	Nitrogen adsorption-desorption isotherms (BET) and inset pore size distribution (BJH) of (a) C-rNV0, (b) C-rNV1, (c) C-rNV2, (d) C-rNV3, and (e) C-rNV4 samples	100
3.31	(a) Comparative CV curves for C-rNV series electrode at 50 mV s <sup>-1</sup> , CV curves at different scan rates for (b) C-rNV0, (c) C-rNV1, (d) C-rNV2, (e) C-rNV3, and (f) C-rNV4 electrodes	102
3.32	Plot of log (current density, A g <sup>-1</sup> ) vs log (scan rate, mV s <sup>-1</sup> )	103
3.33	Charge contribution plots of (a) C-rNV0, (b) C-rNV1, (c) C-rNV2, (d) C-rNV3, and (e) C-rNV4 electrodes	103
3.34	(a) Comparative GCD curves for C-rNV series electrode at 1 A g <sup>-1</sup> , GCD curves at different current densities for (b) C-rNV0, (c) C-rNV1, (d) C-rNV2, (e) C-rNV3, and (f) C-rNV4 electrodes	105
3.35	The plot of C <sub>sp</sub> at various current densities for C-rNV series electrodes	106
3.36	Nyquist plots for C-rNV series electrodes	106
3.37	Plot of capacitive retention and coulombic efficiency vs number of cycles	107

## Chapter-IV: Synthesis of Nickel Vanadium Oxide/rGO Composite Electrodes by SILAR Method: Characterizations and Supercapacitive Performance

4.1	Schematic diagram of SILAR method for NVO thin film deposition	114
4.2	Photograph of SILAR synthesized NVO thin films for different dipping time	114
4.3	Plot of mass loading for S-NV1, S-NV2, and S-NV3 samples	116
4.4	XRD pattern (a) on SS substrate, and (b) Powder sample for S-NV1, S-NV2, and S-NV3	117
4.5	FT-IR spectra for S-NV1, S-NV2, and S-NV3 samples	118
4.6	XPS spectra for S-NV2 sample (a) survey spectrum, (b) Ni 2p, (c) V 2p, and (d) O 1s	119
4.7	FE-SEM images of sample (a <sub>1</sub> , a <sub>2</sub> ) S-NV1, (b <sub>1</sub> , b <sub>2</sub> ) S-NV2, and (c <sub>1</sub> , c <sub>2</sub> ) S-NV3 at the magnification of X5K and X40K, respectively, and (a <sub>3</sub> , b <sub>3</sub> , c <sub>3</sub> ) histograms of particles size distribution	121
4.8	Elemental mapping of the sample (a-d) S-NV1, (e-h) S-NV2 and (i-l) S-NV3	122
4.9	(a-d) HR-TEM images, (e) Lattice distortion images and interplanar distance calculations from the HR-TEM images, and (f) SAED patterns for the S-NV2 sample	123
4.10	Nitrogen adsorption/desorption isotherm of (a) S-NV1, (b) S-NV2, and (c) S-NV3 (inset: pore size distribution)	124
4.11	(a) Comparative CV curves at 20 mV s <sup>-1</sup> scan rate of NV series electrodes, CV curves at various scan rates from 2 to 50 mV s <sup>-1</sup> (a) S-NV1, (b) S-NV2, and (c) S-NV3	126
4.12	Plot of log (peak current, A g <sup>-1</sup> ) vs log (scan rate, mV s <sup>-1</sup> ) for S-NV series electrodes	127
4.13	The plot of surface and diffusive charge contribution with respect to scan rate for (a) S-NV1, (b) S-NV2, and (c) S-NV3 electrodes	127
4.14	(a) Comparative GCD curves of S-NV series electrodes at 1 A g <sup>-1</sup> current density, GCD curves at various current densities from 1 to 3 A g <sup>-1</sup> of (b) S-NV1, (c) S-NV2, and (d) S-NV3 electrodes	128
4.15	The plot of current density as a function of C <sub>sp</sub> for S-NV1, S-NV2, and S-NV3 electrodes	129
4.16	The Nyquist plots of S-NV1, S-NV2, and S-NV3 electrodes and the fitted equivalent circuit for the EIS data is an inset of figure	130
4.17	Plot of capacitive retention and coulombic efficiency versus	131



	number of cycles	
4.18	Schematic representation of SILAR deposition for the NVO/rGO composite thin films	133
4.19	(a) Photograph of deposited S-rNV series thin films, and (b) Mass loading per unit area of S-rNV series samples	133
4.20	XRD Patterns (a) on SS substrate, and (b) Powder sample of S-rNV series	135
4.21	FT-IR spectra of S-rNV series	136
4.22	Raman spectra of S-rNV series	137
4.23	XPS spectra of S-rNV0 and S-rNV3 samples (a) survey spectrum, HR spectra of (b) Ni 2p, (c) V 2p, (d) O 1s, and (e) C 1s	138
4.24	TG analysis of S-rNV series samples	139
4.25	FE-SEM images of (a <sub>1</sub> -a <sub>2</sub> ) S-rNV0, (b <sub>1</sub> -b <sub>2</sub> ) S-rNV1, (c <sub>1</sub> -c <sub>2</sub> ) S-rNV2, (d <sub>1</sub> -d <sub>2</sub> ) S-rNV3, (e <sub>1</sub> -e <sub>2</sub> ) S-rNV4, (f <sub>1</sub> -f <sub>2</sub> ) S-rNV5, and (a <sub>3</sub> -f <sub>3</sub> ) Histograms of average particle size for S-rNV series samples	140
4.26	EDS mapping images of (a) S-rNV0, (b) S-rNV1, (c) S-rNV2, (d) S-rNV3, (e) S-rNV4, and (f) S-rNV5 samples	141
4.27	EDS spectra of (a) S-rNV0, (b) S-rNV1, (c) S-rNV2, (d) S-rNV3, (e) S-rNV4, and (f) S-rNV5 samples	142
4.28	(a-d) HR-TEM images, (e) Lattice distortion images and interplanar distance calculations from the HR-TEM images, (f) SAED patterns for S-rNV3, and (g) HR-TEM elemental mapping images S-rNV3	143
4.29	Nitrogen adsorption-desorption isotherms (BET curves) inset pore size distribution (BJH) curves of (a) S-rNV0, (b) S-rNV1, (c) S-rNV2, (d) S-rNV3, (e) S-rNV4, and (f) S-rNV5 samples	144
4.30	CV curves of (a) S-rNV0, (b) S-rNV1, (c) S-rNV2, (d) S-rNV3, (e) S-rNV4, (f) S-rNV5 electrodes, (h) Plot of log (current density, A g <sup>-1</sup> ) vs log (scan rate, mV s <sup>-1</sup> )	146
4.31	Charge contribution plots of (a) S-rNV0, (b) S-rNV1, (c) S-rNV2, (d) S-rNV3, (e) S-rNV4, and (f) S-rNV5 electrodes	147
4.32	Comparative GCD plots of S-rNV series and GCD plots of (a) S-rNV0, (b) S-rNV1, (c) S-rNV2, (d) S-rNV3, (e) S-rNV4, and (f) S-rNV5 electrodes at various current densities (1-3 A g <sup>-1</sup> )	148
4.33	The plot of C <sub>sp</sub> at various current densities for S-rNV series samples	149
4.34	Nyquist plots for S-rNV series electrodes	150
4.35	Stability plots for S-rNV3 samples	151

## Chapter-V: Hybrid Supercapacitor Devices: Fabrication and Performance Evaluation

5.1	Schematic representation of HASc device	157
5.2	(a) Schematic representation of HSSc device	158
5.3	(a) CV and (b) GCD curves of C-HASc device at different voltages	159
5.4	(a) CV curves at different scan rates and (b) GCD curves at different current densities for C-HASc device	160
5.5	(a) Plot of $C_{sp}$ as a function of current density and (b) Ragone plot for C-HASc device	161
5.6	(a) Nyquist plot of C-HASc device and (b) plot of capacitive retention and coulombic efficiency vs number of cycles	161
5.7	Photograph of solid-state device fabrication	162
5.8	(a) CV and (b) GCD curves at different voltage windows (c) CV curves at different scan rates and (d) GCD curves at different current densities for C-HSSc device	162
5.9	(a) Plot of $C_{sp}$ as a function of current density and (b) Ragone plot for C-HSSc device	163
5.10	(a) Nyquist plot of C-HSSc device, (b) plot of capacitive retention and coulombic efficiency vs cycle number, (c) demonstration of glowing LED table lamp using serially connected C-HSSc devices	164
5.11	(a) CV and (b) GCD curves of S-HASc device at different voltage windows	165
5.12	(a) CV curves at different scan rates and (b) GCD curves at different current densities for S-HASc device	166
5.13	(a) Plot of $C_{sp}$ as a function of current density and (b) Ragone plot for S-HASc device	166
5.14	(a) Nyquist plot of S-HASc device and (b) Plot of capacitive retention and coulombic efficiency vs number of cycles	167
5.15	Photograph of solid-state device fabrication	168
5.16	(a) CV and (b) GCD curves at different voltage windows, (c) CV curves at different scan rates, and (d) GCD curves at different current densities for S-HSSc device	168
5.17	a) Plot of $C_{sp}$ as a function of current density and (b) Ragone plot for S-HSSc device	169
5.18	(a) Nyquist plot of S-HSSc device (b) plot of capacitive retention and coulombic efficiency vs number of cycles, and (c) demonstration of powering an LED table lamp using two serially connected S-HSSc devices	170

## Chapter-VI: Summary and Conclusions

6.1	Demonstration of glowing LED table lamp using serially connected C-HSSc devices	178
6.2	Demonstration of glowing LED table lamp using serially connected S-HSSc devices	179
6.3	FE-SEM images for (a) C-rNV3 and (c) S-rVN3 samples. The plots of $C_{sp}$ vs current densities for (b) C-rNV3 and (d) S-rNV3 electrodes	179

## **LIST OF TABLES AND CHARTS**

Table 1.1	Comparative overview of the literature on electrochemical capacitive performance of NVO-based electrodes	21
Table 1.2	Comparative overview of the literature on electrochemical capacitive performance of NVO-based composite electrodes	23
Table 1.3	An overview of the literature on NVOs and their composites-based symmetric and asymmetric hybrid devices	25
Table 3.1	Preparative parameters for the synthesis of NVO thin films and corresponding notations	63
Table 3.2	EIS fitted circuit parameters for C-NV series electrodes	78
Table 3.3	Preparative parameters for the CBS of NVO/rGO composite and corresponding notations	88
Table 3.4	EIS fitted circuit parameters for C-rNV series electrode	107
Table 4.1	Preparative parameters for the synthesis of NVO thin films and corresponding notations	115
Table 4.2	Electrochemical impedance spectroscopic fitted circuit parameters for Nyquist plots of S-NV1, S-NV2, and S-NV3 electrodes	130
Table 4.3	Preparative parameters for the synthesis of NVO/rGO thin films and corresponding notations	134
Table 4.4	EIS fitted circuit parameters for Nyquist plots of S-rNV series electrodes	150
Table 6.1	Electrochemical performance of fabricated hybrid devices	180
Chart 1.1	Classification of SCs	9
Chart 2.1	Thin film deposition methods	34



# **CONTENTS**

<b>Chapter No.</b>	<b>Chapter Name</b>	<b>Page No.</b>
I	General Introduction and Overview of Literature	1-32
II	Basics of CBS and SILAR Methods and Characterization Techniques	33-58
III	Synthesis of Nickel Vanadium Oxide/rGO Composite Electrodes by CBS Method: Characterizations and Supercapacitive Performance	59-110
IV	Synthesis of Nickel Vanadium Oxide/rGO Composite Electrodes by SILAR Method: Characterizations and Supercapacitive Performance	111-154
V	Hybrid Supercapacitor Devices: Fabrication and Performance Evaluation	155-172
VI	Summary and Conclusions	173-180
VII	80_Recommendation	181-182

# CHAPTER-I

---

## General Introduction and Overview of Literature

---

# Chapter-I

## General Introduction and Overview of Literature

Sr. No.	Title		Page No.
1.1	Energy storage systems		1
1.2	Supercapacitors		4
	1.2.1	Historic overview and recent development	4
	1.2.2	Demand of supercapacitor	6
	1.2.3	Working principle of supercapacitor	7
	1.2.4	Classification of supercapacitor	8
	1.2.5	Electrode materials for supercapacitor	12
1.3	General outlook and retrospective of nickel vanadium oxide		14
	1.3.1	Structures and phases of nickel vanadium oxide	16
1.4	General outlook and retrospective of reduced graphene oxide		18
	1.4.1	Properties of reduced graphene oxide	20
1.5	Overview of Literature		20
	1.5.1	Nickel vanadium oxide-based electrode materials for supercapacitor application	20
	1.5.2	Nickel vanadium oxide-based composite electrode materials for supercapacitor Application	22
	1.5.3	Electrochemical performance of nickel vanadium oxide and their composite-based supercapacitor devices	25
1.6	Orientation and purpose of the thesis		27
1.7	References		29

## 1.1 Energy storage systems

*A contented day, where you sit peacefully in a controlled atmospheric room, the darkness is dispelled with the flick of a switch, and coffee is available at the button press, something you have that can quietly roll your eyes on this page. Yes, it is 'energy' that powers your world for granted. But have you ever thought of the life of humankind without energy? It began at the beginning of the cosmos, and the scientists uncovered the narrative of 'energy', just like the blink of an eye.*

Approximately 1.5 million years ago, humans made a pivotal discovery: they learned how to create and use fire. This breakthrough had far-reaching consequences, triggering a revolution in the way humans harnessed and utilized energy. Since then, energy has been essential in propelling the economic and social advancement of human societies. Around 300 B.C.E., humans began to explore and utilize a diverse range of energy sources while endeavoring to discover novel forms of energy. During the 19<sup>th</sup> century, there occurred a second energy revolution for humankind with the widespread adoption of fossil fuels as an energy source [1]. At present, fossil fuels, comprising coal, oils, and natural gases, constitute the primary source of energy for the world.

With the growing demand for energy, researchers are focused on developing energy storage devices (ESDs) that are more efficient and cost-effective. This is because energy can often be rare when it is needed the most. As a result, there is a growing demand for more affordable and efficient ESDs to address the energy crisis. So, extensive research has been conducted on electrical energy storage materials to address the growing need for storage systems that offer high-power, high-energy capacity, and affordability. In today's world, energy storage has become a crucial necessity due to energy crises and the limited supply of fossil fuels [2]. The insufficient availability of fossil fuels, the environmental pollution caused by them, and their increasing cost have compelled scientists to explore readily accessible, cost-effective, maintenance-free, and environmental friendly ESDs [3].

Wind energy, solar energy, and tidal energy are not consistently available at all times, and their availability varies across region to region. To address this challenge, researchers have dedicated efforts to develop efficient ESDs that can store intermittent energy in cost-effective storage systems. These devices aim to provide a reliable

solution for storing renewable energy in a manner that is both efficient and affordable [4].

Fuel cells, batteries, and supercapacitors (SCs) are examples of electrochemical ESDs that store charges via different mechanisms. For instance, fuel cells rely on a liquid electrolyte to store electric charge during a chemical reaction that occurs during charging. However, a significant drawback of fuel cells is the necessity for a continuous fuel supply, which imposes a limitation on their practical use. Additionally, the supply of hydrogen as a fuel source possesses safety concerns and is expensive. Consequently, the utilization of fuel cells alone may not sufficiently meet the requirements of electrical ESDs [5]. Moreover, batteries exhibit diverse electrolyte characteristics, with liquid electrolytes being common, while dry batteries typically employ dry powder electrolytes. The process of charging and discharging a battery involves a redox reaction, where the transformation of electrical energy into chemical energy while charging and then reversed into electrical energy during discharging. Two primary categories of batteries exist: disposable (primary cells) and rechargeable (secondary cells). Primary cells, or disposable cells, rely on dry materials that gradually release electrical energy until fully discharged, with no option for recharging. In contrast, secondary cells, or rechargeable cells, undergo reversible chemical reactions during the charging and discharging cycles. Batteries are widely used in numerous applications like laptops, cell phones, and automobiles. However, batteries are subject to limitations, including lower specific power (SP) and a reduced cycle life, [6, 7].

Ordinary capacitors are constructed using various electrode materials and incorporate dielectric substances. These capacitors serve as ESD, akin to temporary batteries. The charge storage capacity of capacitors typically falls within the range of  $10^{-6}$  to  $10^{-3}$  Farads [8]. Capacitors play two pivotal roles in electronic circuits. Firstly, they facilitate the charging or discharging of electricity, serving various purposes within circuits. For instance, capacitors are employed to smooth power supply circuits, act as backup circuits for microcomputers, and enable the more organized flow of electricity by regulating charging or discharging periods through timer circuits. Secondly, capacitors serve as effective tools for blocking direct current (DC) flow within circuits. They are particularly useful in eliminating or filtering out specific frequencies, making them highly suitable for applications where only the presence of certain frequencies is desired. However, capacitors do possess a limitation: they store



a relatively small amount of electrical energy [9]. Consequently, capacitors are not well-suited where high energy is required.

Contemporary high-power devices necessitate substantial energy delivered rapidly, a demand that traditional batteries and capacitors struggle to meet. To address these challenges, SCs have emerged as a promising solution over the past few decades, capable of fulfilling the key requirements of conventional ESDs. The SCs, sometimes called electrochemical capacitors or ultracapacitors, stand out by attaining higher capacitance values through the use of materials which having a high surface area and a thin layer of electrolytic dielectrics. This enables them to store significant amounts of energy, surpassing conventional capacitors, while also providing high power capabilities, surpassing batteries. Consequently, SCs find application in scenarios that necessitate the rapid delivery of high energy within shorter time frames while maintaining a satisfactory cycle life [10].

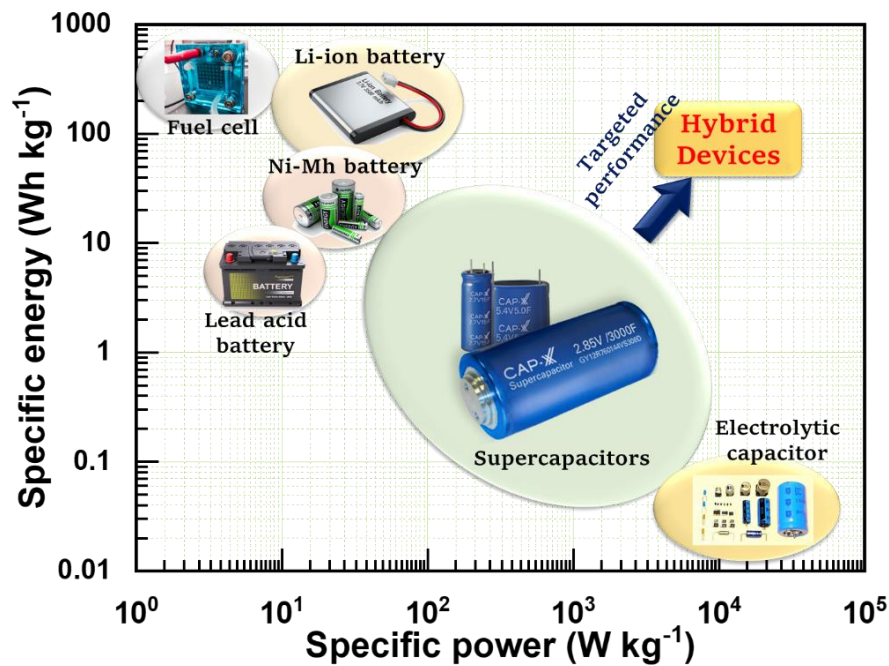


**Figure 1.1:** Comparison of several ESDs using a Ragone plot

Figure 1.1 presents a Ragone plot that depicts the performance of various ESDs. This graph provides insights into the amount of energy ( $\text{Wh kg}^{-1}$ ) exhibited by various ESDs at their corresponding power levels ( $\text{W kg}^{-1}$ ), indicating their energy delivery rate. The comparison highlights the growing interest in SCs, attributed to their high SP exceeding  $10 \text{ kW kg}^{-1}$ , along with moderate specific energy (SE) ( $\sim 10 \text{ Wh kg}^{-1}$ ) [11]. Furthermore, the plot (Figure 1.1) shows that SCs occupy an intermediate position

between batteries and capacitors, effectively bridging the gap between these two technologies.

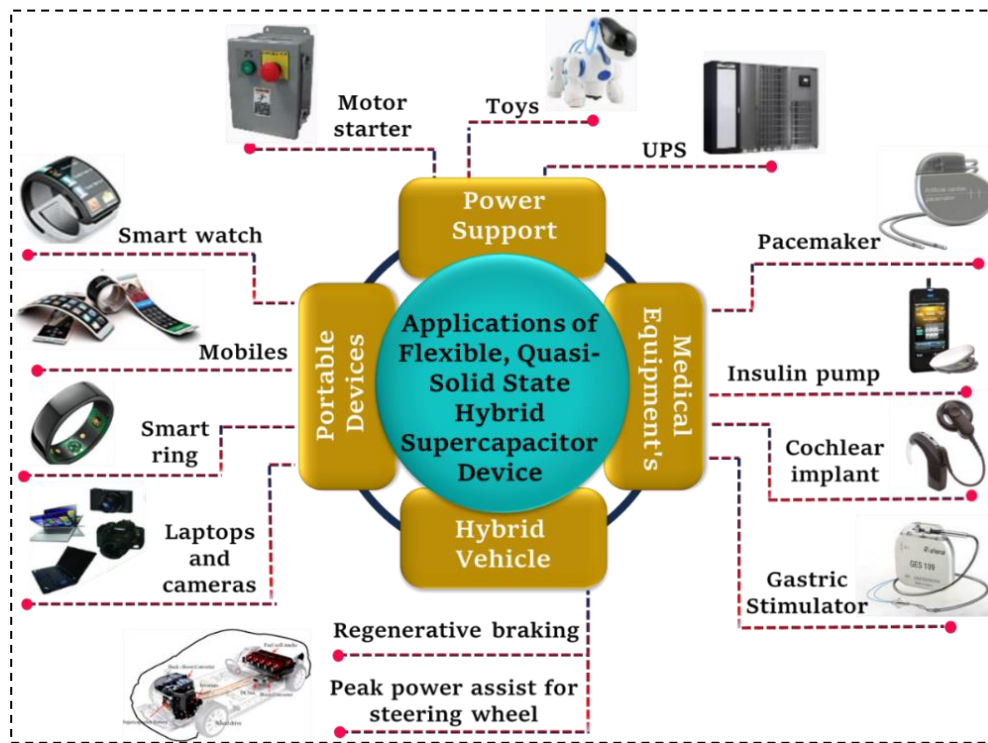


**Figure 1.2:** Possible applications of SCs

The rapid recharge speed, high SP, and remarkable cycle lifespan of SCs have made them a viable option for energy storage. These unique attributes have attracted considerable interest in power source applications (Figure 1.2), including hybrid electric vehicles (HEVs) and portable electronics [12]. Furthermore, SCs work well in high-power applications like light amplification by stimulated emission of radiation (LASER), computer memory, backup systems for pulsed light generators, camera flashes, etc.

## 1.2 Supercapacitors

### 1.2.1 Historical overview and recent development

The developmental trajectory of SCs unfolds through the systematic exploration and revelation of charge storage mechanisms (Figure 1.3). The phenomena of electrical charge storage resulting from triboelectric charging were known to the ancient Greeks. However, the Leyden jar's development in 1745 marked the beginning of the understanding of interfacial double-layer production [13] and was similar to the operation of contemporary electrostatic capacitors. According to Helmholtz, the

electrochemical double-layer formation occurs when the redistribution of electrolytic ions with opposite charges counterbalances a charged electrode surface.

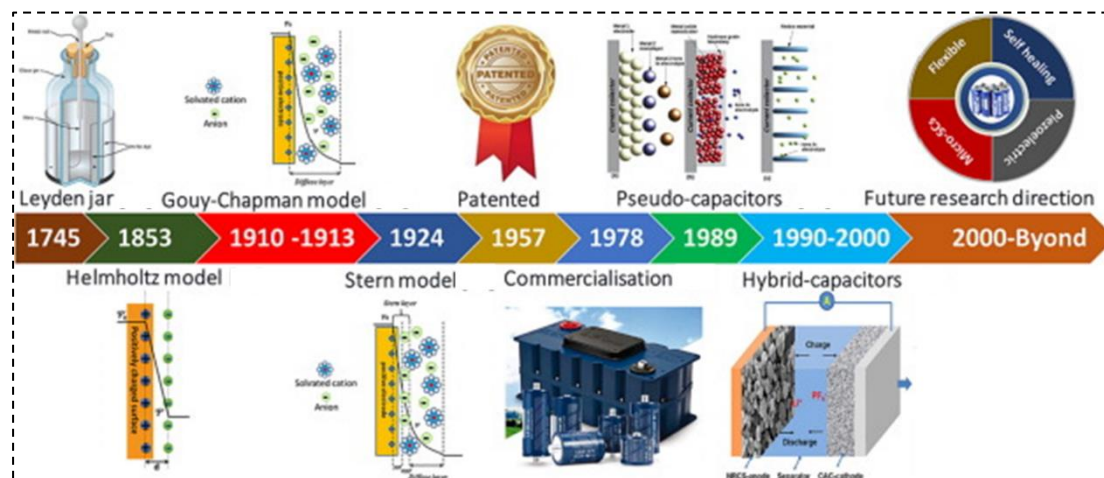


**Figure 1.3:** Development of SCs [14]

Expanding on this model, Gouy-Chapman proposed that electrolytic ions behave as highly mobile point charges. They suggested that the double layer is more diffuse compared to the compact structure described by Helmholtz. Helmholtz and Gouy-Chapman, further made advancements in understanding the intricacies of the double-layer phenomenon. Over the years, researchers have delved deeper into the composition and behavior of the double layer, uncovering additional complexities [15]. The models proposed by Helmholtz and Gouy-Chapman fell short of accurately predicting the experimental capacitance observed in SCs. It was the Stern-Gerlach model that successfully combined elements from both models to provide a more accurate estimation [16]. This combination of theories represented a significant breakthrough in comprehending the behavior of the double layer.

Becker filed the first patent for a SC cell in 1957 while working at ‘General Electric Corporation.’ Later, in 1978, commercialization efforts were initiated by the standard oil company of ohio [17, 18]. Since then, SC technology has undergone significant advancements. Then B. Conway introduced the term ‘pseudocapacitance’ in 1989 to describe capacitive energy storage that involves electrochemical charge transfer [19]. Furthermore, the combination of electrochemical double-layer capacitors (EDLCs) and pseudocapacitors in a single cell in mid-1990 known as hybrid SC, was introduced to improve the SE of SCs [20]. The EDLCs currently lead the SC market, but research is actively exploring hybrid and asymmetric configurations.

The commercialization of SCs has resulted in the advancement of several SC devices, with ongoing research and development aimed at introducing new types of SCs to the market. The projected growth of the SCs market signifies its increasing importance, particularly in the transportation sector.

### 1.2.2 Demand of supercapacitor

The growing demand for energy conversion solutions and high storage capabilities, particularly in automotive, energy, and consumer electronics applications, has been driven by the widespread adoption of SCs in HEVs, trains, aircraft, smart wearables, wind turbines, grid energy storage systems (ESSs), and rail-wayside applications. This trend is a crucial factor in propelling the expansion of the SC industry [21]. As the world transitions towards cleaner energy sources, there has been a substantial increase in the establishment of renewable energy power plants worldwide. The rising demand for renewable energy solutions is a major driver for the growth of the SCs market. SCs find extensive use in various ESSs due to their ability to offer higher SP compared to batteries and higher SE compared to traditional capacitors. Solar and wind power plants are prominent end users of SCs. These capacitors are widely utilized to power microgrids for the generation of renewable energy. Solar photovoltaic panels and solar lighting systems are areas where SCs serve as reliable energy storage solutions [22]. Furthermore, SCs have become the dominant technology for large pitch control applications in wind turbines, and the increasing global adoption of wind energy is expected to drive the growth of the SCs market further.

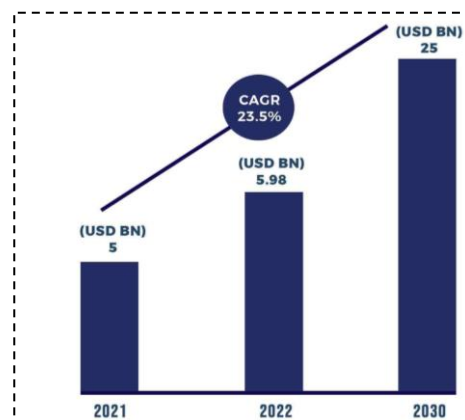


**Figure 1.4:** SCs market size 2021-2030 [23]

The Pacific region is projected to be a major contributor to the growth of the SC market in the coming years. The surge in industrialization and infrastructural

advancements has propelled the consumer electronics and automotive industries in China, leading to an increased demand for SCs in the country. As the largest low-cost vehicle manufacturer worldwide, China's automotive sector is witnessing a rising need for SCs, thus driving market growth. Furthermore, Japan and South Korea have witnessed a notable increase in the establishment of manufacturing facilities, presenting lucrative opportunities for the market [23]. According to market research reports, the global SC market was valued at around US\$ 5 billion in 2021. It is projected to reach a market size of approximately US\$ 25 billion by 2030, growing at a compound annual growth rate of around 23.5% during the forecast period [24]. The SCs market size from 2021 to 2030 is presented in Figure 1.4. Moreover, advancements in SC technology, such as the development of graphene-based SCs and HSCs, are expected to drive market growth further. These technological advancements aim to enhance the SE and performance of SCs, enhancing their versatility across diverse applications. In conclusion, the SC market is experiencing steady growth and is poised for substantial expansion in the coming years. Factors such as a surge in demand for ESDs, the growing popularity of HEVs, and technological advancements are expected to drive the market size and propel the adoption of SCs across various industries.

### **1.2.3 Working principle of supercapacitor**

Both conventional capacitors and electrochemical capacitors operate based on similar charge storage mechanisms, but their distinguishing factor lies in the separating medium they employ. In traditional capacitors, energy is stored within a dielectric material positioned between two metallic plates, which act as the device's terminals. In contrast, electrochemical capacitors store energy by forming the development of an electrochemical double-layer at the boundary between the electrode-electrolyte. This double-layer forms when the electrolyte contacts with an electrode, consisting of a few Angstroms of separation, depending on the electrolyte used [25]. Figure 1.5 illustrates the mechanism of energy storage in electrochemical capacitors schematically. Electrochemical capacitor comprises two separate electrodes that are coated with electroactive materials, and a separator of the porous membrane with electrolyte separates these electrodes. When the electroactive materials come into contact with the electrolyte, an electrochemical double-layer forms, enabling the storage of electrochemical energy.



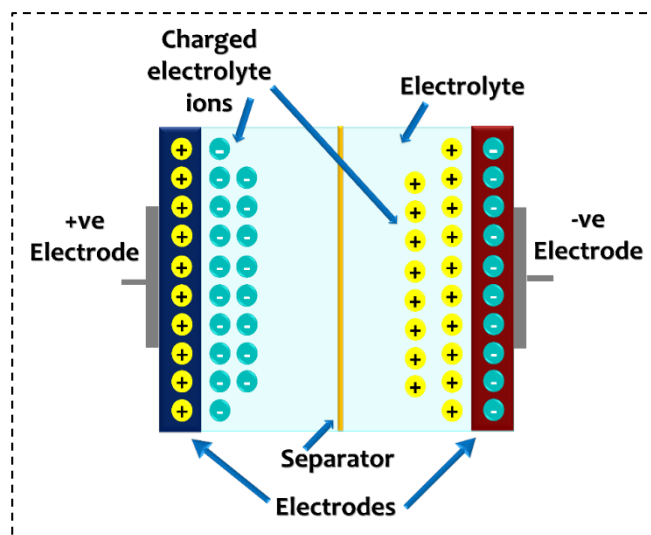


**Figure 1.5:** Schematic representation of the electrochemical charge storage mechanism

When the electrode surface of an electrochemical capacitor comes into contact with the electrolyte, a layer of charges accumulates on both sides of the interface between the electrode-electrolyte. The accumulation of these charges, considering the operating potential, determines the total charge stored, which is commonly referred to as the capacitance [26] and it is given by equation 1.1,

$$C = \frac{Q}{V} \quad (1.1)$$

In the context of an electrochemical capacitor, capacitance ( $C$ ) is described as the amount of charge stored ( $Q$ ) per unit of applied potential ( $V$ ) measured in Farad (F). The various factors influence the  $C$  in an electrochemical capacitor. One of these factors is the thickness of the ions layer adsorbed over the surface ' $d$ ', where the thinner layers result in a higher  $C$ . Conversely, a thicker layer would lead to a lower  $C$  [27], according to equation 1.2,

$$C = \frac{\epsilon_r}{d} A \quad (1.2)$$

Where, ' $\epsilon_r$ ' is the relative permittivity, and ' $A$ ' is the specific surface area of the active electrode.

#### 1.2.4 Classification of supercapacitor

The rapid progress and advancements in SC technology have posed significant challenges in establishing a universally accepted terminology. The continuous evolution of these devices has led to varying definitions and terminology used over the years for classifying SCs. As a result, there is a lack of consensus in the scientific

community regarding a standardized classification system. According to Chart 1.1, electrochemical SCs can be subdivided into the following categories EDLCs, pseudocapacitors, and hybrid capacitors depending on their mechanism of storing charges. This charge storage is employed by these SCs and can be categorized as either faradic, non-faradic, or a combination of both. In the faradic process, charge storage occurs through redox reactions that occur at the interfaces of electrode-electrolyte [28–30]. These reactions involve the transfer of charge, enabling the storage of energy.

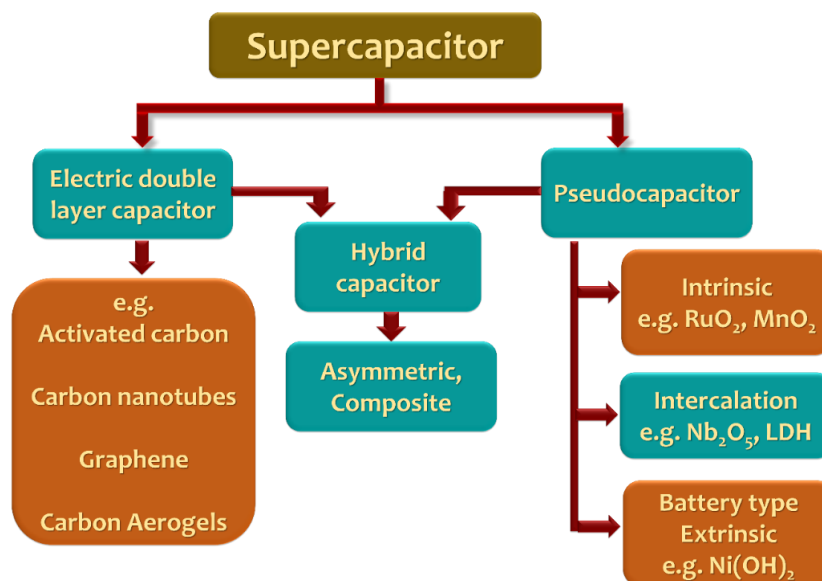


**Chart 1.1:** Classification of SCs

On the other hand, in the non-faradic process, no chemical reactions occur. Accumulation of charges on the surface of the electrode physically and do not entail the breaking or forming of chemical bonds. EDLCs, which rely on electrostatic charge separation, belong to the non-faradaic class. In these capacitors, charges are stored electrostatically in Helmholtz double layer and diffuse layer generally formed by carbonaceous materials [31–33]. This non-faradic mechanism allows for high-speed charge and discharge cycles without chemical changes.

#### **A. Electrochemical double-layer capacitor (EDLC)**

The EDLCs consist of electrodes that are typically made of carbon. The charge is stored non-faradaically, functioning similarly to a conventional capacitor (Figure 1.6 (a)). Consequently, no charge transfer between the electrolyte and the electrodes. Upon applying a voltage, ions from the electrolyte migrate through the separator toward the oppositely charged electrodes due to electrostatic attraction, where they adsorb onto the

electrode surfaces without any chemical reactions or phase transformation. The non-faradaic behavior contributes to the exceptional reversibility of charge storage, which is responsible for the high cyclic stability observed in EDLC electrodes [10, 34, 35]. These capacitors demonstrate stable performance over numerous charge-discharge cycles, with a potential of up to  $10^6$  cycles. The outstanding cyclic stability of EDLCs makes them ideal for use in environments where maintenance is challenging, specifically in remote areas. Moreover, the affordability and well-developed synthesis methods of carbon-based electrode materials contribute to their advantages over other materials. Different forms of carbon, including carbon nanotubes (CNTs), activated carbon (AC), carbon aerogels, and graphene, are employed in EDLC electrodes for charge storage [10, 36]. The remarkable properties of graphene and its derivatives have garnered significant attention in this field.

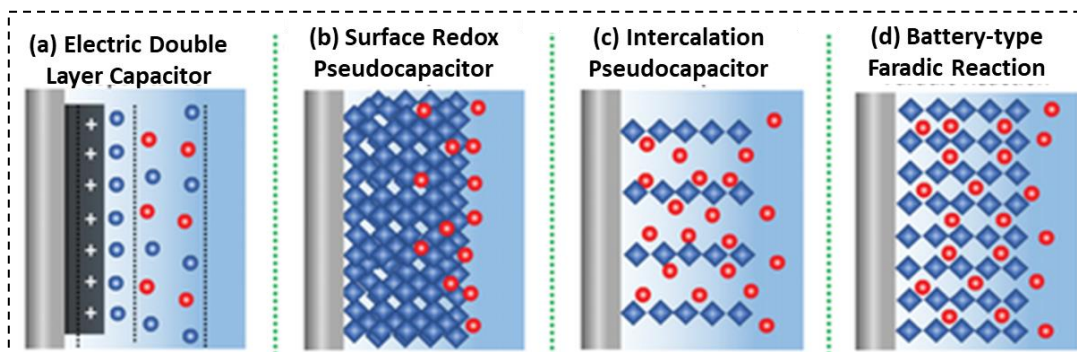


**Figure 1.6:** Schematic illustration of different charge storage mechanisms of SC electrodes [30]

## B. Pseudocapacitor

In pseudocapacitors, charge storage occurs via a faradaic mechanism that involves rapid and reversible oxidation-reduction (redox) reactions at the interface between the electrode-electrolyte. The mechanism of charge storage in the pseudocapacitor electrode is schematically depicted in Figure 1.6 (b-d). This faradaic interaction allows pseudocapacitors to achieve greater specific capacitance ( $C_{sp}$ ) and SE compared to EDLCs. Unlike EDLCs, which primarily depend on ion accumulation at the interface, pseudocapacitors rely on ion exchange between the electrolyte and electrode for charge storage [30, 37].

The performance of pseudocapacitors is greatly influenced by a number of variables, including the particle's size and shape, the active material's surface area and conductivity, and the kind of electrolyte used. The charge storage process in

pseudocapacitors involves intercalation/deintercalation processes and redox reactions, which set them apart as a distinct category of ESDs. Pseudocapacitors are classified into different types based on their storing charge mechanisms: (a) intrinsic pseudocapacitors, (b) intercalation-type pseudocapacitors, and (c) extrinsic pseudocapacitors [30, 38].

**a. Intrinsic pseudocapacitor**

Trasatti [39] initially discovered the pseudocapacitive properties of ruthenium dioxide ( $\text{RuO}_2$ ) and observed quasi-rectangular type cyclic voltammetry (CV) curves, similar to those seen in EDLC materials. In intrinsic pseudocapacitive materials, charge storage occurs through both the double-layer effect and surface redox mechanisms on or near the material's surface as shown in Figure 1.6 (b). Certain transition metal oxides (TMOs) show intrinsic pseudocapacitive behavior that can be attributed to their ability to exist in multiple valence states. The oxidation-reduction reactions occurring at the electrode surface enhance the performance of these materials, making them superior to EDLCs [30]. Additionally, they possess the ability to store high energy and exhibit excellent charging-discharging rates.

**b. Intercalation pseudocapacitor**

The concept of intercalation pseudocapacitors, where charge is stored faradaically through the insertion of electrolyte ions into the layers of a material without resulting in a phase transition, was studied by Augustyn et al. [40]. The structural phase of the electrode material is constant throughout the electrochemical redox processes, which is an essential feature of intercalation pseudocapacitors [41]. In intercalation pseudocapacitors, charge storage extends beyond the material's surface, engaging the bulk of the material in electrochemical reactions as depicted in Figure 1.6 (c). The materials with large interplanar spacing, such as layered double hydroxides,  $\text{Nb}_2\text{O}_5$ , and  $\text{V}_2\text{O}_5$  exhibit intercalation-type pseudocapacitive behavior.

**c. Extrinsic pseudocapacitor**

Augustyn et al. [40] reviewed materials exhibiting battery-type characteristics, which displayed well-defined redox peaks in CV and distinct charge-discharge plateaus in GCD in bulk form, suggesting their potential for battery applications. However, these materials undergo a transformation into pseudocapacitive behavior when their particle size is reduced to the nanoscale [41]. This phenomenon was defined as 'extrinsic

pseudocapacitors.’ The intrinsic phase change property of battery-type materials is overcome when they are reduced to nanosize, resulting in shorter ion diffusion lengths and the manifestation of pseudocapacitive behavior as illustrated in Figure 1.6 (d). When the dimensions of these materials are reduced, their typical battery-type characteristics give way to a surface-dominant ion storage mechanism, thus exhibiting pseudocapacitive behavior for instance nanosized nickel cobalt-based materials demonstrating extrinsic pseudocapacitive behavior [42].

### **C. Hybrid capacitor**

The EDLCs and pseudocapacitors possess complementary merits and demerits, prompting researchers to explore the combination of both systems in order to capitalize on their advantages and address the limitations of SCs [43]. The system can be achieved by integrating electrodes with one EDLC-type and another one with pseudocapacitive-type materials. Numerous studies have extensively investigated such combinations to harness the benefits of both mechanisms.

In these hybrid capacitor systems, both mechanisms coincide, giving rise to the term ‘hybrid capacitor [44]. When carbon-based materials are combined with metal oxides, the resulting electrode exhibits a merged nature, integrating both charge storage mechanisms into a single entity. SCs made from these composite electrodes are referred to as HSCs. For another kind of HSCs, one electrode operates with pseudocapacitive characteristics, while the other functions with an EDLC capacitive behavior. This hybrid arrangement delivers high SE, comparable to batteries, along with the high SP performance typical of capacitors, and it improves cycle life and can serve as a bridge between batteries and SCs [45]. In comparison to pseudocapacitors and EDLCs, respectively, they are appealing choices for enhanced energy storage and stability.

#### **1.2.5 Electrode materials for supercapacitor**

The choice of electrode materials is essential in storing charges and defining the operating potential range. Therefore, from the perspective of materials, the features that determine the proper suitability of an electrode material are listed below,

- Electronic and ionic conductivity: Restricted electron/ion conduction across the electrode materials results in a larger electrochemical series resistance (ESR), leading to low  $C_{sp}$ . To overcome this challenge, it is essential to select electrode

materials that exhibit high electronic/ionic conductivity. Moreover, binder-free design of materials is a vital solution for improving conductivity[46].

- Chemical and mechanical stability: The electrode material's mechanical and chemical strength plays a major role in determining the cyclic stability of an SC.
- Surface area: In EDLCs or pseudocapacitors, most of the charges are stored at or near the electrode surface, therefore, preparing nanostructured materials is essential since it influences the surface area.
- Toxicity and cost-effectiveness: The affordability and environmental impact of the active materials used in electrode design must be considered during material selection.

#### **A. Carbon-based materials**

The twenty-first century is known as the 'carbon age' because almost all new energy technologies, such as batteries, SCs, and hydrogen storage devices use carbon as their fundamental component. The most promising choices for negative materials in HSCs are carbonaceous materials including AC, CNTs, graphene, carbon aerogels, etc. because of their abundance, affordability, low toxicity, and environmental friendliness in addition to their superior mechanical stability and electronic conductivity [35, 47]. Rather than in the bulk of the material, carbon compounds frequently store charges largely in an electrochemical double-layer generated at the electrode-electrolyte interface. Capacitance is primarily influenced by the surface area available for interaction with electrolyte ions. These materials are often utilized in EDLCs owing to their high surface area and favorable surface chemistry. Additionally, the excellent electrical conductivity of carbon-based materials is a key factor in adjusting electrode properties to achieve optimal SC performance.

#### **B. Conducting polymers**

Conducting polymers (CPs) are regarded as promising materials due to their high pseudocapacitance, high charge-discharge cycles, and excellent electrical conductivity. Polyaniline [48], polythiophene [49] polypyrrole [50], are the most often utilized CPs. A key limitation of CPs is their tendency to expand and contract when ions are intercalated and deintercalated, which can lead to mechanical failure of the electrodes over extended cycling [51]. To improve the energy storage capacity and stability of CP electrodes, the proper architecture of the polymer morphology has been



developed into various nanostructures such as nanofibers, nanowires, nanorods, and nanotubes which can significantly enhance their stability by reducing diffusion lengths, thereby improving electrolyte penetration.

### **C. Metal oxides**

Overall, metal oxides can offer higher SE for electrochemical SC than typical carbon-based materials and superior electrochemical durability over CPs. They exhibit electrochemical faradaic reactions between electrode materials and ions in addition to storing energy like electrostatic carbon materials. They offer a wide operating voltage window and numerous oxidation states. The various metal oxides, such as  $\text{RuO}_2$  [52],  $\text{MnO}_2$  [53],  $\text{NiO}$  [54],  $\text{Fe}_2\text{O}_3$  [55],  $\text{V}_2\text{O}_5$  [56], etc. were explored for SC application. The fundamental criteria for metal oxides employed in SCs are as follows: (1) A metal should exhibit multiple oxidation states simultaneously across a continuous range without undergoing any phase transition, and (2) the oxides must be electronically conductive [57]. Among a variety of TMOs, metallic vanadium oxide such as  $\text{Zn}_3\text{V}_2\text{O}_8$ ,  $\text{Co}_3\text{V}_2\text{O}_8$ , and  $\text{Ni}_3\text{V}_2\text{O}_8$ , etc., possess superior capacitance on account of their multiple valance states, higher conductivity, numerous stoichiometric compositions, and variety of microstructures.

### **1.3 General outlook and retrospective of nickel vanadium oxide**

Among the family of transition metals, some precious transition metals play a key role in many applications and are usually not available in large amounts on the Earth's crust [58]. From the industrial viewpoint, expensive, less availability, and more toxicity limit their practical applications. Comparably, nickel and vanadium are the usually available transition metals found in the Earth's crust. Nickel and vanadium are widely spread on Earth with 0.0084% and 0.012% occurrence, respectively [36]. Also, these materials are available in malleable and ductile forms, are cost-effective, have good heat as well as electrical conductors, and are environmentally friendly.

In recent decades, diverse crystal phases and compositions of nickel vanadium oxides (NVOs) have attracted booming attention because of their complex interplay of interatomic bonding, which provides chemical abundance in nature. Due to the variety of compounds of vanadium that exist in nature, it is found in a different form  $\text{VO}_2$ ,  $\text{V}_4\text{O}_9$ ,  $\text{V}_3\text{O}_7$ ,  $\text{V}_2\text{O}_3$ ,  $\text{V}_2\text{O}_5$ , etc. [59–62]. Particularly, vanadium and nickel, with their richer valences, such as vanadium from  $\text{V}^{2+}$  to  $\text{V}^{5+}$  and nickel from  $\text{Ni}^{2+}$  to  $\text{Ni}^{3+}$  can make diverse atomic ratios [63, 64]. Also, each formula can relate to different crystal

structures, which provide different intriguing properties. Their Kagome-staircase-like geometry of crystalline structure shows astonishing magnetic features additionally, interesting catalytic behavior due to their unique structural characteristics [65]. The combination of nickel and vanadium enhances redox reversibility and stabilizes the material, which leads to improved electrochemical activities in contrast to pure nickel and vanadium oxide [66-67].

Significant conclusions have been drawn regarding the electrochemical performance of nickel and cobalt vanadium oxide nanostructures for various applications. Their multiple valances and unique dielectric and magnetic behavior are especially suitable as electrode materials for batteries, electrocatalysis, photocatalysis, sensors, and SC applications, and a few of them are shown in Figure 1.7. In the last four years, NVO has received great attention in lithium-ion batteries [68]. Also, nickel and cobalt vanadium oxide have attracted more attention for gas sensing because of their low working temperature and high response [69]. Hence, the NVO is a multifaceted class that grabs more attention.

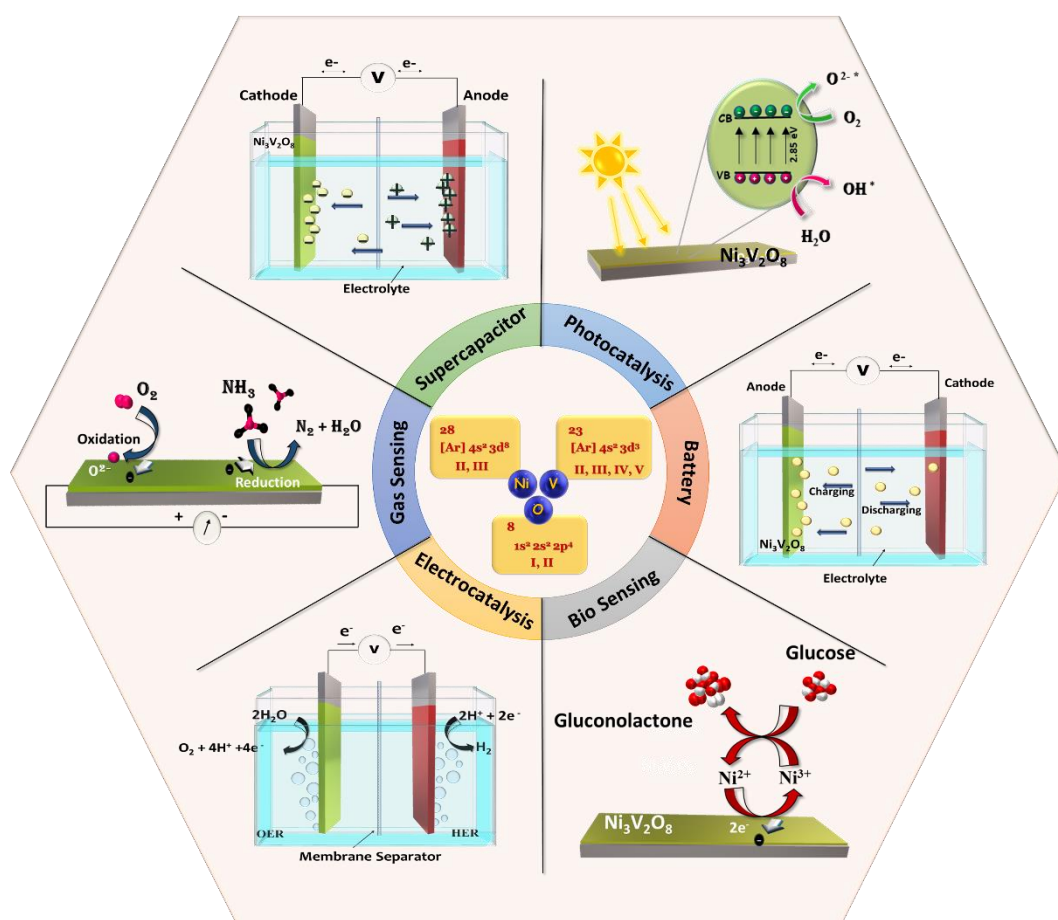


**Figure 1.7:** Illustration of diverse applications of NVO

### 1.3.1 Structures and phases of nickel vanadium oxide

#### a) $\text{Ni}_3\text{V}_2\text{O}_8$

NVO with a phase of  $\text{Ni}_3\text{V}_2\text{O}_8$  arranges itself in the orthorhombic  $\text{Cmce}$  space group as shown in Figure 1.8. Within this structure,  $\text{V}^{5+}$  connects to four  $\text{O}^{2-}$  atoms, shaping  $\text{VO}_4$  tetrahedra. These tetrahedra share corners with nine  $\text{NiO}_6$  octahedra, which have corner-sharing tilt angles ranging between  $51$ - $57^\circ$ . The V-O bond lengths span from  $1.72$ - $1.80$  Å. This compound features two different  $\text{Ni}^{2+}$  sites. In the first,  $\text{Ni}^{2+}$  coordinates with six  $\text{O}^{2-}$  atoms, forming  $\text{NiO}_6$  octahedra. These octahedra share corners with six equivalent  $\text{VO}_4$  tetrahedra and edges with four identical  $\text{NiO}_6$  octahedra. The Ni-O bonds present two shorter ( $2.01$  Å) and four longer ( $2.05$  Å) distances. The second  $\text{Ni}^{2+}$  site involves similar bonding as the first site, however bond length spans between  $1.99$ - $2.09$  Å. The  $\text{O}^{2-}$  ions exhibit three distinct sites within the structure. In the first site,  $\text{O}^{2-}$  adopts a rectangular see-saw-like configuration, bonding to one  $\text{V}^{5+}$  and three  $\text{Ni}^{2+}$  atoms. The second site shows  $\text{O}^{2-}$  in a distorted trigonal planar geometry, linked to one  $\text{V}^{5+}$  and two equivalent  $\text{Ni}^{2+}$  atoms. Finally, in the third site,  $\text{O}^{2-}$  is in a 3-coordinate geometry, bonded to one  $\text{V}^{5+}$  and two  $\text{Ni}^{2+}$  atoms [70, 71].

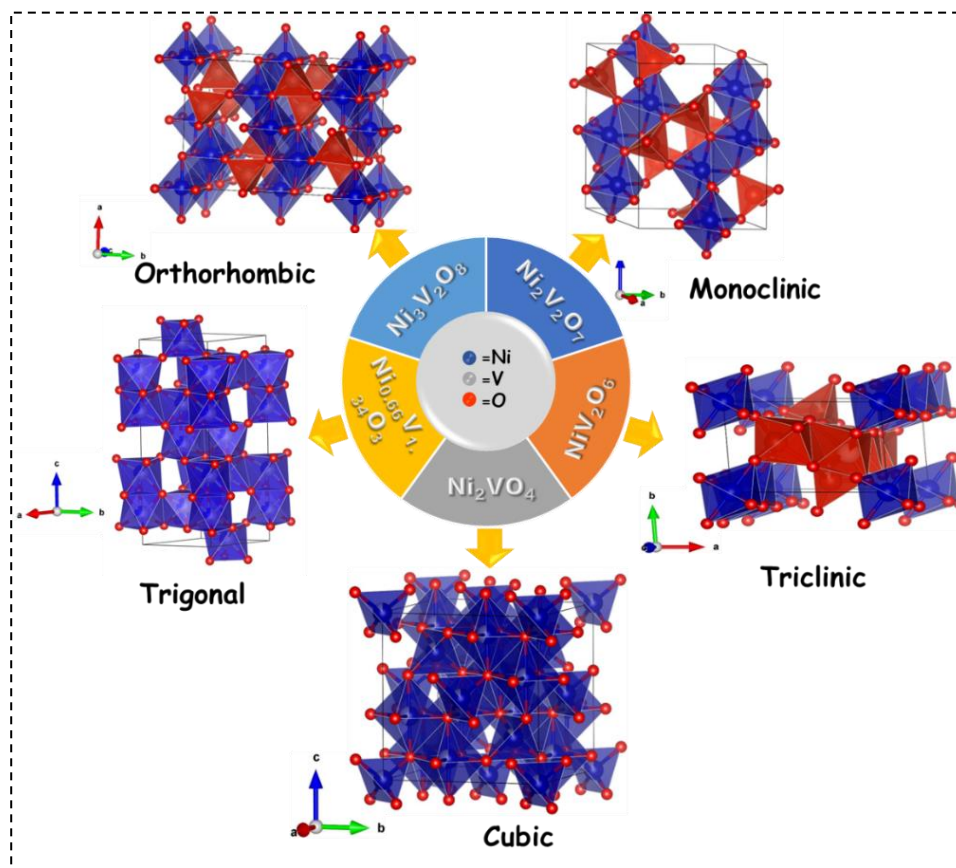


**Figure 1.8:** Different structures and phases of NVO

**b)  $\text{Ni}_2\text{V}_2\text{O}_7$** 

$\text{Ni}_2\text{V}_2\text{O}_7$  crystallizes in the monoclinic  $P2/c$  space group as illustrated in Figure 1.8. There are two different V sites. In the first type, V is connected to four O atoms, forming  $\text{VO}_4$  tetrahedra. These tetrahedra share corners with seven  $\text{NiO}_6$  octahedra and one more  $\text{VO}_4$  tetrahedra. The angles between the shared corners of the octahedra range from  $45$ - $58^\circ$ . The V-O bond lengths vary from  $1.70$ - $1.84$  Å. The second type of V site also forms  $\text{VO}_4$  tetrahedra, connected to four O atoms. These tetrahedra share corners with six  $\text{NiO}_6$  octahedra and one additional  $\text{VO}_4$  tetrahedra. The angles between the shared corners of the octahedra range from  $38$ - $62^\circ$ , and the V-O bond lengths range from  $1.65$ - $1.85$  Å. There are two distinct Ni sites. In the first type, Ni is surrounded by six O atoms, forming  $\text{NiO}_6$  octahedra. These octahedra connect to seven  $\text{VO}_4$  tetrahedra and two equivalent  $\text{NiO}_6$  octahedra. The Ni-O bond lengths range from  $1.97$ - $2.09$  Å. In the second type, Ni is bonded to six O atoms, creating  $\text{NiO}_6$  octahedra. These octahedra share corners with six  $\text{VO}_4$  tetrahedra and three  $\text{NiO}_6$  octahedra. The Ni-O bond lengths vary from  $2.00$ - $2.04$  Å. There are seven different O sites, and they have different bonding configurations. For instance, in some cases, O atoms are bonded to V and Ni atoms, forming various geometries such as distorted trigonal planar or bent arrangements [72–74].

**c)  $\text{NiV}_2\text{O}_6$** 

$\text{NiV}_2\text{O}_6$  crystallizes in the triclinic  $\bar{P}1$  space group as depicted in Figure 1.8. There are three inequivalent  $\text{V}^{5+}$  sites.  $\text{V}^{5+}$  is joined to four  $\text{O}^{2-}$  atoms in the first  $\text{V}^{5+}$  site to create  $\text{VO}_4$  tetrahedra, sharing corners with octahedra of  $\text{NiO}_6$ . The octahedral tilt angles that share corners fall between  $48$  and  $52^\circ$ . Six  $\text{O}^{2-}$  atoms and  $\text{V}^{5+}$  are joined in a 6-coordinate geometry at the second and third  $\text{V}^{5+}$  site. V-O bond distances vary widely, ranging from  $1.64$  to  $2.26$  Å for second and  $1.63$ - $2.27$  Å for third sites. Two inequivalent  $\text{Ni}^{2+}$  sites are present. In the first  $\text{Ni}^{2+}$  site,  $\text{Ni}^{2+}$  forms bonds with six  $\text{O}^{2-}$  atoms to produce  $\text{NiO}_6$  octahedra. These octahedra share edges with two  $\text{NiO}_6$  octahedra and a corner with one  $\text{VO}_4$  tetrahedra. There is a spread of Ni-O bond distances ranging from  $1.98$ - $2.07$  Å.  $\text{Ni}^{2+}$  is linked to six  $\text{O}^{2-}$  atoms in the second  $\text{Ni}^{2+}$  site to produce  $\text{NiO}_6$  octahedra, which share edges and corners with two equivalent  $\text{VO}_4$  tetrahedra and  $\text{NiO}_6$  octahedra. There is a spread of Ni-O bond distances ranging from  $1.93$ - $2.01$  Å. There are nine inequivalent  $\text{O}^{2-}$  sites and they are bonded with  $\text{V}^{5+}$  in

trigonal planar geometry, 3-coordinate geometry, distorted trigonal planar geometry, and bent  $150^\circ$  geometry [75, 76].

**d)  $\text{NiV}_2\text{O}_4$**

$\text{NiV}_2\text{O}_4$  adopts a spinel structure and organizes itself within the monoclinic  $C2/m$  space group as shown in Figure 1.8. There are three different  $\text{V}^{3+}$  sites. In the first site, each  $\text{V}^{3+}$  is connected to six  $\text{O}^{2-}$  atoms, forming  $\text{VO}_6$  octahedra. These octahedra share corners with six  $\text{NiO}_4$  tetrahedra and edges with six other  $\text{VO}_6$  octahedra. The V-O bond lengths vary, with four at  $2.04 \text{ \AA}$  and two at  $2.09 \text{ \AA}$ . Similar to the first site,  $\text{V}^{3+}$  creates  $\text{VO}_6$  octahedra and shares corners with six  $\text{NiO}_4$  tetrahedra in the second and third sites. The V-O bond lengths range between  $2.05 - 2.08 \text{ \AA}$  and  $2.05 - 2.06 \text{ \AA}$  at the second and third  $\text{V}^{3+}$  sites, respectively.  $\text{Ni}^{2+}$  atoms are connected to four  $\text{O}^{2-}$  atoms, shaping  $\text{NiO}_4$  tetrahedra and these tetrahedra share corners with twelve  $\text{VO}_6$  octahedra. The Ni-O bond distances range from  $1.99\text{-}2.02 \text{ \AA}$ , and the corner-sharing octahedral tilt angles fall between  $57\text{-}59^\circ$ . There are three distinct  $\text{O}^{2-}$  sites. In each site,  $\text{O}^{2-}$  is bonded to three  $\text{V}^{3+}$  and one  $\text{Ni}^{2+}$  atom, forming a combination of distorted corner and edge-sharing  $\text{NiV}_3\text{O}$  trigonal pyramids.

Along with this, there are many phases and structures reported by many researchers [77], which can result from changes in synthesis conditions, temperature, or chemical modifications during the material's preparation. Each phase may possess unique physical, chemical, or electronic properties, making them interesting for various applications in electronics, energy storage, catalysis, or other fields of materials science. Understanding and controlling these phases can help tailor the properties of NVO for specific technological applications. Among all types of NVOs,  $\text{Ni}_3\text{V}_2\text{O}_8$ ,  $\text{Ni}_2\text{V}_2\text{O}_7$ , and  $\text{NiV}_2\text{O}_6$  have attracted great attention for the application of SCs owing to their open-framework and tunneling structure and strong covalent bonds in metal-oxygen octahedra which allow for easy ion transport and diffusion through the material during charge-discharge processes and improve stability.

#### **1.4 General outlook and retrospective of reduced graphene oxide**

Carbon atoms form the fundamental building blocks of various forms of carbon-based materials. Carbon stands out for its adaptability, being both lightweight and capable of assuming diverse structures with unique bonding arrangements. These different configurations result in carbon allotropes showcasing distinct properties.

Among these, graphene stands out prominently, alongside its variants like graphene oxide (GO) and/or reduced graphene oxide (rGO).

There is numerous top-down and bottom-up techniques for creating graphene. Though substantial progress is being made, it is still very difficult to produce inexpensive, high-quality graphene on an industrial scale over huge areas. This is due to the fact that many top-down methods are restricted to using liquid media for stabilizing graphene, eliminating solvents, and producing extremely low yields of graphene, which often contains defects. Conversely, bottom-up methods are more expensive and require high temperatures for synthesis. Conversely, GO may be inexpensively and quickly manufactured in desirable quantities. GO exhibits a similar 2D structure to graphene.

However, its monolayer of carbon atoms is chemically modified with functional groups, such as carbonyl, epoxide, hydroxyl, and others through covalent bonds. These functional groups allow GO to be processed easily in dispersion and confer high colloidal stability in water. Unfortunately, the method that is applied to the synthesis of GO requires strong oxidants-based chemicals like potassium permagnet, which reduces the conductivity of the GO. Fortunately, GO has the potential to regain properties similar to graphene through additional reductive exfoliation treatments. These treatments transform GO into rGO, which represents a notable compromise between graphene and GO. The rGO not only demonstrates graphene-like properties, such as good conductivity, but also offers the advantage of being easily produced in desired amounts from GO. Various methods, including electrochemical approaches such as microwave techniques and thermal methods, enable the efficient preparation of rGO from GO [78].

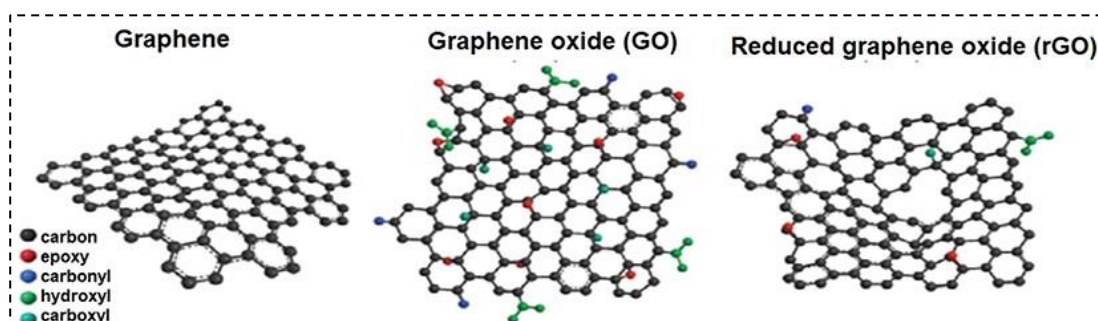


**Figure 1.9:** Structures of graphene, GO and rGO [79]



### 1.4.1 Properties of reduced graphene oxide

- Thermal Property: The high-temperature responsiveness of graphene in 2D is attributed to strong in-plane carbon bonding. Defects, doping, and edge scattering all make rGO thermally less conductive.
- Electrical Property: The  $\pi$ - $\pi$  bond in graphene, which is made up of 2D layers of one-atom-thick  $sp^2$  carbon, is intimately linked to its electrical properties. It's a highly electrically conductive substance with high electrical conductivity ( $6500 \text{ S m}^{-1}$ ) and electron mobility ( $25 \text{ m}^2 \text{ V}^{-1} \text{ s}^{-1}$ ). Due to the need for rGO for commercial applications, researchers have been investigating a number of ways to improve the production of electrically conducting rGO by selecting suitable GO reduction techniques. The good conducting rGO is highly desirable for SCs since it reduces the ESR.
- Mechanical Property: With a tensile strength of 130 GPa, graphene is 200 times stronger than steel, making it the strongest substance ever discovered. Additionally, the material is extremely light, weighing only  $0.77 \text{ mg m}^{-2}$  and having Young's modulus of  $1.0 \pm 0.1 \text{ T Pa}$  (estimated thickness of 0.335 nm). Because of this remarkable mechanical property, graphene is a prospective candidate for use in flexible SCs.
- Chemical Property: Functional groups comprising oxygen and nitrogen are frequently added to rGO nanosheets to increase their wettability and conductivity respectively. The rGO sample's high surface area, microporosity, conductivity, and availability of an oxygen-containing functional group make it a compelling candidate for a SC application.

## 1.5 Overview of literature

### 1.5.1 Nickel vanadium oxide-based electrode materials for supercapacitor application

In the earlier years, diverse structures of NVO with nano/micro-scaled morphologies have received the utmost attention, as they possess better electrochemical performance than bulk material. Various synthetic methods can significantly influence the control of NVO properties. A variety of synthetic methods, such as the hydrothermal, solvothermal, co-precipitation, sol-gel, chemical bath deposition (CBD), electrospinning, and microwave-assisted synthesis methods [63, 64, 80-86], have been employed to produce diverse crystal structures and morphologies, which can influence

electrochemical performance. Among many synthetic approaches, hydrothermal and co-precipitation methods are commonly used to produce different structures of NVO. The structures, morphologies, and corresponding electrochemical performance for previously reported NVO material are compared in Table 1.1.

The hollow nanospheres of 3D urchin-shaped  $\text{Ni}_3(\text{VO}_4)_2$  were developed through the hydrothermal approach by Kumar et al. [80]. The prepared nanosphere provided a maximum specific capacity of  $402.8 \text{ C g}^{-1}$  at  $1 \text{ A g}^{-1}$ , along with an excellent stability of 88% after 1000 cycles. Nandi et al. [81] prepared nanopetals of NVO through the facile and cost-effective hydrothermal route. The prepared nanopetals provide a high specific surface area of  $436 \text{ m}^2 \text{ g}^{-1}$ , which provides an outstanding  $C_{\text{sp}}$  of  $1252 \text{ F g}^{-1}$  at  $10 \text{ A g}^{-1}$ .

**Table 1.1:** Comparative overview of the literature on electrochemical capacitive performance of NVO-based electrodes

Sr. No.	Material (current collector)	Method	Morphology	Electrolyte	Specific Capacitance ( $\text{F g}^{-1}$ ) at current density	Stability after cycles	Ref.
1.	$\text{Ni}_2\text{V}_2\text{O}_7$ (NF)	Hydrothermal	Porous spheres	1 M KOH	$77.1 \mu\text{Ah cm}^{-2}$ at $1 \text{ mA cm}^{-2}$	82.3% After 2000	[63]
2.	$\text{NiV}_2\text{O}_6$ (NF)	Hydrothermal combined with liquid phase synthesis	Nanospheres	2 M KOH	$565 \text{ at } 1 \text{ A g}^{-1}$	84% After 3000	[64]
3.	$\text{Ni}_3(\text{VO}_4)_2$ (NF)	Hydrothermal	Urchin-shaped hollow nanospheres	6 M KOH	$402.8 \text{ C g}^{-1}$ at $1 \text{ A g}^{-1}$	88% After 1000	[80]
4.	$\text{NiV}_2\text{O}_6$ (NF)	Hydrothermal	Nanopetals	1 M KOH	$1252 \text{ at } 10 \text{ A g}^{-1}$	-	[81]
5.	$\text{Ni}_2\text{V}_2\text{O}_7$ (NF)	Co-precipitation	Nanorods	1 M KOH	$894 \text{ at } 0.4 \text{ mA cm}^{-2}$	94.1% After 3000	[82]
6.	$\text{Ni}_3\text{V}_2\text{O}_8$	Hydrothermal	Nanoparticles	0.1 M HCl	$193.5 \text{ at } 10 \text{ mV s}^{-1}$	-	[83]
7.	$\text{Ni}_3\text{V}_2\text{O}_8$ (NF)	Hydrothermal	Nanosheets	3 M KOH	$1300 \text{ at } 1 \text{ A g}^{-1}$	80.63% after 7000	[84]
8.	$\text{Ni}_3\text{V}_2\text{O}_8$ (NF)	Hydrothermal	Stone like	1 M KOH	$548 \text{ at } 2 \text{ A g}^{-1}$	-	[85]
9.	$\text{Ni}_2\text{V}_2\text{O}_7$ (NF)	Hydrothermal	Microspheres	1 M KOH	$959 \text{ at } 5 \text{ mA cm}^{-2}$	90% after 4000	[86]

Furthermore, the porous microsphere chains of  $\text{Ni}_2\text{V}_2\text{O}_7$  were synthesized by Chandra Sekhar et al. [63] via a hydrothermal route followed by thermal decomposition.

The prepared porous spheres delivered an areal capacitance of  $77.1 \mu\text{Ah cm}^{-2}$  at current density of  $1 \text{ mA cm}^{-2}$ . Additionally, the  $\text{Ni}_2\text{V}_2\text{O}_7$  microsphere chains demonstrated strong cycling stability, retaining 82.3% of their capacity even after 2000 GCD cycles. Pyrochlore-structured  $\text{Ni}_2\text{V}_2\text{O}_7$  nanorods prepared through the co-precipitation approach by Arasi et al. [82]. The obtained nanorods provide the maximum  $C_{\text{sp}}$  of  $894 \text{ F g}^{-1}$  at  $0.4 \text{ mA cm}^{-2}$ . Furthermore, the hydrothermal route combined with the subsequent liquid phase synthesis route was used by Li et al. [64] to prepare  $\text{NiV}_2\text{O}_6$  nanospheres. The obtained nanospheres show excellent supercapacitive performance, including a maximum specific capacity of  $565.5 \text{ C g}^{-1}$  at  $1 \text{ A g}^{-1}$  current density. Moreover, the electrode provides 84% of its initial capacitance even after 3000 cycles. The  $\text{Ni}_3\text{V}_2\text{O}_8$  was prepared by Ramavathu et al. [83] via hydrothermal method. The obtained nanoparticles provided a maximum  $C_{\text{sp}}$  of  $193.5 \text{ F g}^{-1}$  at  $10 \text{ mV s}^{-1}$ .

Furthermore, Merum et al. [84] reported binder-free preparation of  $\text{Ni}_3\text{V}_2\text{O}_8$  over nickel foam (NF) through the facile hydrothermal method. The obtained nanosheets over NF provided a maximum  $C_{\text{sp}}$  of  $1300 \text{ F g}^{-1}$  at  $1 \text{ A g}^{-1}$  current density, along with excellent cycling stability of 80.63% even after 7000 charge-discharge cycles. Recently, Singh et al. [85] reported a hydrothermal method to develop a stone-like structure of  $\text{Ni}_3\text{V}_2\text{O}_8$ . The surfactant-assisted development of a stone-like structure exhibited a  $C_{\text{sp}}$  of  $548 \text{ F g}^{-1}$  at  $2 \text{ A g}^{-1}$ . Recently, Magadum et al. [86] reported a hydrothermal route to synthesize microspheres of nickel pyrovanadate ( $\text{Ni}_2\text{V}_2\text{O}_7$ ) over NF. The prepared microspheres show a maximum  $C_{\text{sp}}$  of  $959 \text{ F g}^{-1}$  at  $5 \text{ mA cm}^{-2}$ , along with cycling stability of 90% after 4000 cycles.

### **1.5.2 Nickel vanadium oxide-based composite electrode materials for supercapacitor Application**

So far, from the reported literature, NVO and their composites has emerged as an encouraging material for SC owing to its remarkable electrochemical performance. However, their limited specific surface area and less cycling stability thereby hinder their suitability for real-world applications. In particular, carbonaceous material can provide more surface area, a porous structure, and higher structural stability. Improving ionic conductivity and other electrochemical activities is the only purpose of accompanying transition metal vanadium oxide with carbonaceous materials. The structures, morphologies, and corresponding electrochemical performance for previously reported NVO composite with other materials are summarized in Table 1.2.

Zhang et al. [87] studied the coupling effect between nickel vanadate and nickel oxide. The hydrothermal route is used to prepare the  $\text{Ni}_3\text{V}_2\text{O}_8@\text{NiO}$  nanohybrid. The obtained nanoflakes provided a maximum  $C_{\text{sp}}$  of  $2068 \text{ F g}^{-1}$  at  $0.5 \text{ A g}^{-1}$  current density. Moreover, the nanohybrid retained 75% of its initial  $C_{\text{sp}}$  value after 5000 cycles. **Table 1.2:** Comparative overview of the literature on electrochemical capacitive performance of NVO-based composite electrodes

Sr. No.	Material (current collector)	Method	Morphology	Electrolyte	Specific Capacitance ( $\text{F g}^{-1}$ ) at current density	Stability after cycles	Ref.
1.	$\text{Ni}_3\text{V}_2\text{O}_8/\text{NiO}$ (NF)	Hydrothermal	Nanoflakes	2 M KOH	2068 at 5	75% After 5000	[87]
2.	$\text{Ni}_3\text{V}_2\text{O}_8@\text{MWCNT}$ (NF)	Hydrothermal	Nanobelts	3 M KOH	2920 at 2	96% After 10000	[88]
3.	$\text{Ni}_3\text{V}_2\text{O}_8/\text{r-GO}$ (NF)	Hydrothermal	Nanosheets	6 M KOH	$170 \text{ C g}^{-1}$ at 0.5	92.7% After 1400	[89]
4.	$\text{Ni}_3\text{V}_2\text{O}_8@\text{GO}$ (NF)	Co-precipitation	Small stone-like	6 M KOH	547 at $5 \text{ mV s}^{-1}$	95% After 1500	[90]
5.	$\text{Ni}_3\text{V}_2\text{O}_8/\text{NG}$ (NF)	Hydrothermal	Nanoparticles	3 M KOH	1898 at 1	87.1% After 10000	[91]
6.	Graphene $\text{Ni}_3\text{V}_2\text{O}_8$ Composite (Aluminum foil)	Solvothermal	Nanoparticle	2 M KOH	748 at 0.5	71% After 3000	[92]
7.	$\text{NiO}/\text{Ni}_3\text{V}_2\text{O}_8$ (NF)	Solvothermal	Nanorods	1 M NaOH	653 at 1	96% After 1000	[93]
8.	$\text{NiV}_2\text{O}_6/\text{C}$ (NF)	Reflux	Sponge-like	2 M KOH	745.6 at 0.5	77.8% After 12000	[94]
9.	$\text{NiV}_2\text{O}_6/\text{Ni}(\text{HCO}_3)_2$ (NF)	Hydrothermal	Nanoflakes	2 M KOH	$7.94 \text{ F cm}^{-2}$ at $1 \text{ mA cm}^{-2}$	106.2% After 10000	[95]
10.	$\text{Ni}_3\text{V}_2\text{O}_8@\text{PANI}$ (PET/ITO)	CBD	Nanosheets	2 M KOH	2232 at $10 \text{ mV s}^{-1}$	88% After 10000	[96]
11.	$\text{Ni}_3\text{V}_2\text{O}_8@\text{Co-B}$ (NF)	CBD/Co-precipitation	Nanoparticles@nanoflakes	1 M KOH	1789 at 0.5	-	[97]

Furthermore, the  $\text{Ni}_3\text{V}_2\text{O}_8$  composite with multi-walled carbon nanotubes (MWCNT) was developed by Sahoo et al. [88] using the modified hydrothermal route. The obtained nanoparticles over nanobelts provided the maximum  $C_{\text{sp}}$  of  $2920 \text{ F g}^{-1}$  at a current density of  $2 \text{ A g}^{-1}$ , along with the outstanding capacitive retention of 96% after 10000 GCD cycles. Kumar et al. [89] reported  $\text{Ni}_3(\text{VO}_4)_2$  nanosheet arrays over animated rGO sheets via the hydrothermal method. The prepared nanocomposite provides a maximum specific capacity of  $170 \text{ C g}^{-1}$  at  $0.5 \text{ A g}^{-1}$ , and it retains 97.2% after 1400 cycles. The nanocomposite of  $\text{Ni}_3\text{V}_2\text{O}_8@\text{GO}$  was reported by Thiagarajan et al. [90] through the co-precipitation method. The obtained stone-like particles of  $\text{Ni}_3\text{V}_2\text{O}_8@\text{GO}$  exhibited a maximum  $C_{\text{sp}}$  of  $547 \text{ F g}^{-1}$  at a  $5 \text{ mV s}^{-1}$  scan rate, along with a capacitive retention of 95% after 1500 cycles. Guo et al. [91] developed nitrogen-doped graphene-anchored NVO ( $\text{Ni}_3\text{V}_2\text{O}_8/\text{NG}$ ) using a hydrothermal route. The homogeneously anchored nanoparticles of  $\text{Ni}_3\text{V}_2\text{O}_8$  over the matrices of graphene show excellent supercapacitive performance with  $C_{\text{sp}}$  of  $1898 \text{ F g}^{-1}$  at  $1 \text{ A g}^{-1}$  current density. Furthermore, the solvothermal approach was used by Low et al. [92] to prepare graphene/ $\text{Ni}_3\text{V}_2\text{O}_8$  nanocomposite. The optimized weight ratio between graphene and  $\text{Ni}_3\text{V}_2\text{O}_8$  provides a maximum  $C_{\text{sp}}$  of  $748 \text{ F g}^{-1}$  at  $0.5 \text{ A g}^{-1}$  current density. Also, the prepared nanocomposite provided a remarkable stability of 71% after 3000 GCD cycles.

The  $\text{NiO}/\text{Ni}_3\text{V}_2\text{O}_8$  nanocomposite was developed by Vishnukumar et al. [93] through the solvothermal method. The prepared nanocomposite delivers a maximum  $C_{\text{sp}}$  of  $653 \text{ F g}^{-1}$ . Zhou et al. [94] prepared  $\text{NiV}_2\text{O}_6/\text{C}$  composite via the reflux method. The obtained sponge-like morphology of  $\text{NiV}_2\text{O}_6/\text{C}$  composite exhibited the maximum  $C_{\text{sp}}$  of  $745.6 \text{ F g}^{-1}$  at a current density of  $0.5 \text{ A g}^{-1}$ , along with capacitive retention of 77.8% even after 12000 cycles. Zhao et al. [95] prepared co-incorporated  $\text{NiV}_2\text{O}_6/\text{Ni}(\text{HCO}_3)_2$  nanoflake arrays via hydrothermal route, which provided maximum areal capacitance of  $7.94 \text{ F cm}^{-2}$  at  $1 \text{ mA cm}^{-2}$  with long-time cycle stability of 106.2% of its initial capacitance even after 10000 GCD cycles. Furthermore, the  $\text{Ni}_3\text{V}_2\text{O}_8/\text{PANI}$  composite was developed by Liu et al. [96] through the CBD method. The obtained nanosheets provided a maximum  $C_{\text{sp}}$  of  $2565.7 \text{ F g}^{-1}$  at a scan rate of  $5 \text{ mV s}^{-1}$ . The nanocomposite of the crystalline  $\text{Ni}_3\text{V}_2\text{O}_8$  over amorphous cobalt boride was prepared using CBD and co-precipitation methods by Hou et al. [97], and obtained nanoparticles@nanoflakes provided the maximum  $C_{\text{sp}}$  of  $1789 \text{ F g}^{-1}$  at  $0.5 \text{ A g}^{-1}$  current density.

### 1.5.3 Electrochemical performance of nickel vanadium oxide and their composite-based supercapacitor devices

The assessment of the practical utility of electroactive materials involves the evaluation of their suitability via the fabrication and subsequent characterization of SC devices. The literature study of fabricated asymmetric devices is summarized in Table 1.3.

**Table 1.3:** An overview of the literature on NVOs and their composites-based symmetric and asymmetric hybrid devices

Sr. No.	Positive electrode	Negative electrode	Specific capacitance ( $F g^{-1}$ ) at $A g^{-1}$	Specific Energy ( $Wh kg^{-1}$ )	Specific Power ( $W kg^{-1}$ )	Stability After cycles	Ref.
1.	$NiV_2O_6$	rGO	93.3 $C g^{-1}$ at 1 (Liquid state)	23.4	800	73.5% after 3000	[64]
			33.1 $C g^{-1}$ at 1 (Solid state)	7.8	850	53.3% after 3000	
2.	$Ni_3(VO_4)_2$	AC	114 at 0.3 $A g^{-1}$	25.3	240	92% after 1000	[80]
3.	$Ni_3V_2O_8/NF$	AC	166 at 4 $A g^{-1}$	33.2	2400	93% after 10000	[84]
4.	$Ni_2V_2O_7/NF$	AC/NF	212 at 5 $mA cm^{-2}$	47	2300	94 % after 5000	[86]
5.	$Ni_3V_2O_8@MWCNT$	$\beta$ -FeOOH@rGO	976 at 0.25	86.7	198.7	85 % after 5000	[88]
6.	$Ni_3V_2O_8/NG$	$Fe_2VO_4/N G$	217 at 1	77.2	863	83.3 % after 20000	[91]
7.	$NiV_2O_6/C$	AC	92 at 0.5	28.75	375	77.8% after 12000	[94]
8.	$NiV_2O_6/Ni(HCO_3)_2/NF$	AC	0.58 mAh $cm^{-2}$ at 0.5 $mA cm^{-2}$	0.533 $mWh cm^{-2}$	0.232 $mW cm^{-2}$	106.2% after 10000	[95]
9.	$Ni_3V_2O_8@PANI$	$Ni_3V_2O_8@PANI$	58.5 $mF cm^{-2}$ at 5 $mV s^{-1}$	20.8 $\mu Wh cm^{-2}$	230 $\mu W cm^{-2}$	88% after 20000	[96]
10.	$Ni_3V_2O_8@Co-B$	AC	257 at 0.5	91.2	400	47 % after 10000	[97]
11.	$Ni_3V_2O_8/NF$	$Ni_3V_2O_8/N F$	263.12 at 0.5 $mA cm^{-2}$	32.98	189.96	68 % after 5000	[98]

Li et al. [64] reported both aqueous as well as solid state devices of SC consisting of a  $NiV_2O_6$  electrode as a cathode and rGO as an anode (rGO// $NiV_2O_6$ ).

The liquid-state device provided a maximum specific capacity of  $93.3 \text{ C g}^{-1}$  along with  $24.3 \text{ Wh kg}^{-1}$  and  $800 \text{ W kg}^{-1}$  energy density (ED) and power densities (PD), respectively, and the solid-state device reported a specific capacity of  $33.1 \text{ C g}^{-1}$  along with the ED and PD of  $7.8 \text{ Wh kg}^{-1}$  and  $850 \text{ W kg}^{-1}$ , respectively. Liu et al. [96] fabricated a transparent symmetric SC comprising two  $\text{Ni}_3\text{V}_2\text{O}_8\text{@PANI}$  electrodes. The prepared symmetric device demonstrated a high areal capacitance of  $58.5 \text{ mF cm}^{-2}$  and a maximum ED of  $20.8 \mu\text{Wh cm}^{-2}$  at a PD of  $230 \mu\text{W cm}^{-2}$ . Also, Haldar et al. [98] developed a symmetric device consisting of  $\text{Ni}_3\text{V}_2\text{O}_8\text{/NF//Ni}_3\text{V}_2\text{O}_8\text{/NF}$ , which delivers a maximum  $C_{\text{sp}}$  of  $263.12 \text{ F g}^{-1}$  along with a high ED of  $32.98 \text{ Wh kg}^{-1}$  at a PD of  $189.96 \text{ W kg}^{-1}$ . Zhao et al. [95] developed an asymmetric SC device made up of  $\text{NiV}_2\text{O}_6\text{/Ni(HCO}_3)_2\text{/NF}$  and AC as positive and negative electrodes, respectively. The device  $\text{NiV}_2\text{O}_6\text{/Ni(HCO}_3)_2\text{/NF//AC}$  delivered a maximum areal capacity of  $0.58 \text{ mAh cm}^{-2}$  along with a high ED of  $0.533 \text{ mWh cm}^{-2}$  at a  $0.232 \text{ mW cm}^{-2}$  PD. Hou et al. [97] fabricated an asymmetric SC device consisting of  $\text{Ni}_3\text{V}_2\text{O}_8\text{@Co-B}$  and AC as positive and negative electrodes, respectively. Prepared  $\text{Ni}_3\text{V}_2\text{O}_8\text{@Co-B//AC}$  exhibited a maximum  $C_{\text{sp}}$  of  $257 \text{ F g}^{-1}$ . Also, the device attained a high ED of  $91.2 \text{ Wh kg}^{-1}$  at  $400 \text{ W kg}^{-1}$ . Merum et al. [84] fabricated an asymmetric SC device using  $\text{Ni}_3\text{V}_2\text{O}_8\text{/NF}$  and AC as the positive and negative electrodes, respectively, which delivered a maximum  $C_{\text{sp}}$  of  $166 \text{ F g}^{-1}$  along with the ED of  $33.2 \text{ Wh kg}^{-1}$  at an PD of  $2.4 \text{ kW kg}^{-1}$ . Moreover, a solid-state asymmetric device was prepared by Guo et al. [91]. The device consists of  $\text{Ni}_3\text{V}_2\text{O}_8\text{/NG}$  as positive electrode and  $\text{Fe}_2\text{VO}_4\text{/NG}$  as the negative electrode, which demonstrated a maximum  $C_{\text{sp}}$  of  $217 \text{ F g}^{-1}$ , with a high ED of  $77.2 \text{ Wh kg}^{-1}$  at a PD of  $863 \text{ W kg}^{-1}$ .

An asymmetric device prepared by Kumar et al. [80] using  $\text{Ni}_3(\text{VO}_4)_2$  as a positive electrode and AC as the negative electrode. The fabricated  $\text{Ni}_3(\text{VO}_4)_2\text{//AC}$  delivered a maximum specific capacity of  $114 \text{ C g}^{-1}$  along with the ED of  $25.3 \text{ Wh kg}^{-1}$  at a PD of  $240 \text{ W kg}^{-1}$ . Zhou et al. [94] built a device consisting of  $\text{NiV}_2\text{O}_6\text{/C}$  and AC, which delivered a maximum  $C_{\text{sp}}$  of  $92 \text{ F g}^{-1}$ . Also, the prepared device  $\text{NiV}_2\text{O}_6\text{/C//AC}$  achieves a high ED of  $28.75 \text{ Wh kg}^{-1}$  at a PD of  $375 \text{ W kg}^{-1}$ . Putting efforts toward the increasing capacitance value, which further increases the SE, Sahoo et al. [88] fabricated an asymmetric SC device utilizing  $\text{Ni}_3\text{V}_2\text{O}_8\text{@MWCNT}$  and  $\beta\text{-FeOOH@rGO}$  as the positive and negative electrodes, respectively. The developed cell  $\text{Ni}_3\text{V}_2\text{O}_8\text{@MWCNT//}\beta\text{-FeOOH@rGO}$  delivered a high  $C_{\text{sp}}$  of  $976 \text{ F g}^{-1}$  along with enhanced SE of  $86.7 \text{ Wh kg}^{-1}$  at an SP of  $198.7 \text{ W kg}^{-1}$ .



In summary, the overview of the literature provides valuable insights into the practical utility of NVO based electroactive materials in the fabrication of SC devices. The study reveals that the prepared symmetric and asymmetric hybrid devices provide unique benefits and unique advantages in terms of  $C_{sp}$ , SE, and SP. Some studies explored the use of composite materials, such as  $Ni_3V_2O_8@MWCNT$  and  $\beta$ -FeOOH@rGO, as ac cathode and anode, to enhance  $C_{sp}$  and SE, indicating the potential for further improvements through material engineering. Nevertheless, these materials failed to attain their theoretically predicted capacitance values. Indeed, there exists a continued opportunity to augment the capacitance, SE, and cyclic stability of the device, which may be achieved through the fabrication of electrodes consisting of a composite of NVO with carbonaceous materials to improve the capacitive performance of composite electrodes by preparing it using different binder-free synthetic approaches.

## **1.6 Orientation and purpose of the thesis**

Recent research on SCs gives insights into cutting-edge energy storage technologies used in laptops, power backup, HEVs, portable electronics, etc. Among the consortium of clean ESSs, SCs are the most common alternative to batteries in many applications and have been extensively studied for many decades because of their high SP, rapid discharge-recharge rate, and exceptional cyclic stability. However, less SE sometimes limits the practical use of SCs compared to battery systems. Hence, it is necessary to contribute more significant potential for developing high-energy SCs without sacrificing the SP. Additionally, for the SC to produce pulse power, a somewhat quick response is required; this can be done by reducing ESR. As a result, producing an active electrode material that meets the parameters mentioned above becomes an intriguing topic for many electrochemists.

As we know, the electrode material and choice of electrolyte play a crucial role in identifying high-performance electrode materials that are essential to developing hybrid energy storage devices (HESDs) [8].

A material with a substantial surface area, mesoporous nature, electrochemical stability, and more significant conductivity can achieve high energy-storing performance. The evolution of vanadium compounds with transition metals displays superior redox behaviour due to their coordination environment and manifold valences. With their richer valences of Vanadium and nickel, such as vanadium from  $V^{2+}$  to  $V^{5+}$

and nickel from  $\text{Ni}^{2+}$  to  $\text{Ni}^{3+}$ , they can make a diverse atomic ratio, which makes NVO suitable for the SC application. Apart from choosing the suitable electrode material, producing a rationally designed structure with an enhanced specific surface area and plenty of diffusion channels is essential for active site exposure and ease of electrolyte transportation. Also, it is well known that most redox activities in pseudocapacitors occur on or near the surface of the material. Thus, preparing nanostructured materials is essential and mainly relies on synthetic approaches and preparative parameters. The objectives of the thesis are as follows,

- 1) To prepare NVO/rGO composite electrodes using chemical methods such as CBS and SILAR.
- 2) To characterize the prepared NVO/rGO composite electrode using different physico-chemical and electrochemical techniques.
- 3) To study supercapacitive performance of NVO/rGO composite electrode and utilization of NVO/rGO composite electrodes for the fabrication of hybrid SC prototype.

Therefore, the current study focuses primarily on the simple chemical bath synthesis (CBS) and successive ionic layer adsorption and reaction (SILAR) method for the synthesis of NVO/rGO composite thin films. These methods provide essential material characteristics such as controlled mass loading, surface architecture, and crystal structure.

Several characterization techniques have been employed to study the physico-chemical characteristics of prepared NVO/rGO materials. The X-ray diffraction (XRD) technique is used to identify the phase of the material. Fourier transform-infrared spectroscopy (FT-IR) and Raman analysis are used to examine chemical bonding in material. The X-ray photoelectron spectroscopy (XPS) technique is used to study chemical composition, feasible oxidation states, and confirm the prepared material. The surface architecture and composition of elements of the prepared material were investigated by using field emission scanning electron microscopy (FE-SEM), high-resolution transmission electron microscopy (HR-TEM), and energy-dispersive electron spectroscopy (EDS) techniques. Thermogravimetric analysis (TG) was utilized to study the composition of the NVO and rGO composite material. Brunauer-Emmett-Teller (BET) and Barrett-Joyner-Halenda (BJH) techniques were used to examine the specific surface area and pore size distribution, respectively. The electrochemical activities of prepared electrodes were performed using a three-

electrode system (Half-test cell). The prepared electrodes were used as working electrodes. Platinum plate and mercury/mercury oxide (Hg/HgO) were utilized as counter and reference electrodes, respectively. Moreover, the hybrid device performance is tested by forming two electrode systems (full-test cell) comprising of prepared NVO/rGO material as a cathode and rGO as an anode. Electrochemical analysis was carried out by using CV, galvanostatic charge-discharge (GCD), electrochemical impedance spectroscopy (EIS), and cycling stability tests in 1 M aqueous potassium hydroxide (KOH) electrolyte.

The main objective of this work is to prepare a composite of NVO/rGO with optimized composition of NVO and rGO to attain the superior electrochemical performance. And further development of hybrid aqueous and solid-state devices using NVO/rGO composite electrodes as a cathode. The prepared hybrid devices are evaluated in terms of  $C_{sp}$ , SE, SP, and stability, and conclusions are assessed based on the SC performance of NVO/rGO composite electrodes.

## 1.7 References

- [1] G. Suppes and T. Storvick, Sustainable Nuclear Power, (2007) 9-32.
- [2] S. Qadir, H. Al-Motairi, F. Tahir, L. Al-Fagih, Energy Rep., 7 (2021) 3590-3606.
- [3] N. Khan, S. Dilshad, R. Khalid, A. Kalair, N. Abas, Energy Storage, 1 (2019) 1–49.
- [4] S. Pawar, B. Pawar, J. Kim, O. Joo, C. Lokhande, Curr. Appl. Phys., 11 (2011) 117–161.
- [5] L. Fan, Z. Tu, S. Chan, Energy Rep., 7 (2021) 8421–8446.
- [6] Y. Liang, C. Zhao, H. Yuan, Y. Chen, W. Zhang, J. Huang, D. Yu, Y. Liu, M. M. Titirici, Y. Chueh, H. Yu, Q. Zhang, InfoMat, 1 (2019) 6–32.
- [7] R. Miller, Sustain. Sci., 8 (2013) 279–293.
- [8] G. Wang, Z. Lu, Y. Li, L. Li, H. Ji, A. Feteira, D. Zhou, D. Wang, S. Zhang, I. M. Reaney, Chem. Rev., 121 (2021) 6124–6172.
- [9] J. Sun, B. Luo, H. Li, Adv. Energy Sustain. Res., 3 (2022) 2100191..
- [10] N. Jalal, R. Ibrahim, M. Oudah, J. Phys. Conf. Ser., 1973 (2021) 012015.
- [11] U. Patil, S. Lee, S. Kulkarni, J. Sohn, M. Nam, S. Han, S. Jun, Nanoscale, 7 (2015) 6999–7021.
- [12] D. Wu, X. Xie, Y. Zhang, D. Zhang, W. Du, X. Zhang, B. Wang, Front. Mater., 7 (2020) 1–16.
- [13] V. Lokhande, A. Lokhande, C. Lokhande, J. Kim, T. Ji, J. Alloys Compd., 682 (2016) 381–403.
- [14] P. Shinde, Q. Abbas, N. Chodankar, K. Ariga, M. Abdelkareem, A. Olabi, J. Energy Chem., 79 (2023) 611–638.
- [15] K. Oldham, J. Electroanal. Chem., 613 (2008) 131–138.
- [16] Bharti, A. Kumar, G. Ahmed, M. Gupta, P. Bocchetta, R. Adalati, R. Chandra, Y. Kumar, Nano Ex., 2 (2021) 022004.
- [17] A. Balakrishnan, K. Subramanian, Nanostructured ceramic oxides for supercapacitor application, India, (2014).
- [18] E. Goikolea, R. Mysyk, Emerging Nanotechnologies in Rechargeable Energy Storage Systems, (2017) 131-169.
- [19] M. Mastragostino, F. Soavi, C. Arbizzani, Advances in Lithium-Ion Batteries, (2002) 481–505.

- [20] A. Muzaffar, M. Ahamed, K. Deshmukh, J. Thirumalai, *Renew. Sustain. Energy Rev.*, 101 (2019) 123–145.
- [21] F. Alptekin, M. Cakir, M. Celiktas, *Com. Exi.*, (2018) 45–58.
- [22] J. Zhang, M. Gu, X. Chen, *Micro Nano Eng.*, 21 (2023) 100229.
- [23] S. Bhosale, S. Kumbhar, S. Pujari, V. Patil, N. Kumar, R. Salunkhe, C. Lokhande, J. Gunjekar, U. Patil, *J. Energy Storage*, 72 (2023) 108417.
- [24] S. Huang, X. Zhu, S. Sarkar, Y. Zhao, *APL Mater.*, 7 (2019) 100901.
- [25] A. Davies and A. Yu, *Can. J. Chem. Eng.*, 89 (2011) 1342–1357.
- [26] D. Dubal, O. Ayyad, V. Ruiz, P. Gómez-Romero, *Chem. Soc. Rev.*, 44 (2015) 1777–1790.
- [27] T. Pandolfo, V. Ruiz, S. Sivakkumar, J. Nerkar, *Mater. Syst. Appl.*, (2013) 69–109.
- [28] Y. Jiang and J. Liu, *Energy Environ. Mater.* 2 (2019) 30–37.
- [29] Poonam, K. Sharma, A. Arora, S. Tripathi, *J. Energy Storage*, 21 (2019) 801–825.
- [30] N. Chodankar, H. Pham, A. Nanjundan, J. Fernando, K. Jayaramulu, D. Golberg, Y. Han, D. Dubal, *Small*, 16 (2020) 1–35.
- [31] T. Chen and L. Dai, *Mater. Today*, 16 (2013) 272–280.
- [32] W. Wang, S. Wu, *Appl. Surf. Sci.*, 396 (2017) 1360–1367.
- [33] M. Ren, Z. Sun, M. Zhang, X. Yang, D. Guo, S. Dong, R. Dhakal, Z. Yao, Y. Li, N. Kim, *Nanoscale Adv.*, 4 (2022) 3987–3995.
- [34] A. Mittal, *Mater. Today*, 13 (2011) 253–271.
- [35] Q. Wu, T. He, Y. Zhang, J. Zhang, Z. Wang, Y. Liu, L. Zhao, Y. Wu, F. Ran, *J. Mater. Chem. A*, 9 (2021) 24094–24147.
- [36] Z. Zhai, L. Zhang, T. Du, B. Ren, Y. Xu, S. Wang, J. Miao, Z. Liu, *Mater. Des.*, 221 (2022) 111017.
- [37] Y. Liu, S. Jiang, Z. Shao, *Mater. Today Adv.*, 7 (2020) 100072.
- [38] M. Salanne, B. Rotenberg, K. Naoi, K. Kaneko, P. Taberna, C. Grey, B. Dunn, P. Simon, *Nat. Energy*, 1 (2016) 16070.
- [39] S. Trasatti, *Electrochim. Acta*, 28 (1983) 1083–1093.
- [40] V. Augustyn, P. Simon, B. Dunn, *Energy Environ. Sci.*, 7 (2014) 1597–1614.
- [41] P. Simon, Y. Gogotsi, B. Dunn, *Science*, 343 (2014) 1210–1211.
- [42] H. Li, M. Yu, F. Wang, P. Liu, Y. Liang, J. Xiao, C. Wang, Y. Tong, G. Yang, *Nat. Commun.*, 4 (2013) 1–7.
- [43] D. Dubal, R. Holze, P. Gomez-Romero, *Sci. Rep.*, 4 (2014) 1–10.
- [44] T. Lin, C. Dai, K. Hung, *Sci. Rep.*, 4 (2014) 1–10.
- [45] A. Platek, C. Nita, C. Ghimbeu, E. Frackowiak, K. Fic, *Electrochim. Acta*, 338 (2020) 135788.
- [46] N. Choudhary, C. Li, J. Moore, N. Nagaiah, L. Zhai, Y. Jung, J. Thomas, *Adv. Mater.*, 29 (2017) 1605336.
- [47] X. Chen, R. Paul, L. Dai, *Natl. Sci. Rev.*, 4 (2017) 453–489.
- [48] H. Wang, J. Lin, Z. Shen, *J. Sci. Adv. Mater. Devices*, 1 (2016) 225–255.
- [49] A. Laforgue, P. Simon, C. Sarrazin, J. Fauvarque, *J. Power Sources*, 80 (1999) 142–148.
- [50] J. Wang, Y. Xu, X. Chen, X. Du, *J. Power Sources*, 163 (2007) 1120–1125.
- [51] Y. Huang, H. Li, Z. Wang, M. Zhu, Z. Pei, Q. Xue, Y. Huang, C. Zhi, *Nano Energy*, 22 (2016) 422–438.
- [52] U. Patil, S. Kulkarni, V. Jamadade, C. Lokhande, *J. Alloys Compd.*, 509 (2011) 1677–1682.
- [53] C. Ye, Z. Lin, S. Hui, *J. Electrochem. Soc.*, 152 (2005) A1272.
- [54] U. Patil, R. Salunkhe, K. Gurav, C. Lokhande, *Appl. Surf. Sci.*, 255 (2008) 2603–2607.
- [55] L. Chen, D. Liu, P. Yang, *RSC Adv.*, 9 (2019) 12793–12800.
- [56] B. Balamuralitharan, I. Cho, J. Bak, H. Kim, *New J. Chem.*, 42 (2018) 11862–11868.
- [57] U. Patil, K. Gurav, V. Fulari, C. Lokhande, O. Joo, *J. Power Sources*, 188 (2009) 338–342.
- [58] M. Seehra, A. Bristow, *Nanoscale Eff. Appl.*, (2018) 3–12.
- [59] J. Qi and C. Niu, *Energy Procedia*, 17 (2012) 1953–1959.
- [60] S. Yamazaki, C. Li, K. Ohoyama, M. Nishi, M. Ichihara, H. Ueda, Y. Ueda, *J. Solid State*

- Chem., 183 (2010) 1496–1503.
- [61] M. Chine, F. Sediri, N. Gharbi, *Mater. Sci. Appl.*, 2 (2011) 964–970.
- [62] I. Mjejri, A. Rougier, M. Gaudon, *Inorg. Chem.*, 56 (2017) 1734–1741.
- [63] S. Sekhar, G. Nagaraju, B. Ramulu, D. Narsimulu, J. Yu, *Inorg. Chem. Front.*, 6 (2019) 1087–1096.
- [64] Y. Li, H. Sun, Y. Yang, Y. Cao, W. Zhou, H. Chai, *J. Colloid Interface Sci.*, 580 (2020) 298–307.
- [65] Y. Kobayashi, Y. Yasui, M. Sato, *J. Magn. Magn. Mater.*, 310 (2007) 1160–1161.
- [66] S. Prasad, V. Leite, R. Santana, E. Moura, A. Neto, A. Souza, *J. Braz. Chem. Soc.*, 15 (2004) 427–432.
- [67] J. Gunjekar, B. Hou, A. Inamdar, S. Pawar, A. Ahmed, H. Chavan, J. Kim, S. Cho, S. Lee, Y. Jo, S. Hwang, T. Kim, S. Cha, H. Kim, H. Im, *Small* 14 (2018) 1–10.
- [68] D. Xia, H. Gao, M. Li, F. Gong, M. Li, *Energy Storage Mater.*, 35 (2021) 169–191.
- [69] A. Yan, *Sensors Mater.*, 30 (2018) 1277–1282.
- [70] Z. Qin, J. Pei, G. Chen, D. Chen, Y. Hu, C. Lv, C. Bie, *New J. Chem.*, 41 (2017) 5974–5980.
- [71] J. Laverock, B. Chen, A. Preston, K. Smith, N. Wilson, G. Balakrishnan, P. Glans, J. Guo, *Matter Mater. Phys.*, 87 (2013) 1–10.
- [72] W. Ji, L. Yin, W. Zhu, C. Kumar, C. Li, H. Li, W. Jin, S. Nandi, X. Sun, Y. Su, T. Brückel, Y. Lee, B. Harmon, L. Ke, Z. Ouyang, Y. Xiao, *Phys. Rev.*, B 100 (2019) 13–15.
- [73] Z. He, J. Yamaura, Y. Ueda, W. Cheng, *Matter Mater. Phys.*, 79 (2009) 6–9.
- [74] S. Bhosale, S. Kumbhar, S. Patil, A. Ransing, V. Parale, C. Lokhande, J. Gunjekar, H. Park, U. Patil, *J. Colloid Interface Sci.*, 666 (2024) 101–117.
- [75] X. Wang, B. Chen, G. Liu, H. Lin, H. Hu, *J. Organomet. Chem.*, 695 (2010) 827–832.
- [76] H. Muller-Buschbaum and M. Kobel, *Anorg. Allg. Chem.*, 596 (1991) 23–28.
- [77] P. Rozier, A. Ratuszna, J. Galy, *Zeitschrift Für Anorg. Und Allg. Chemie*, 628 (2002) 1236–1242.
- [78] R. Tarcan, O. Todor-Boer, I. Petrovai, C. Leordean, S. Astilean, I. Botiz, *J. Mater. Chem. C*, 8 (2020) 1198–1224.
- [79] S. Sastry, S. Panjekar, R. Raman, *Nanotechnol. Sci. Appl.*, 14 (2021) 197–220.
- [80] R. Kumar, P. Rai, A. Sharma, *J. Mater. Chem. A*, 4 (2016) 9822–9831.
- [81] D. Nandi, M. Gnanaseelan, F. Simon, J. Pionteck, *New J. Chem.*, 41 (2017) 5620–5627.
- [82] S. Arasi, R. Ranjithkumar, P. Devendran, M. Krishnakumar, A. Arivarasan, *Ceram. Int.*, 46 (2020) 22709–22717.
- [83] L. Ramavathu, S. Harapanahalli, N. Pernapati, B. Tumma, *Int. J. Nano Dimens*, 12 (2021) 411–421.
- [84] D. Merum, R. Nallapureddy, M. Pallavolu, T. Mandal, R. Gutturu, N. Parvin, A. Banerjee, S. Joo, *ACS Appl. Energy Mater.*, 5 (2022) 5561–5578.
- [85] J. Singh, J. Kumar, C. Kumar Rastogi, B. Mandal, *Mater. Today Proc.*, 79 (2023) 231–234.
- [86] M. Magadum, U. Shembade, T. Bhosale, N. Chougale, P. Pawar, T. Dongale, A. Moholkar, *J. Solid State Chem.*, 335 (2024).
- [87] W. Zhang, L. Kong, X. Ma, Y. Luo, L. Kang, *RSC Adv.*, 4 (2014) 41772–41777.
- [88] R. Sahoo, A. Pal, T. Pal, *J. Mater. Chem. A*, 4 (2016) 17440–17454.
- [89] R. Kumar, P.K. Gupta, P. Rai, A. Sharma, *New J Chem.*, 3 (2017) 2–6.
- [90] K. Thiagarajan, J. Theerthagiri, R. Senthil, P. Arunachalam, J. Madhavan, M. Ghanem, *J. Solid State Electrochem.*, 22 (2018) 527–536.
- [91] M. Guo, J. Balamurugan, N. Kim, J. Lee, *Appl. Catal. B Environ.*, 239 (2018) 290–299.
- [92] W. Low, P. Khiew, S. Lim, C. Siong, E. Ezeigwe, *J. Alloys Compd.*, 768 (2018) 995–1005.
- [93] P. Vishnukumar, B. Saravanakumar, G. Ravi, V. Ganesh, R. Guduru, R. Yuvakkumar, *Mater. Lett.*, 219 (2018) 114–118.
- [94] Q. Zhou, Y. Gong, J. Lin, *J. Electroanal. Chem.*, 823 (2018) 80–91..
- [95] S. Zhao, K. Tao, Y. Gong, *Dalt. Trans.*, 48 (2019) 5315–5326.

- [96] X. Liu, J. Wang, G. Yang, ACS Appl. Mater. Interfaces, 10 (2018) 20688–20695.
- [97] J. Hou, J. Gao, L. Kong, Electrochim. Acta, 377 (2021) 138086.
- [98] K. Haldar, R. Biswas, A. Arya, I. Ahmed, S. Tanwar, A. Sharma, Energy Storage, 4 (2022) 1–12.



# **CHAPTER-II**

---

## **Basics of CBS and SILAR Methods and Characterization Techniques**

---

## Chapter-II

### Basics of CBS and SILAR Methods and Characterization Techniques

Sr. No.	Title	Page No.
2.1	Introduction: nanomaterials and thin films	33
2.2	Basics of chemical bath synthesis (CBS) method	35
	2.2.1 Concept of ionic and solubility product	36
	2.2.2 Nucleation and growth in CBS method	37
	2.2.3 Preparative parameters of the CBS method	39
	2.2.4 Advantages of the CBS method	40
2.3	Basics of successive ionic layer adsorption and reaction (SILAR) method	40
	2.3.1 Background and fundamentals of the SILAR method	41
	2.3.2 Mechanism and film growth in SILAR method	46
	2.3.3 Preparative parameters of SILAR method	46
	2.3.4 Advantages of the SILAR method	47
2.4	Physico-chemical characterization techniques	48
	2.4.1 X-ray diffraction (XRD)	48
	2.4.2 Fourier transform infrared spectroscopy (FT-IR)	48
	2.4.3 Raman spectroscopy	49
	2.4.4 X-ray photoelectron spectroscopy (XPS)	49
	2.4.5 Field emission scanning electron microscopy (FE-SEM)	50
	2.4.6 High resolution transmission electron microscopy (HR-TEM)	50
	2.4.7 Thermogravimetric (TG) Analysis	50
	2.4.8 Brunauer-Emmett-Teller (BET) and Barrete-Joyner - Halenda (BJH)	51
2.5	Electrochemical characterization techniques	51
	2.5.1 Cyclic voltammetry (CV)	53

	2.5.2	Galvanostatic charge-discharge (GCD)	54
	2.5.3	Electrochemical impedance spectroscopy (EIS)	55
2.6	References		56

## **2.1 Introduction: Nanomaterials and thin films**

Nanomaterials are defined as materials with at least one dimension in the range of 1 to 100 nm. These materials exhibit distinct features, such as size, shape, surface area, and reactivity, which differentiate them from bulk materials and contribute to their superior performance in various applications. Nanomaterials have revolutionized industries by enabling more efficient products, including sensors, electronics, paints, cosmetics, and energy storage and conversion devices, many of which have already entered commercial markets. Over the past few decades, the field of nanotechnology has grown rapidly, leading to the development of new nanomaterials and advances in synthesis techniques that allow better control over their properties. Material synthesis plays a significant role in many fields, especially when it comes to energy-related applications such as energy generation, conversion, and storage. Different types of nanomaterials are synthesized in two forms in all of the aforementioned study fields: 1) bulk form and 2) thin film form [1].

Globally, thin film technology is emerging as a significant area of research. At the moment, the rapid rise in demand for thin film materials and devices has given rise to new prospects for the growth of novel materials, processes, and technologies. As a result, much thought has gone into developing improved materials in the form of thin film to boost the effectiveness of current ESSs. The first thin solid films were developed through electrolysis in 1838. “Any solid or liquid object with one of its dimensions very much less than that of the other two called a thin film.” A thin film is defined as a material’s layer that measures just a few micrometers in thickness. The procedure used to prepare such thin films on a substrate is known as a deposition of thin film. The characteristics and qualities of these thin films are closely tied to the specific deposition method employed [2].

To develop nanomaterials in thin film forms, two primary branches of thin film deposition processes can be broadly classified as either physical or chemical methods [3, 4]. There are two categories of physical methods: sputtering and vacuum evaporation. In vacuum evaporation, the melt experiences a reduction in pressure below its vapor pressure, which causes the melt to evaporate and move into the gaseous phase, and condense to deposit on a substrate. A slab of the material that is deposited onto the substrates is electrically energized in a vacuum chamber with an inert atmosphere when using the sputtering process. The positively charged gas ions strike the target material’s atoms, or gas atoms that have lost their electrons inside the plasma, with enough kinetic

energy. As a result, a stream of vapor is created that travels through the chamber, strikes, and adheres to the substrate. Radiofrequency (RF) sputtering, Glow discharge DC sputtering, Magnetron sputtering, etc. are examples of a sputtering method. The chemical approach also uses the gas and liquid phases depending on the phase of the precursor. Chemical vapor deposition (CVD), metal-organic CVD (MOCVD), etc., are examples of gas-phase chemical deposition methods. These techniques provide the necessary deposition by reacting precursor vapors with the surface of a solid substrate [4, 5].

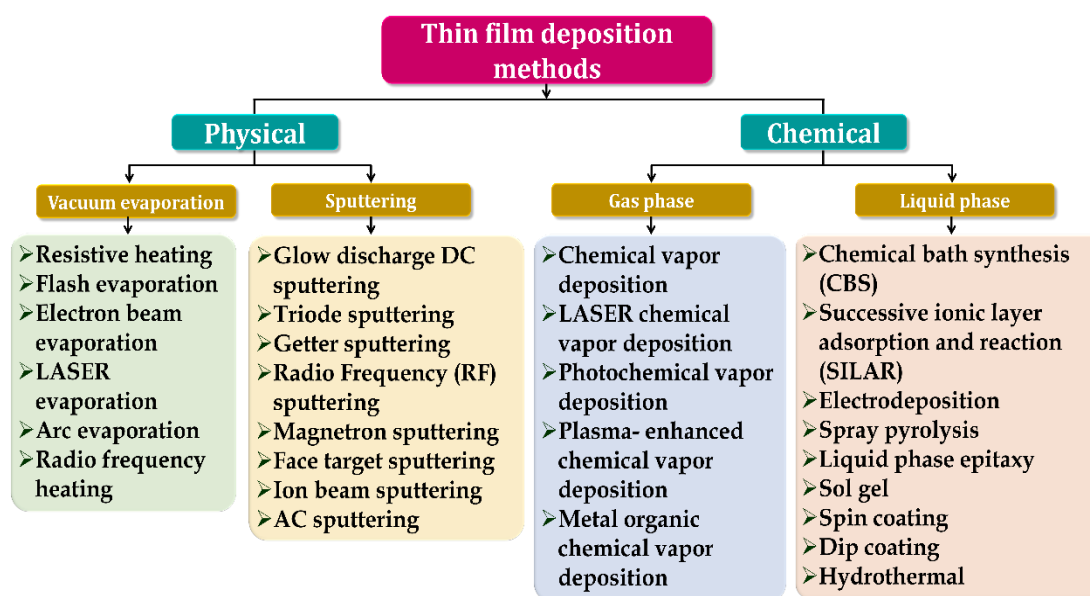


**Chart 2.1:** Thin film deposition methods

Liquid phase chemical deposition is a distinctive method involving a gentle process where a thin film is prepared on a substrate employing a ligand-exchange reaction under varying experimental parameters. The liquid phase chemical approach includes several different methods like electrodeposition, hydrothermal, spray pyrolysis, sol-gel, CBS, SILAR, etc. Physical and gas-phase chemical deposition have certain shortcomings, including high operating pressure and temperature, complex instrumentation, maintenance requirements, and high cost. On the other hand, large-scale material deposition is made easy, inexpensive, and convenient by solution-phase chemical methods [6, 7]. As a result, chemical techniques are frequently employed to create nanostructured materials for various applications.

## 2.2 Basics of chemical bath synthesis (CBS) method

For more than a century and a half, CBS has been employed as a synthesis process [8] and it has been frequently utilized effectively in the last two decades for the synthesis of several types of transition metal chalcogenides [9, 10], TMOs [11, 12], transition metal phosphate [13], transition metal vanadium oxides (TMVOs) [14] thin film electrodes and applied in various applications like solar cells, optoelectronics, SC, gas sensors, etc. Figure 2.1 shows the photograph of the CBS instrument. When it comes to the method for chemical synthesis, there are two ways to approach the preparation of nanomaterials: from a thermodynamic perspective or a kinetic perspective. The CBS method primarily relies on an approach of thermodynamics. Within this framework the synthesis process involves three stages; firstly, preparation of supersaturation; secondly, nucleation, and finally subsequent growth. When it comes to producing nanomaterials the CBS method is widely preferred. This method starts by initiating nanomaterials' nucleation on a solid surface, from a liquid-phase medium [15].



**Figure 2.1:** Photograph of instrument for CBS method

The CBS approach is currently gaining popularity because it does not necessitate complicated instruments such as a vacuum system or other costly equipment. The initial compounds are widely accessible and inexpensive. The CBS approach is used to prepare nanomaterials with monitored composition, size, and shape, and characteristics are determined by preparative factors, which are simple to regulate. The formation of a solid phase from a solution involves two stages: nucleation and particle growth. The relative rates at which these two continuous processes which affect particle size in a solid phase. Any precipitate needs a minimum quantity of ions or molecules, known as the nucleus, in order to form a stable phase in



contact with a solution [6, 8]. The idea behind nucleation in solution is that as molecules form clusters, they break down quickly, and the particles coalesce to increase the particle size. The process of formation of nanomaterials can occur through ion-by-ion condensation or by adsorption of solution particles on the solid surface, contingent upon deposition conditions such as bath temperature, pH, concentration of the solution, etc.

### 2.2.1 Concept of ionic and solubility product

The CBS method for nanomaterial development is based on the controlled precipitation in the solution. The formation of nanomaterials via controlled reaction consists of three stages: (i) species production, (ii) species transit, and (iii) species condensation [6]. When the soluble salt AB dissolves in a solvent, it establishes an equilibrium between the solid form of AB and the ions A and B in the solution. This leads to the formation of a saturated solution, where the ions A and B coexist with the undissolved solid AB.



According to the mass action law,

$$K = \frac{C_A^+ C_B^-}{C_{AB}} \quad (2.2)$$

In this context,  $C_A^+$ ,  $C_B^-$  and  $C_{AB}$  represent the concentrations of the ions  $A^+$ ,  $B^-$ , and the solid compound AB in the solution. The concentration of the pure solid remains constant, making it a fixed value in the equilibrium expression then,

$$C_{AB}(S) = \text{constant } (K') \quad (2.3)$$

$$K = \frac{C_A^+ C_B^-}{K'} \quad (2.4)$$

$$KK' = C_A^+ C_B^- \quad (2.5)$$

The product of  $KK'$  is represented as  $K_s$ ,

$$K_s = C_A^+ C_B^- \quad (2.6)$$

Constant  $K_s$  known as the solubility product ( $S_p$ ), while  $C_A^+$  and  $C_B^+$  are known as the ionic product ( $I_p$ ). The  $I_p$  equals the  $S_p$  when the solution is saturated. However, when  $I_p$  surpasses  $S_p$ , or when  $I_p/S_p = S > 1$ , precipitation happens, and the solution becomes supersaturated, which causes nuclei to develop both on the solid surface (heterogeneous) and in the solution (homogeneous) [16–18]. A homogeneous and heterogeneous reaction in a supersaturated state causes the ions to form nuclei in the solution and on the solid surface, respectively. A supersaturation condition needs to be

established in the solution in order for nucleation and growth to produce nanomaterials [19].

### 2.2.2 Nucleation and growth in CBS method

In CBS method, nanomaterials are formed through a chemical reaction occurring within a solution. Nucleation, crystal growth, are processes in the nanomaterial's preparation process. Depending on the synthesis mechanism, CBS can occur by either initial homogeneous nucleation in solution or heteronucleation on a solid surface [19].

#### (a) Homogeneous/Heterogeneous nucleation

In accordance with basic solubility aspects, a precipitate will occur when the product of anions and cations concentrations exceeds the  $S_p$ . Small fluctuations in the solution, whether in concentration, temperature, or other factors, can cause homogeneous nucleation. Collisions between individual ions or molecules generate embryos, embryos which are nuclei that are naturally unstable to redissolution. Embryos develop by accumulating individual species that collide with them. These species could be molecules, atoms, or ions. Adsorption of ions in the embryo appears to be the most likely growth mechanism for CBS. Collisions between embryos may also contribute to their growth; however, this is less likely until the embryo concentration is high. These embryos may redissolve in the solution before they have a chance to grow into stable particles.

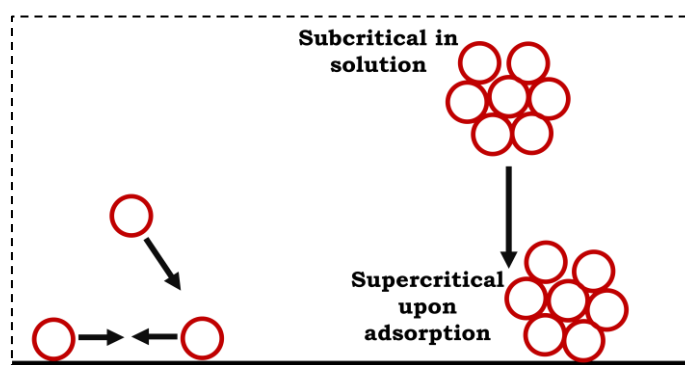


**Figure 2.2:** Heterogenous nucleation on the surface of the solid surface

Heterogeneous nucleation occurs when individual ions or subcritical clusters are deposited onto the substrate surface. When an interface forms between the embryo and the solid substrate, less energy is usually needed than during homogenous

nucleation, in which no interface forms; in contrast to the high level of supersaturation that is frequently required for homogeneous nucleation, heterogeneous nucleation is therefore energetically preferable to homogeneous nucleation and can occur at equilibrium saturation conditions. These subcritical nuclei can expand by adding material from solution or by surface diffusion. Schematic Figure 2.2 depicts the adsorption process of the ion/subcritical embryo on the solid surface.

### (b) Crystal growth

Two main processes lead to growth: self-assembly and deconstruction and reconstruction. In the first procedure, self-assembly can carry out growth after nuclei are formed. Conversely, growth results from the reorganization of particles as a result of the aggregation and coalescence process, also known as the second process and Ostwald ripening. As seen in Figure 2.3, aggregation occurs when individual particles adhere to one another, while coalescence occurs when smaller or less stable particles close to a bigger crystal, combine and develop into a larger crystal.

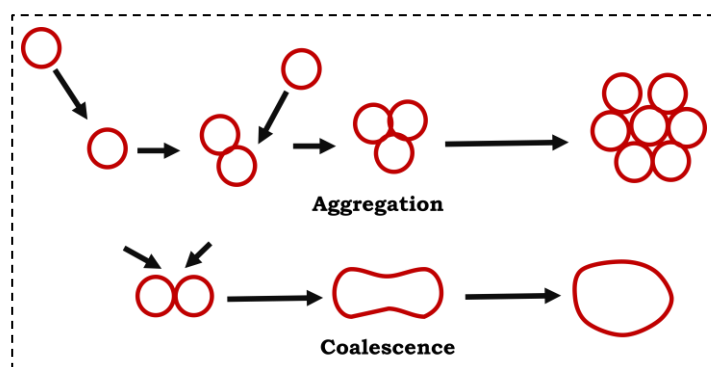


**Figure 2.3:** Particle growth by aggregation and coalescence process

### (c) Growth of nanomaterials

Growth in chemical processes is accomplished using hydroxide cluster mechanisms or ion-by-ion processes. Homogeneous nucleation in the ion-by-ion growth mechanism necessitates a substantial level of saturation. The introduction of heterogeneity through surface imperfections and available free particles is essential for facilitating nucleation. The substrate surface provides a catalytic environment for initiating nucleation. The nucleation commences, and it accelerates material growth, resulting in a higher deposition rate at the nucleation site compared to other areas of the substrate. Material growth persists until it is paused by certain processes or disrupted by external substances.

### **2.2.3 Preparative parameters of the CBS method**

The achievement of a nanomaterials having uniformity and size and shape via the CBS method varies with the reaction rate. The growth rate of material is influenced by the solution's supersaturation and the occurrence of nucleation sites. Several factors influence the growth kinetics of the materials, including pH, temperature, the use of complexing agents, and more [9].

#### **(a) pH of the solution**

As the pH of the reaction increases, it stabilizes the metal ion complex, reducing the availability of free metal ions. This decrease in free metal ions slows the reaction rate, which in turn affects the deposition process, potentially leading to variations in the thickness of the resulting film [20].

#### **(b) Concentration of the solution**

In the CBS mechanism of deposition usually takes place in a supersaturated solution. The concentration of cations or anions rises with an increase in the concentration of ionic precursors. In certain cases, high growth of nanomaterials can be achieved by increasing the concentration of ionic precursors up to some limit. Following this limit, increasing reaction rates cause a decrease in material growth and subsequently raise the rate of precipitation. On the other hand, material cannot develop if the concentration of ionic precursors is below their optimal value. For the synthesis of nanomaterials, the ideal precursor concentrations are therefore crucial [21].

#### **(c) Complexing agent**

An increase in the concentration of a complexing agent leads to a decrease in the concentration of free metal ions within the solution. This reduction in free metal ion concentration subsequently slows down the reaction rate that governs the particle size of the material.

#### **(d) Temperature of the solution**

The bath temperature also plays a role in influencing the reaction rate. When the solution temperature rises, the complex dissociates at a faster pace. This increased temperature also provides molecules with more kinetic energy and promotes ion interaction. The terminal growth of material is influenced by the degree of supersaturation, which can either increase or decrease with temperature changes [22].

**(e) Synthesis time**

Synthesis time is one of the factors that affect thin film formation in the CBS method. It typically has a significant impact on the particle size of the material, which can influence the morphological, and structural characteristics of the material [23].

**(f) Nature of solid surface**

The solid surface's structure significantly impacts the reaction kinetics and material growth. In order to initiate and sustain development, nucleation centers must be present on the solid surface. When the solid surface's lattice characteristics align well with the material growth, rapid formation and a significant particle size can be achieved.

**2.2.4 Advantages of CBS method**

The CBS method provides several advantages over physical and chemical methods which are as mentioned below,

- The CBS approach is affordable, simple, and convenient for high-yield nanomaterial preparation.
- The preparation of nanomaterials can be carried out at a desired temperature.
- The CBS process does not produce any toxic gases or organo-metallic solvents.
- Processing slowly at room temperature allows for better crystallographic alignment and improved grain structure.
- Along with this, higher producibility, and uniformity in size and shape of nanomaterials can be achieved.

**2.3 Basics of the successive ionic layer adsorption and reaction (SILAR) method**

In 1985, Nicolau [25] published a report on the deposition of ZnS and CdS, which was established by the SILAR methodology. Ristov et al. [3] then used this protocol to synthesize polycrystalline copper oxide ( $\text{Cu}_2\text{O}$ ) in the same year. The outstanding structural, electrical, and optical properties of the films synthesized in these two investigations served as inspiration for the method continuance, and a wide range of metal chalcogenides were deposited using it in the same decade [25–27]. Currently, SILAR is a highly sought-after technique in research, having proven itself as an easy way to deposit thin films of metal hydroxides, sulfides, selenides, oxides,

and peroxides, as well as more complicated heterostructure systems, on a desired substrate.

### 2.3.1 Background and fundamentals of the SILAR method

The SILAR method, as suggested by its acronym, relies on successive ionic layer adsorption and reaction on a surface. The initial adsorption creates a monolayer, and this is followed by a reaction triggered by the subsequent adsorption of another ionic species. This reaction results in the formation of an insoluble product, which serves as the foundation for the thin-film coating. The procedure is subsequently repeated to augment the thickness of the deposited layer. A SILAR setup employs a series of steps, as depicted in Figure 2.4.

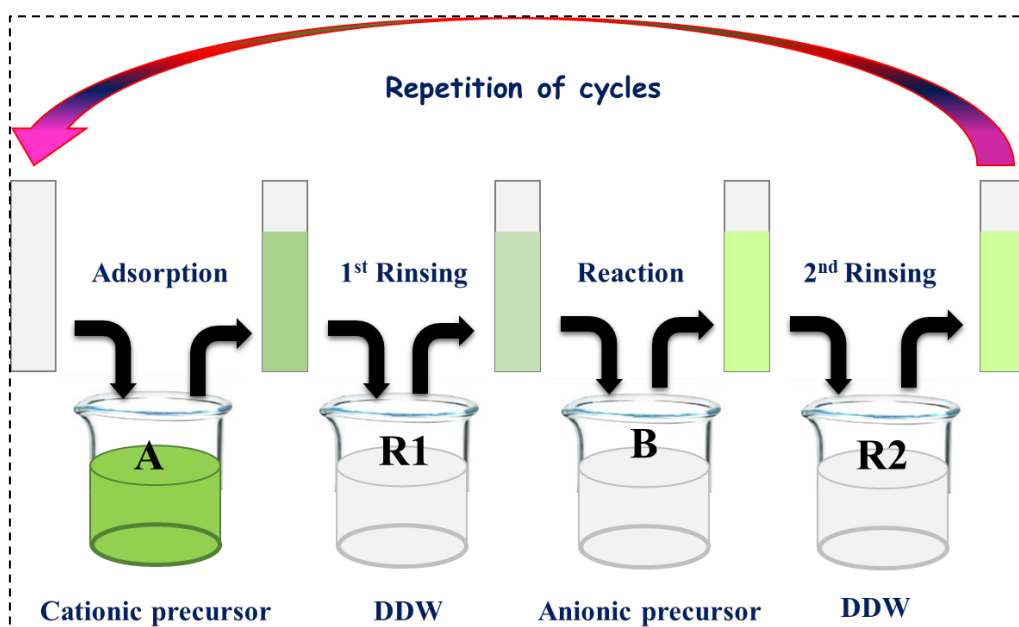


**Figure 2.4:** A schematic representation of the SILAR setup

Solution A serves as the primary ionic solution, typically containing aqueous metal cations. Meanwhile, R1 and R2 act as containers for pure solvents, usually double distilled water (DDW). In order to obtain a uniform and highly ordered film throughout the formation of the atomic film, an adsorbed monolayer of the primary ionic precursor plays a crucial role. Thus, it is essential to remove the excess ions that have settled on the substrate, which can be attained by the immersion of the substrate into rinsing solution R1. A similar rinsing process is performed with R2 after the desired product layer is formed in solution B, which contains the secondary ionic precursor. After the final rinse with R2, the deposition cycle is completed, and the substrate is returned to



solution A to initiate a new deposition cycle. The layer-by-layer assembly of the thin film proceeds through four steps.

### (a) Adsorption

In theory, adsorption is a phase transfer process that takes place at the interface between two different phases. It is believed that active sites on solid surfaces have different energies than those on neighboring liquid phases [28]. These energetically heterogeneous active sites are able to interact with surrounding liquid phase solutes as illustrated in Figure 2.5.

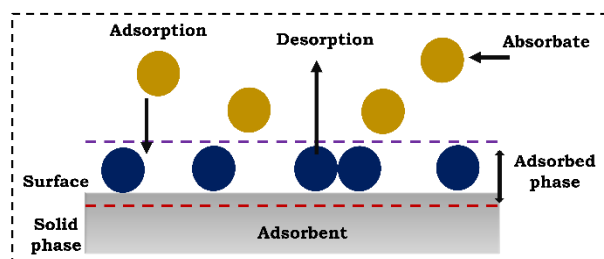


**Figure 2.5:** The schematic of the adsorption process on the adsorbent

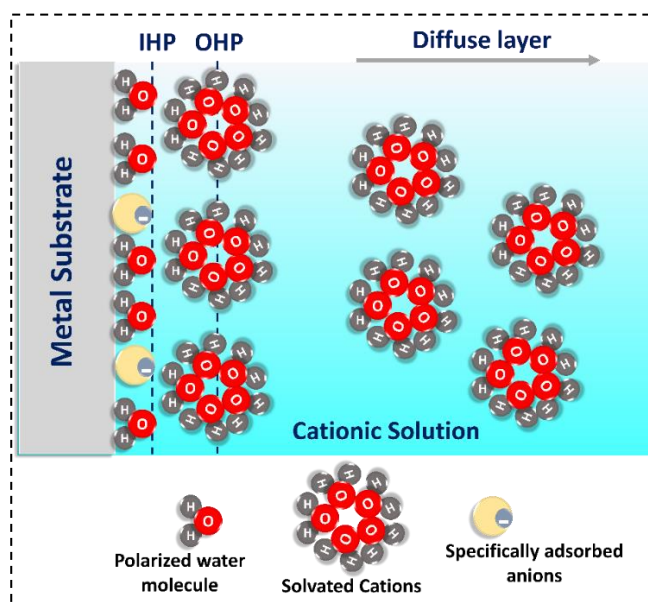


**Figure 2.6:** Schematic of Helmholtz double layer during the adsorption step in the SILAR method

The innermost layer is composed of solvent molecules, predominantly water molecules, formed most adjacent to the substrate surface and is referred to as the inner layer. This inner layer may also contain additional species known as especially adsorbed anions and the centers of adsorbed anions are located in the inner Helmholtz

plane (IHP) as depicted in Figure 2.6. Solvated cations (solvated ions are surrounded or complexed by solvent molecules), approach the substrate and adhere to its surface. This process neutralizes the surface charges. The chemical attractive forces between them allow for this adsorption [29]. The outer Helmholtz plane (OHP) marks the position of the centers of the closest solvated cations. These nonspecifically adsorbed solvated cations are found between the OHP and the bulk of the solution.

### (b) First rinsing

To avoid homogeneous precipitation from the rapid reaction with anion in the third stage, the loosely bound and excess solvated cations in the Helmholtz layer are removed in this step by rinsing in DDW (Figure 2.7). This is the advantage of the SILAR approach over the other chemical methods for applying a thin layer of material. In the SILAR process, homogenous precipitation is not possible unless the substrates are thoroughly rinsed.

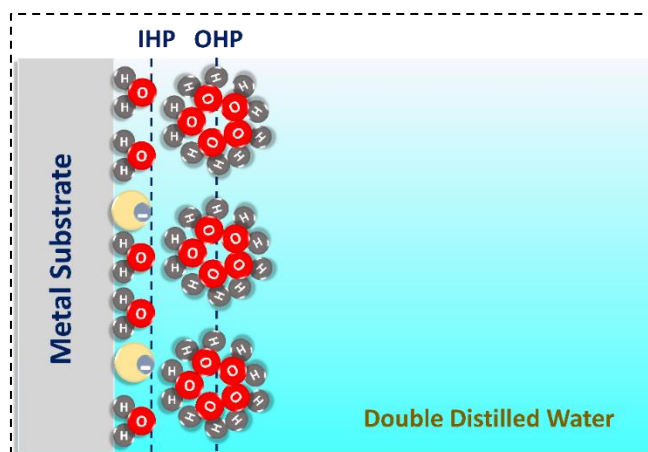


**Figure 2.7:** Schematic of excessive ions removal during first rinsing in the second step of the SILAR method

### (c) Reaction

During this stage, the pre-adsorbed cations and newly adsorbed anions react, forming a water-insoluble solid compound, as illustrated in Figure 2.8. Additionally, certain counter ions from the anionic solution are attached to this solid compound.

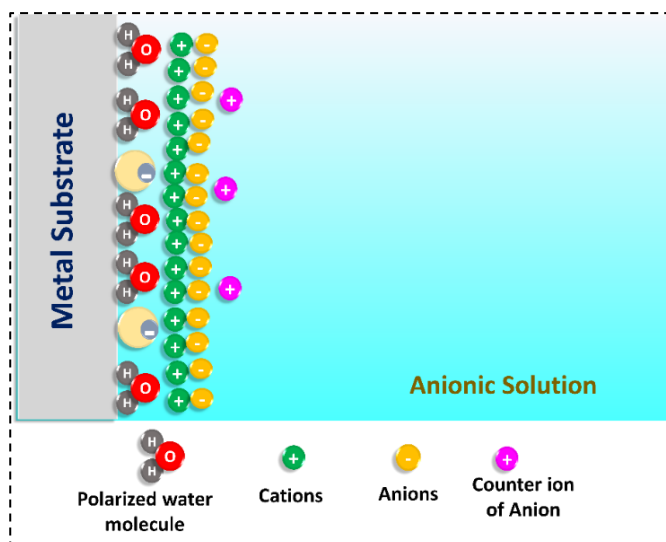


**Figure 2.8:** Schematic of solid compound formation during the reaction process in the third step of SILAR method

**(d) Second rinsing**

Second rinsing represents the final phase of the SILAR method, where surplus and unreacted components, as well as any by-products of the reaction, are eliminated. Upon completion of this step, a monolayer of the desired material is deposited onto the substrate, as depicted in Figure 2.9. These four separate stages constitute one SILAR deposition cycle. After a specific number of cycles, sufficient material is deposited on the substrate as a uniform and adhering thin film. The adsorption, reaction, and rinsing times utilized have a considerable influence on the thin film's quality (in terms of adhesion, homogeneity, etc).

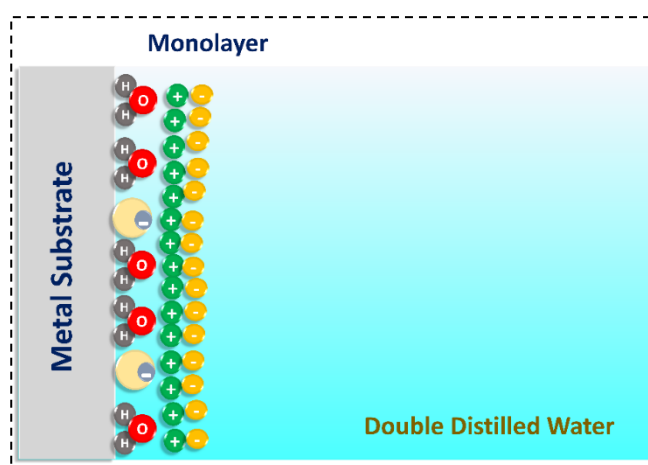


**Figure 2.9:** Schematic of monolayer formation during the second rinsing after the fourth step of the SILAR method

While the use of rinsing solutions is not obligatory, it serves the purpose of eliminating excess material from the substrate after each dip in the precursor solution. This process ensures that only one ionic layer remains on the substrate before it is submerged in the subsequent solution. There could be uncontrollably high material deposition without the rinsing stage [30]. Furthermore, too much precursor that has been trapped on the substrate's surface may be released into the solution that contains the second precursor, which would precipitate the target chemical inside the precursor solution. In the current study, the adsorption, reaction, and rinsing times in the fourth chapter were experimentally optimized through various trials to achieve uniform and adherent deposition.



**Figure 2.10:** Photograph of SILAR Instrument

The SILAR deposition can be performed using three different methods, that includes manual deposition, computer-controlled system, and microprocessor-controlled system. In the present study, a microprocessor-based SILAR instrument from Holmarc optomechanotronics PVT.LTD. (Figure 2.10) is utilized for the thin film preparation. In this method, substrates are attached to a vertical robotic arm and controlled by a microcontroller for both vertical and horizontal movement. Using vertical tweezers, the substrates are positioned on the line and then secured onto the spindle. A stepping motor drives the spindle as it turns and slides into the Teflon bearing. Up to six beakers can be utilized, with each beaker having its own adjustable dipping and retrieval speed, as well as customizable time settings for each. The spindle

can be adjusted to move vertically and rotates at various speeds, ranging from 1 to 200 rotations per minute (rpm).

### 2.3.2 Mechanism and film growth in SILAR method

The SILAR process for the deposition of compounds can be summarized by the chemical equations given below,



The solution comprising the first constituent of the final material is the compound  $A_xB_y$  completely dissolved in the desired solvent, as shown in reaction 2.7. Usually,  $A_xB_y$  is a metal salt in which  $A^{y+}$  represents cations such as  $Ni^{2+}$ ,  $Cu^{2+}$ ,  $Mn^{2+}$ ,  $Cd^{2+}$ ,  $Bi^{3+}$ , etc., and  $B^{x-}$  represents anions such as  $Cl^-$ ,  $NO_3^-$ ,  $SO_4^{2-}$ , etc. This solution's metal cation ( $A^{y+}$ ) serves as the cationic precursor for the SILAR deposition. The anionic precursor ( $C^{k-}$ ) is placed in a separate bath which is required to form the final material over the substrate, and it is prepared by dissolving a suitable precursor in DDW [28]. Anionic and cationic precursors react at the interface to produce a monolayer of the product ( $A_kC_y$ ) on the surface according to equation 2.9. At this point, the primary need that must be met is that the compound  $A_kC_y$  has an extremely low solubility in water, which results in its immediate solid precipitation. Furthermore, counter ions such as  $B^{x-}$  and  $D^{z+}$  produce compounds that exhibit high solubility in water, preventing the formation of deposits on the growing film. In the case of the SILAR method, film growth initiates after the first or second deposition cycle because the monolayer of water-insoluble compounds formed during the first SILAR cycle serves as nucleation centers, and with the repetition of such SILAR cycles, the desired thickness of material can be achieved.

### 2.3.3 Preparative parameters of SILAR method

Several factors influence the growth kinetics of thin films during the SILAR process, including the adsorption, reaction and rinsing time, temperature, complexing agent, solution concentration, and reaction solution composition. The following section discusses different deposition parameters that affect the growth of films:

**(a) Adsorption, reaction and rinsing time**

The preparation of thin films is significantly influenced by adsorption and reaction time. Shinde et al. [31] provide a thorough discussion of the impact of adsorption and reaction time on film growth. Performing rinsing steps between each immersion is essential to prevent unwanted precipitation within the reaction bath. Within a rinsing bath, species that are only loosely bound to the substrate surface are dislodged. The adsorption, reaction, and rinsing time also alters the morphology of the material [32].

**(b) Number of cycles**

The number of cycles in the SILAR method is a key parameter that one can easily alter the thickness of the thin film and material growth over the substrate.

**(c) Complexing agent**

Common complexing agents utilized in chemical deposition methods include polyvinylpyrrolidone, polyvinyl alcohol (PVA), ethylene diamine tetra acetic acid, triethanolamine, ammonia ( $\text{NH}_3$ ), etc. The complexing agent's ions attach themselves to the metal ions to create complex ions. As a chemical reaction progresses, metal ions are gradually liberated and made available for interaction with other ions. Consequently, a complexing agent performs a pivotal role in regulating the concentration of these metal ions throughout the course of the reaction. In the SILAR method, the gradual and controlled release of metal ions contributes to a controlled growth rate of the film. Thus, the incorporation of a complexing agent enables control over the film's growth kinetics.

**(d) Temperature**

The extent of dissociation of a complex compound is contingent on the temperature. Elevated temperatures promote increased dissociation, leading to a higher concentration of cations and consequently yielding an increased deposition rate. With these optimizing parameters one can control the growth kinetics of and achieve the desired properties of thin film.

**2.3.4 Advantages of SILAR method**

In addition to its simplicity, the SILAR method offers numerous advantages, which are outlined below:



- Thin film thickness is a significant factor in various applications, and in the SILAR method, it can be easily altered by changing the number of deposition cycles.
- Any substrate, regardless of its composition or size, can be deposited with a thin film.
- Thin film materials can be doped with foreign elements by simply introducing them into the cationic/anionic solution.
- Oxidation or corrosion of metallic substrates is effectively prevented during deposition due to the process being conducted at or in close proximity to room temperature.
- This method is highly convenient for producing composites of transition metal-based and carbon-based materials with high yield since it avoids wastage of material due to quick precipitation.

With these several advantages, SILAR method is highly efficient in producing nanomaterials and their composites in thin film form.

## **2.4 Physico-chemical characterization techniques**

The effectiveness of a material is closely related to its various physical and chemical characteristics. Consequently, the thorough examination of materials using diverse techniques and the meticulous analysis of the outcomes are essential responsibilities within the realm of research. This approach helps identify the most appropriate material for a particular application while also enabling the specification of the desired material characteristics and methods for their improvement. In the current study various material characterization techniques were employed to analyze the as prepared nanomaterials and their composites. This section provides a comprehensive overview of the fundamental principles and operation of these techniques.

### **2.4.1 X-ray diffraction (XRD)**

The XRD is a widely used characterization technique for analyzing the crystal structure of a sample, offering insights into the unit cell dimensions and the material's phase. The basic principle of XRD involves directing monochromatic X-rays at a crystalline sample at an incidence angle  $\theta$ ; these X-rays undergo diffraction due to parallel lattice planes separated by the interplanar distance,  $d$ . The intensity of the diffracted X-rays, as recorded with respect to the scattering angle, produces a diffraction pattern. Constructive interference occurs when the path difference is

equivalent to a whole-number multiple of the incident X-ray's wavelength [33]. Under these specific conditions, the peaks observed in diffraction patterns are commonly referred to as Bragg's law as follows,

$$n\lambda = 2d\sin\theta \quad (2.10)$$

Where, 'n' signifies the order of diffraction, 'λ' symbolizes incident X-ray wavelength.

#### **2.4.2 Fourier transform infrared spectroscopy (FT-IR)**

The FT-IR Spectroscopy is a technique used to identify chemical bonds in a molecule by detecting the absorption of infrared (IR) radiation at a specific wavelength. The spectrum is a fingerprint of investigating material. The principle is based on the fact that different molecular bonds absorb IR radiation at characteristic frequencies, causing vibrations such as stretching or bending. In FTIR, a broad-spectrum IR light passes through a sample, and some of this light is absorbed while the rest is transmitted. The resulting absorption pattern, which corresponds to the vibrational modes of the molecular bonds, is recorded as an interferogram. This is then converted into a spectrum using the Fourier transform, showing peaks that indicate the presence of specific functional groups. FTIR is widely used for molecular identification, structural analysis, and material characterization [34].

#### **2.4.3 Raman spectroscopy**

Raman spectroscopy is a molecular spectroscopic approach that uses light-matter interaction to reveal information about the composition or properties of a material. The scattered light (Raman scattering) can be used to identify particular bonding in the prepared material. Upon exposure to monochromatic light, a sample absorbs a portion of the light, allowing a significant fraction to pass through. Nevertheless, a small fraction of the light scatters in various directions due to the sample. When the incident and scattered light have the same frequency, and scattering occurs at an angle aligned with the incident beam, which is referred to as Rayleigh scattering. In contrast, only 1% of the scattered light deviates in frequencies from the incident frequency, and this phenomenon is known as Raman scattering [35].

#### **2.4.4 X-ray photoelectron spectroscopy (XPS)**

The XPS serves as a chemical analysis method primarily employed to investigate the surface chemistry and elemental composition of the samples. When an incoming X-ray possesses ample energy, it undergoes absorption by an atom, triggering

the photoelectric effect, which results in the ejection of an inner shell and measures its kinetic energy. Also, the binding energy of the photoelectron is computed using the formula below.

$$E_{\text{binding}} = E_{\text{photon}} - (E_{\text{kinetic}} + \varphi) \quad (2.11)$$

Where,  $\varphi$  represents the work function,  $E_{\text{binding}}$  is the binding energy of the emitted photoelectrons,  $E_{\text{photon}}$  is the energy of X-ray photons, and  $E_{\text{kinetic}}$  is the kinetic energy of the atomic orbital. By analyzing the number of emitted photoelectrons as a function of their binding energy, one can determine the elemental composition of the sample and identify the different oxidation states of the constituent elements [36].

#### **2.4.5 Field emission scanning electron microscopy (FE-SEM)**

Rather than light, the FE-SEM makes use of electrons. Electrons generated by a field emission source are accelerated in an electric field. The primary electrons are focused into a narrow beam using electromagnetic lenses. When the beam hits the sample, it releases secondary electrons from the specimen. These secondary electrons carry the topographical details of the sample. A detector processes these electrons, generating an electrical signal that is amplified and converted into an image. Sample preparation is a crucial part of FE-SEM characterization. Before placing the sample on a holder, a thin layer of platinum or gold is applied to make it conductive.

#### **2.4.6 High resolution transmission electron microscopy (HR-TEM)**

The HR-TEM distinguishes itself from FE-SEM primarily by the speed of the primary electrons employed. Specifically, HR-TEM employs electrons of significantly higher velocity compared to those used in FE-SEM. Furthermore, while electrons in FE-SEM interact by bouncing off the sample surface, HR-TEM electrons transmit through the sample itself, enabling a distinct mode of observation. The basic principle of HR-TEM is electrons at high-velocity traverse within a vacuum chamber, passing through an ultra-thin sample deposited on a TEM grid. The imaging process involves the utilization of a charge-coupled device camera to capture precisely focused images. A metal grid holds up the sample and it is a mesh-covered flat disc that is used to hold a very thin sample segment.

#### **2.4.7 Thermogravimetric (TG) analysis**

TG analysis is a powerful technique used to study the thermal characteristics of materials. TG analysis measures the change in mass of a sample in relation to change

in temperature or time. This helps identify events like dehydration, decomposition, or desorption that cause weight loss [37]. The sample is heated at a specified rate in an inert or reactive gas (like nitrogen or oxygen), and the mass is continuously recorded. As the temperature increases, the sample may undergo processes such as decomposition, oxidation, or evaporation, causing a mass change. The resulting TG analysis curve (mass vs. temperature/time) provides insight into the material's thermal stability, composition, and degradation behavior. This analysis is useful for understanding properties like thermal decomposition, volatile content, and reaction kinetics.

#### **2.4.8 Brunauer-Emmett-Teller (BET) and Barrette-Joyner-Halenda (BJH)**

The BET surface area analysis is a widely used technique to measure the specific surface area of materials, particularly porous and powdered substances. It is based on the principle of gas adsorption, where an inert gas, often nitrogen is allowed to adsorb onto the surface of a material at a low temperature. By measuring the amount of gas adsorbed and applying the BET equation, the surface area of the sample can be calculated. This technique is crucial in determining the surface properties of materials in fields like catalysis, adsorption studies, and material science, as it helps evaluate the effectiveness of materials in applications that rely on surface interactions [38]. The specific surface area, expressed in  $\text{m}^2 \text{g}^{-1}$ , furnishes vital insights into the influence of materials architecture and surface porosity. The characterization of pore size distribution, known as BJH analysis, involves determining the distribution of pore volume based on pore size which is expressed in nm.

### **2.5 Electrochemical characterization techniques**

Electrochemical characterization techniques, using half-cell and full-cell testing, are essential for evaluating the performance of energy storage materials like batteries and SCs. In half-cell testing, one electrode is tested against a reference electrode, allowing for the isolated study of the electrochemical properties of a single electrode material, such as its capacity, stability, and voltage profile. This method is often used in the primary phase of research to understand the behavior of new materials. Full-cell testing, on the other hand, involves testing the complete device, where both the anode and cathode materials are present, simulating practical application. Full-cell testing provides insights into the overall performance, including SE, SP, and cycle life of the device. Together, these techniques offer a complete understanding of the

electrochemical properties of materials and the performance of ESSs [39]. Figure 2.11 (a) illustrates the schematic representation of the three-electrode cell system. The electrochemical potentiostat regulates the voltage between the working electrode and reference electrodes while measuring the current passing through the counter electrode to the working electrode.

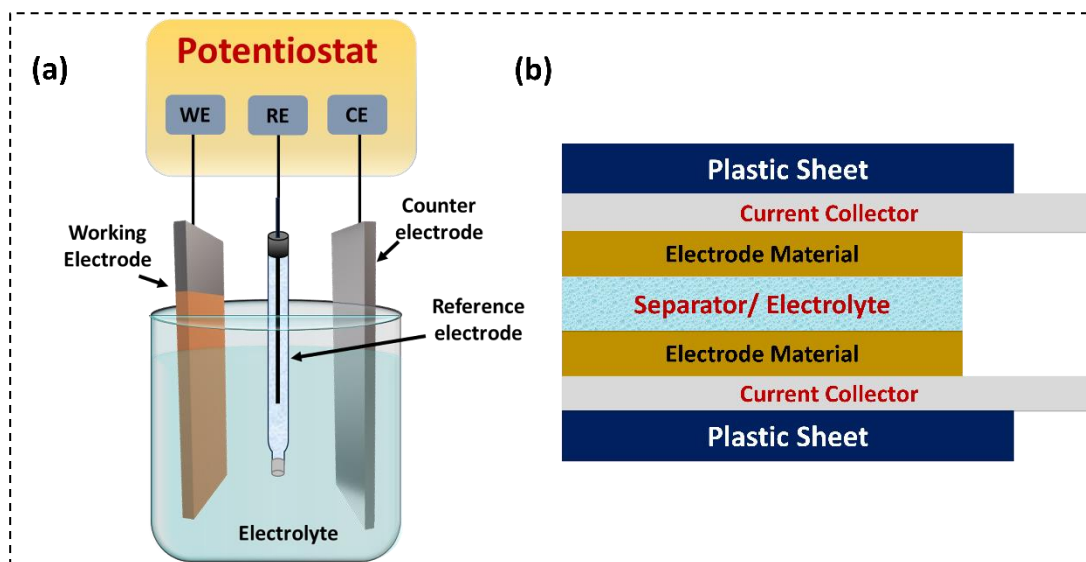


**Figure 2.11:** Schematic of (a) half-test cell and (b) Full-test cell for electrochemical performance evaluation

The resultant current correlates with the voltage created between the working electrode and a reference electrode. A current to voltage converter then converts this current into a voltage, and the system records the voltage over time. It is noted that an ideal electrometer should possess significant electrical resistance to ensure minimal input current. This feature is crucial because the flow of current through a reference electrode has the potential to alter the actual potential, subsequently impacting the accuracy of collected data [40]. Within two-electrode systems, a setup involves two working electrodes enclosed within a solid gel/aqueous electrolyte, which serves the dual role of electrodes and a separator. Figure 2.11 (b) depicts a schematic resembling a packaged SC cell. Various methodologies, such as CV, GCD, and EIS, can be utilized to explore the electrochemical capacitive capabilities of prepared materials. Assessing the electrochemical attributes of thin films is crucial when employing them as active electrodes in SC devices.

### 2.5.1 Cyclic voltammetry (CV)

The CV serves as an electroanalytical method, often referred to as two-way linear sweep voltammetry. Its primary application involves the electrochemical assessment of active materials within an electrolyte solution, particularly for evaluating their suitability in SCs. This method, known as a potentiodynamic technique, involves the potential of working electrode scanning between predefined potential window limits at a consistent scan rate, as illustrated in Figure 2.12. It provides fundamental insights into redox behavior, charge transfer kinetics, reversibility, and material stability, among other key characteristics.

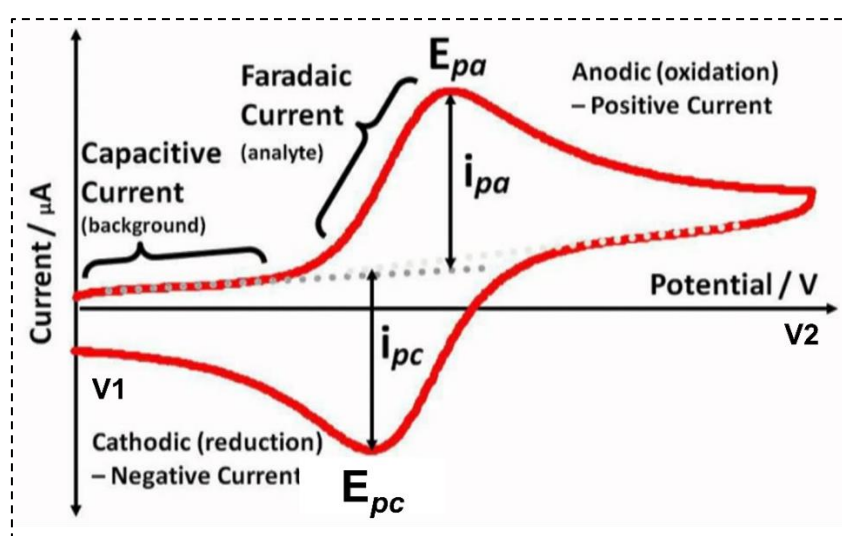


**Figure 2.12:** The CV plot with forward and reverse scan [41]

Choosing the initial and final potential values holds the utmost importance in CV measurement. Employing a three-electrode system helps mitigate ohmic resistance. The operating potential window in this technique can differ based on the electrolyte used, influenced by both the electrode material and the composition of the electrolyte. Furthermore, the material's redox potential and the electrolyte's decomposition capacity influence the working electrode's operational potential window [42]. In a CV analysis, the potential is gradually altered between two set values, forming a defined potential window. Once the voltage reaches V2, the scan reverses direction, moving back towards V1. Here, V1 and V2 indicate the boundaries of the potential range. The terms  $i_{pc}$  refer to the cathodic peak current and  $i_{pa}$  refer to the anodic peak current, while  $E_{pc}$  is a cathodic peak voltage and  $E_{pa}$  correspond to the anodic peak voltages observed in the voltammogram, as depicted in Figure 2.12. In the forward sweep, the current rises as the potential nears the oxidation potential of the material, but then starts

to decrease as the potential continues rising, mainly due to the high concentration of electrolyte ions [43].

### 2.5.2 Galvanostatic charge-discharge (GCD)

The GCD, also known as chronopotentiometry, stands as a widely recognized method crucial for obtaining insightful data regarding  $C_{sp}$ , SE, SP, equivalent series resistance, and cycle life in various systems. This method entails applying a constant current to the working electrode while monitoring the potential relative to a reference electrode. Throughout the charge and discharge cycles at a fixed current density, the amount of charge transferred within the electrode stays the same. Changes in potential and time are noted, depending on the current density applied and the schematic of the GCD curve, illustrated in Figure 2.13.

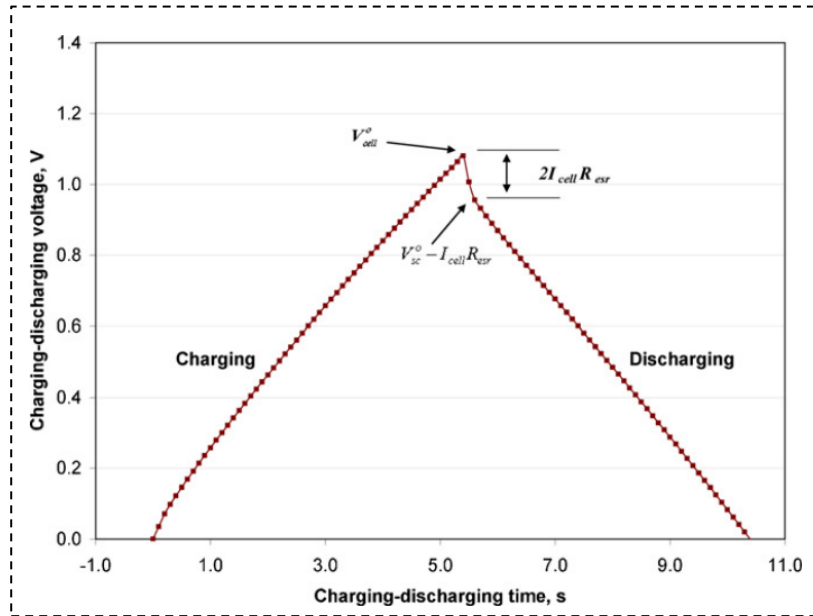


**Figure 2.13:** Plot of the charge-discharge curve [44]

For assessing the cycle life of SCs, employing a two electrode test cell proves advantageous as it closely mimics real-world operational scenarios. The charge-discharge curve's characteristics unveil the mechanism of charge storage within a specific electrode. A linear GCD curve signifies the storage of charges via an electrochemical double-layer mechanism, while a non-linear nature suggests that charges are stored through a pseudocapacitive mechanism [45].

The calculation of  $C_{sp}$  ( $F\ g^{-1}$ ), based on GCD, is determined using the following equation:



$$C_{sp} = \frac{I \times \Delta t}{m \times \Delta V} \quad (2.12)$$

Where,  $I$  is an applied current density,  $\Delta t$  is discharging time,  $\Delta V$  denotes the potential window and  $m$  signifies a loaded mass of active material.

### 2.5.3 Electrochemical impedance spectroscopy (EIS)

The EIS assesses material impedance across a range of frequencies, offering valuable insights into the resistance at the electrode-electrolyte interface and the charge transfer process. This technique involves applying a small alternating current to the SC cell across frequencies spanning from 10 mHz to 0.1 MHz. The resulting signals comprise the current response to the applied alternating current. Analysts typically interpret the EIS spectra using Nyquist and Bode plots for comprehensive analysis and understanding. Figure 2.14 depicts a Nyquist plot featuring Randles equivalent circuit, showcasing several circuit elements: solution resistance ( $R_s$ ), for charge transfer resistance ( $R_{ct}$ ),  $W$  denoting the warburg impedance element, and constant phase element (CPE) representing the imperfect capacitance. The significance of the EIS technique lies in its ability to delineate both frequency-dependent and independent electrical constituents through the Nyquist plot [47]. Utilizing equivalent circuit models composed of fundamental electrical components like capacitors and resistors enables the simulation of intricate electrochemical processes occurring near the electrode-electrolyte interface.

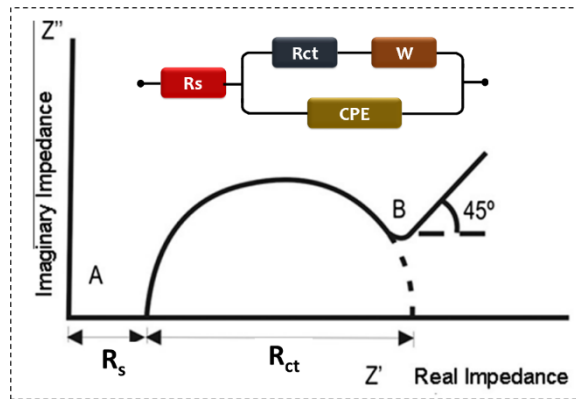


**Figure 2.14:** Nyquist plot and equivalent Randles circuit [46]

The Nyquist plot showcased in Figure 2.14 delineates the real and imaginary parts of impedance, with the X and Y axes representing these respective components. Within this plot, an inset of Figure 2.14 exhibits a fitted equivalent circuit related with the EIS representation. Notably, the semi-circular loop in Figure 2.14 correlates with

the resistance related to charge transfer. Warburg impedance tends to diminish at higher frequencies since the diffusing reactant covers shorter distances. At higher frequencies, the intercept on the real axis corresponds to the ohmic resistance. In contrast, at lower frequencies, reactants must travel longer distances, leading to an increase in Warburg impedance. In the Nyquist plot, Warburg impedance appears as a diagonal line with a 45° slope, reflecting the impact of ion mass transport within the system.

All electrochemical tests described in Section 2.5 were analyzed using VersaSTAT4 500 and ZIVE MP1 electrochemical workstations and the collected data was utilized to evaluate the electrochemical capacitive performance of electrodes.

## 2.6 References

- [1] L. Yu, H. Zhou, J. Sun, F. Qin, F. Yu, J. Bao, Y. Yu, S. Chen, Z. Ren, *Energy Environ. Sci.*, 10 (2017) 1820–1827.
- [2] I. Gurrappa and L. Binder, *Sci. Technol. Adv. Mater.*, 9 (2008) 043001.
- [3] M. Ristov, G. Sinadinovski, I. Grozdanov, *Thin Solid Films*, 123 (1985) 63–67.
- [4] J. George, *Preparation of Thin Films*, Marcel Dekker, Inc., New York, (1992).
- [5] A. Roth, *Vacuum Technology*, A. Roth, North Holland, (1990).
- [6] K. Chopra and I. Kaur, *Thin Film Device Applications*, Springer, (1983) 1-54.
- [7] M. Kiamahalleh, S. Zein, *Nanostructured ceramic oxides for supercapacitor application*, A. Balakrishnan and K. Subramanian, CRC Press, (2014).
- [8] B. Ezekoye, P. Offor, V. Ezekoye, F. Ezema, *Int. J. Sci. Res.*, 2 (2012) 452–456.
- [9] F. Hone and T. Abza, *Int. J. Thin Film Sci. Technol.*, 8 (2019) 43–52.
- [10] S. Pawar, B. Pawar, J. Kim, O. Joo, C. Lokhande, *Curr. Appl. Phys.*, 11 (2011) 117–161.
- [11] A. Alshoaibi, C. Awada, N. Alnaim, N. Almulhem, R. Obodo, M. Maaza, F. Ezema, *Crystals*, 12 (2022) 1–15.
- [12] Y. Wang, J. Guo, T. Wang, J. Shao, D. Wang, Y. Yang, *Nanomaterials*, 5 (2015) 1667–1689.
- [13] S. Marje, V. Patil, V. Parale, H. Park, P. Shinde, J. Gunjekar, C. Lokhande, U. Patil, *Chem. Eng. J.*, 429 (2022) 132184.
- [14] X. Liu, J. Wang, G. Yang, *ACS Appl. Mater. Interfaces* 10 (2018) 20688–20695.
- [15] B. Ghosh, B. Singh, P. Banerjee, S. Das, *Optik*, 127 (2016) 4413–4417.
- [16] K. Chopra, *Thin Film Phenomena*, McGraw-Hill, New York, (1969).
- [17] Y. Jiang and J. Liu, *Energy Environ. Mater.*, 2 (2019) 30–37.
- [18] J. Banerjee and K. Dutta, *Int. J. Energy Res.*, 46 (2022) 3983–4000.
- [19] X. Chen, R. Paul, L. Dai, *Natl. Sci. Rev.*, 4 (2017) 453–489.
- [20] M. Lewis and C. Bamforth, *Essays in Brewing Science*, (2006) 13-19.
- [21] A. Kariper, E. Güneri, F. Göde, C. Gümüş, *Chalcogenide Lett.*, 9 (2012) 27–40.
- [22] K. Preetha, K. Deepa, A. Dhanya, T. Remadevi, *Mater. Sci. Eng.*, 73 (2015) 012086.
- [23] W. Kumarage, L. Wijesundara, V. Seneviratne, C. Jayalath, B. Dassanayake, *Procedia Eng.*, 139 (2016) 64–68.
- [24] A. El-Shaer, S. Ezzat, M. Habib, O. Alduaij, T. Meaz, S. El-Attar, *Crystals*, 13 (2023) 788-801.
- [25] Y. Nicolau, *Appl. Surf. Sci.*, 22 (1985) 1061–1074.
- [26] Y. Nicolau and J. Menard, *J. Cryst. Growth*, 92 (1988) 128–142.
- [27] C. Grenoble, *J. Electrochem.*, 137 (1990) 2915–2923.
- [28] X. Gao, X. Li, W. Yu, *Wuji Cailiao Xuebao/Journal Inorg. Mater.*, 19 (2004) 610–616.
- [29] S. Ratnayake, J. Ren, E. Colusso, M. Guglielmi, A. Martucci, E. Gaspera, *Small*, 17 (2021) 2101666.
- [30] E. Worch, *Adsorption Technology in Water Treatment*, De Gruyter, Berlin, Boston,

- (2012).
- [31] V. Shinde, T. Gujar, C. Lokhande, *Sol. Energy Mater. Sol. Cells*, 91 (2007) 1055–1061.
  - [32] S. Bhosale, S. Kumbhar, S. Pujari, V. Patil, N. Kumar, R. Salunkhe, C. Lokhande, J. Gunjekar, U. Patil, *J. Energy Storage*, 72 (2023) 108417.
  - [33] V. Tolstoy, *Russ. Chem. Rev.*, 75 (2006) 161–175.
  - [34] G. Harrington and J. Santiso, *J. Electroceramics*, 47 (2021) 141–163.
  - [35] J. White, *Soil Sci.*, 112 (1971) 22–31.
  - [36] G. Bumbrah and R. Sharma, *Egypt. J. Forensic Sci.*, 6 (2016) 209–215.
  - [37] G. Greczynski and L. Hultman, *Prog. Mater. Sci.*, 107 (2020) 100591.
  - [38] P. Sinha, A. Datar, C. Jeong, X. Deng, Y. Chung, L. Lin, *J. Phys. Chem. C*, 123 (2019) 20195–20209.
  - [39] M. Stoller and R. Ruoff, *Energy Environ. Sci.*, 3 (2010) 1294–1301.
  - [40] W. Clarke and P. Orazio, *Contemporary Practice in Clinical Chemistry*, (2020) 159-170.
  - [41] N. Elgrishi, K. Rountree, B. McCarthy, E. Rountree, T. Eisenhart, J. Dempsey, *J. Chem. Educ.*, 95 (2018) 197–206.
  - [42] M. Khan, A. Asif, S. Khawaldeh, *J. Electr. Bioimpedance*, 9 (2018) 3–9.
  - [43] P. Joshi and S. Sutrave, *Int. J. ChemTech Res.*, 11 (2018) 77–88.
  - [44] S. Ban, J. Zhang, L. Zhang, K. Tsay, D. Song, X. Zou, *Electrochim. Acta*, 90 (2013) 542–549.
  - [45] N. Chodankar, H. Pham, A. Nanjundan, J. Fernando, K. Jayaramulu, D. Golberg, Y. Han, D. Dubal, *Small*, 16 (2020) 1–35.
  - [46] D. Ribeiro and J. Abrantes, *Constr. Build. Mater.*, 111 (2016) 98–104.
  - [47] H. Magar, Y. Rabeay, A. Mulchandani, *Sensors*, 21 (2021) 6578-6598.



# **CHAPTER-III**

---

## **Synthesis of Nickel Vanadium Oxide/rGO Composite Electrodes by CBS Method: Characterizations and Supercapacitive Performance**

---

# Chapter III

## Synthesis of Nickel Vanadium Oxide/rGO Composite Electrodes by CBS Method: Characterizations and Supercapacitive Performance

Sr. No.	Title		Page No.
3.1	Introduction		59
3.2	<b>Section A</b> <b>Nickel Vanadium Oxide by CBS Method: Synthesis and Characterizations</b>		
3.2.A.1	Introduction		60
3.2.A.2	Experimental details		60
	3.2.A.2.1	Chemicals	60
	3.2.A.2.2	Substrate cleaning	61
	3.2.A.2.3	Synthesis of nickel vanadium oxide	61
	3.2.A.2.4	Material characterizations	63
3.2.A.3	Results and discussion		64
	3.2.A.3.1	Film formation and reaction mechanism of C-NV series thin films	64
	3.2.A.3.2	XRD analysis	65
	3.2.A.3.3	FT-IR analysis	66
	3.2.A.3.4	XPS analysis	67
	3.2.A.3.5	FE-SEM and EDS analysis	69
	3.2.A.3.6	BET and BJH analysis	70
	3.2.A.3.7	Electrochemical performance analysis	71
3.2.A.4	Conclusions		79
3.3	<b>Section B</b> <b>Reduced Graphene Oxide: Synthesis and Characterizations</b>		
3.3.B.1	Introduction		80

<b>3.3.B.2</b>	Experimental details	80
	<b>3.3.B.2.1</b> Synthesis of rGO	81
	<b>3.3.B.2.2</b> Preparation of rGO electrode	81
<b>3.3.B.3</b>	Results and discussion	82
	<b>3.3.B.3.1</b> XRD analysis	82
	<b>3.3.B.3.2</b> Raman analysis	82
	<b>3.3.B.3.3</b> Electrochemical analysis	83
<b>3.3.B.4</b>	Conclusions	85
<b>3.4</b>	<p style="text-align: center;"><b>Section C</b>  <b>Nickel Vanadium Oxide/rGO Composite by CBS Method:</b>  <b>Synthesis and Characterizations</b></p>	
<b>3.4.C.1</b>	Introduction	87
<b>3.4.C.2</b>	Experimental details	88
	<b>3.4.C.2.1</b> Synthesis of nickel vanadium oxide/rGO composite material	88
	<b>3.4.C.2.2</b> Electrode preparation of nickel vanadium oxide/rGO composite material	88
	<b>3.4.C.2.3</b> Material characterizations	89
<b>3.4.C.3</b>	Results and discussion	89
	<b>3.4.C.3.1</b> XRD analysis	90
	<b>3.4.C.3.2</b> FT-IR analysis	91
	<b>3.4.C.3.3</b> Raman analysis	91
	<b>3.4.C.3.4</b> XPS analysis	92
	<b>3.4.C.3.5</b> TG analysis	94
	<b>3.4.C.3.6</b> FE-SEM and EDS analysis	95
	<b>3.4.C.3.7</b> HR-TEM analysis	98
	<b>3.4.C.3.8</b> BET and BJH analysis	99
	<b>3.4.C.3.9</b> Electrochemical analysis	101
<b>3.4.C.4</b>	Conclusions	108
<b>3.5</b>	References	108



### 3.1 Introduction

In the past few years, SCs have garnered significant interest on account of their advantageous properties, such as extended lifespan, high power output coupled with a substantial energy yield, and simple fabrication methods requiring minimal maintenance [1]. However, the SE of SCs still falls short of meeting the demands of contemporary portable electrical equipment, which are crucial for enhancing lifestyles and fostering economic advancement. To attain the required SE, researchers have conscientiously explored various materials suitable for SC electrodes, including metal oxides, hydroxides, sulfides, etc. [2, 3]. However, the extensive adoption of these materials has been hindered by issues such as insufficient stability, low conductivity, and low  $C_{sp}$ , thereby limiting their practical application in SCs. Achieving an effective and high-performing device necessitates the utilization of electrode materials exhibiting superior  $C_{sp}$ , robust cycling capabilities, and inexpensive synthesis processes. Researchers are actively looking for innovative solutions to address these challenges and develop SCs that meet the escalating demands of modern technology and lifestyle enhancements [4]. Metal vanadium oxide (MVO) based materials have gained significant attention owing to their exceptional conductivity, numerous active sites, and expansive and open structural channels that facilitate ion transformation [5]. The presence of a stable V-O covalent bond further enhances the structural stability. Despite their promise, there remains a noticeable gap between the theoretically predicted performance and the actual achieved performance of MVO-based electrodes. The NVO is particularly favored in energy storage applications owing to its widespread availability in the Earth's atmosphere and its involvement in excellent redox reactions among various MVOs.

In the present study, NVO and NVO/rGO composite electrodes were synthesized using the CBS method. This research investigated the impact of urea composition variations on the structure, morphology, and other relevant factors. Additionally, the study thoroughly examined how changes in composition (NVO and rGO) and their physico-chemical properties influenced electrochemical properties. The chapter is subdivided into three parts: Section A focuses on the synthesis of NVO electrodes via the CBS method and their characterizations for physicochemical and electrochemical properties. Section B focuses on the synthesis of rGO and characterizations for physicochemical and electrochemical properties; moreover,

Section C, demonstrates NVO/rGO composite electrode preparation and their physicochemical. The overall study analyzed the effects of varying the concentration of rGO in the optimized NVO sample (as discussed in Section A) and investigated the impact on electrochemical SC application.

### 3.2 Section A

## Nickel Vanadium Oxide by CBS Method: Synthesis and Characterizations

### 3.2.A.1 Introduction

Among the TMOs, significant strides have highlighted the potential of TMVOs as promising and lucrative candidates for SCs [5]. The concurrent presence of two distinct metal species within the crystalline framework of TMVOs can facilitate diverse redox reactions, thereby fostering a remarkable  $C_{sp}$  compared to distinct TMOs. NVO is one of the investigated electroactive materials for SCs owing to their multistep redox reactions and more electron transfer upon intercalation [6]. NVO offers many other merits, such as natural abundance, cost-effectiveness, and environmentally friendly nature [7]. Consequently, a simple CBS method was utilized to produce binder-free NVO thin film electrodes at desired temperature. This process involved meticulous optimization of preparatory parameters such as deposition time, bath temperature, pH of the solution, precursor concentration, etc. The present study emphasizes the influence of the concentration of hydrolyzing agent (urea) on the growth kinetics and consequent physicochemical properties of NVO thin film electrodes. Following that, NVO thin films are subjected to various characterizations, including XRD for scrutinizing structural properties, FT-IR for dissecting chemical bonding, XPS for determining oxidation states, BET and BJH analyses for evaluating surface area and pore size, and FE-SEM for examining micro/nano-structural features on the surface. Along with this prepared NVO electrodes are utilized for electrochemical SC application.

### 3.2.A.2 Experimental details

#### 3.2.A.2.1 Chemicals

Nickel nitrate hexahydrate ( $Ni(NO_3)_2 \cdot 6H_2O$ ), ammonium metavanadate ( $NH_4VO_3$ ), urea ( $CO(NH_2)_2$ ), graphite flakes, sodium nitrate ( $NaNO_3$ ), KOH, potassium permanganate ( $KMnO_4$ ), sulfuric acid ( $H_2SO_4$ ), PVA, N-methyl-2-

pyrrolidone (NMP), hydrogen peroxide ( $\text{H}_2\text{O}_2$ ), polyvinylidene fluoride (PVDF), and hydrazine hydrate ( $\text{N}_2\text{H}_4$ ) were purchased from Sigma Aldrich. Purchased chemicals are analytical grade and afterward utilized as received without purification. In addition, stainless-steel (SS) substrates (grade 304) were purchased from the local market of Kolhapur, India, for the electrode preparation.

#### **3.2.A.2.2 Substrate cleaning**

A critical prerequisite to ensure optimal electrode preparation is substrate cleaning. Any impurities on the substrate can lead to uncontrolled material growth and non-uniform coatings of material. For SC electrodes, SS is a preferred current collector due to its cost-effectiveness and high conductivity. The cleaning procedure for these SS substrates is outlined as follows:

- The zero-grade abrasive paper is used to clean and achieve a smooth surface of the SS substrate.
- Following the polishing step, the substrate is meticulously cleaned using detergent and DDW to remove any residual impurities.
- Subsequently, the substrate is subjected to ultrasonic cleaning for 15 minutes to ensure thorough removal of any remaining impurities.
- After the ultrasonic cleaning process, the substrate is left to air dry at ambient temperature, afterward which it is deemed ready for electrode preparation.

This cleaning protocol ensures that the SS substrate is free from any contaminants that could compromise the uniformity and quality of the material coated over substrates.

#### **3.2.A.2.3 Synthesis of nickel vanadium oxide**

In the synthesis of NVO thin films by CBS method, nickel nitrate and ammonium metavanadate as sources of nickel and vanadate, respectively were used. Urea was introduced as a hydrolyzing agent during synthesis to maintain a controlled reaction process. In detail, 0.05 M of nickel nitrate hexahydrate dissolved in DDW along with 0.075 M urea was added into the solution. Simultaneously, 0.05 M ammonium metavanadate was dissolved separately at a temperature of 343 K, of DDW. The prepared solution was then poured into the previously prepared nickel nitrate hexahydrate solution and the mixed solution (50 ml) underwent vigorous stirring until a homogeneous solution was prepared. Then the SS substrate was placed

vertically in a solution as shown in Figure 3.1. After Immersing the substrates, the prepared solution beaker was placed in the water bath and maintained at a 363 K constant temperature. After continuous heating for 8 h, the solution bath was taken out of the water bath and deposited thin films were removed from the solution and rinsed with DDW to remove any residual substances on the surface.

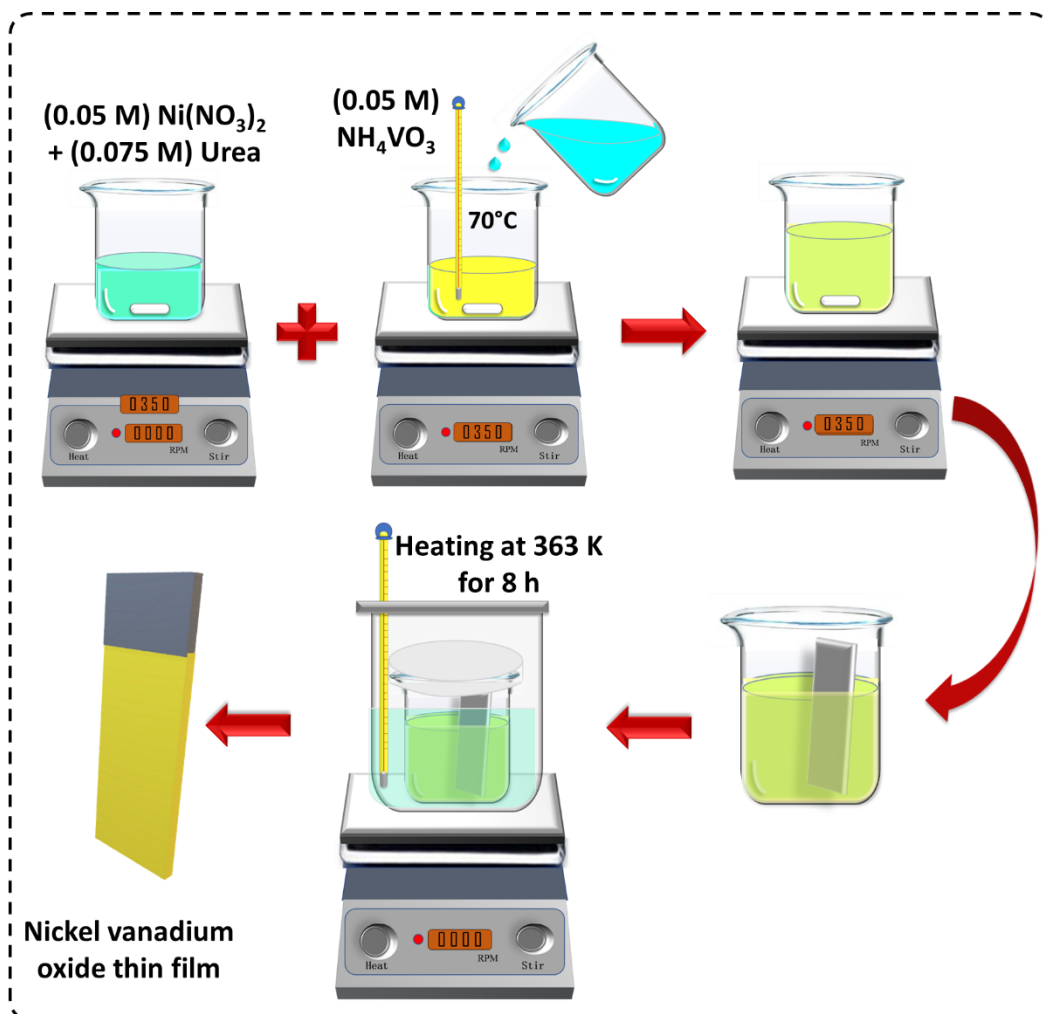


**Figure 3.1:** Schematic representation of the CBS process for NVO preparation

To assess the influence of the hydrolyzing agent's concentration on the physicochemical properties of NVO, urea was added at varying concentrations as 0.025 M, 0.05 M, 0.075 M, and 0.1 M, and labeled as C-NV1, C-NV2, C-NV3, and C-NV4, respectively. Also, the ratio of nickel nitrate to ammonium metavanadate was maintained as 1:1 and detailed preparative parameters are provided in Table 3.1. Finally, the synthesized films were air-dried and subsequently utilized for various characterizations. The resulting greenish-yellow colored C-NV series thin films are illustrated in the photograph provided in Figure 3.2.

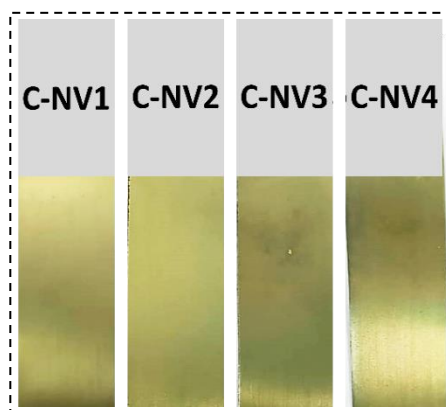


**Figure 3.2:** Photograph of SILAR synthesized NVO thin films for different urea concentrations

**Table 3.1:** Preparative parameters for the synthesis of NVO thin films and corresponding notations

Nickel Nitrate hexahydrate (M)	Ammonium Metavanadate (M)	Urea (M)	Notation
0.05	0.05	0.025	C-NV1
0.05	0.05	0.05	C-NV2
0.05	0.05	0.075	C-NV3
0.05	0.05	0.1	C-NV4
pH		~6	
Time		8h	
Temperature		363 K	

#### 3.2.A.2.4 Material characterizations

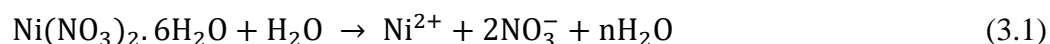
Various analytical characterization techniques were employed to assess the structural, chemical, and surface architecture of the prepared C-NV series thin films. XRD utilizing target radiations of Cu K $\alpha$  ( $\lambda=0.15425$  nm) was conducted via a Rigaku miniflex-600 instrument, within an angle between 10° to 80°. FT-IR was performed within the range of 400 to 4000 cm<sup>-1</sup> utilizing the Alpha (II) Bruker unit to elucidate functional groups and chemical bonding within the materials. The surface morphology and elemental composition of C-NV series thin films were studied using FE-SEM and EDS utilizing Hitachi S4800 and JEOL JSM-2100F instruments. The specific surface area and pore size distribution of the NVO thin films were examined through BET and BJH techniques, utilizing the Belsorp II mini and QuaraSorb Station 4 instruments. Electrochemical measurements, including CV, GCD, EIS, and stability of the C-NV

series electrode were conducted using a VersaStat4 500 and ZIVE MP1 electrochemical workstations.

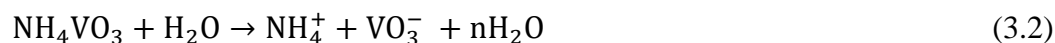
### 3.2.A.3 Results and discussion

#### 3.2.A.3.1 Film formation and reaction mechanism of C-NV series thin films

The present study comprises the binder-free synthesis of C-NV series thin-film electrodes through a straightforward “bottom-up” CBS method, illustrated in Figure 3.1. In this process, film formation commences through heterogeneous nucleation on the substrate, followed by subsequent growth via either coalescence or oriented stacking of particles. Nickel nitrate hexahydrate and ammonium metavanadate served as the sources of nickel and vanadate ions, respectively, while various concentrations of urea (0.025-0.1 M) were employed as hydrolyzing agents. At 363 K, urea releases  $\text{NH}_3$ , which complexes with  $\text{Ni}^{2+}$  ions. This amine complex functions as the source of  $\text{Ni}^{2+}$ , facilitating the deposition process through the controlled reaction rates as follows. Initially, dissociation of nickel nitrate hexahydrate in the DDW takes place, as per equation 3.1,



Similarly, ammonium metavanadate dissociates in DDW as per the following equation,



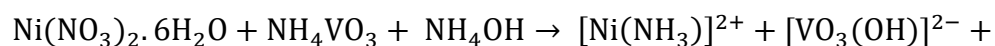
Additionally, urea plays a critical role in regulating hydrolysis by facilitating delayed breakdown processes. This involves the thermal decomposition of urea at 363 K, as represented by equation (3.3), yielding ammonia ( $\text{NH}_3$ ) and carbon dioxide ( $\text{CO}_2$ ).

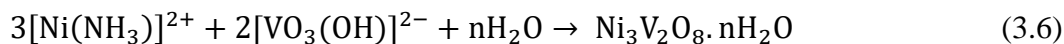


Furthermore, released ammonia rapidly converts to ammonium hydroxide,



The decomposition of urea induces alkalinity within the solution, a condition particularly conducive to the formation of complexes with metal ion species [8], as well as, at alkaline conditions ionization of monovalent anions  $[\text{VO}_3(\text{OH})]^{2-}$ . Finally, the overall reactions (equation 3.5 and 3.6) drive the formation of C-NV samples as follows,





The deposition of a loading mass across the substrate changes in response to changes in urea concentrations, consistent with constant concentrations of nickel and vanadate and reaction durations, which are plotted in Figure 3.3. A greater concentration of the hydrolyzing agent, urea, leads to an increased production of metal amine-complexed ions and slow releases. This implies that higher concentrations of the urea significantly influence the reaction rate and, consequently, the deposition through heterogeneous reactions over the substrate. Conversely, lower concentrations of urea facilitate a higher reaction rate by reducing the number of complex metal ions, leading to their rapid release into the solution and producing excessive homogeneous precipitation in the solution, which results in decreased mass loading over the substrate through heterogeneous reaction. These phenomena significantly influence the reaction dynamics and the deposition rate of the material.

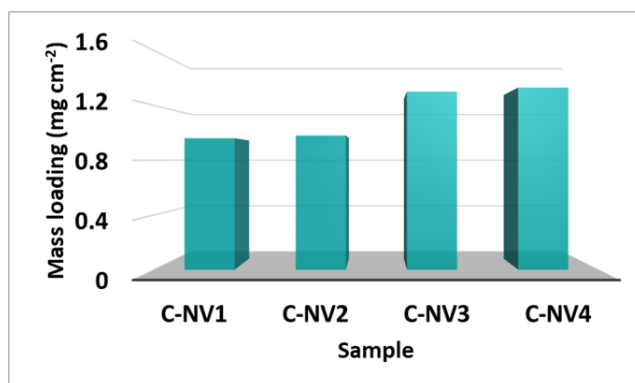


**Figure 3.3:** Plot of mass loading for C-NV series samples over SS substrates

### 3.2.A.3.2 XRD analysis

The XRD analysis was employed to study the structural characteristics of prepared NVO thin films. XRD patterns of the NV series thin film samples exhibit analogous diffraction profiles without any significant diffraction peak obtained from NVO material. Three intense peaks labeled with the symbol ‘♦’ at 44.2°, 51.8°, and 74.8° correspond to the current collector SS substrate are observed for all C-NV series samples in Figure 3.4 (a). The XRD patterns acquired within the 10° to 80° range do not reveal any notable peaks associated with the material, indicating the formation of amorphous NVO over the SS substrates. Hence, in order to diminish the potential interference from the SS substrate and strengthen the validation of the material phase,



XRD analysis of powdered samples (scratched from of C-NV thin films) and the resulting XRD patterns are depicted in Figure 3.4 (b). The XRD patterns obtained from the C-NV series powder samples reveal three distinct low crystalline peaks at  $2\theta$  values of  $34.9^\circ$ ,  $44.3^\circ$ , and  $63.9^\circ$ , which correspond to the indexed planes of (122), (042), and (442), respectively, of orthorhombic  $\text{Ni}_3\text{V}_2\text{O}_8$  (Joint committee on powder diffraction standards (JCPDS) card No. 01-074-1484). The weak intensity and broadening observed in the diffraction peaks suggest the nano-crystalline nature of the C-NV series samples. This characteristic can significantly affect the electrochemical performance through two primary mechanisms: enhancing the material's surface area (surface-to-volume ratio) and facilitating deeper ion diffusion from the electrolyte to access the electroactive sites of the material [9, 10].

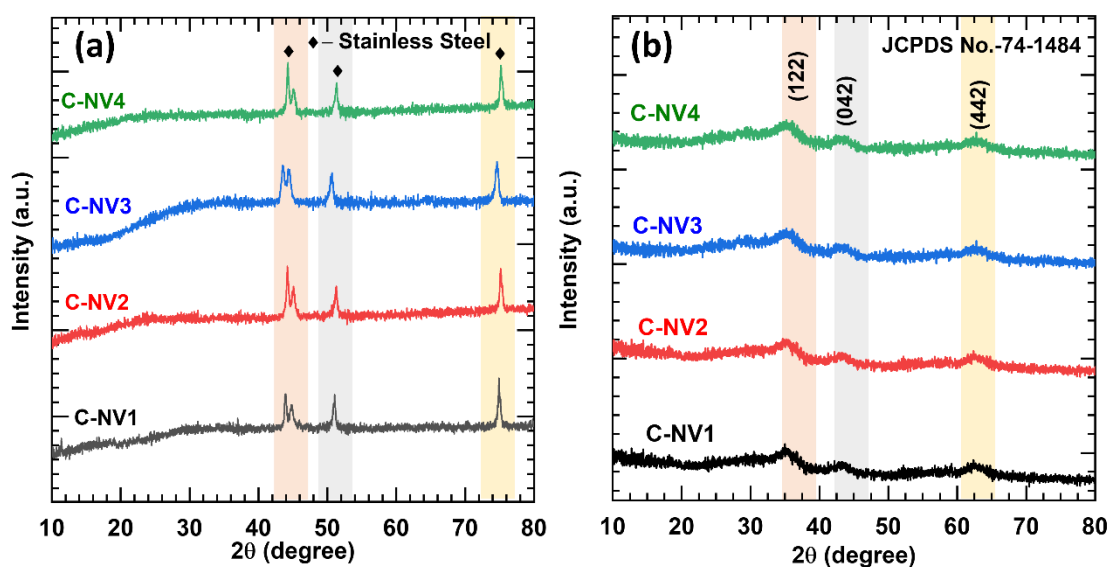


**Figure 3.4:** XRD patterns of C-NV series samples (a) over SS substrate and (b) powder sample

### 3.2.A.3.3 FT-IR analysis

FT-IR analysis was employed to investigate the presence of different functional groups in the C-NV series samples, as depicted in Figure 3.5. The plotted FT-IR spectra exhibit similar characteristics for all samples. Absorption bands within the  $400\text{--}900\text{ cm}^{-1}$  range are particularly associated with the stretching vibrations of metal oxides, with the band  $\nu_1$  observed at  $492\text{ cm}^{-1}$  attributed to Ni-O vibrations in the stretching mode. Furthermore, the presence of the band  $\nu_2$  at  $682\text{ cm}^{-1}$  is attributed to the antisymmetric stretching vibrations associated with V-O-V bonds [11]. The occurrence of band  $\nu_3$  at around  $930\text{ cm}^{-1}$  is assigned to the symmetric stretching mode

of the V=O group [12]. Furthermore, the absorption band  $\nu_4$  associated with N-O stretching vibrations occurs at approximately  $1353\text{ cm}^{-1}$ , originating from the trapping of nitrate  $(\text{NO})_3^{2-}$  ions from the precursor [13, 14]. Moreover, the bands at  $\nu_5$  situated at  $3411\text{ cm}^{-1}$ , are attributed to the bending and stretching vibrations of the hydroxyl group (H-O-H), respectively [8, 15]. The XRD and FT-IR spectra confirm nano-crystalline and hydrous NVO material formation in all C-NV series samples.

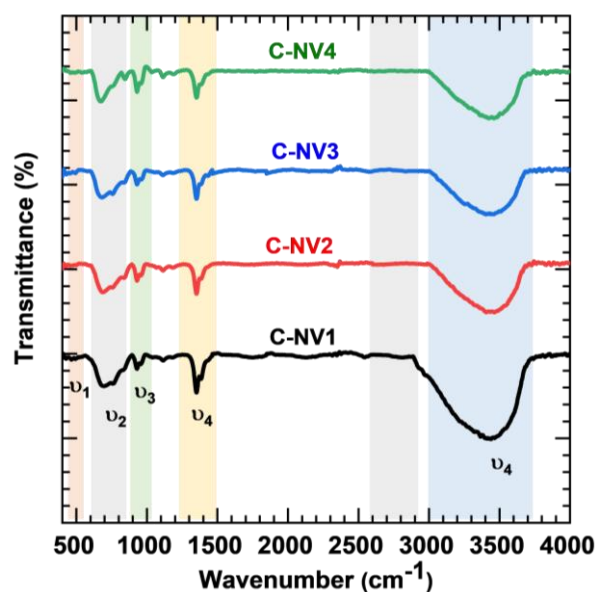


**Figure 3.5:** FT-IR patterns for C-NV series samples

### 3.2.A.3.4 XPS analysis

The electronic structure and the surface chemistry of a prepared C-NV3 sample were examined utilizing XPS analysis. Figure 3.6 (a) shows the XPS survey scan spectrum, which reveals peaks corresponding to nickel (Ni 2p), vanadium (V 2p), and oxygen (O 1s). High-resolution (HR) XPS spectra of Ni 2p, V 2p, and O 1s were acquired to elucidate the oxidation states and refine the understanding of the electronic structures of the elements present in the synthesized C-NV3 material. Figure 3.6 (b) displays the deconvoluted HR XPS spectrum of Ni 2p. The spectrum reveals two main peaks corresponding to Ni  $2p_{3/2}$  and Ni  $2p_{1/2}$  at binding energies of  $\sim 855.5\text{ eV}$  and  $873.4\text{ eV}$ , respectively [16]. These peaks were further deconvoluted to represent the  $\text{Ni}^{2+}$  and  $\text{Ni}^{3+}$  oxidation states. Additionally, two satellite peaks were observed at higher binding energies ( $861.3$  and  $879.5\text{ eV}$ ) for each main peak. The HR V 2p core level spectrum is shown in Figure 3.6 (c), which reveals the presence of two peaks at  $516.7\text{ eV}$  and  $524.2\text{ eV}$  corresponding to the V  $2p_{3/2}$  and V  $2p_{1/2}$  states, respectively.

Moreover, the V 2p<sub>3/2</sub> peak is fitted in two peaks associated with V<sup>4+</sup> and V<sup>5+</sup> valance states [17].

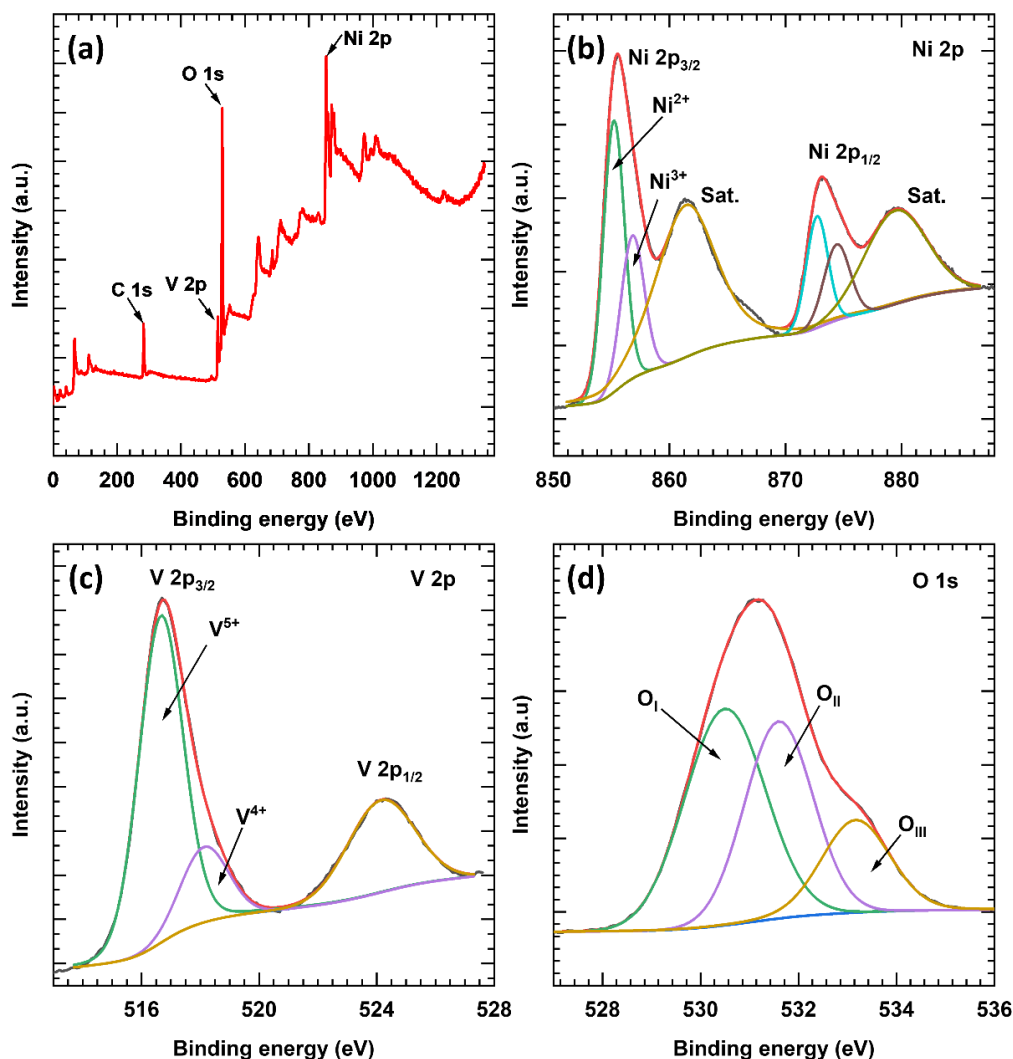


**Figure 3.6:** XPS spectra of C-NV3 samples (a) survey spectrum, HR spectra of (b) Ni 2p, (c) V 2p, and (d) O 1s

The O 1s core level spectrum is as shown in Figure 3.6 (d), deconvoluted into three distinct peaks at binding energies of 530.4, 531.6, and 533.18 eV which are associated with lattice oxygen (O<sub>I</sub>), oxygen vacancies (O<sub>II</sub>), and adsorbed water (O<sub>III</sub>), respectively. Oxygen vacancies within the material not only function as redox-active centers for energy storage but also significantly improve electrical conductivity by facilitating charge carrier transport across potential energy barriers [18]. Alongside, the dominant oxidation states of nickel as Ni<sup>2+</sup> and vanadium as V<sup>5+</sup> within the C-NV3 series thin films support the formation of the Ni<sub>3</sub>V<sub>2</sub>O<sub>8</sub>·nH<sub>2</sub>O phase.

### 3.2.A.3.5 FE-SEM analysis

The surface morphology of prepared C-NV series samples is investigated using FE-SEM surface analysis. The morphologies of prepared thin films are depicted in Figure 3.7 (a<sub>1</sub>-d<sub>3</sub>) at different magnifications of X15K and X70K. At lower magnification (X15K), small cracks on the surface are observed for all samples. However, at higher magnification (X70K) fine nanoparticles are observed. The FE-SEM image (Figure 3.7 (a<sub>2</sub>)) of the C-NV1 sample, taken at a high magnification of X70K, provides a detailed visualization of the surface morphology.

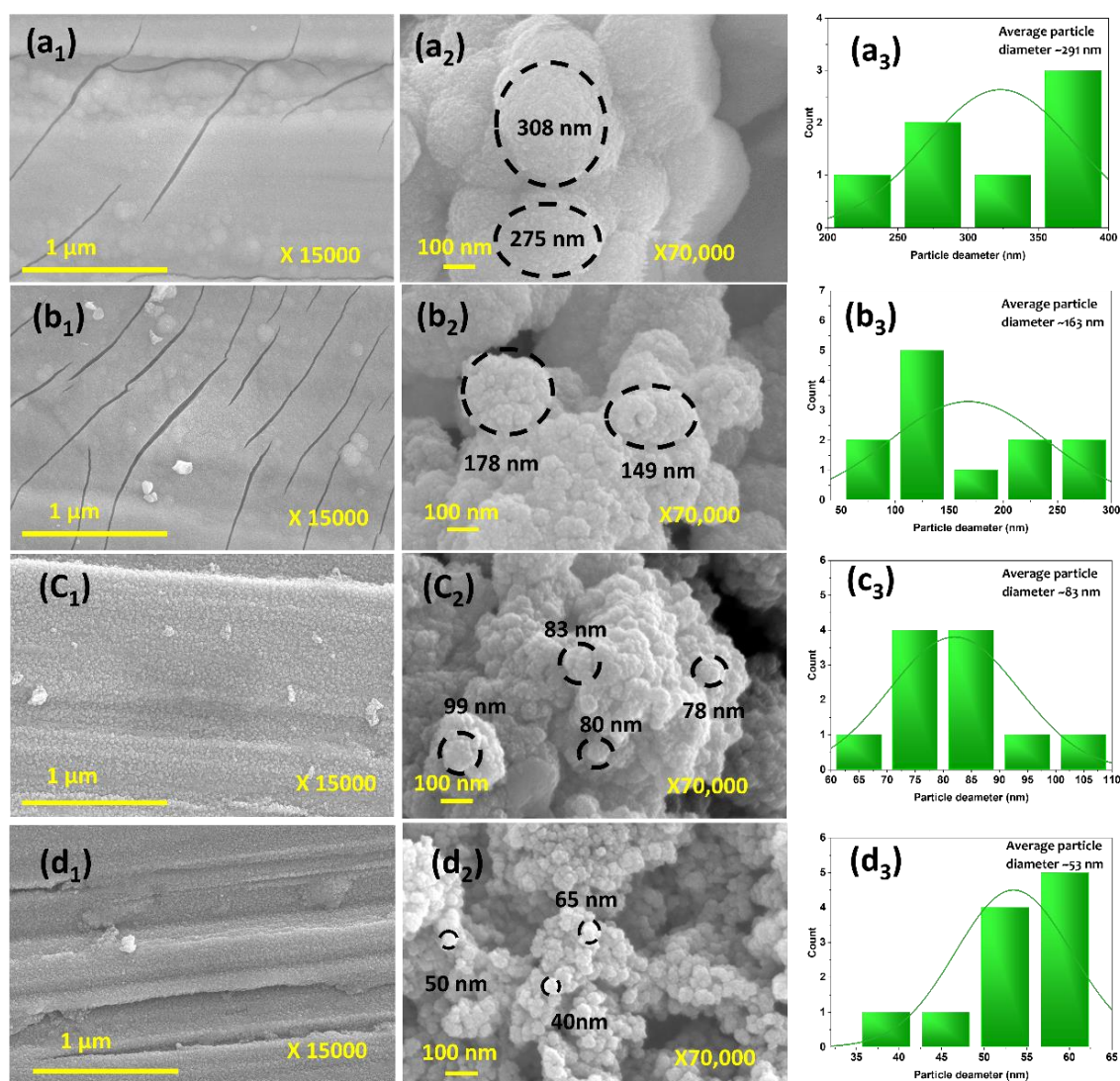


**Figure 3.7:** FE-SEM images of sample (a<sub>1</sub>, a<sub>2</sub>) C-NV1, (b<sub>1</sub>, b<sub>2</sub>) C-NV2, (c<sub>1</sub>, c<sub>2</sub>) C-NV3, and (d<sub>1</sub>, d<sub>2</sub>) C-NV4 at the magnification of X15K and X70K, respectively, and (a<sub>3</sub>-d<sub>3</sub>) histograms of particles size distribution

This image reveals that the substrate is completely covered with spherical particles. Notably, these spherical particles are composed of agglomerated

nanoparticles, indicating a complex hierarchical structure. As the concentration of the hydrolyzing agent (urea) is increased, a noticeable change in the morphology is observed. Specifically, there is a transition from larger spherical particles to smaller and more discrete clusters of nanoparticles. This suggests that higher urea concentrations prone to form a smaller spherical aggregate of nanoparticles. To quantify this observation, particle size distributions for the C-NV series were analyzed and are presented in histograms, Figure 3.7 (a<sub>3</sub>-d<sub>3</sub>). The histograms show a clear trend of decreasing particle diameter with increasing urea concentration. The average particle diameters were measured to be approximately 291 nm for C-NV1, 163 nm for C-NV2, 83 nm for C-NV3, and 53 nm for C-NV4. This systematic reduction in average particle size with higher urea concentrations indicates that the hydrolyzing agent plays a crucial role in controlling the formation and aggregation of nanoparticles and, consequently, the overall particle size.

#### **3.2.A.3.6 BET and BJH analysis**

The BET and BJH measurements were utilized to examine the surface area and porosity of the C-NV series samples. Figure 3.8 displays the N<sub>2</sub> adsorption-desorption isotherms recorded for the C-NV series samples. In the relative pressure range of 0.25-0.99, the curve exhibits a distinct loop characteristic of hysteresis, closely resembling the H3-type loop. The obtained maximum specific surface areas are 24.8, 29.7, 42.1, and, 35.7 m<sup>2</sup> g<sup>-1</sup> for C-NV1, C-NV2, C-NV3, and C-NV4 samples, respectively. Specifically, with the increasing molar concentration of urea up to 0.075 M, the specific surface area increases up to C-NV3, and further, this trend declines with increasing concentration of urea. Moreover, the obtained BJH plots are provided in Figure 3.8. The obtained mean pore size is mainly attributed to the range of 5 to 8 nm, which powerfully reveals the mesoporous nature of C-NV samples. The obtained high surface area with the mesoporous structure having a shortened pore diameter can introduce hierarchical channels to contact the electrolyte and allow easy ion diffusion in the deep pores of the particles [19].



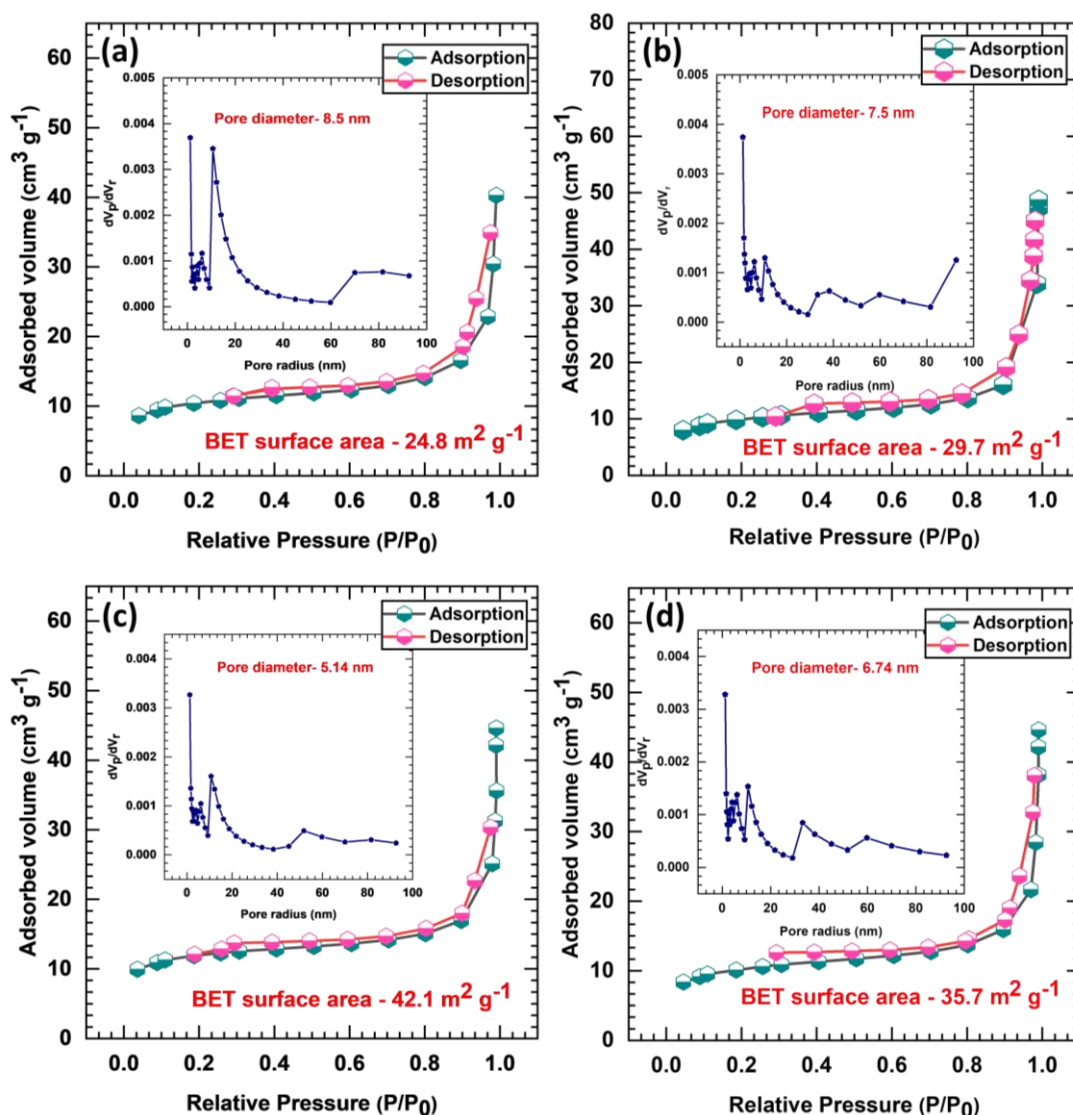


**Figure 3.8:** Nitrogen adsorption/desorption isotherm of C-NV series (inset: pore size distribution)

### 3.2.A.3.7 Electrochemical performance analysis

The influence of change in morphological properties, due to the variation in concentration of hydrolyzing agent, on the electrochemical performance was examined by utilizing the three-electrode system. The performance of the C-NV series electrodes was conducted in an aqueous electrolyte of 1 M KOH. The system consists Hg/HgO as a reference electrode, while a platinum plate serves as the counter electrode. The C-NV series electrodes serve as the working electrode, with an electrochemical accessible area of  $1 \times 1 \text{ cm}^2$ .

#### (a) CV analysis

The CV measurements of prepared C-NV series electrodes were conducted within an optimized potential range of 0 to 0.6 V vs Hg/HgO. In Figure 3.9 (a), the comparative CV profiles of C-NV series thin-film electrodes are depicted.

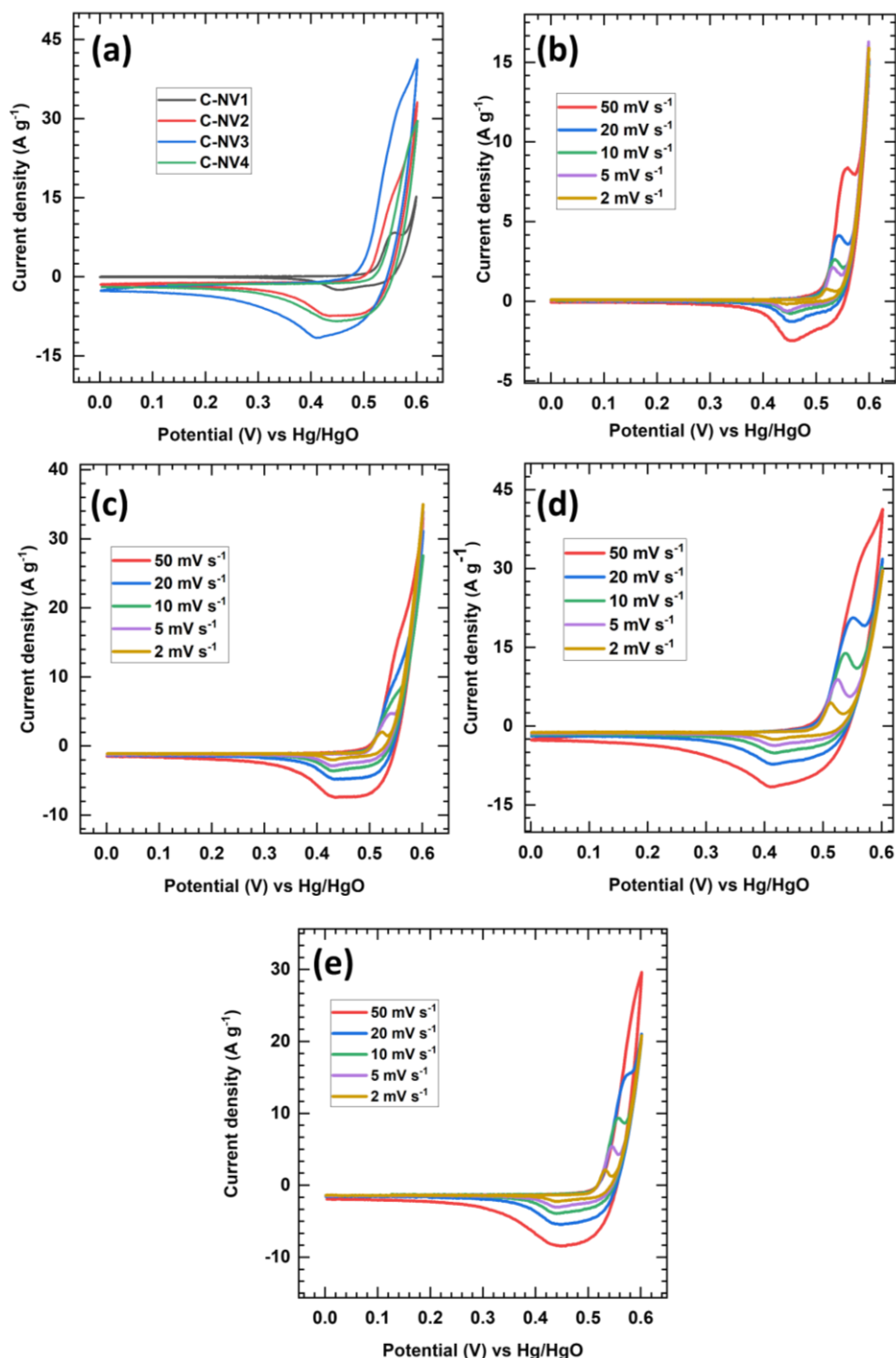
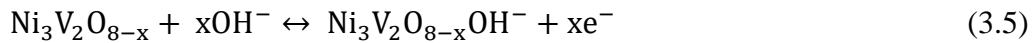


**Figure 3.9:** (a) Comparative CV curves at 50 mV s<sup>-1</sup> scan rate, (b-e) CV curves of C-NV series samples at different scan rates of 2-100 mV s<sup>-1</sup>



The CV curve of the C-NV3 electrode exhibits a larger current area compared to that of other C-NV series electrodes, suggesting the maximum charge-storing capability of the other electrodes. During the process of intercalation and de-intercalation, OH<sup>-</sup> ions get exchanged into the bulk of the material and near the electrode-electrolyte interface, and the electrochemical reactions of NV series electrodes could be presented as follows,



The typical CV curves display non-rectangular curves characteristic of battery-type behaviour, featuring a single pair of redox peaks. These peaks, evident across all samples, indicate faradaic redox reactions involving Ni<sup>2+</sup> and Ni<sup>3+</sup>. Additionally, the absence of additional redox peaks attributed to impurity phases such as V<sub>4</sub>O<sub>9</sub>, V<sub>2</sub>O<sub>5</sub>, VO<sub>2</sub>, V<sub>3</sub>O<sub>7</sub>, etc., confirms that the redox couple peaks originate specifically from Ni<sub>3</sub>V<sub>2</sub>O<sub>8</sub>. Furthermore, the C-NV series electrodes demonstrated similar redox behaviour across various scanning rates in range of 2-100 mV s<sup>-1</sup> (Figure 3.9 (b-e)), indicating that the prepared material exhibits improved rate capability.

The CV technique offers a more comprehensive approach to quantitatively understanding the charge storage mechanism, providing deeper insights into the storage process. In order to study the degree of capacitive or diffusiveness of prepared material based on scan rate (v) and obtained current (i), the relationship between them is as follows,

$$i_{\text{peak}} = av^b \quad (3.6)$$

$$\log(i_{\text{peak}}) = b \log(v) + \log(a) \quad (3.7)$$

The cathodic peak current 'i<sub>peak</sub>' is directly proportional to the scan rate, whereas 'a' and 'b' parameters are coefficients. The determination of the 'b' parameter relies on the slope of the logarithmic plot of 'i<sub>peak</sub>' vs 'v', as illustrated in Figure 3.10. A value of b=1 indicates that charge storage is primarily due to surface-controlled, non-diffusive redox processes, reflecting a capacitive nature. In contrast, a value of b=0.5 signifies diffusion-controlled battery-type behavior [20]. The resulting 'b' values fall within the range of 0.5 to 0.65. This range confirms the battery-type faradic charge storage mechanism.

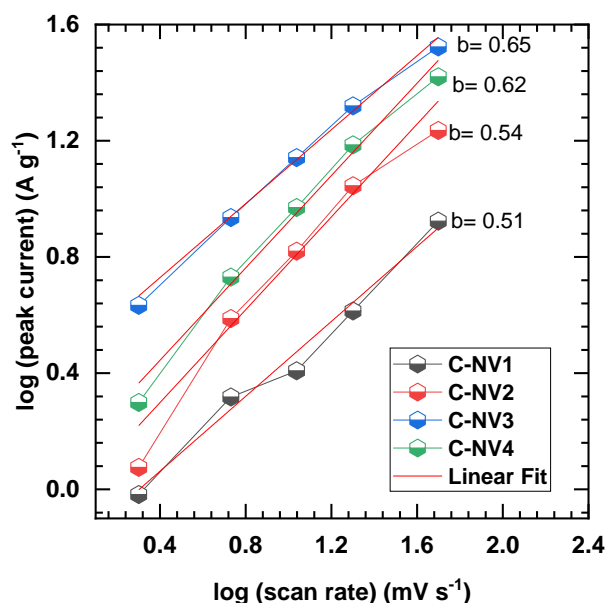


**Figure 3.10:** Plot of log (peak current, A g<sup>-1</sup>) vs log (scan rate, mV s<sup>-1</sup>)

To further elucidate the charge storage kinetics of C-NV series electrodes, the total capacitance is deconvoluted into the diffusion-controlled and surface-controlled mechanism. According to the Trasatti analysis, the total charge storage ( $Q_t$ ) of the electrode is the combination of diffusive charge storage ( $Q_d$ ) and capacitive charge storage ( $Q_s$ ) [21] and can be estimated by the following equation,

$$Q_t = Q_s + Q_d \quad (3.8)$$

The  $Q_d$  follows slow diffusion kinetics and is a function of the inverse reciprocal of the square root of the scan rate, while  $Q_s$  is mainly ascribed to quick kinetics and is independent of the scan rate. The plot of the total charge versus the square root of the inverse reciprocal of the scan rate ( $v$ )<sup>-1/2</sup> yields the  $Q_s$ . The following Equation 3.9 aids in examining the charge components that depend on scan rate and the overall charge contribution using CV curves.

$$Q_t = Q_s + \text{Const} \cdot v^{-1/2} \quad (3.9)$$

The plots of scan rate-dependent charge contribution for C-NV series electrodes are displayed in Figure 3.11, and a gradual decrement in surface contribution with scan rate is observed for all C-NV series electrodes. For the C-NV3 electrode, the surface capacitive contribution is 45% at a 2 mV s<sup>-1</sup> scan rate, while 55% of the total charge is diffusive. Moreover, at 20 mV s<sup>-1</sup>, the capacitive contribution increases up to 68%, whereas a decrease in the diffusive contribution of 32% is

observed for the same electrode. The falling tendency of diffusive contribution with increment in scan rate indicates that, at a lower scan rate, electrolytic ions have sufficient time to perform numerous redox activities, which gives rise to the more diffusion-controlled contribution [22]. Also, a lower reaction time for electrolytic ions to react with electrode materials at a higher scan rate leads to lower diffusion-controlled contribution and vice versa.

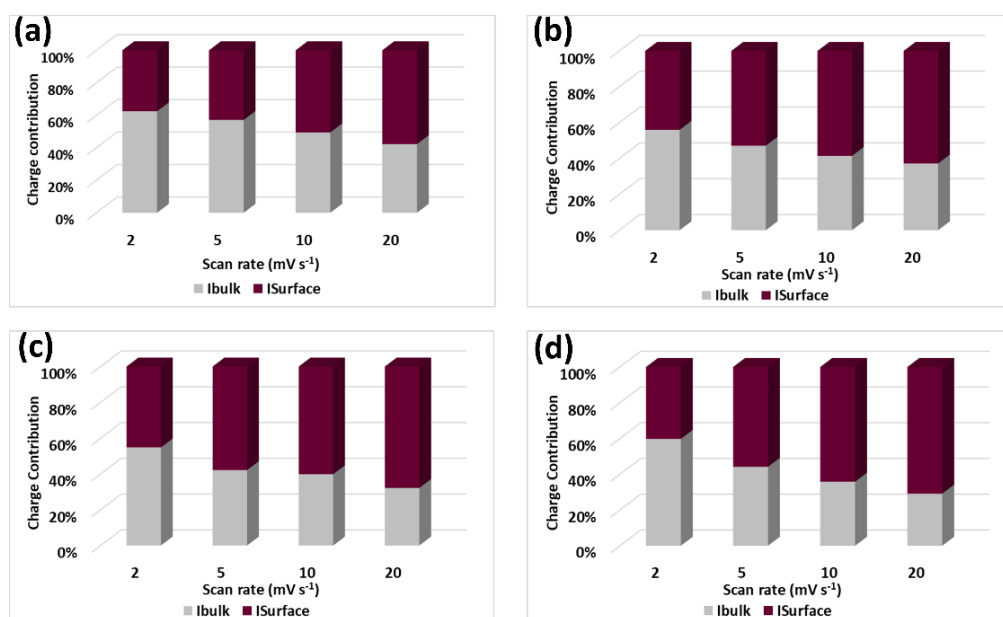


**Figure 3.11:** Charge contribution plots of (a) C-NV1, (b) C-NV2, (c) C-NV3, and (d) C-NV4 electrodes

### (b) GCD analysis

The GCD profiles of the C-NV series electrodes are recorded in an optimized potential window of 0 to 0.5 V (vs Hg/HgO). The comparative GCD curves of C-NV series electrodes at 1 A g<sup>-1</sup> current density are displayed in Figure 3.12 (a). The obtained plateau of the charge-discharge curve matches well with the associated CV curves, demonstrating the battery-type behavior of C-NV series. Also, the C-NV3 electrode unequivocally demonstrates its exceptional storage capacity through its prolonged charge and discharge time. Furthermore, GCD curves with various current densities of 1 to 5 A g<sup>-1</sup> for C-NV series electrodes are depicted in Figure 3.12 (b-e). The calculated  $C_{sp}$  of 411, 482, 692, and 594 F g<sup>-1</sup> at 1 A g<sup>-1</sup> current density for C-NV1, C-NV2, C-NV3, and C-NV4 samples (Figure 3.12 (f)). By leveraging the characteristics of active material, C-NV3 demonstrates the maximum  $C_{sp}$  (692 F g<sup>-1</sup>) compared to other C-NV series electrodes.

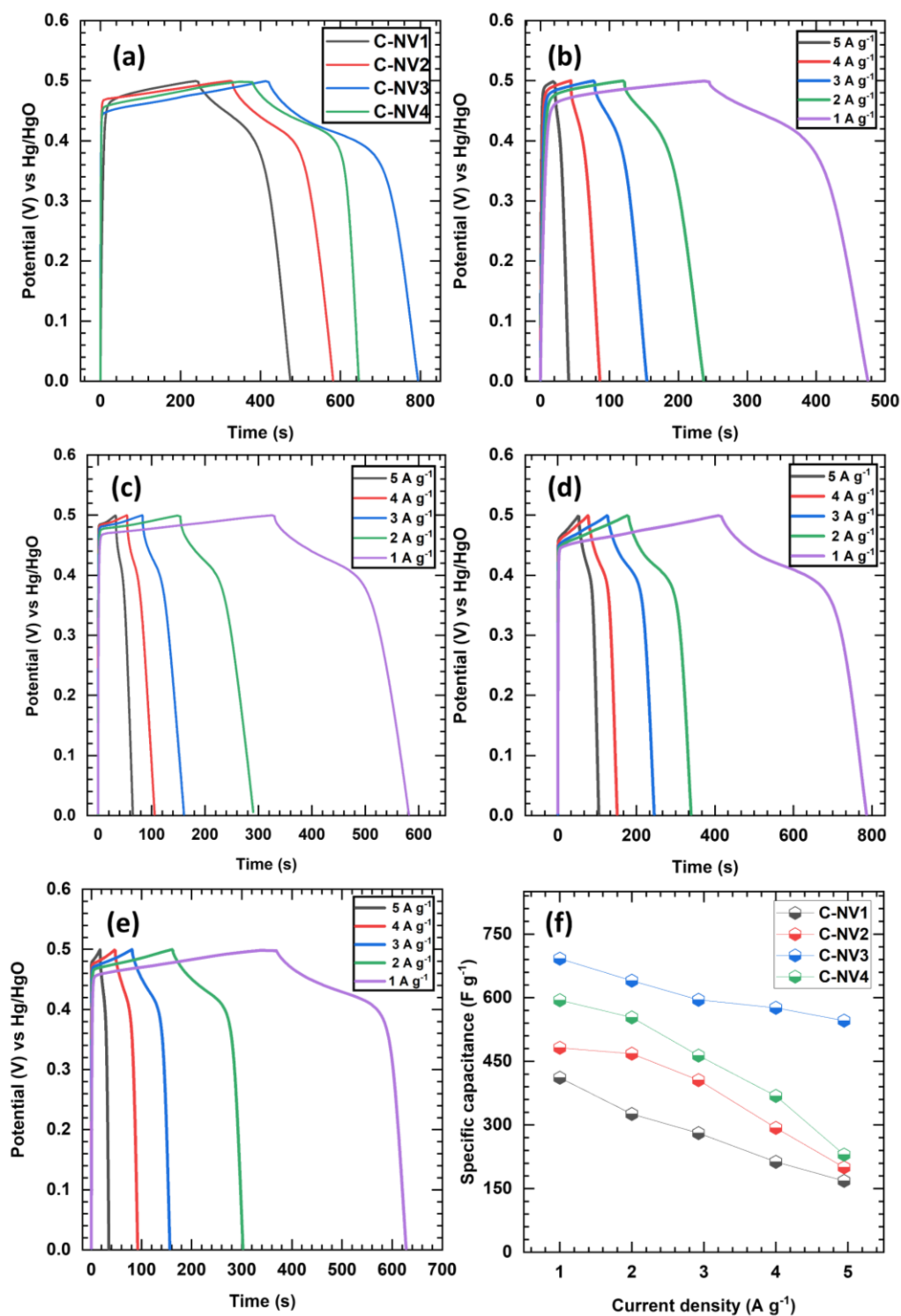


**Figure 3.12:** (a) Comparative GCD plots for C-NV series electrodes at 1 A g<sup>-1</sup> current density, GCD plots at various current densities for (b) C-NV1, (c) C-NV2, (d) C-NV3, (e) C-NV4 electrode, and (f) The plot of  $C_{sp}$  at various current densities (1-5 A g<sup>-1</sup>) for C-NV series electrodes

(c) **EIS analysis**

To study the charge transfer characteristics, EIS measurement of prepared C-NV series thin film electrodes was carried out at open circuit potential (OCP). The frequency range is between 0.01 Hz to 0.1 MHz with 10 mV AC amplitude. The obtained Nyquist plots for the C-NV series electrodes are provided in Figure 3.13. All plots are fitted with the circuit provided in the inset of Figure 3.13 using the ‘ZView-Impedance’ fitting software. The values for fitted parameters related to the Nyquist plot, such as  $R_s$ ,  $R_{ct}$ , CPE, and W, are provided in Table 3.2. The initial point of the curve delineates the  $R_s$ , while the diameter of the semicircle corresponds to the  $R_{ct}$ . Furthermore, the straight line observed in the lower-frequency region characterizes the W, indicating the rate of mass transfer. The obtained Nyquist plots for all C-NV series samples show smaller values of  $R_s$ , indicating the favorable interaction between active material and electrolyte [21, 22].

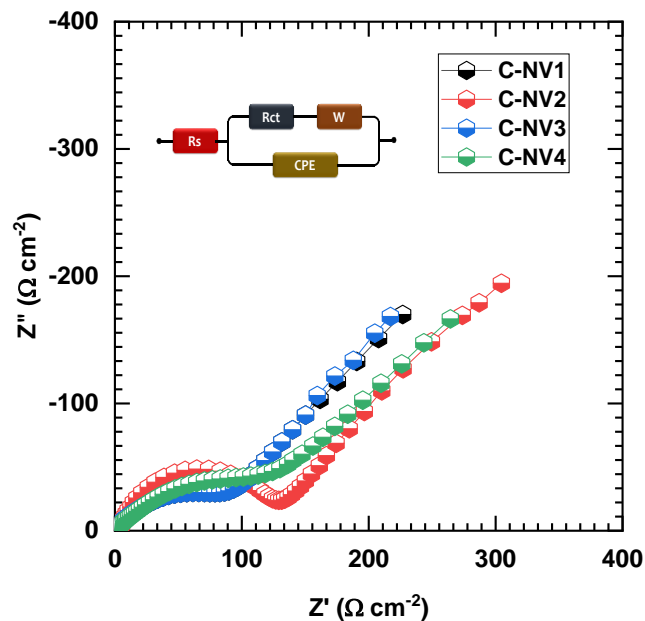


**Figure 3.13:** The Nyquist plots of C-NV series samples

The overall obtained values of  $R_s$  are between 0.26 to 0.29  $\Omega \text{ cm}^{-2}$  for C-NV series electrodes. Additionally, the smallest semicircle for the same electrode (C-NV3) implies that the lower  $R_{ct}$  of 86.8  $\Omega \text{ cm}^{-2}$  is attributed to the mesoporous structure of nanoparticles and binder-free synthesis of an electrode, which enables the easy penetration of electrolytic ions. Moreover, the correction factor ‘n’ of CPE related to surface roughness provides more insights into the behavior of the electrode. If ‘n’ is 1, the electrode displays pure capacitor behavior, the null value represents the purely

resistive behavior of the material, and the obtained value of 'n' is between 0 and 1, which suggests the pseudocapacitive behavior of C-NV material [25, 26].

**Table 3.2:** EIS fitted circuit parameters for C-NV series electrodes

Fitted Parameters	C-NV1	C-NV2	C-NV3	C-NV4
$R_s (\Omega \text{ cm}^{-2})$	0.35	0.29	0.26	0.34
$R_{ct} (\Omega \text{ cm}^{-2})$	123.4	120.3	86.8	118.4
$W-P (\Omega \text{ cm}^{-2})$	0.47	0.24	0.27	0.23
$CPE-T (\text{mF cm}^{-2})$	0.12	0.24	1.0	1.6
$CPE-P (n)$	0.4	0.8	0.6	0.6

**(d) Stability analysis**

The electrochemical cycling stability of the best-performed C-NV3 electrode was carried out for 5000 GCD cycles at  $10 \text{ A g}^{-1}$  current density, and the cyclic stability graph is provided in Figure 3.14. Exploiting the properties of active material and surface structure, the sample C-NV3 electrode demonstrates good capacitive retention of 73.3%. Also, it maintains the 78.1% coulombic efficiency even after 5000 cycles, even at a high charge-discharge rate.

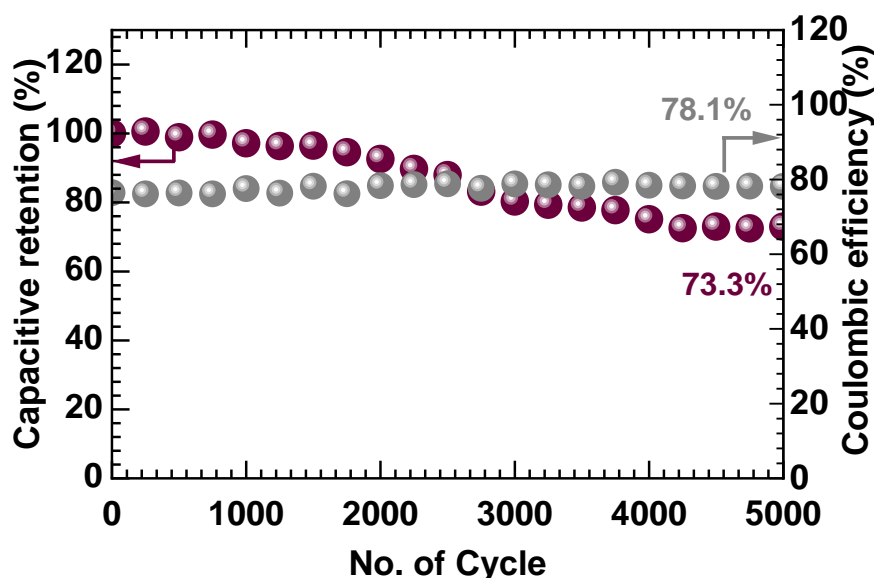


**Figure 3.14:** Plot of capacitive retention and coulombic efficiency vs number of cycles

Inclusively, the binder-free nanocrystalline NVO (C-NV3) thin film electrode synthesized via the CBS method demonstrated remarkable electrochemical

performance due to several crucial factors: a) the alteration in the concentration of the hydrolyzing agent facilitates an enhanced growth rate, and results in the morphological transition from agglomerated particles to clusters of nanoparticles which facilitates increased the number of electroactive sites, b) the obtained mesoporous clusters of nanoparticles provide a high surface area ( $42.1 \text{ m}^2 \text{ g}^{-1}$ ) that facilitating efficient access to electrolytic ions, c) moreover, binder-free preparation of cathodes, eliminates inactivity associated with resistive binders and minimizes electrochemical impedance. Thus, by precisely adjusting the molar concentration of urea, the CBS method offers a promising approach for fabricating C-NV thin film cathodes with controlled nanostructures and surface areas, enhancing their performance.

#### **3.2.A.4 Conclusions**

In summary, binder-free NVO thin film electrodes were successfully synthesized on SS substrates using the CBS method at 363 K using different concentrations of hydrolyzing agent. The morphological study of prepared NVO shows the fine particles-like morphology along a maximum specific surface area of  $42.1 \text{ m}^2 \text{ g}^{-1}$  for the C-NV3 sample with a pore diameter of 5.14 nm. The prepared C-NV3 thin film electrode shows excellent supercapacitive performance in terms of a  $C_{sp}$  of  $692 \text{ F g}^{-1}$  at  $1 \text{ A g}^{-1}$  current density, along with excellent charge-discharge cyclic stability of 73.3%. The obtained results suggest the prepared C-NV3 thin film is the promising electrode as a cathode for SC application.



### 3.3 Section B

## Reduced Graphene Oxide: Synthesis and Characterizations

### 3.3.B.1 Introduction

Extensive research has been dedicated to carbon nanostructures due to their outstanding properties and wide-ranging applications [27]. The initial acquisition of single-layer transferable graphene nanosheets involved mechanical exfoliation from bulk graphite using the “Scotch tape” method [28] and epitaxial chemical vapor deposition [29]. While these methods are favored for precise device assembly, they fall short in terms of scalability for large-scale production. Chemical approaches offer a practical route for the bulk synthesis of graphene materials [27]. Among these, a common method involves the oxidation of graphite to yield GO, a nonconductive hydrophilic carbon material [28, 29]. GO exhibits a disrupted aromatic lattice compared to graphene, featuring epoxides, alcohols, ketone carbonyls, and carboxylic groups [30, 31]. Brodie’s first synthesis of graphite oxide in 1859 utilized a mixture of potassium chlorate and fuming nitric acid, while Staudenmaier’s 1898 improvement involved a mixture of concentrated sulfuric acid and fuming nitric acid with gradual chlorate addition, simplifying the production of highly oxidized GO [27]. In 1958, Hummers introduced an alternative synthesis method using  $\text{KMnO}_4$  and  $\text{NaNO}_3$  in concentrated  $\text{H}_2\text{SO}_4$ , allowing the preparation of large amounts of GO [34].

Despite its abundant oxygen-containing groups, GO is electrically insulating and lacks the chemical stability required for many advanced applications. Reduction of functional groups, significantly improves the properties of GO. The GO can be reduced through various reduction methods, including chemical, thermal, electrochemical, and microbial reductions. Chemical reduction involves using reducing agents like hydrazine, sodium borohydride ( $\text{NaBH}_4$ ), ascorbic acid, and ammonia, which remove oxygen groups and restore the graphitic structure. Thermal reduction is performed at high temperatures (above  $1000^\circ\text{C}$ ) in an inert atmosphere, leading to the significant reduction of oxygen functionalities. Electrochemical reduction involves applying a potential to GO in an electrolyte solution, resulting in a controlled reduction process. Microbial reduction uses biological agents like bacteria or enzymes to reduce GO in an eco-friendly manner. Recent trends in rGO research focus on environmentally sustainable reducing agents, such as plant extracts or green chemistry approaches, which provide high efficiency while minimizing environmental impact.

Additionally, rGO is being explored in applications like energy storage, sensors, and catalysis due to its improved electrical conductivity, mechanical properties, and surface area.

### **3.3.B.2 Experimental details**

#### **3.3.B.2.1 Synthesis of reduced graphene oxide**

To prepare GO, a mixture of 5 g of graphite flakes and 2.5 g of sodium nitrate was combined and introduced to 120 ml of sulfuric acid. The whole mixture was stirred for 30 minutes within an ice bath to maintain a controlled temperature not exceeding 20 °C. Following this, 15 g of potassium permanganate was added, ensuring a slow and controlled introduction to the mixture. Once the addition of potassium permanganate was complete, the ice bath was removed, and the reaction mixture was allowed to stir overnight. As a result of this process, a brownish-yellow pasty solution was obtained, indicating the formation of GO. The next step involved introducing 150 ml of DDW into the mixture. This addition led to a rapid increase in temperature, signifying an exothermic reaction. Subsequently, 50 ml of 30% hydrogen peroxide was added carefully to the mixture to facilitate further oxidation. To isolate the synthesized GO, the mixture was subjected to centrifugation, and the obtained precipitate was washed repeatedly with DDW to remove any impurities and neutralize the pH of the supernatant. The final GO product was then collected as a powder and subjected to vacuum drying to ensure the complete removal of any remaining solvents and water.

The prepared GO was further reduced utilizing hydrazine hydrate. A standard reduction process was employed to reduce the prepared powder of GO. Initially, 1 mg ml<sup>-1</sup> of GO powder was dispersed in DDW through sonication until the solution achieved homogeneity. Subsequently, the dispersion was carefully transferred to a round bottom flask equipped with a water-cooled condenser, and hydrazine hydrate was cautiously added. The mixture was then heated for an hour at 95 °C. The resulting reduced GO was subjected to filtration using a funnel and washed 3 to 4 times with DDW. Finally, the collected rGO was dried in an oven at 70 °C [35].

#### **3.3.B.2.2 Preparation rGO electrode**

The rGO electrodes were fabricated using the slurry coating technique onto SS substrates. To construct the electrode of rGO, the slurry comprised 80 wt% of rGO powder, 15 wt% of carbon black, and 5 wt% of PVDF were combined with a trace

amount of NMP. The prepared slurry was uniformly coated on a pre-cleaned SS substrate, heated for an hour at 50 °C, and used for the electrochemical study.

### 3.3.B.3 Results and discussion

#### 3.3.B.3.1 XRD analysis

The XRD patterns depicted in Figure 3.15 unveil distinctive features for both GO and rGO. Specifically, the prominent peak observed at 11° corresponds to the (001) plane for GO, indicative of its layered structure. Conversely, the emergence of a peak at 24.8° signifies the successful reduction of GO into rGO nanosheets, affirming the transformation process. This transition in peak positions from 11° to 24.8° underscores the structural modification endured during the reduction process and confirms the effective conversion of GO to rGO [36].

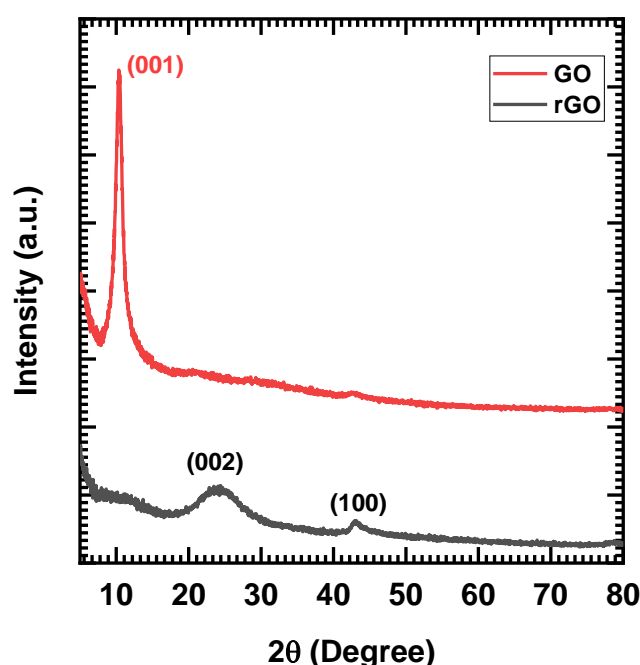


**Figure 3.15:** XRD patterns for GO and rGO

#### 3.3.B.3.2 Raman analysis

Raman spectroscopy is widely employed to analyze the structural and electronic attributes of graphene, offering particular efficacy in detecting defects and disordered configurations. This technique finds significant utility in characterizing carbon-based materials. Notably, rGO exhibits distinctive features in Raman spectra, prominently the G-band and D-band. The D-band originates from disruptions in translational symmetry or structural defects [37], while the G-band emerges from

first-order scattering within the  $sp^2$  domain of graphite [38]. The relative intensities of these bands are contingent upon the extent of disorder within the graphitic structure. The obtained Raman spectrum (Figure 3.16) for rGO shows D and G peaks with the D/G intensity ratio of 1.01, which indicates the successful preparation of rGO. Moreover, the peaks observed at wavenumbers of 2689 and 2936  $\text{cm}^{-1}$  are attributed to the 2D and D+G bands, respectively [39]. These bands signify enhanced graphitization and the absence of charge transfer, indicative of the lack of impurities [40]. The XRD and Raman spectroscopy analyses confirm the successful transition of GO to rGO.

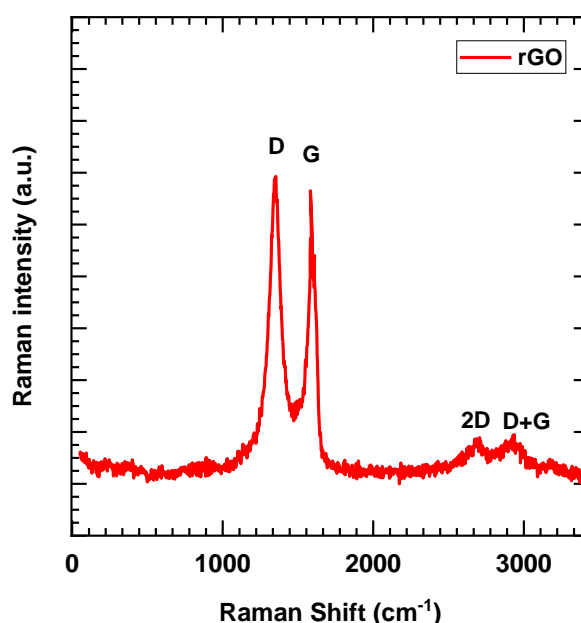


**Figure 3.16:** Raman spectrum of rGO

### 3.3.B.3.3 Electrochemical analysis

The electrochemical performance of the prepared rGO electrode as a working electrode was evaluated using the three-electrode's system, as detailed in subsection 3.2.A.3.7, with an electrochemical accessible area of  $1 \times 1 \text{ cm}^2$ .

#### (a) CV analysis

The CV curves of the rGO electrode were obtained at various scan rates ranging from 5 to 100  $\text{mV s}^{-1}$  within the optimized potential window of -1 to 0 V vs Hg/HgO using a 1 M KOH electrolyte, as depicted in Figure 3.17. The quasi-rectangular shape observed in these curves unequivocally confirms the electrode's capacitive nature of EDLC. Additionally, the substantial and symmetrical current responses observed in both the anodic and cathodic directions further affirm the

EDLC capacitive behaviour of the material. It is noteworthy that as the scan rate increases, the area under the CV curve also increases. This observation highlights a fundamental characteristic of EDLC capacitive electrodes, where the voltametric current is directly proportional to the scan rate of the CV [8].

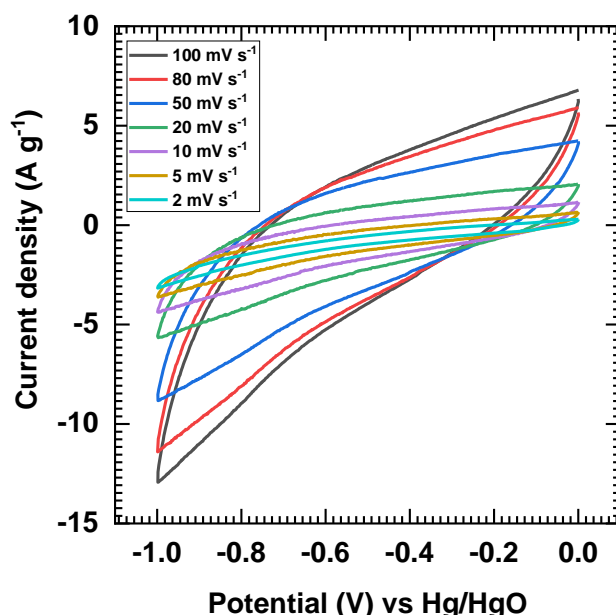


**Figure 3.17:** CV curves at various scan rates from 2 to 100 mV s<sup>-1</sup> of rGO electrode

#### (b) GCD analysis

Figure 3.18 (a) illustrates the GCD study conducted on the rGO electrode within the potential range of 0 to -1 V vs Hg/HgO. The observed charge-discharge curves exhibit a nearly linear behaviour, indicative of the double-layer capacitive nature inherent in the rGO electrode.

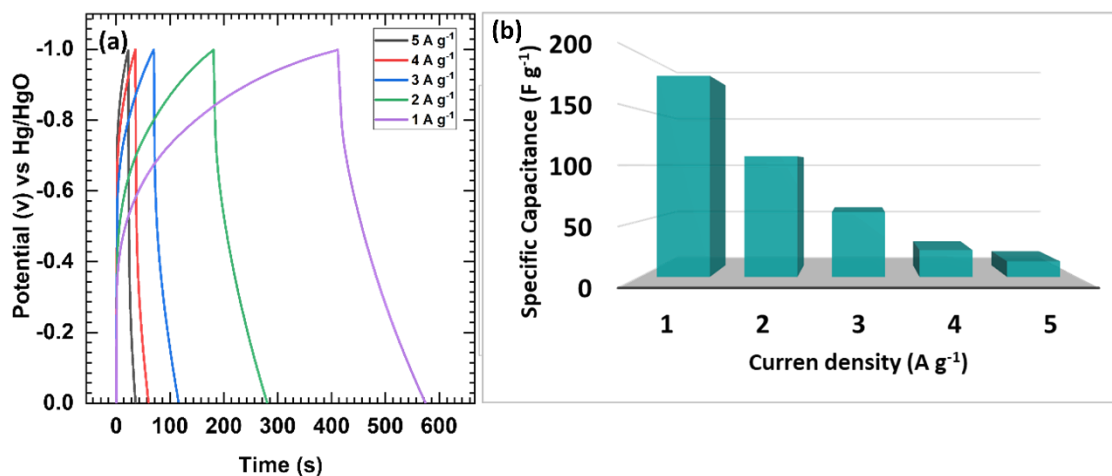


**Figure 3.18:** (a) GCD curves at various current densities from 1 to 5 A g<sup>-1</sup>, and (b) The plot of obtained  $C_{sp}$  values as a function of current densities for rGO electrode

Furthermore, the  $C_{sp}$  of the rGO electrode was determined through GCD analysis and is depicted in Figure 3.18 (b) as a function of current density. At a current density of  $1 \text{ A g}^{-1}$ , the  $C_{sp}$  reaches  $180 \text{ F g}^{-1}$  and the obtained results underscore the promising capacitive properties of the rGO electrode, showcasing its potential for various HSCs.

### (c) EIS analysis

The Nyquist plot of the rGO electrode is depicted in Figure 3.19, fitted with Randel's circuit, which is provided in the inset of the figure. The obtained value of  $R_s$  is  $0.75 \text{ } \Omega \text{ cm}^{-2}$  along with a lower  $R_{ct}$  of  $144 \text{ } \Omega \text{ cm}^{-2}$ . The lower values of  $R_s$  and  $R_{ct}$  suggest a quick charge transfer response and high electrical conductivity. The enhanced electrochemical performance observed in the rGO electrode is attributed to the comparatively smaller values of  $R_s$  and  $R_{ct}$ . Moreover, fitted  $W$  is 0.32, CPE-T is  $0.26 \text{ mF cm}^{-2}$ , and  $n$  is 0.8. These parameters signify lower hindrances to ion transfer and charge transfer processes, respectively, thus facilitating improved charge storage and faster reaction kinetics within the electrode material [41]. Further, prepared rGO is utilized to make a composite with NVO.

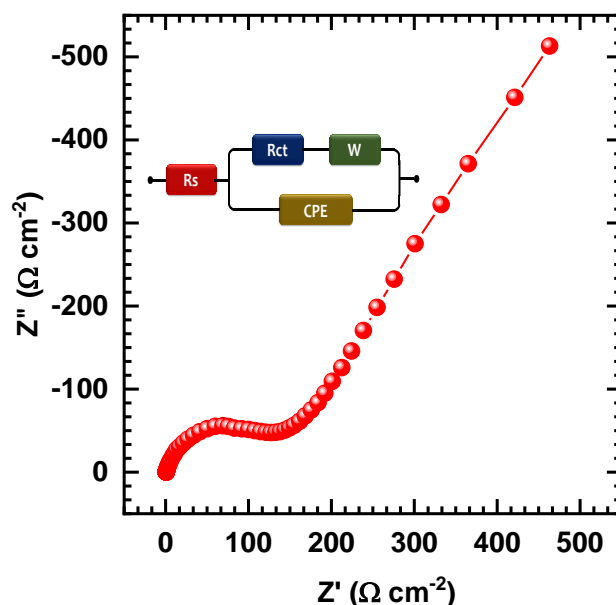


**Figure 3.19:** Nyquist plot of rGO electrode (inset equivalent circuit of the data)

### 3.3.B.4 Conclusions

The synthesis of rGO is achieved through a two-step process involving a modified Hummer's method to prepare GO, and further, it was reduced using

hydrazine hydrate. The reduction of GO to rGO is validated through XRD and Raman analyses. Moreover, the rGO electrode demonstrates notable supercapacitive performance, exhibiting a high  $C_{sp}$  of  $180 \text{ F g}^{-1}$  at a current density of  $1 \text{ A g}^{-1}$  in the potential window of -1 to 0 V along with a lower charge transfer value of  $144 \Omega \text{ cm}^{-2}$ . These findings strongly suggest the suitability of the rGO electrode as a promising anode material for SC applications.



### 3.4 Section C

## Nickel Vanadium Oxide/rGO composite by chemical bath synthesis Method: Synthesis and Characterizations

### 3.4.C.1 Introduction

The NVO stands as a prominent candidate among investigated electroactive materials for SCs due to its multistep redox reactions and enhanced electron transfer during intercalation processes [42]. Additionally, NVOs boast advantages, including abundant availability, cost-effectiveness, and eco-friendly properties. Nevertheless, challenges persist with NVO, notably its less surface area, low electrical conductivity, and insufficient cycling stability [42–44]. To address these challenges, a promising approach involves hybridizing  $\text{Ni}_3\text{V}_2\text{O}_8$  with carbonaceous materials to enhance electrical conductivity and accelerate the kinetics of ions/electron migration within electrodes and electrolytes [45]. The incorporation of carbonaceous materials offers plentiful electroactive sites for efficient Faradaic redox reactions and mitigates volume fluctuations during charge-discharge cycles. Among these materials, graphene has garnered significant attention due to its exceptional properties, including high theoretical surface area, excellent electrical conductivity, notable electrochemical stability, flexibility, and structural integrity [46–48]. However, pristine GO exhibits drawbacks such as low  $C_{\text{sp}}$  and irreversible agglomeration or restacking, leading to graphite formation due to Van der Waals forces upon drying [49]. Numerous studies have focused on integrating TMVOs with graphene to address these issues. For instance, Thiagarajan et al. [6] demonstrated the fabrication of a  $\text{Ni}_3\text{V}_2\text{O}_8/\text{GO}$  nanocomposite through a co-precipitation method, yielding a  $C_{\text{sp}}$  of  $547 \text{ F g}^{-1}$  at  $5 \text{ mV s}^{-1}$ . Similarly, Kumar et al. [50] employed a hydrothermal synthesis approach to produce  $\text{Ni}_3\text{V}_2\text{O}_8$  nanosheet arrays on animated rGO, resulting in a specific capacity of  $170 \text{ C g}^{-1}$  at  $0.5 \text{ A g}^{-1}$ . The uniform distribution of TMVOs on rrGO hinders restacking, providing synergistic advantages.

Hence, the present study focuses on examining the impact of varying concentrations of rGO on physicochemical properties and their influence on electrochemical properties. The synthesis involved preparation of pristine NVO and NVO/rGO composites at different concentrations of rGO (0, 0.025, 0.05, 0.075, and  $0.1 \text{ mg ml}^{-1}$ ). The electrochemical properties of these materials were thoroughly compared with the pristine material for the intended purpose.

### 3.4.C.2 Experimental details

#### 3.4.C.2.1 Synthesis of nickel vanadium oxide/rGO composite

The NVO/rGO composites were synthesized using a simple CBS method as shown in Figure 3.20. The concentrations of precursors were consistent with those detailed in Section A, subsection 3.2.A.2.3 for the sample C-NV3. To prepare the composite, the rGO solution was introduced into the precursor solution at varying concentrations: 0.025, 0.050, 0.075, and 0.1 mg ml<sup>-1</sup>. The mixture was stirred for 30 minutes until homogeneity was achieved. The prepared solutions were placed in a water bath and kept at a stable temperature of 363 K for 8 hours. The preparative parameters for the synthesis are provided in Table 3.3.

**Table 3.3:** Preparative parameters for the CBS of NVO/rGO composite and corresponding notations

Nickel Nitrate Hexahydrate (M)	Ammonium Metavanadate (M)	Urea (M)	rGO (mg ml <sup>-1</sup> )	Notation
0.05	0.05	0.075	0	C-rNV0
0.05	0.05	0.075	0.025	C-NV1
0.05	0.05	0.075	0.050	C-NV2
0.05	0.05	0.075	0.075	C-NV3
0.05	0.05	0.075	0.10	C-NV4
Time		8h		
Temperature		363 K		

Following continuous heating, the solution bath was taken out from the water bath. After the reaction time concluded, the reactions were left to cool down naturally. Subsequently, the residues underwent several washes with DDW and were dried at room temperature. The resultant materials, comprising NVO/rGO composites, were labelled based on rGO concentration specifically, 0, 0.025, 0.05, 0.075, and 0.1mg mL<sup>-1</sup> as C-rNV0, C-rNV1, C-rNV2, C-rNV3, and C-rNV4 respectively. These synthesized C-rNV series materials were subjected to further physicochemical characterizations.

#### 3.4.C.2.2 Electrode preparation of nickel vanadium oxide/rGO composite

The NVO/rGO composite electrodes were prepared using the slurry coating technique as discussed in section 3.3.B.2.2 onto SS substrates utilizing NVO/rGO composite, carbon black, and PVDF as 80:15:5 wt % with a trace amount NMP. The

prepared slurry was uniformly coated on a pre-cleaned SS substrate, as shown in the schematic (Figure 3.20), heated for an hour at 50 °C, and used for the electrochemical study.

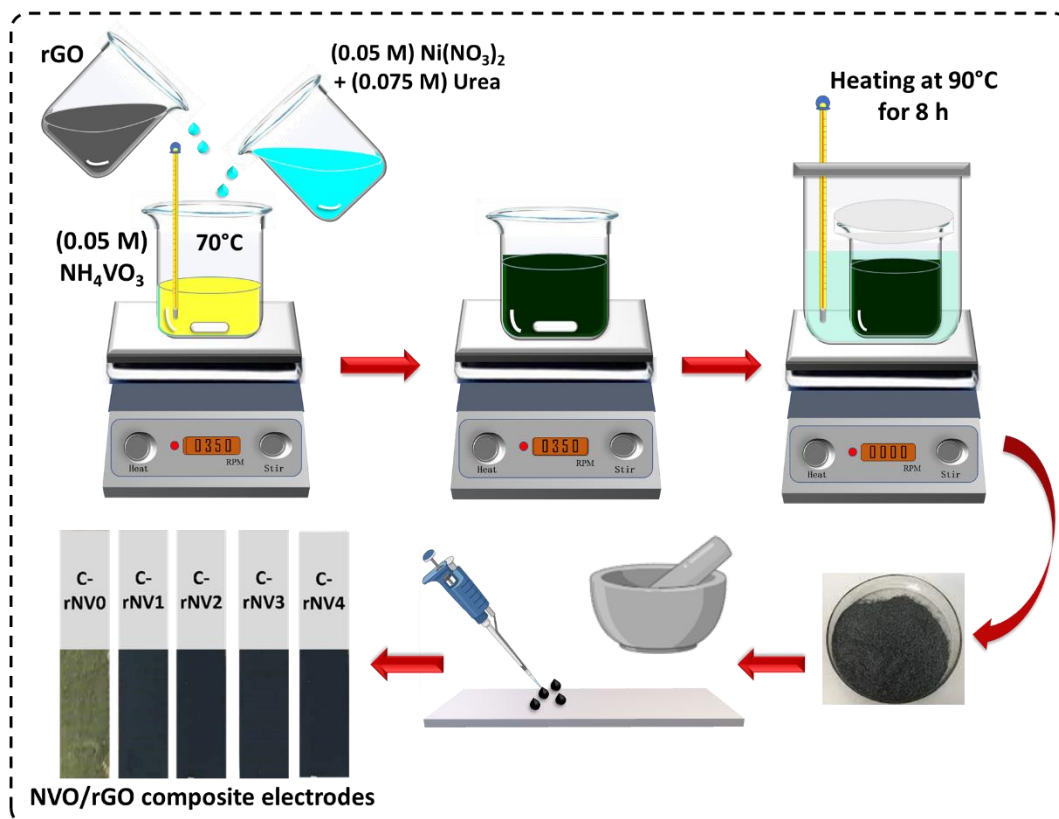


**Figure 3.20:** Schematic representation of the synthesis of NVO/rGO composite through the CBS method and electrode preparation

### 3.4.C.2.3 Material characterizations

The characterization techniques and instrumentation described in Subsection 3.2.A.2.4 were similarly applied to evaluate the NVO/rGO composite. Furthermore, Raman spectroscopy and TG analysis (thermal analyzer STA: Hitachi instrument) were employed to verify and investigate the composition of the NVO/rGO composite.

### 3.4.C.3 Results and discussion

The NVO/rGO composite material was prepared using the CBS method, a highly efficient ‘bottom-up’ approach for developing both nanostructures and microstructures. The NVO/rGO composite, specifically from the C-rNV series, was developed to assess the impact of varying rGO concentrations on the pristine C-rNV0. During the formation of the C-rNV material, NVO synthesis followed a similar process as described in section 3.2.A.3.1. As urea decomposes, as illustrated in

equations 3.3 and 3.4, the solution becomes alkaline, promoting the formation of additional epoxy, hydroxyl, and carboxyl groups on the graphene surface. The increased number of these functional groups facilitates the development of more nucleation sites. The ammine-complexed metal ions, described in equation 3.5, are attached to these functional groups and defect sites through electrostatic or Van der Waals forces. rGO's large specific surface area allows it to adsorb a significant amount of ammine-complexed ions. Concurrently, vanadate ions interact with the ammine-complexed ions via electrostatic forces (equation 3.4), forming nuclei that enable further growth. Ultimately, the NVO grows on the rGO surface by stacking or oriented attachment of particles at the nucleation sites. Through this reaction mechanism, NVO was successfully grown on rGO nanosheets.

#### 3.4.C.3.1 XRD analysis

The XRD patterns of prepared composites comprising NVO/rGO were investigated and illustrated in Figure 3.21. As noted in the previous XRD analysis within section A, subsection 3.2.A.3.2, the sample C-NV3 exhibits orthorhombic  $\text{Ni}_3\text{V}_2\text{O}_8$ . Similarly, all rGO composite materials, including C-rNV1 to C-rNV4, also demonstrate the orthorhombic structure of  $\text{Ni}_3\text{V}_2\text{O}_8$  (JCPDS card No. 01-074-1484). The obtained characteristics peak at  $2\theta$  values of  $35.2^\circ$ ,  $44.5^\circ$ , and  $63.8^\circ$ , which correspond to the indexed planes (122), (042), and (442), respectively. Along with this, the additional peak is observed in samples C-rNV1 to C-rNV4 at  $2\theta$  value of  $25.2^\circ$  with (002) plane confirming the presence of rGO.

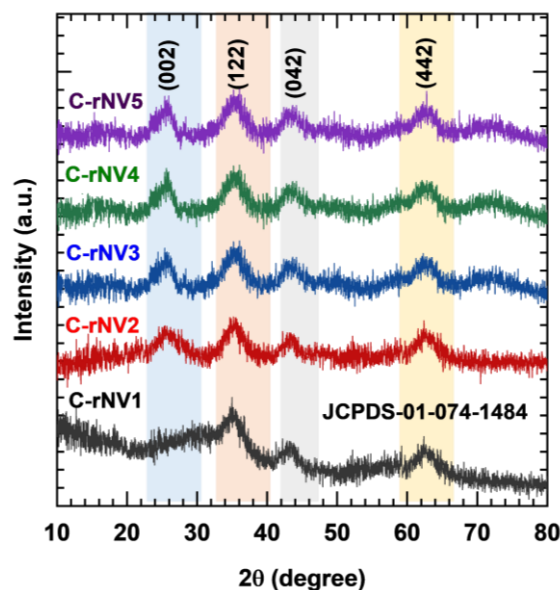


**Figure 3.21:** XRD patterns for C-rNV series samples

### 3.4.C.3.2 FT-IR analysis

Figure 3.22 illustrates the FTIR spectra for all C-rNV series composite materials within the range of 400 to 4000  $\text{cm}^{-1}$ . The appearance of absorption bands between 400 and 550  $\text{cm}^{-1}$  is specifically associated with the metal-oxygen (M-O) Bonding, where peaks attributed at  $\nu_1$  (441  $\text{cm}^{-1}$ ) correspond to the Ni-O stretching vibrations [41]. The presence of peaks within the range of 500-1000  $\text{cm}^{-1}$  ( $\nu_2$ ) is attributed to the symmetric and asymmetric stretching vibrations of the metal-oxygen bond between V-O-V [11]. The observed peak  $\nu_3$  (1374  $\text{cm}^{-1}$ ) in all samples which is originated from trapped nitrate ( $\text{NO}_3$ ) $_3^{2-}$  [14]. Moreover, the obtained additional absorption band  $\nu_4$  in samples C-rNV1 to C-rNV4 at 1639  $\text{cm}^{-1}$ , which is attributed to the presence of  $\text{sp}^2$  hybridized carbon atoms ( $\text{C}=\text{C}$ ), confirms the existence of rGO [51]. Furthermore, the broad band observed at  $\nu_5$  (2600-3700  $\text{cm}^{-1}$ ) corresponds to the stretching vibrations of O-H groups in interlayer water molecules [9], indicating the hydrous nature of C-rNV samples, which can be beneficial for enhancing the electrochemical activities [52].

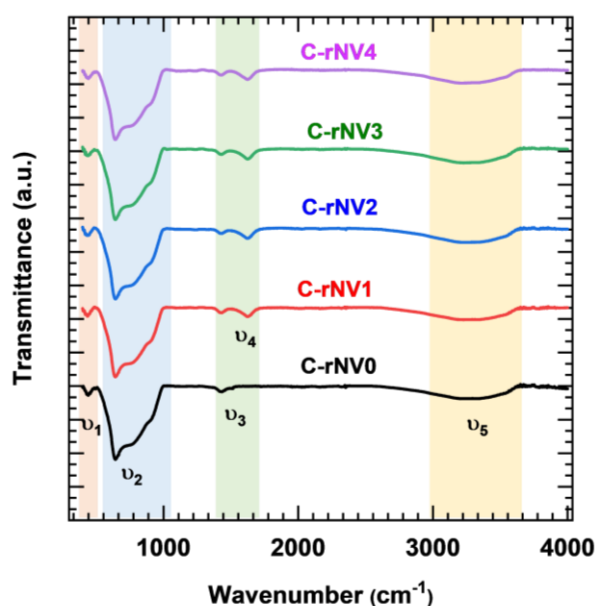


**Figure 3.22:** FT-IR spectra of C-rNV series samples

### 3.4.C.3.3 Raman analysis

Raman spectroscopy stands out as a highly effective technique for examining the structure and electron conjugation state of carbon materials [53]. Figure 3.23 displays the Raman spectra of C-rNV series samples. The Raman spectra acquired from the C-rNV series sample exhibit two distinctive peaks of NVO.

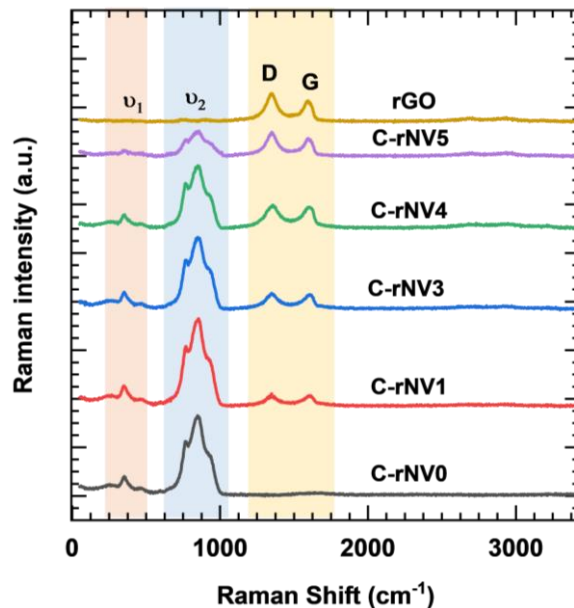


**Figure 3.23:** Raman spectra of C-rNV series samples

The peak  $\nu_1$  at  $350\text{ cm}^{-1}$  corresponds to the asymmetric stretching vibration of V-O-Ni, while the broad peak observed at  $\nu_2$  ( $844\text{ cm}^{-1}$ ) is attributed to the symmetric vibration of the V-O band. Two additional peaks were observed in samples C-rNV1 to C-rNV4 at  $1350\text{ cm}^{-1}$  and  $1590\text{ cm}^{-1}$ , corresponding to the D-band and G-band, respectively. The G bands indicate the existence of  $\text{sp}^2$  hybridized C=C bonds, which are characteristic of rGO. Conversely, the D bands suggest lattice distortions and  $\text{sp}^3$  defects induced by the oxidation process [47]. The obtained D and G peaks with a D/G intensity ratio of 1.01, 1.02, 1.02, and 1.03 for C-rNV1, C-rNV2, C-rNV3, and C-rNV4 samples, respectively, indicate an elevated  $\text{sp}^2$  carbon in NVO/rGO composite. As the concentration of rGO rises, there is a concurrent increase in the intensity of both the D and G bands and, consequently, lowering the intensity of the peak associated with NVO.

#### 3.4.C.3.4 XPS analysis

The XPS was measured to examine the chemical environment along with the electronic states of the C-rNV0, C-rNV3, and rGO samples, and the existence of Ni 2p, V 2p, C 1s, and O 1s peaks are designated by survey scan spectrum as provided in Figure 3.24 (a). The HR spectra of Ni 2p, V 2p, and O 1s for the C-rNV3 sample exhibit a deconvolution pattern comparable to that of the pristine C-rNV0. The HR spectrum in Figure 3.24 (b) displays the deconvolution of the Ni 2p spectrum. The Ni  $2\text{p}_{3/2}$  fitted into dual peaks at the binding energies related to 855.6 and 873.6 eV

correspond to the  $\text{Ni}^{2+}$ , whereas the peak at 857.1 eV is associated with  $\text{Ni}^{3+}$  along with satellite two shakeup satellite peak at 861.2 and 879.4 eV [38].

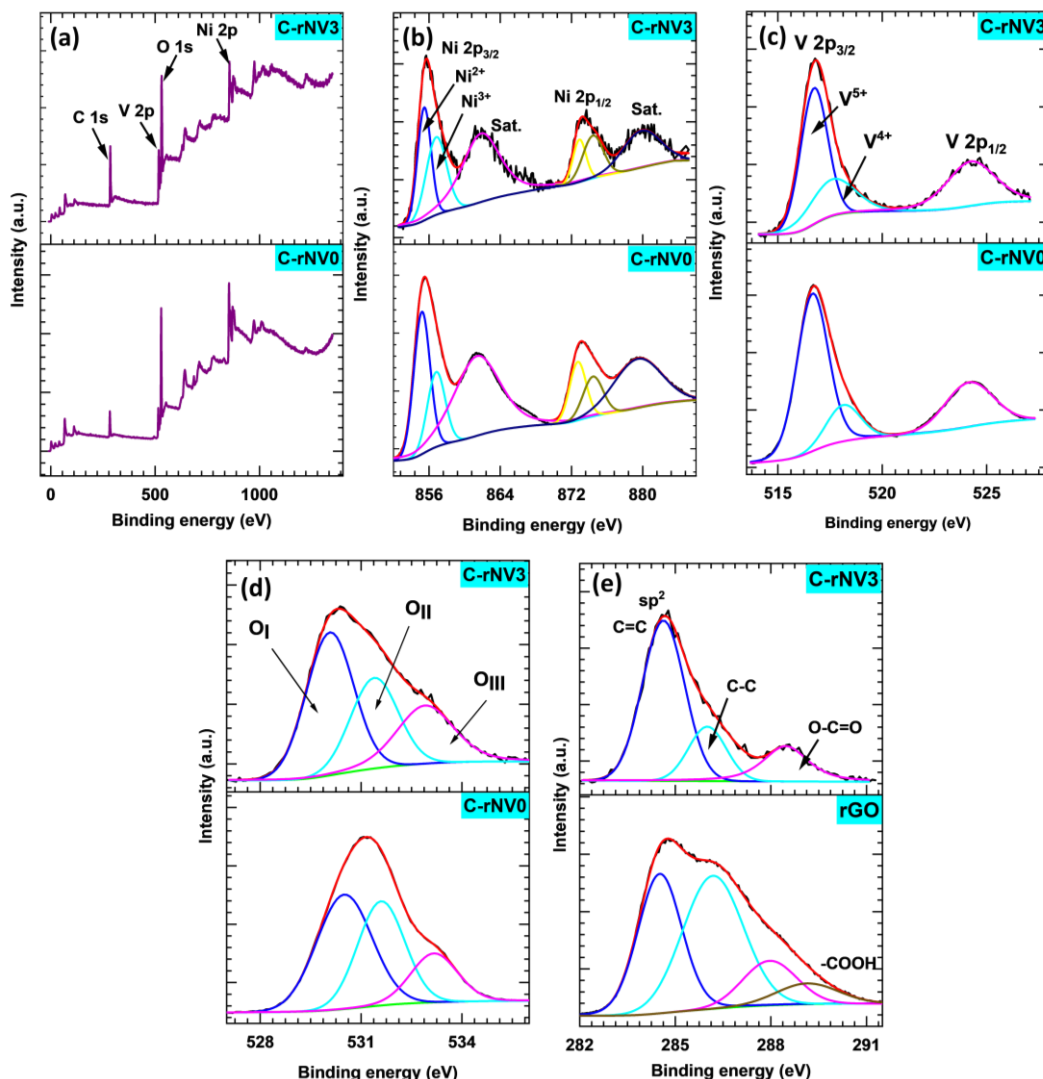


**Figure 3.24:** XPS spectra of C-rNV0 and C-rNV3 samples (a) survey spectrum, HR spectra of (b) Ni 2p, (c) V 2p, (d) O 1s, and (e) C 1s

Figure 3.24 (c) demonstrates the HR XPS spectrum of V 2p, which shows two major peaks at 516.6 eV corresponding to the V  $2p_{3/2}$  and 524.1 eV associated with V  $2p_{1/2}$  [54]. The peak corresponds to V  $2p_{3/2}$ , further deconvoluted into peaks at two different binding energies of 516.4 and 517.6 eV associated with  $\text{V}^{5+}$  and  $\text{V}^{4+}$ , respectively [55]. The XPS spectrum of oxygen (O 1s) fitted into three peaks (Figure 3.24 (d)), which are related to the various oxygen environments within the samples. The binding energy observed at 530.0 eV was related to the oxygen ( $\text{O}_I$ ) from the lattice. The fitted ( $\text{O}_{II}$ ) peak (531.4 eV) is associated with the oxygen vacancies, and the peak ( $\text{O}_{III}$ ) assigned at 533.0 eV is related to the molecules of water that have been



adsorbed on the surface of the sample [17]. Figure 3.24 (e) shows that the rGO sample exhibits more prominent peaks compared to the C-rNV3 sample, with a notable peak at 284.5 eV corresponding to C=C in-plane bonding associated with  $sp^2$  hybridization. In contrast, the out-of-plane  $sp^3$  hybridized C-C bonding appears noticeable reduction at 286.08 eV for NVO/rGO composite. XPS analysis further reveals the presence of functional groups in the rGO sample, such as carboxylate carbon (O-C=O) at 288.3 eV and carboxyl (-COOH) at 289 eV. The carboxyl group is reduced due to its interaction with the attached NVO in the composite, leading to a lower carbon peak intensity in pure rGO than in the composite C-rNV3 [56]. Furthermore, the dominance of  $Ni^{2+}$  and  $V^{5+}$  states of nickel and vanadium, respectively, and the presence of a carbon environment endorse the configuration of C-rNV series thin films with the  $Ni_3V_2O_8$  phase. The XPS results conclude that NVO material is well-grown over rGO and forms an intact NVO/rGO composite.

#### 3.4.C.3.5 TG analysis

The rGO content in the composites was quantified through the TG analysis of the C-rNV series samples. Figure 3.25 illustrates the weight loss profiles for the composites synthesized via a CBS method. All the TG analysis curves exhibit a characteristic thermal decomposition process under an air atmosphere. The initial weight loss observed below 150 °C is attributed to the evaporation of surface-adsorbed moisture and interlayer water [57]. Between 150 and 400 °C, a gradual weight loss occurs, which is ascribed to the removal of labile oxygen-containing functional groups and water vapor resulting from the decomposition of these groups in the C-rNV series samples [58, 59]. In the pristine C-rNV0 sample, the TG analysis curve stabilizes beyond 400 °C. In contrast, significant weight loss is observed beyond 400 °C for the C-rNV1 to C-rNV4 samples, which is attributed to the decomposition of rGO. The rGO and NVO content in the composites were calculated as follows: 4.71% rGO and 95.29% NVO for C-rNV1; 11.99% rGO and 88.01% NVO for C-rNV2; 20.8% rGO and 79.2% NVO for C-rNV3; and 26.34% rGO and 73.66% NVO for C-rNV4. The TGA results indicate that the weight loss corresponding to rGO increases with its content in the NVO matrix. These findings confirm the successful synthesis of NVO/rGO composites with varying rGO concentrations during CBS synthesis.

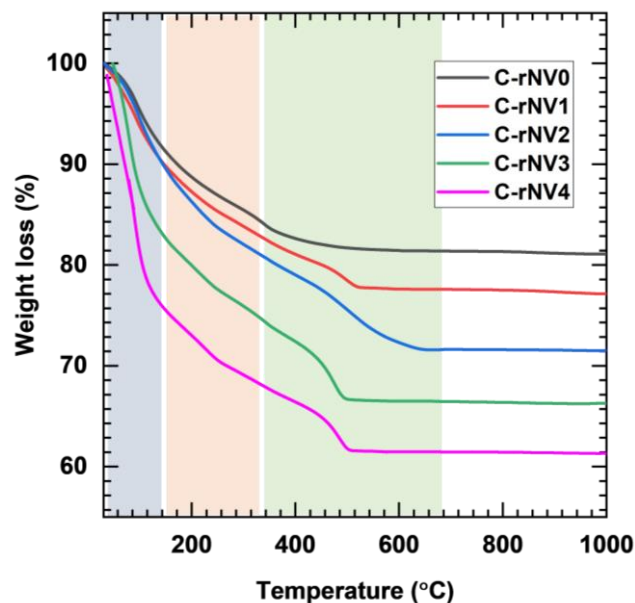


**Figure 3.25:** TG analysis of C-rNV series samples

#### 3.4.C.3.6 FE-SEM analysis

The surface morphological study of C-rNV series samples was probed by FE-SEM analysis at different magnifications of X5K and X40K, as displayed in Figure 3.26. At a lower magnification of X5K, closely packed, spherical particles are observed for all C-rNV samples. As the content of rGO increases, the size of the particles increases. The calculated average particle size is found to be an average diameter of ~291, ~357, ~418, ~475, and ~483 nm for samples C-rNV0, C-rNV1, C-rNV2, C-rNV3, and C-rNV4, respectively, as histograms displayed in Figure 3.26 (a<sub>3</sub>, b<sub>3</sub>, c<sub>3</sub>). With the incorporation of rGO, nanosheets of rGO become evident at higher concentrations (Figure 3.26 d<sub>2</sub> and e<sub>2</sub>). However, at lower rGO concentrations, excessive growth of NVO obstructs the visibility of rGO. The combined surface structure potentially presents a substantial surface area, thereby offering an increased quantity of electrochemically active sites for the electrochemical activities [60].

The elemental mapping was carried out to probe the composition and elemental distribution of major elements (Ni, V, C, and O) for all C-rNV series samples. The elements Ni, V, and O are distributed homogeneously in sample C-rNV0, which is observed in Figure 3.27 (a), confirming the formation of pure NVO with no detectable carbon content in a sample. Furthermore, the distribution of carbon varies with the concentration of rGO in samples C-rNV1 to C-rNV4 (Figure 3.27 (b-e)); however, the distribution of nickel, vanadium, and oxygen elements remains constant.

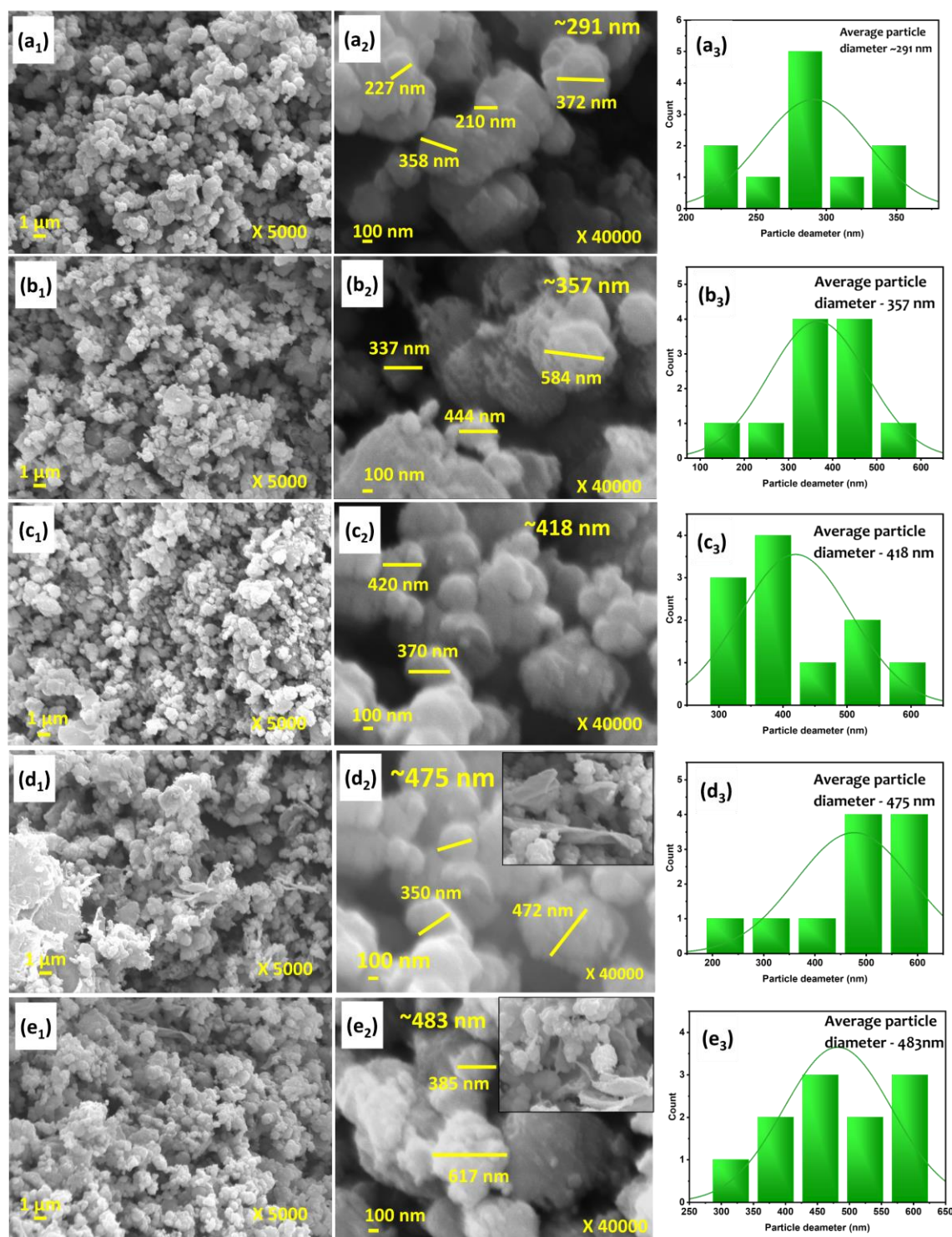


**Figure 3.26:** FE-SEM images of sample (a<sub>1</sub>, a<sub>2</sub>) C-rNV1, (b<sub>1</sub>, b<sub>2</sub>) C-rNV2, (c<sub>1</sub>, c<sub>2</sub>) C-rNV3, (d<sub>1</sub>-d<sub>2</sub>) C-rNV4, (e<sub>1</sub>-e<sub>2</sub>) C-rNV5 at the magnification of X5K and X40K, respectively, and (a<sub>3</sub>-e<sub>3</sub>) histograms of particles size distribution



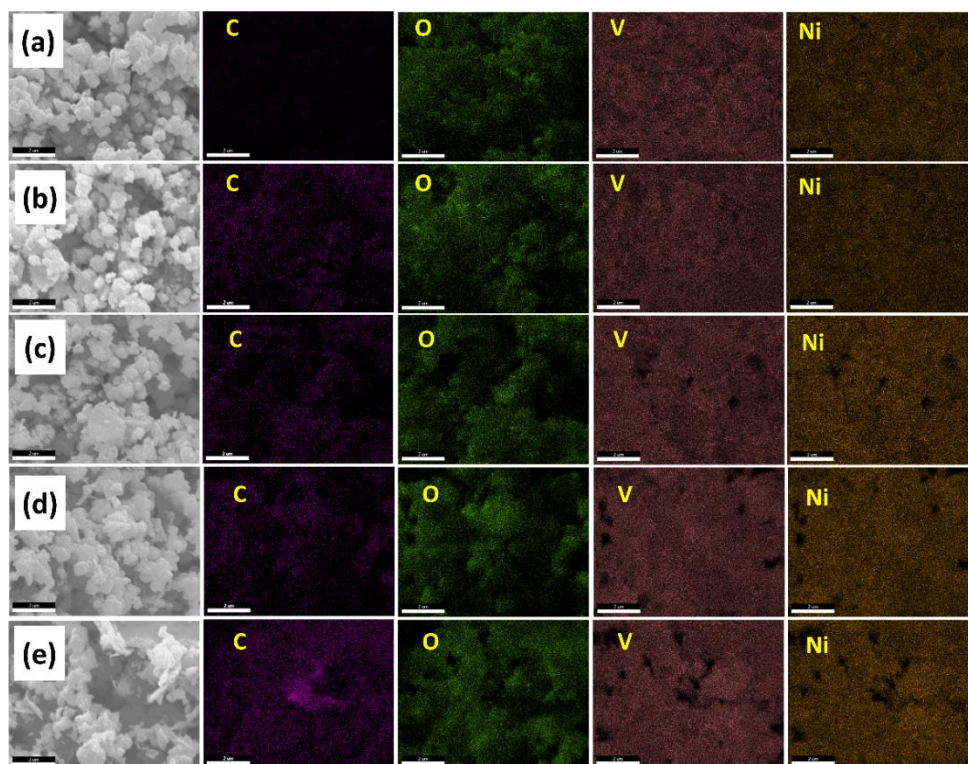


**Figure 3.27:** EDS mapping images of (a) C-rNV0, (b) C-rNV1, (c) C-rNV2, (d) C-rNV3, and (e) C-rNV4 samples

The chemical composition in prepared C-rNV series samples was quantitatively examined from EDS measurement as spectra shown in Figure 3.28. For the C-rNV0 sample, there is no trace of carbon element, confirming the pure nickel vanadate material is prepared. Besides the remaining samples, C-rNV1 to C-rNV4, the EDS spectra confirm the successful preparation of NVO/rGO composite material, as they contain nickel, vanadium, carbon, and oxygen elements. As shown in Figure 3.28 (d), the obtained EDS spectrum for C-rNV3 reveals the presence of nickel (37.71%), vanadium (28.32%), oxygen (8.58%), and carbon (25.39%). The obtained atomic percentage of nickel, vanadium, and oxygen remains consistent across the whole C-rNV series, as shown in the inset of Figure 3.28 in the form of a pie chart. The relatively lower percentage of oxygen is due to the vanadium peaks which may overlap or obscure the oxygen peak. This can make it difficult to distinguish oxygen in the spectrum and lead to an underestimation of its content. Also, in consistent with the experiment, the percentage of carbon elements increases with the content of rGO.

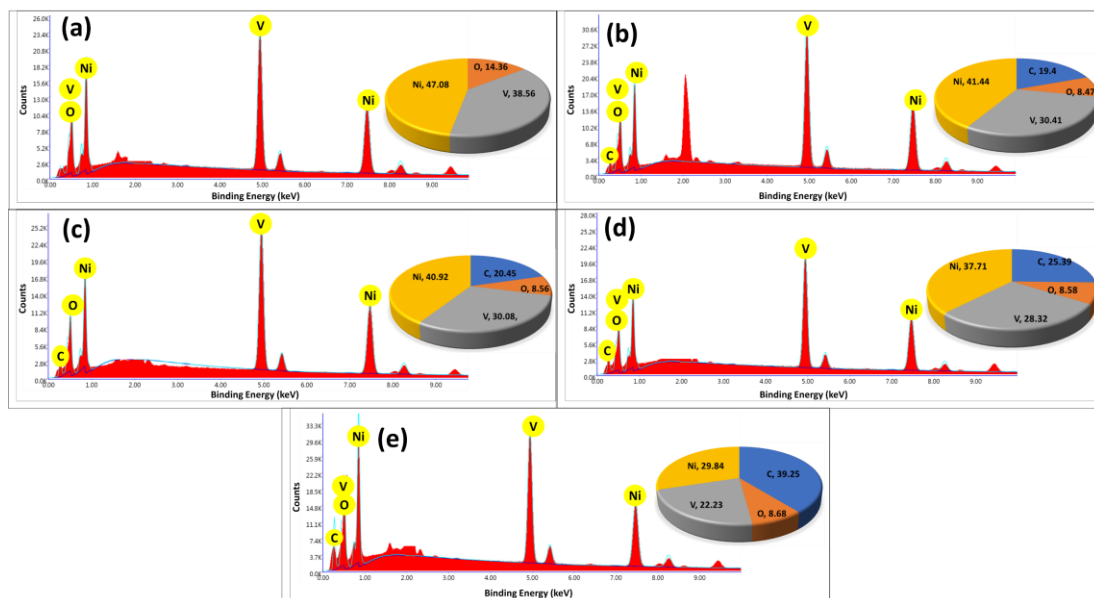


**Figure 3.28:** EDS spectra of (a) C-rNV0, (b) C-rNV1, (c) C-rNV2, (d) C-rNV3, (e) C-rNV4 samples

### 3.4.C.3.7 HR-TEM analysis

In constituent with FE-SEM analysis, particles with rGO sheets along with NVO particles are observed in the HR-TEM images of the C-rNV3 (Figure 3.29 (a-c)) sample. Furthermore, the interplanar distance is tailored using the digital microscopy software and determined through the analysis of line profiles observed at higher magnification, as shown in Figure 3.29 (e). The observed lattice fringes are depicted in Figure 3.29 (e), and the measured lattice distance is  $\sim 0.25$  nm for the C-rNV3 sample, affirming the existence of (122) crystalline plane within the respective sample. The margins of the crystalline fringes are discontinuous (Figure 3.29 (e)), resulting in a significant number of defects, which are more beneficial in increasing the material's conductivity [61].

Furthermore, the selected area electron diffraction (SAED) pattern presented in Figure 3.29 (f), shows unclear but ordered rings, confirming the lower crystallinity with polycrystalline characteristics of the material. The obtained rings in the SAED pattern confirm the existence of (122) and (042) crystalline planes of NVO and are well analogous with XRD results. Figure 3.30 (g) displays HR-TEM images and elemental mapping images highlighting the presence and distribution of Ni, V, C, and O elements and also reveals a uniform distribution of elements. Thus, the HR-TEM images confirm the well decoration of NVO particles over nanosheets of rGO.

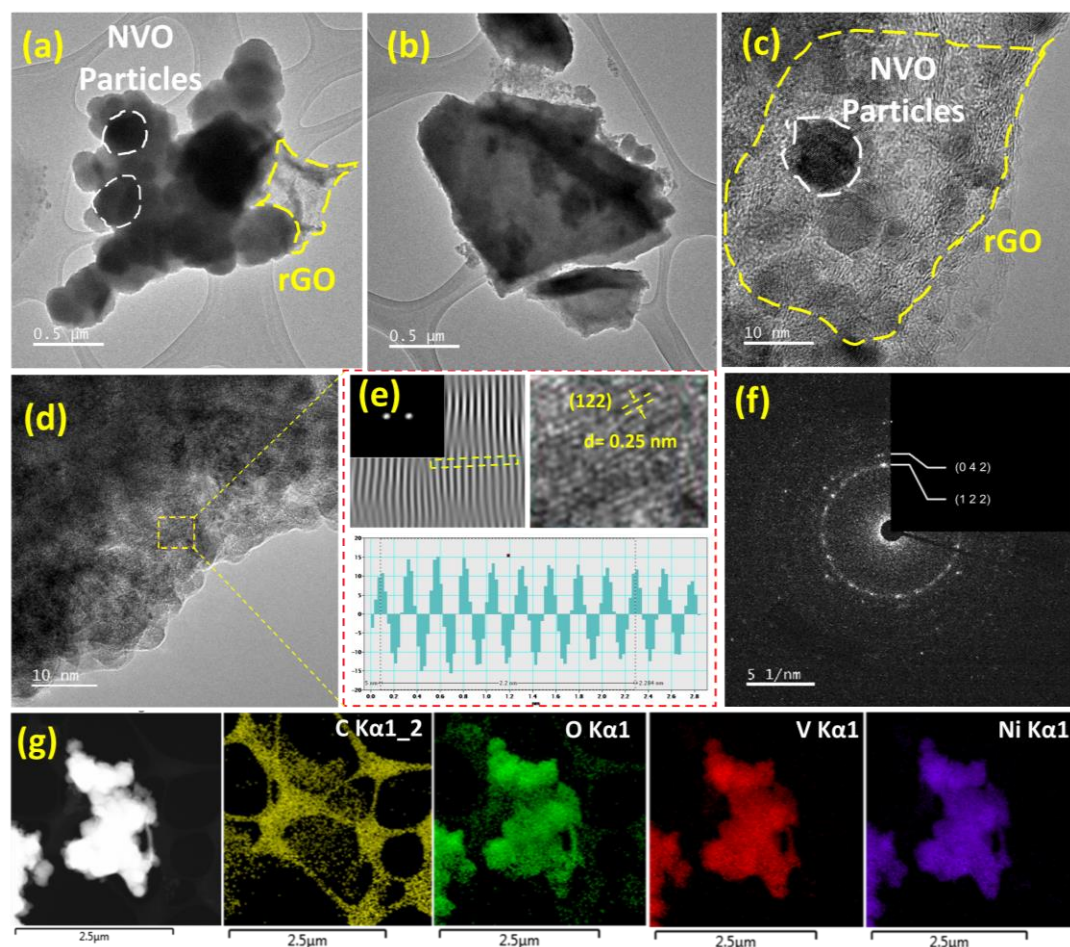


**Figure 3.29:** (a-d) HR-TEM images (e) lattice distortion image and interplanar distance calculation using HR-TEM patterns (f) SAED pattern, and (g) EDS elemental mapping for C-rNV3 sample

#### 3.4.C.3.8 BET and BJH analysis

The surface area and porous nature of C-rNV series samples are investigated using BET and BJH measurements. The recorded  $N_2$  adsorption-desorption isotherms for C-rNV series samples are shown in Figure 3.30 (a-e). The curve demonstrates a well-defined loop of hysteresis in the relative pressure range of 0.25-0.99, and the curve resembles the H3-type hysteresis loop, which mainly underlies the type-II isotherm with high adsorption energy. All C-rNV samples provide a specific surface area ranging from  $\sim 34.1$  to  $\sim 144.5 \text{ m}^2 \text{ g}^{-1}$ , and the C-rNV3 sample provides a maximum specific surface area of  $144.5 \text{ m}^2 \text{ g}^{-1}$ . Moreover, a BJH analysis was carried out to study the distribution of pore size. The obtained BJH plots for C-rNV series samples are depicted in the inset of Figure 3.31.



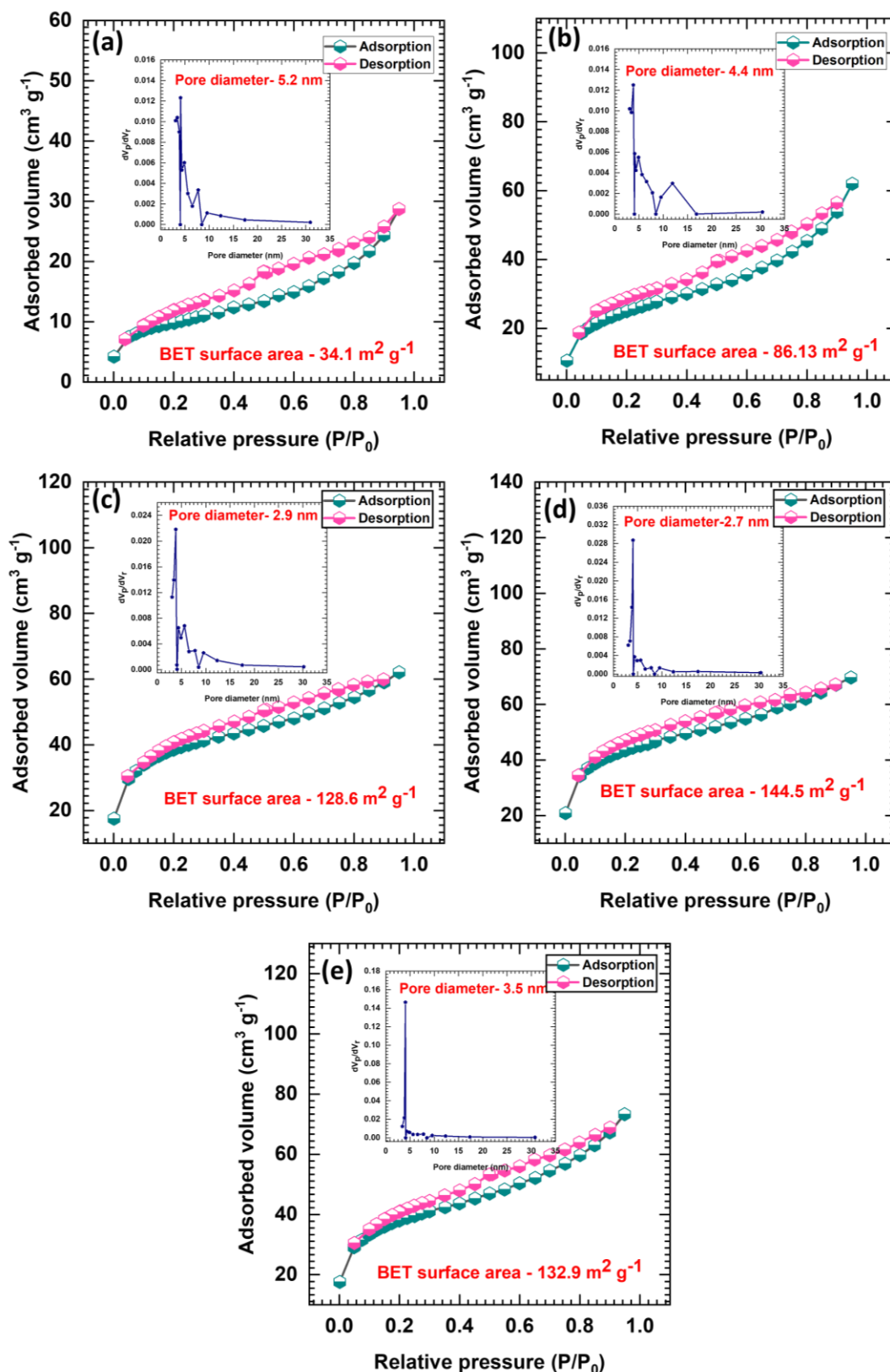


**Figure 3.30:** Nitrogen adsorption-desorption isotherms (BET) and inset pore size distribution (BJH) of (a) C-rNV0, (b) C-rNV1, (c) C-rNV2, (d) C-rNV3, and (e) C-rNV4 samples



The BJH plots display the average pore size distribution of 5.2, 4.4, 2.9, 2.7, and 3.5 nm for C-rNV0, C-rNV1, C-rNV2, C-rNV3, and C-rNV4 samples, respectively, confirms the mesoporous nature of the material. The considerable specific surface area and mesoporous nature of these composite materials can elevate electrochemical activity by facilitating a multitude of active sites and easy ion transfer through the mesopores [62].

#### 3.4.C.3.9 Electrochemical analysis

The electrochemical performance of C-rNV series samples was performed using three three-electrode's system in 1 M aqueous KOH electrolyte, as discussed in subsection 3.2.A.3.7, while NVO/rGO composite electrode as a working electrode. The performances of the prepared C-rNV series electrodes were investigated using CV, GCD, and EIS measurements.

##### (a) CV analysis

The CV curves of C-rNV0 to C-rNV4 electrodes were tested in a potential range of 0 to 0.6 V (vs Hg/HgO) and depicted in Figure 3.31. The comparative CV curves at a constant scan rate of  $50 \text{ mV s}^{-1}$  are provided in Figure 3.31 (a). All obtained CV curves show reversible surface redox reactions of  $\text{Ni}^{2+}$  and  $\text{Ni}^{3+}$ , as discussed in section 3.2.A.3.7, equation 3.4. Furthermore, the area under the CV curves shows an increment with the rise in rGO content within the electrode, reaching its maximum at the C-rNV3 sample. However, beyond the C-rNV3 sample, there is a reduction in area under the curve is observed, as there is a further increase in rGO content. It is also observed that as the concentration of rGO increases, a corresponding expansion in the region linked with EDLC and slight shifting redox peaks toward lower potential corresponds to enhanced conductivity of the material. The maximum area under the curve in the C-rNV3 electrode confirms its capability to accumulate a maximum amount of energy. Moreover, Figure 3.31 (b-f) shows the CV curves at different scan rates from 5 to  $100 \text{ mV s}^{-1}$ .

Furthermore, the determination of the 'b' value for C-rNV series electrodes involves calculating the slope of the graph by plotting  $\log(i)$  vs  $\log(v)$ , as depicted in Figure 3.32. The resulting 'b' values fall within the range of 0.6 to 0.7, indicating the combined (capacitive as well as battery type) charge storage mechanism of the material.

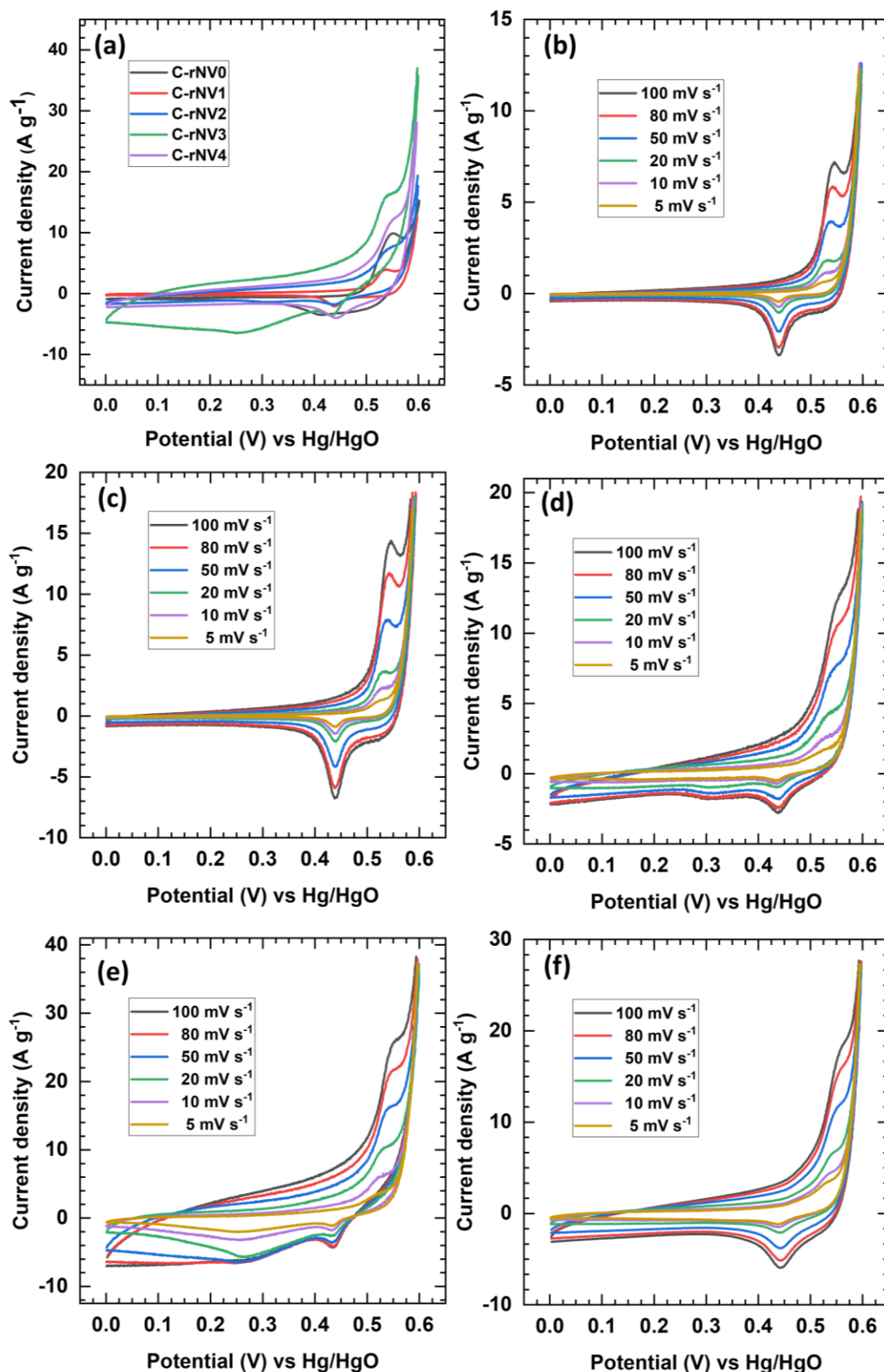


**Figure 3.31:** (a) Comparative CV curves for C-rNV series electrode at 50 mV s<sup>-1</sup>, CV curves at different scan rates for (b) C-rNV0, (c) C-rNV1, (d) C-rNV2, (e) C-rNV3, and (f) C-rNV4 electrodes

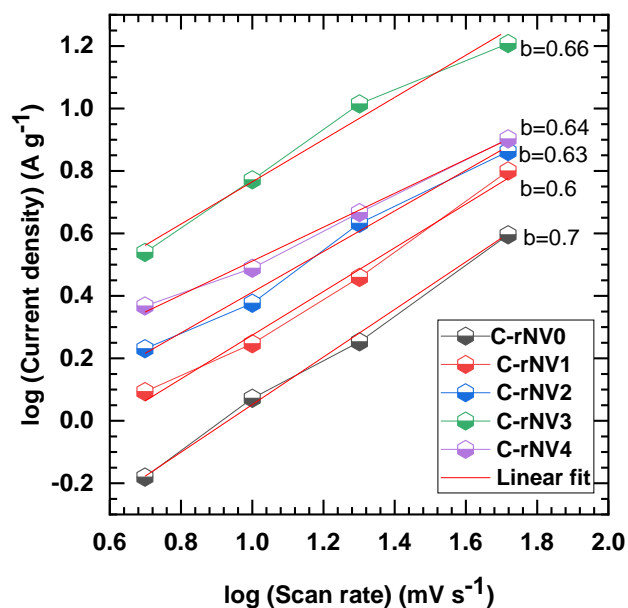


**Figure 3.32:** Plot of log (current density,  $\text{A g}^{-1}$ ) vs log (scan rate,  $\text{mV s}^{-1}$ )

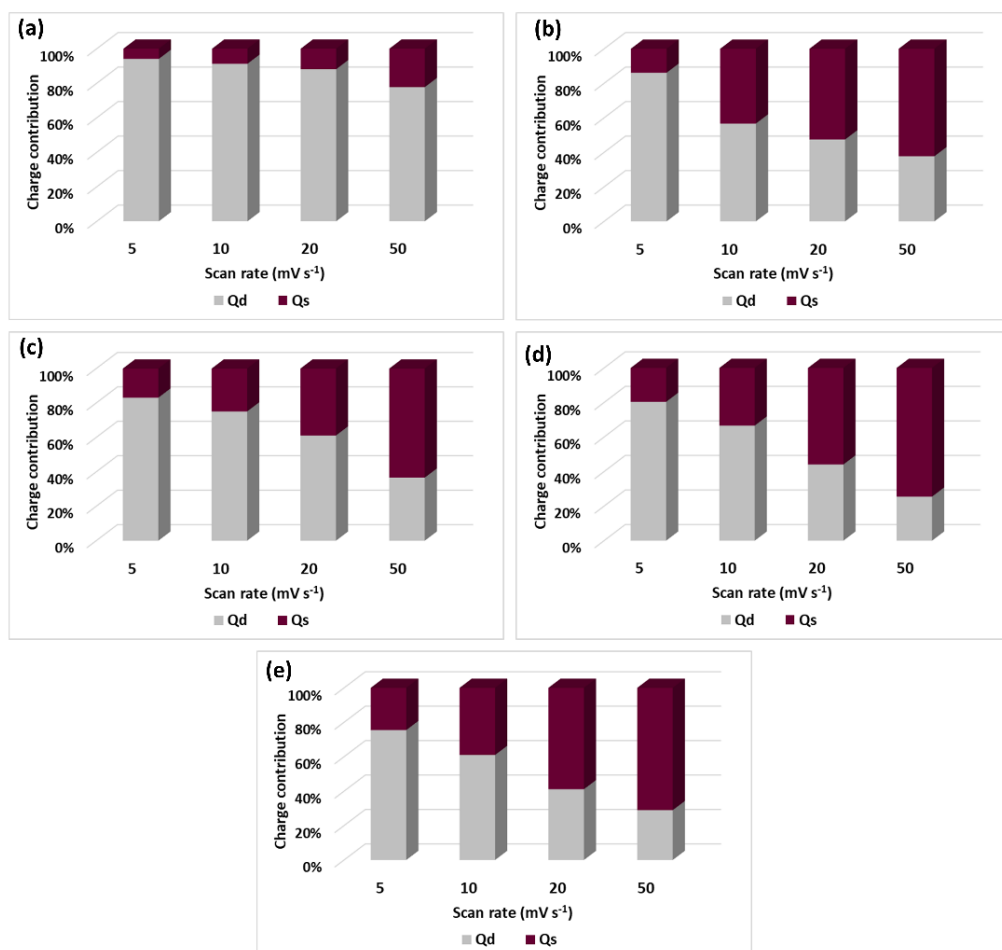


**Figure 3.33:** Charge contribution plots of (a) C-rNV0, (b) C-rNV1, (c) C-rNV2, (d) C-rNV3, and (e) C-rNV4 electrodes

Additionally, the comprehensive study of the charge storage kinetics of the prepared electrodes is conducted through an analytical approach, distinguishing between diffusion-controlled and extrinsic pseudocapacitive charge storage processes. The surface redox (extrinsic pseudocapacitive) charge ( $Q_s$ ) and the contribution of diffusion-controlled charge ( $Q_d$ ) were assessed using the CV-dependent total current response. The total charge ( $Q_t$ ) comprises both extrinsic pseudocapacitive and diffusion-controlled charge, as expressed by equation 3.8 (subsection 3.2.A.3.7), and the obtained charge contribution for all C-rNV series samples is plotted in Figure 3.33. For the C-rNV3 electrode, surface capacitive contribution is 19.63% at  $5 \text{ mV s}^{-1}$  scan rate, while 80.37% of the total charge corresponds to diffusive. Moreover, at  $50 \text{ mV s}^{-1}$ , the capacitive contribution increases up to 74.5%, whereas the decrease in the diffusive contribution of 25.5% is observed for the same electrode (Figure 3.33 (d)) The figure illustrates that the surface contribution increases with the higher content of rGO in the sample.

#### **(b) GCD analysis**

Furthermore, the electrochemical capacitive performance of the C-rNV series electrodes was examined utilizing the GCD measurement technique. To prevent water electrolysis during the charging process, the potential window was set within the range of 0 to 0.5 V vs Hg/HgO for testing [63]. Figure 3.34 displays the GCD curves for the C-rNV series electrodes at a constant current density of  $1 \text{ A g}^{-1}$ . The C-rNV3 electrode exhibits the longest discharge time compared to the other electrodes, as depicted in Figure 3.34 (d), indicating superior electrochemical performance. Based on the GCD plots,  $C_{sp}$  values of C-rNV series electrodes are computed using equation 2.10 (Chapter II, Section 2.5.2) and illustrated in Figure 3.35. Notably, the C-rNV3 electrode exhibits a longer discharging time, contributing to its higher  $C_{sp}$  compared to other electrodes. The C-rNV3 electrode shows a maximum  $C_{sp}$  of  $854 \text{ F g}^{-1}$  at  $1 \text{ A g}^{-1}$  current density, and it decreases to  $530 \text{ F g}^{-1}$  at  $5 \text{ A g}^{-1}$  current density. Likewise, the C-rNV0, C-rNV1, C-rNV2, C-rNV3, and C-rNV4 electrodes offer maximum  $C_{sp}$  of 302, 346, 493, 854, and  $616 \text{ F g}^{-1}$ , respectively, at  $1 \text{ A g}^{-1}$  current density.

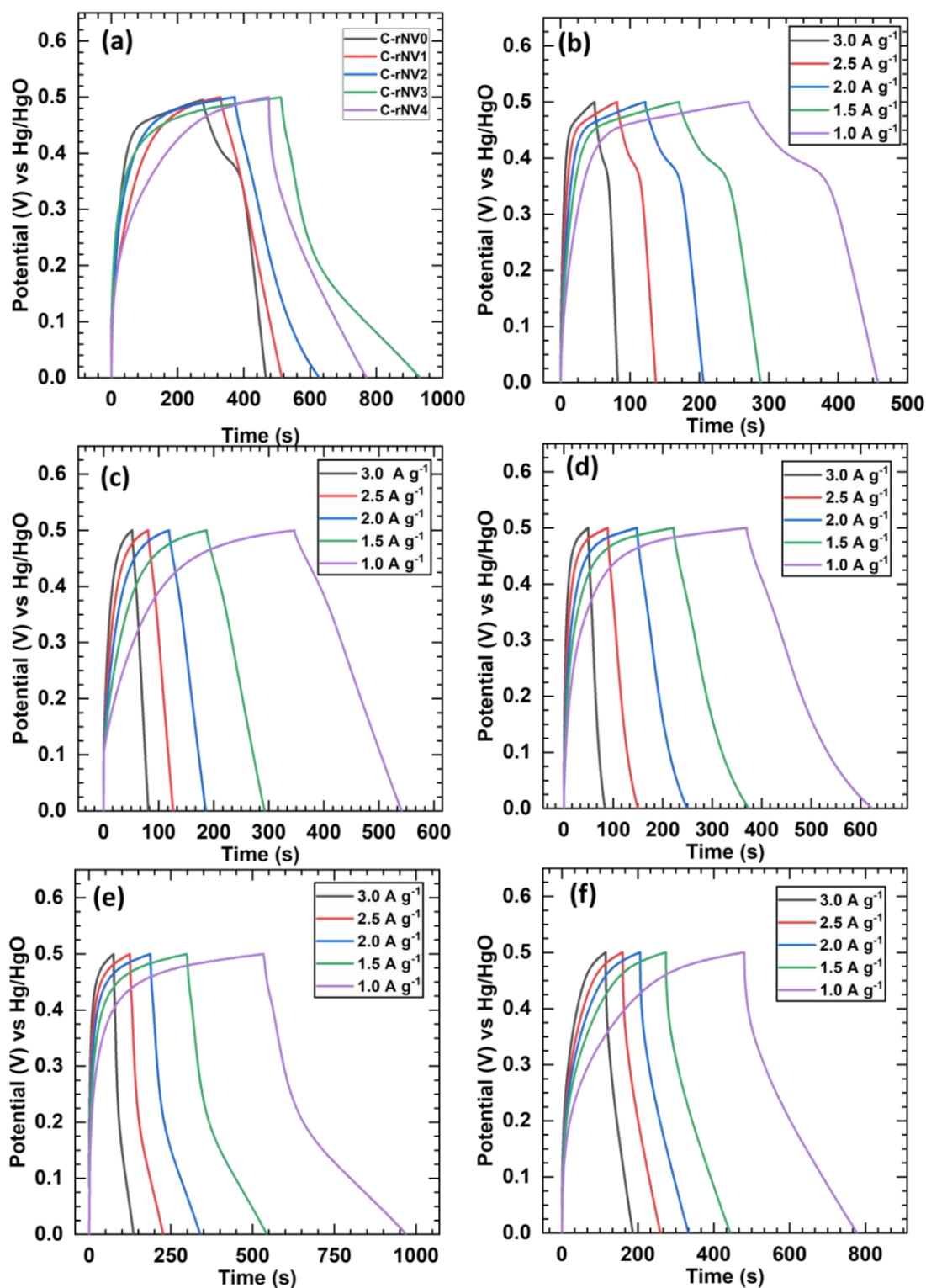


**Figure 3.34:** (a) Comparative GCD curves for C-rNV series electrode at  $1 \text{ A g}^{-1}$ , GCD curves at different current densities for (b) C-rNV0, (c) C-rNV1, (d) C-rNV2, (e) C-rNV3, and (f) C-rNV4 electrodes

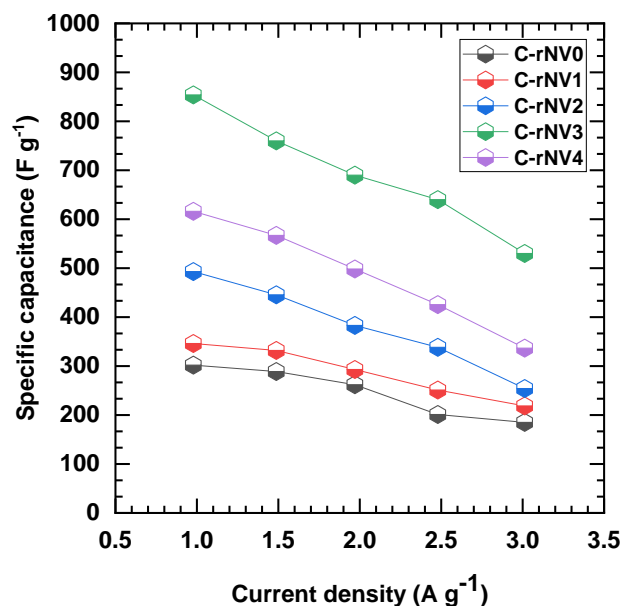


**Figure 3.35:** The plot of  $C_{sp}$  at various current densities for C-rNV series electrodes

### (c) EIS analysis

The EIS was conducted on C-rNV series electrodes to analyze their charge transfer characteristics. The measurements were performed at OCP over a frequency range spanning from 0.01 Hz to 0.1 MHz. Figure 3.36 illustrates the Nyquist plots obtained for the C-rNV series electrodes, with each plot fitted using the circuit depicted in the inset of Figure 3.36.

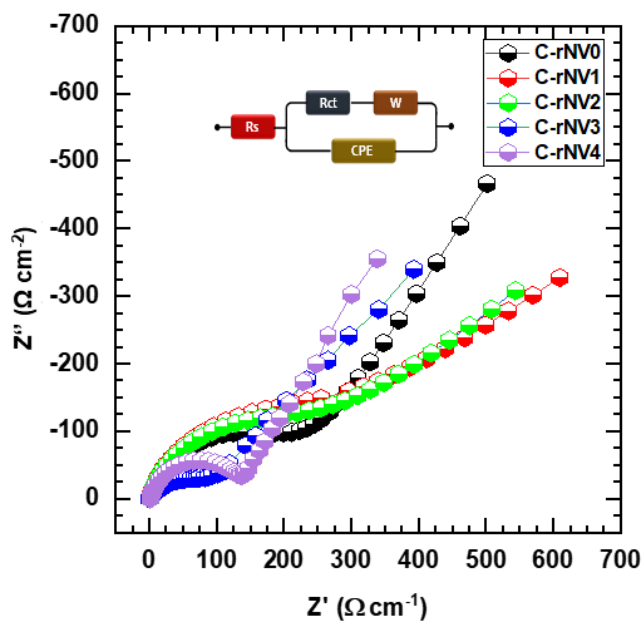


**Figure 3.36:** Nyquist plots for C-rNV series electrodes

The fitted parameters, such as  $R_s$ ,  $R_{ct}$ , CPE, and  $W$ , are detailed in Table 3.4. The Nyquist plots for all C-rNV samples exhibit smaller  $R_s$  values, indicating favorable interactions between the active material and electrolyte. The values of  $R_s$  range from 0.54 to 1.52  $\Omega \text{ cm}^{-2}$  across the C-rNV series electrodes. Moreover, the smallest semicircle observed for the same electrode (C-rNV3) implies a lower  $R_{ct}$  of 139  $\Omega \text{ cm}^{-2}$ . The obtained ‘n’ values close to 1 suggest pseudocapacitive behaviour of composite material.

**Table 3.4:** EIS fitted circuit parameters for C-rNV series electrode

Fitted Parameters	C-rNV0	C-rNV1	C-rNV2	C-rNV3	C-rNV4
$R_s (\Omega \text{ cm}^{-2})$	1.52	1.47	1.27	1.54	1.38
$R_{ct} (\Omega \text{ cm}^{-2})$	229	238	225	139	152
$W-P (\Omega \text{ cm}^{-2})$	0.22	0.35	0.22	0.32	0.47
CPE-T (mF $\text{cm}^{-2}$ )	0.91	0.89	0.91	1.23	1.02
CPE-P (n)	0.83	0.64	0.83	0.82	0.74

**(d) Stability analysis**

Electrochemical cyclic stability measurement is an essential parameter for SC applications. The cycling stability of the best-performed C-rNV3 electrode was carried out for 5000 charge-discharge cycles at 10  $\text{A g}^{-1}$  current density.

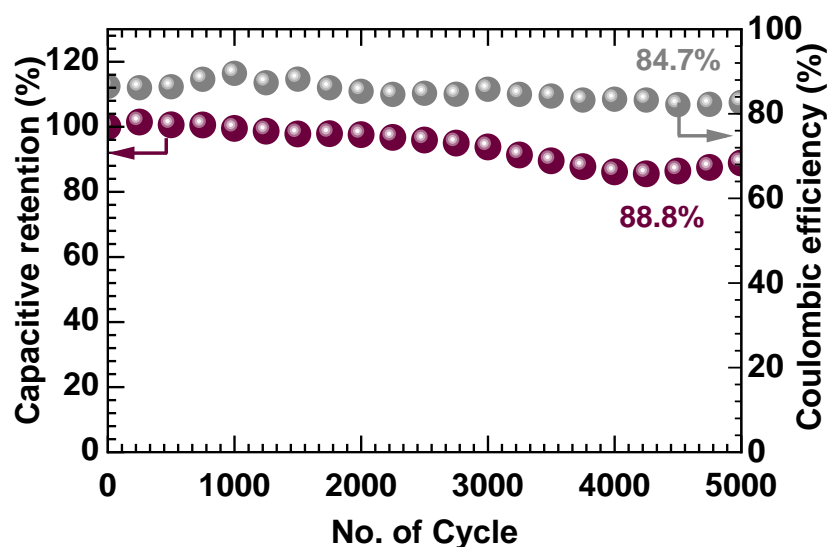


**Figure 3.37** Plot of capacitive retention and coulombic efficiency vs number of cycles



Figure 3.37 shows the obtained capacitive retention and coulombic efficiency for the C-rNV3 sample. From plots, it is observed that NVO combined with rGO can help to improve the stability of the material. The sample C-rNV3 exhibits remarkable capacitive retention, maintaining 88.8% even after 5000 charge-discharge cycles. Also, the prepared NVO/rGO composite upheld 84.7% coulombic efficiency.

#### 3.4.C.4 Conclusions

In summary, NVO/rGO nanocomposites were successfully synthesized utilizing a facile CBS method. Experimental findings unveiled substantial variations in structural and electrochemical properties contingent upon the concentration of rGO. The C-rNV3 electrode, with an optimal composition of rGO (20.08%), yields a maximum specific surface area of  $144 \text{ m}^2 \text{ g}^{-1}$  along with a pore diameter of 2.7 nm, thereby contributing to enhanced electrochemical performance. Furthermore, the C-rNV3 sample exhibited the highest  $C_{\text{sp}}$  of  $854 \text{ F g}^{-1}$  at a current density of  $1 \text{ A g}^{-1}$ . Additionally, it demonstrated satisfactory cycling stability, retaining 88.8% of its capacitance, and displayed a superior coulombic efficiency of 84% after 5000 charge-discharge cycles. The remarkable electrochemical performance observed in the NVO/rGO composite suggests its potential as a promising cathode for SCs.

#### 3.5 References

- [1] Z. Yan, S. Luo, Q. Li, Z. Wu, S. Liu, *Adv. Sci.*, 2302172 (2023) 1–22.
- [2] S. Delbari, L. Ghadimi, R. Hadi, S. Farhoudian, M. Nedaei, A. Babapoor, A. Namini, Q. Le, M. Shokouhimehr, M. Asl, M. Mohammadi, *J. Alloys Compd.*, 857 (2021) 1405–1419.
- [3] M. Maksoud, R. Fahim, A. Shalan, M. Elkodous, S. Olojede, A. Osman, C. Farrell, A. Al-Muhtaseb, A. Awed, A. Ashour, D. Rooney, *Environ. Chem. Lett.*, 19 (2021) 375–439.
- [4] P. Forouzandeh, V. Kumaravel, S. Pillai, *Catalysts*, 10 (2020) 1–73.
- [5] H. Qin, S. Liang, L. Chen, Y. Li, Z. Luo, S. Chen, *Sustain. Energy Fuels*, 4 (2020) 4902–4933.
- [6] K. Thiagarajan, J. Theerthagiri, R. Senthil, P. Arunachalam, J. Madhavan, M. Ghanem, *J. Solid State Electrochem.*, 22 (2018) 527–536.
- [7] D. Xia, H. Gao, M. Li, F. Gong, M. Li, *Energy Storage Mater.*, 35 (2021) 169–191.
- [8] S. Marje, P. Katkar, S. Pujari, S. Khalate, P. Deshmukh, U. Patil, *Mater. Sci. Eng. B*, 261 (2020) 114641.
- [9] V. Patil, S. Pujari, S. Bhosale, S. Kumbhar, V. Parale, J. Gunjekar, H. Park, C. Lokhande, M. Mali, D. Mhamane, U. Patil, *Energy and Fuels*, 36 (2022) 12791–12806.
- [10] Q. Li, Y. Xu, S. Zheng, X. Guo, H. Xue, H. Pang, *Small*, 14 (2018) 1–19.
- [11] S. Arasi, R. Ranjithkumar, P. Devendran, M. Krishnakumar, A. Arivarasan, *Ceram. Int.*, 46 (2020) 22709–22717..
- [12] X. Liu, C. Huang, J. Qiu, Y. Wang, *Appl. Surf. Sci.*, 253 (2006) 2747–2751.
- [13] S. Sadavar, N. Padalkar, R. Shinde, S. Kochuveedu, U. Patil, A. Patil, R. Bulakhe, C. Lokhande, I. In, R. Salunkhe, J. Gunjekar, *J. Power Sources*, 524 (2022) 231065.
- [14] M. Rajkumar, S. Xavier, S. Anbarasu, P. Devarajan, *Optik.*, 127 (2016) 2187–2192..

- [15] S. Pujari, S. Kadam, Y. Ma, P. Katkar, S. Marje, S. Khalate, A. Lokhande, U. Patil, J. Electron. Mater., 49 (2020) 3890–3901.
- [16] S. Marje, P. Deshmukh, J. Gunjekar, C. Lokhande, U. Patil, Energy and Fuels 35 (2021) 14110–14121.
- [17] S. Bhosale, S. Kumbhar, S. Pujari, V. Patil, N. Kumar, R. Salunkhe, C. Lokhande, J. Gunjekar, U. Patil, J. Energy Storage 72 (2023) 108417.
- [18] S. Kumbhar, S. Bhosale, S. Pujari, V. Patil, N. Kumar, R. Salunkhe, C. Lokhande, U. Patil, Energy Technol. 11 (2023) 1–16.
- [19] Y. Cui, J. Zhang, C. Jin, Y. Liu, W. Luo, W. Zheng, Small, 15 (2019) 1–10.8.
- [20] S. Pujari, S. Kadam, Y. Ma, S. Jadhav, S. Kumbhar, S. Bhosale, J. Gunjekar, C. Lokhande, U. Patil, J. Energy Storage, 52 (2022) 105037.7.
- [21] Z. Huang, T. Liu, Y. Song, Y. Li, X. Liu, Nanoscale, 9 (2017) 13119–13127.
- [22] P. Katkar, S. Marje, S. Pujari, S. Khalate, P. Deshmukh, U. Patil, Synth. Met., 267 (2020) 116446.
- [23] B. Mei, J. Lau, T. Lin, S. Tolbert, B. Dunn, L. Pilon, J. Phys. Chem. C, 122 (2018) 24499–24511.
- [24] J. Huang, Electrochim. Acta, 281 (2018) 170–188.6.
- [25] C. Alexander, B. Tribollet, M. Orazem, Electrochim. Acta, 173 (2015) 416–424.
- [26] S. Marje, S. Pujari, S. Khalate, V. Patil, V. Parale, T. Kim, H. Park, J. Gunjekar, C. Lokhande, U. Patil, J. Mater. Chem. A, 10 (2022) 11225–11237.
- [27] L. Shahriary and A. Athawale, Int. J. Renew. Energy Environ. Eng., 02 (2014) 58–63.
- [28] W. Choi, I. Lahiri, R. Seelaboyina, Y. Kang, Crit. Rev. Solid State Mater. Sci., 35 (2010) 52–71.
- [29] K. Novoselov, A. Geim, S. Morozov, D. Jiang, Y. Zhang, S. Dubonos, I. Grigorieva, A. Firsov, Science, 306 (2004) 666–669.
- [30] A. Higginbotham, J. Lomeda, A. Morgan, J. Tour, GACS Appl. Mater. Interfaces, 1 (2009) 2256–2261.
- [31] A. Lerf, H. He, M. Forster, J. Klinowski, J. Phys. Chem. B, 102 (1998) 4477–4482.
- [32] H. He, J. Klinowski, M. Forster, A. Lerf, Chem. Phys. Lett., 287 (1998) 53–56.
- [33] F. Uhl and C. Wilkie, Polym. Degrad. Stab., 84 (2004) 215–226.
- [34] W. Hummers and R. Offeman, J. Am. Chem. Soc., 208 (1957) 1937.
- [35] K. Zhang, L. Zhang, X. Zhao, J. Wu, Chem. Mater., 22 (2010) 1392–1401.
- [36] C. Fu, G. Zhao, H. Zhang, S. Li, Int. J. Electrochem. Sci., 8 (2013) 6269–6280.
- [37] A. Lee, K. Yang, N. Anh, C. Park, S. Lee, T. Lee, M. Jeong, Appl. Surf. Sci., 536 (2021) 147990.
- [38] S. Marje, V. Patil, V. Parale, H. Park, P. Shinde, J. Gunjekar, C. Lokhande, U. Patil, Chem. Eng. J., 429 (2022) 132184.
- [39] S. Gurunathan, J. Han, A. Dayem, V. Eppakayala, J. Kim, Int. J. Nanomedicine, 7 (2012) 5901–5914.
- [40] J. Zhang, Y. Liu, P. Wang, G. Wang, B. Duan, T. Wang, F. Li, J. Phys. D. Appl. Phys., 53 (2020) 354002.
- [41] S. Khalate, S. Kadam, Y. Ma, S. Pujari, S. Marje, P. Katkar, A. Lokhande, U. Patil, Electrochim. Acta, 319 (2019) 118–128.
- [42] X. Liu, J. Wang, G. Yang, Mater. Interfaces, 10 (2018) 20688–20695.
- [43] M. Liu, L. Kong, L. Kang, X. Li, F. Walsh, M. Xing, C. Lu, X. Ma, Y. Luo, J. Mater. Chem. A, 2 (2014) 4919–492.
- [44] W. Zhang, L. Kong, X. Ma, Y. Luo, L. Kang, RSC Adv., 4 (2014) 41772–41777.
- [45] S. Al-Rubaye, R. Rajagopalan, S. Dou, Z. Cheng, J. Mater. Chem. A, 5 (2017) 18989–18997.
- [46] L. Ma, X. Shen, H. Zhou, Z. Ji, K. Chen, G. Zhu, Chem. Eng. J., 262 (2015) 980–988.
- [47] W. Low, P. Khiew, S. Lim, C. Siong, E. Ezeigwe, J. Alloys Compd., 768 (2018) 995–1005.
- [48] R. Tamilselvi, N. Padmanathan, K. Rahulan, P. Priya, R. Sasikumar, M. Mandhakini, J. Mater. Sci. Mater. Electron., 29 (2018) 4869–4880.

- [49] Y. Xu, J. Wei, L. Tan, J. Yu, Y. Chen, *J. Mater. Chem. A*, 3 (2015) 7121–7131.
- [50] R. Kumar, P. Gupta, P. Rai, A. Sharma, *J. Electrochem. Soc.*, 3 (2017) 2–6.
- [51] R. Rochman, S. Wahyuningsih, A. Ramelan, Q. Hanif, *IOP Conf. Ser. Mater. Sci. Eng.*, 509 (2019) 012119.
- [52] C. Hu, K. Chang, M. Lin, Y. Wu, *Nano Lett.*, 6 (2006) 2690–2695.
- [53] D. Tran and V. Nguyen, *Mater. Res. Express*, 7 (2020) 75501.
- [54] L. Aissani, M. Fellah, A. Chadli, M. Samad, A. Cheriet, F. Salhi, C. Nouveau, S. Weiß, A. Obrosof, A. Alhussein, *J. Mater. Sci.*, 56 (2021) 17319–17336.
- [55] A. Held, J. Kowalska-Kuś, E. Janiszewska, A. Jankowska, K. Nowińska, *J. Catal.*, 404 (2021) 231–243.
- [56] J. Zhang, Y. Xu, Z. Liu, W. Yang, J. Liu, *RSC Adv.*, 5 (2015) 54275–54282.
- [57] J. Fuente, M. Ruiz-Bermejo, C. Menor-Salván, S. Osuna-Esteban, *Polym. Degrad. Stab.*, 96 (2011) 943–948.
- [58] F. Farivar, P. Yap, K. Hassan, T. Tung, D. Tran, A. Pollard, D. Losic, *Carbon*, 179 (2021) 505–513.
- [59] Y. Wang, Q. He, H. Qu, X. Zhang, J. Guo, J. Zhu, G. Zhao, H. Colorado, J. Yu, L. Sun, S. Bhana, M. Khan, X. Huang, D. Young, H. Wang, X. Wang, S. Wei, Z. Guo, *J. Mater. Chem. C*, 2 (2014) 9478–9488.
- [60] A. Manalu, K. Tarigan, S. Humaidi, M. Ginting, I. Manalu, Ikhwanuddin, *Energy Technol.*, 5 (2022) 444–451.
- [61] A. Patil, S. Moon, Y. Seo, S. Roy, A. Jadhav, D. Dubal, K. Kang, S. Jun, *Small*, 19 (2023) 2305264.
- [62] S. Phanichphant, A. Nakaruk, K. Chansaenpak, D. Channei, *Sci. Rep.*, 9 (2019) 1–9.
- [63] P. Katkar, S. Marje, V. Parale, C. Lokhande, J. Gunjakar, H. Park, U. Patil, *Langmuir*, 37 (2021) 5260–5274.

# **CHAPTER-IV**

---

**Synthesis of Nickel Vanadium  
Oxide/rGO Composite  
Electrodes by SILAR Method:  
Characterizations and  
Supercapacitive Performance**

---

## Chapter-IV

### Synthesis of Nickel Vanadium Oxide/rGO Composite Electrodes by SILAR Method: Characterizations and Supercapacitive Performance

Sr. No.	Title	Page No.
4.1.	Introduction	111
4.2.	<b>Section A</b> <b>Nickel Vanadium Oxide by SILAR Method: Synthesis and Characterizations</b>	
4.2.A.1	Introduction	112
4.2.A.2	Experimental details	113
	4.3.B.2.1. Chemicals	113
	4.3.B.2.2. Synthesis of nickel vanadium oxide	113
	4.3.B.2.3. Material Characterizations	115
4.2.A.3	Results and discussion	115
	4.2.A.3.1 Film formation and reaction mechanism	115
	4.2.A.3.2 XRD analysis	116
	4.2.A.3.3 FT-IR analysis	117
	4.2.A.3.4 XPS analysis	118
	4.2.A.3.5 FE-SEM and EDS analysis	120
	4.2.A.3.6 HR-TEM analysis	122
	4.2.A.3.7 BET and BJH analysis	123
	4.2.A.3.8 Electrochemical performance analysis	125
4.2.A.4	Conclusions	131
4.3.	<b>Section B</b> <b>Nickel Vanadium Oxide/rGO composite by SILAR Method: Synthesis and Characterizations</b>	
4.3.B.1.	Introduction	132
4.3.B.2.	Experimental details	132

	4.3.B.2.1.	Synthesis of reduced graphene oxide	132
	4.3.B.2.2.	Synthesis of nickel vanadium oxide/reduced graphene oxide composite thin films	132
	4.3.B.2.3.	Material Characterizations	134
4.3.B.3.	Results and discussion		134
	4.3.B.3.1	Thin film formation	134
	4.3.B.3.2	XRD analysis	135
	4.3.B.3.3	FT-IR analysis	135
	4.3.B.3.4	Raman analysis	136
	4.3.B.3.5	XPS analysis	137
	4.3.B.3.6	TG analysis	139
	4.3.B.3.7	FE-SEM and EDS analysis	140
	4.3.B.3.8	HR-TEM analysis	142
	4.3.B.3.9	BET and BJH analysis	144
	4.3.B.3.10	Electrochemical analysis	145
4.3.B.4.	Conclusions		151
4.4.	References		151

#### 4.1 Introduction

Increasing concern over the depletion of fossil fuels has turned this generation's attention to environmentally friendly energy generation and conversion systems. On the other hand, the fluctuations, intermittency, and less continuity of conventional energy generation have urged researchers toward sources of ESDs [1, 2]. Hence, efforts toward a highly efficient, sustainable, low-cost, and environmentally friendly ESSs are still in progress. Among the various ESSs, electrochemical energy storage devices, such as SCs, batteries, fuel cells, etc., are highly desirable and environmentally friendly [3, 4]. As we know, the electrode material and choice of electrolyte play a crucial role in the performance of applicable technologies; hence, identifying high-performance electrode materials is essential to developing HESDs [5]. A material with a substantial surface area, mesoporous nature, electrochemical stability, and more significant conductivity can achieve high energy-storing performance.

The evolution of vanadium compounds with transition metals displays superior redox behavior due to their coordination environment and manifold valences. With their richer valences of vanadium and nickel, such as vanadium from 2+ to 5+ and nickel from 2+ to 3+, they can make a diverse atomic ratio. Apart from choosing the suitable electrode material, producing a rationally designed structure with an enhanced specific surface area and plenty of diffusion channels are essential for active site exposure and ease of electrolyte transportation [6]. The electrochemical properties of the materials are significantly influenced by their composition, crystal phase, and morphology as a result of the specific synthetic approach. Nanostructured cathode materials not only shorten the transportation distance of ions or charges and yield faster diffusion but also provide more active sites for multifarious redox reactions compared to their bulk counterparts. Thus, controlling factors such as the morphology and size of the nanoparticles, and thus the porosity and surface area of the NVO cathode, can improve the electrode performance. Thus, preparing nanostructured materials is essential and mainly relies on synthetic approaches and preparative parameters.

The hydrothermal method has been mostly employed to develop the different nanostructures of NVO for HESD applications. For instance, Li et al. [7] prepared  $\text{NiV}_2\text{O}_6$ , Singh et al. [8] designed a stone-like morphology of  $\text{Ni}_3\text{V}_2\text{O}_8$ , Nandi et al. [9]



synthesized nanopetals of  $\text{NiV}_2\text{O}_6$ ,  $\text{Ni}_3\text{V}_2\text{O}_8$  nanosheets were developed by Merum et al. [10],  $\text{Ni}_3(\text{VO}_4)_2$  prepared by Kumar et al. [11] through the hydrothermal method. Also, the hydrothermal method is used by Chandra Sekhar et al. [12] to prepare  $\text{Ni}_2\text{V}_2\text{O}_7$ , the nanorods of  $\text{Ni}_2\text{V}_2\text{O}_7$  were prepared by Ezhil Arsi et al. [13] through the co-precipitation method.

In addition, binder-free cathode synthesis improves the interfacial contact compared to binder-enriched coating methods, primarily owing to the resistive nature of PVDF hindering the charge storage kinetics. Nevertheless, the binder-free development of NVO thin film electrodes and fine-tuning of the material's intrinsic features (electrical conductivity and surface area) through the synthetic process to increase energy storage capacity is very desirable. In addition to the preparation methods mentioned above, the SILAR method stands out as the most effective for the binder-free production of nanocrystalline NVO thin film electrodes. However, no reports are available on NVO synthesized by the SILAR method for SC applications.

The current chapter is structured into two distinct parts: Section A focuses on the synthesis and optimization of NVO thin films via the SILAR method and subsequent physicochemical and electrochemical characterizations. Section B delves into the assessment of the SC performance NVO/rGO composite electrodes prepared by the SILAR method.

## **4.2 Section A**

### **Nickel Vanadium Oxide by SILAR Method: Synthesis and Characterizations**

#### **4.2.A.1 Introduction**

To meet the diverse operational demands in the SC market, electrode materials necessitate high energy and power density, prolonged cycle performance, and cost-effectiveness. Therefore, a straightforward SILAR method was employed to fabricate binder-free NVO thin films on an SS substrate at room temperature, optimizing preparatory parameters like adsorption, reaction, and rinsing duration. This fine-tuning resulted in the production of high-quality NVO thin films. It offers numerous benefits, including a LBL growth pattern, heightened efficiency in utilizing precursors, and a controllable deposition process that facilitates achieving the desired thickness of the film [14]. Following that, thin films of NVO undergo characterizations utilizing

various techniques, including XRD, to investigate structural properties, FT-IR for analyzing chemical bonding, XPS to ascertain oxidation states, BET and BJH for surface area and pore size analysis, FE-SEM to examine micro/nanostructural features of the surface.

So far, this is the very first time a facile SILAR approach has been applied to develop binder-free NVO electrodes and utilized for SC application. Apart from the precursor concentrations, immersion cycles, pH of the cationic and anionic solutions, and bath temperature, the present study emphasizes the influence of rinsing, adsorption/reaction time interval on the growth kinetics, and consequent physicochemical properties of NVO thin film electrodes.

#### **4.2.A.2 Experimental Details**

##### **4.2.A.2.1 Chemicals**

For the synthesis of NVO, nickel nitrate hexahydrate ( $\text{Ni}(\text{NO}_3)_2 \cdot 6\text{H}_2\text{O}$ ) and sodium orthovanadate ( $\text{Na}_3\text{VO}_4$ ) are utilized as a precursor. For the synthesis of rGO, the required chemicals are provided in Chapter III, section A, subsection 3.2.A.2.1. For electrochemical testing, potassium hydroxide (KOH) is utilized.

##### **4.2.A.2.2 Synthesis of nickel vanadium oxide**

The NVO thin films are synthesized via a binder-free SILAR process at ambient temperature. The deposition of NVO was performed on the SS substrates used as the current collector. Briefly, LBL formation of the NVO thin films comprises nickel cations adsorption over SS substrate from the first bath containing 0.05 M of nickel nitrate solution, followed by rinsing in a second beaker containing DDW, where excessive and loosely adsorbed ionic species of nickel were rinsed away. Then, the third beaker contains the 0.05 M solutions of sodium orthovanadate, where the reaction occurs between nickel and vanadium species. Rinsing in DDW is also performed after the formation of the NVO thin layer to eliminate loosely bounded NVO molecules/particles. This entire process is repeated a hundred times to achieve the desired thickness of the NVO thin film, as depicted in Figure 4.1.

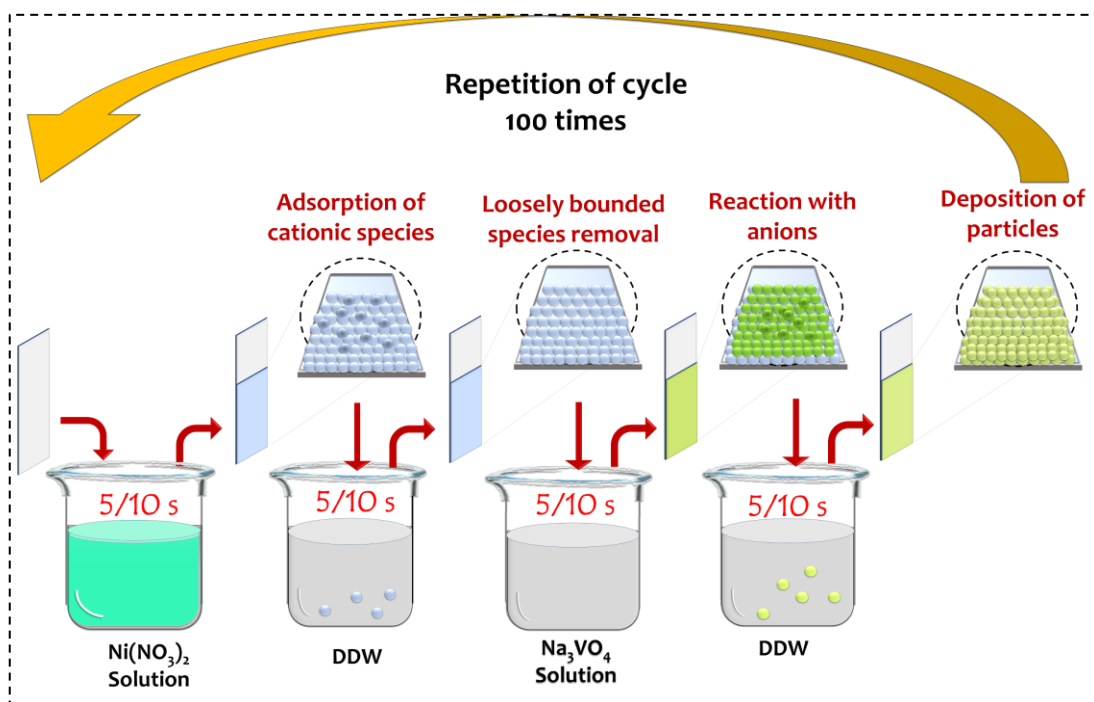


**Figure 4.1:** Schematic diagram of SILAR method for NVO thin film deposition

Furthermore, obtained lively yellow-colored NVO thin films, the photograph shown in Figure 4.2, were rinsed 2 to 3 times in DDW. To investigate the effect of dipping time in adsorption/reaction and rinsing baths on growth kinetics of NVO films, it varied in the ratio of 1:1, 1:2, and 2:1, and termed as S-NV1, S-NV2, and S-NV3, respectively. Furthermore, the thickness of NV series thin films, after 100 cycles. The optimized preparative parameters for the synthesis of NVO are provided in Table 4.1. Unlike other chemical methods, such as co-precipitation and hydrothermal, the sequential LBL assembly of the SILAR process avoids precipitate formation and wastage of material. Finally, the prepared NVO series samples were dried at ambient conditions. The dried NVO series sample was further characterized for structural, morphological, and electrochemical analysis.

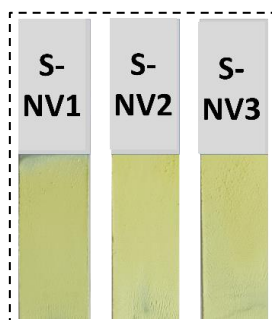


**Figure 4.2:** Photograph of SILAR synthesized NVO thin films for different dipping time

**Table 4.1:** Preparative parameters for the synthesis of NVO thin films and corresponding notations

Sr. No.	Ni(NO <sub>3</sub> ) <sub>2</sub> ·6H <sub>2</sub> O (0.05 M)	DDW	Na <sub>3</sub> VO <sub>4</sub> (0.05M)	DDW	Number of cycles	Notation
1.	5 s	5 s	5 s	5 s	100	S-NV1
2.	5 s	10 s	5 s	10 s	100	S-NV2
3.	10 s	5 s	10 s	5 s	100	S-NV3

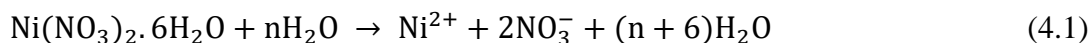
#### 4.2.A.2.3 Material characterizations

The prepared NVO thin films is characterized using various analytical characterization techniques which are provided in chapter III section (3.2.A.2.4).

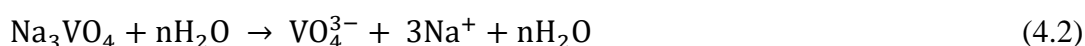
#### 4.2.A.3 Results and discussion

##### 4.2.A.3.1 Film formation and reaction mechanism

The SILAR method employs a series of steps, including the adsorption of cations onto the surface of the substrate, followed by rinsing in ion exchange water. The same water rinsing procedure is pursued after the reaction among pre-adsorbed cations and anions in the anionic solution. Then, the whole process is repeated to increase the thickness of the thin film, as shown in the schematic synthesis procedure of the NVO thin film in Figure 4.1. In SILAR deposition, the layers of cations and anions are consecutively performed to grow nucleated species; the LBL deposition procedure takes place to develop thin films. To carefully control the deposition process, LBL assembly executes the following steps: adsorption of nickel ions produced as per reaction (equation 4.1) from nickel nitrate precursor over SS substrate and removal of excessive ionic species in a pure solvent of DDW in rinsing.

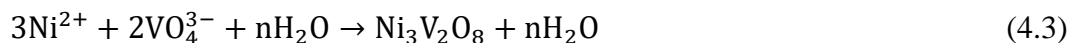


The exact process of rinsing and removing the excessive ionic species is followed even after the pre-adsorbed nickel ions reacted with vanadium ion species obtained as per reaction (equation 4.2) from an anionic precursor containing sodium orthovanadate. The dissolution of sodium orthovanadate in water gives,



Additionally, the reaction is carried out by immersing a substrate with a layer of Ni<sup>2+</sup> ions on it in a precursor solution of sodium orthovanadate, in which a reaction

between vanadium and nickel ions results in the deposition of adherent NVO on the substrate as per the subsequent reaction 4.3,



Apart from the noticeable benefits of high yield and energy-preserving, the leading advantages of the SILAR method are the control over growth kinetics and the film thickness, which can be accomplished by changing adsorption/reaction and rinsing time and changing deposition cycles. The obtained mass loading was quantified by the gravimetric weight difference method by means of the mass per unit area ( $\text{mg cm}^{-2}$ ) over the SS substrate, as shown in Figure 4.3. Change in the deposited weight with variation in dipping time suggests that the thickness of the NVO thin films particularly belongs to the alteration in growth rate, which in the SILAR method is associated with adsorption/reaction along with rinsing periods. As a result, it is found that the S-NV3 achieves a maximum thickness; on the other hand, sample S-NV2 shows less thickness, which concludes that more rinsing time results in lowering the thickness due to the slow growth rate of the material [14, 15]. Hence, the growing rate of NVO material is influenced by the duration of the substrate in cationic/anionic precursor and rinsing solutions, where more rinsing time slows down the growth rate and results in less thickness and vice versa. Therefore, such a change in the growth kinetics of the NVO materials can lead to a change in the physicochemical properties of the material over the SS substrate, and it can influence the electrochemical properties of S-NV series electrodes.

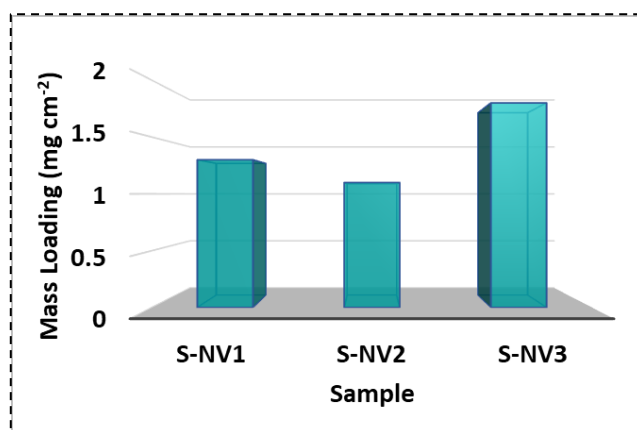


**Figure 4.3:** Plot of mass loading for S-NV1, S-NV2, and S-NV3 samples

#### 4.2.A.3.2 XRD analysis

The structural examination of prepared NVO thin films was performed using

the XRD technique, as shown in Figure 4.4. The XRD patterns of all the S-NV series thin film samples illustrate similar diffraction spectra without any significant peaks from the material, except peaks from the SS substrate. The diffraction peaks highlighted by the emblem (\*) in Figure 4.4 (a) appeared from the SS substrate. The obtained spectra in the range of  $10^\circ$  to  $80^\circ$  do not contain any significant peak of the material. The poor crystallinity of NVO samples resulted from the lack of periodic arrangement of atoms due to the atomic shielding between the nucleated species and adsorbed layers of material [16]. In order to improve the confirmation of the material phase and reduce the possibility of interference from the SS substrate, powdered samples obtained from scratching NVO thin films were subjected to XRD analysis, and resulting XRD patterns are presented in Figure 4.4 (b). Three low crystalline peaks with  $2\theta$  values of  $35.6^\circ$ ,  $44.5^\circ$ , and  $62.4^\circ$  are visible in the XRD patterns of the S-NV series samples. These peaks correspond to the orthorhombic  $\text{Ni}_3\text{V}_2\text{O}_8$  indexed planes (122), (042), and (004), respectively (JCPDS card No. 01-074-1484). Moreover, such a nano-crystalline structure of NVO significantly enhances the electrochemical performance by providing an improved surface area of the material and structural flexibility, allowing deeper diffusion of the electrolyte ions to access the active materials [17].

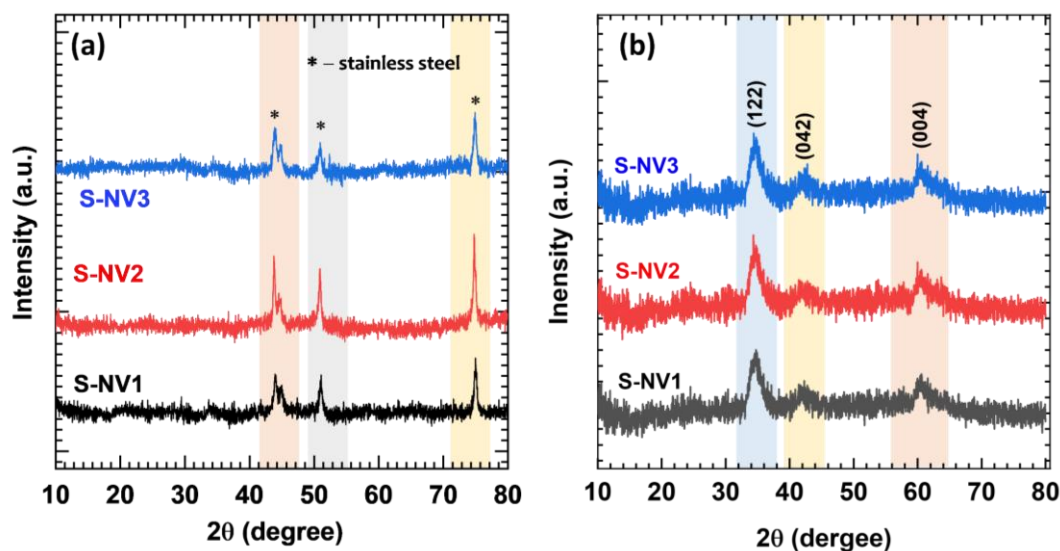


**Figure 4.4:** XRD pattern (a) on SS substrate and (b) Powder sample for S-NV1, S-NV2, and S-NV3

#### 4.2.A.3.3 FT-IR analysis

The presence of various functional groups in the S-NV series samples was

probed by FT-IR analysis, as shown in Figure 4.5. It represents the FT-IR spectra of synthesized S-NV1, S-NV2, and S-NV3 samples in the scanning range of 400 to 4000  $\text{cm}^{-1}$ . As plotted, FT-IR spectra show similar features for all samples, and the band  $\nu_1$  at 476  $\text{cm}^{-1}$  is allocated to Ni-O vibrations (stretching) [18, 19]. Moreover, the occurrence of band  $\nu_2$  at 650 to 950  $\text{cm}^{-1}$  corresponds to the symmetric and antisymmetric stretching of M-O bonding the bond at 693  $\text{cm}^{-1}$  is associated with V-O-V vibrations (antisymmetric stretching) [20]. The presence of a bond around 909  $\text{cm}^{-1}$  is attributed to the symmetric stretching mode of the V=O group [21]. Also, the absorption band  $\nu_3$  related to N-O stretching vibrations is around 1351  $\text{cm}^{-1}$ , obtained from trapped nitrate  $(\text{NO})_3^{2-}$  ions from the precursor [22]. Furthermore, the band  $\nu_4$  at 3429  $\text{cm}^{-1}$  is accredited to the bending and vibrations of the hydroxyl group (H-O-H, stretching), respectively, from structural water entrapped during the rinsing process in the synthesis [23]. Obtained characteristic peaks underscore the presence of structural water content in prepared material. Regardless of the growth rate variation, the FT-IR spectra confirm hydrous NVO material formation in thin films in all S-NV series samples.

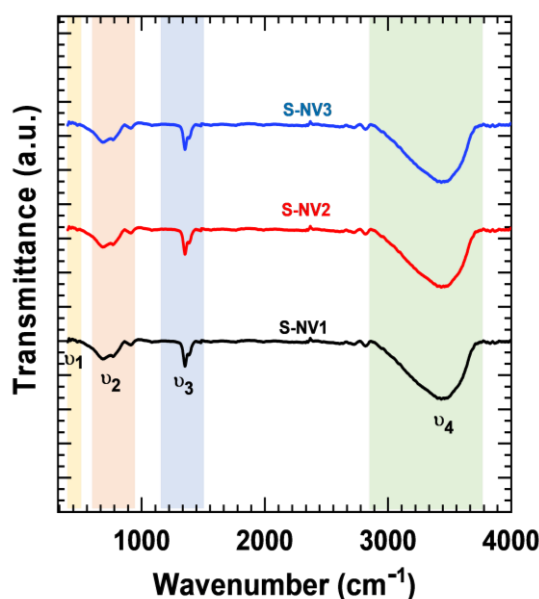


**Figure 4.5:** FT-IR spectra for S-NV1, S-NV2, and S-NV3 samples

#### 4.2.A.3.4 XPS analysis

The detailed chemical oxidation states of each element contained in the S-NV series sample were uncovered by XPS analysis. Observing Ni, V, and O elements in the XPS survey spectrum for the S-NV2 sample (Figure 4.6 (a)) indicates the presence



of the elements, as mentioned earlier, on the surface of the NVO samples. As illustrated in Figure 4.6 (b), Ni 2p has two leading spectral peaks, which rise from the spin-orbit splitting at a binding energy of 855.58 and 873.28 eV and are termed Ni 2p<sub>3/2</sub> and Ni 2p<sub>1/2</sub>, respectively. The two prominent peaks of Ni 2p<sub>3/2</sub> and Ni 2p<sub>1/2</sub> are separated by a 17.7 eV binding energy difference along with better-christened ‘satellite peaks’ at energies of 861.28 and 879.58 eV.

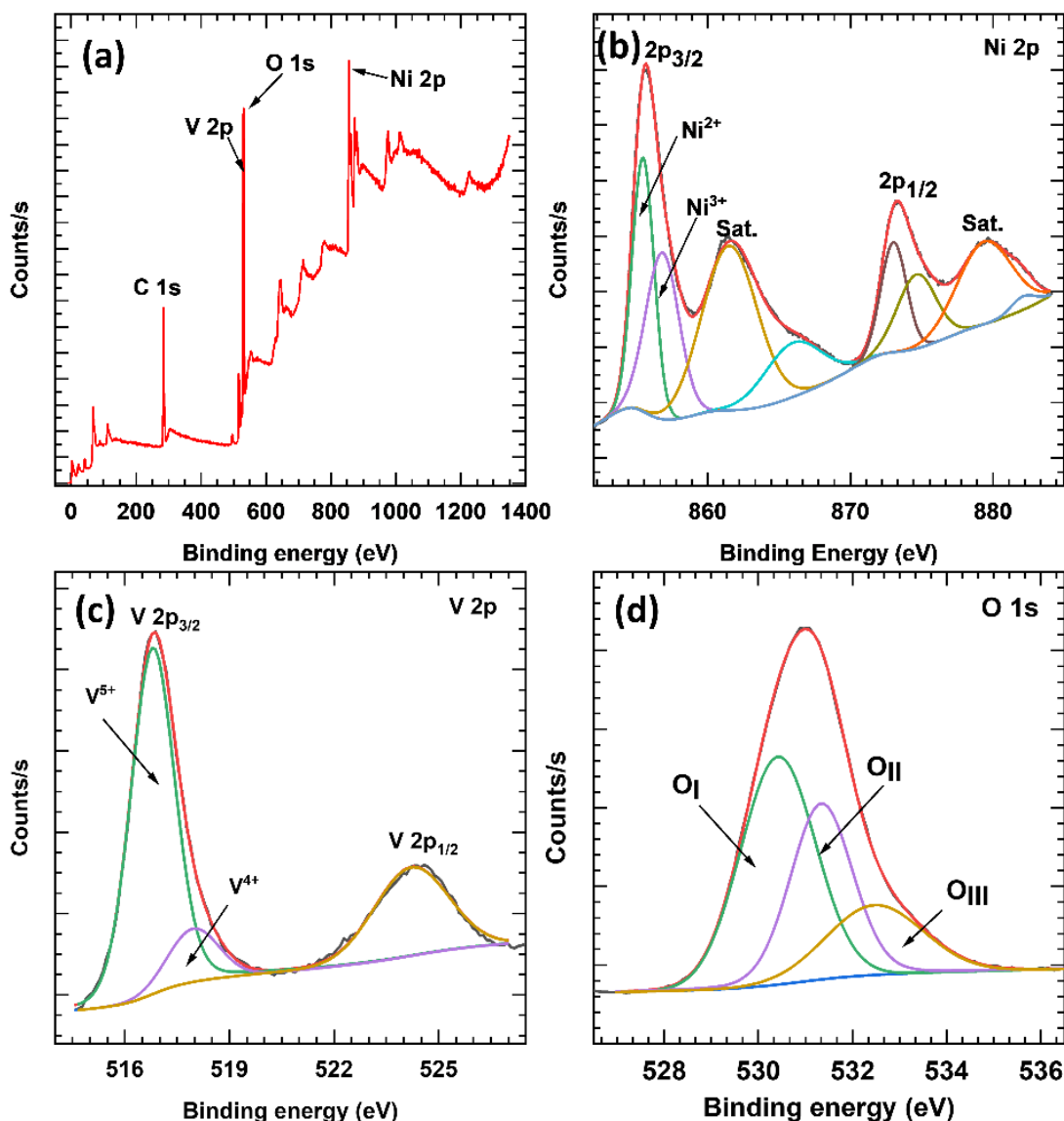


**Figure 4.6:** XPS spectra for S-NV2 sample (a) survey spectrum, (b) Ni 2p, (c) V 2p, and (d) O 1s

The peaks reveal the presence of Ni<sup>2+</sup> and Ni<sup>3+</sup> species [23, 24], which confirms the divalent and trivalent states of nickel in bulk and near the surface of NVO material, respectively. The fitted spectra of V 2p, as shown in Figure 4.6 (c),

demonstrated two peaks at a binding energy of 517.88 and 524.28 eV are designated to  $V^{5+}$  state, and the formfitting peak at a binding energy of 516.78 eV represents the  $V^{4+}$  state [25–27]. The presence of 2+ and 5+ states of nickel and vanadium, respectively, validate the formation of the  $Ni_3V_2O_8$  phase in NVO thin film. The deconvoluted O 1s spectra for all NVO series samples are demonstrated in Figure 4.6 (d). The decomposition of O 1s peaks in three parts manifests the different environments of oxygen in the samples. The peak located at a binding energy of 530.48 eV is attributed to the lattice oxygen ( $O_I$ ), whereas the peak situated at 531.58 eV corresponds to the oxygen vacancies ( $O_{II}$ ) and at 533.18 eV assigned to the adsorbed water ( $O_{III}$ ) [28, 29]. In addition to providing electroactive sites for redox processes, oxygen vacancies can significantly increase conductivity by facilitating the transit of charge barriers [30]. Moreover, the deconvolution of O 1s spectra affirms the presence of hydrous content in NVO samples and confirms the deposition of hydrous NVO ( $Ni_3V_2O_8 \cdot nH_2O$ ) in thin films over SS substrate.

#### 4.2.A.3.5 FE-SEM analysis

The surface morphologies were recorded at different magnifications (X5K and X40K) of the NVO thin films and are shown in Figure (4.7 ( $a_1$ ,  $a_2$ ), ( $b_1$ ,  $b_2$ ), ( $c_1$ ,  $c_2$ )). The overview of FE-SEM images at lower magnification (Figure 4.7 ( $a_1$ ), ( $b_1$ ), and ( $c_1$ )) demonstrated the congested spherical nanoparticle-like morphology decorated over conducting plate of SS. Besides, randomly decorated particles are entwined, creating large cavities and void space. Obtained voids and cavities in the surface texture are more beneficial by providing a lower diffusion length for the migration of ions [31]. The agglomeration of spherical nanoparticles is observed in FE-SEM images recorded at higher magnification, as displayed in Figure 4.7 ( $a_2$ ), ( $b_2$ ), and ( $c_2$ )).

The calculated average particle size is found to be an average diameter of 120, 101.4, and 167.1 nm for samples S-NV1, S-NV2, and S-NV3, respectively, as histograms displayed in Figure 4.7 ( $a_3$ ,  $b_3$ ,  $c_3$ ). This difference in the average particle size reveals the impact of alteration in the duration of adsorption/reaction and rinsing time in their respective baths and the subsequent change in growth rate. The slow growth rate of NVO particles reduces the size of the particles when the rinsing time is twofold that of the adsorption and reaction duration. Relatively higher and sufficient time for rinsing of ions in DDW, lowering the particle size by removing most loosely bounded or unreacted species. In contrast, comparatively large particle size is observed

while the adsorption/reaction period was twice that of rinsing in DDW owing to the agglomeration of the particles due to increased growth rates of film formation. Thus, FE-SEM analysis confirms that the growth rate variation by dip time adjustment significantly alters the morphology of NVO thin film electrodes, which can influence the electrochemical performance.

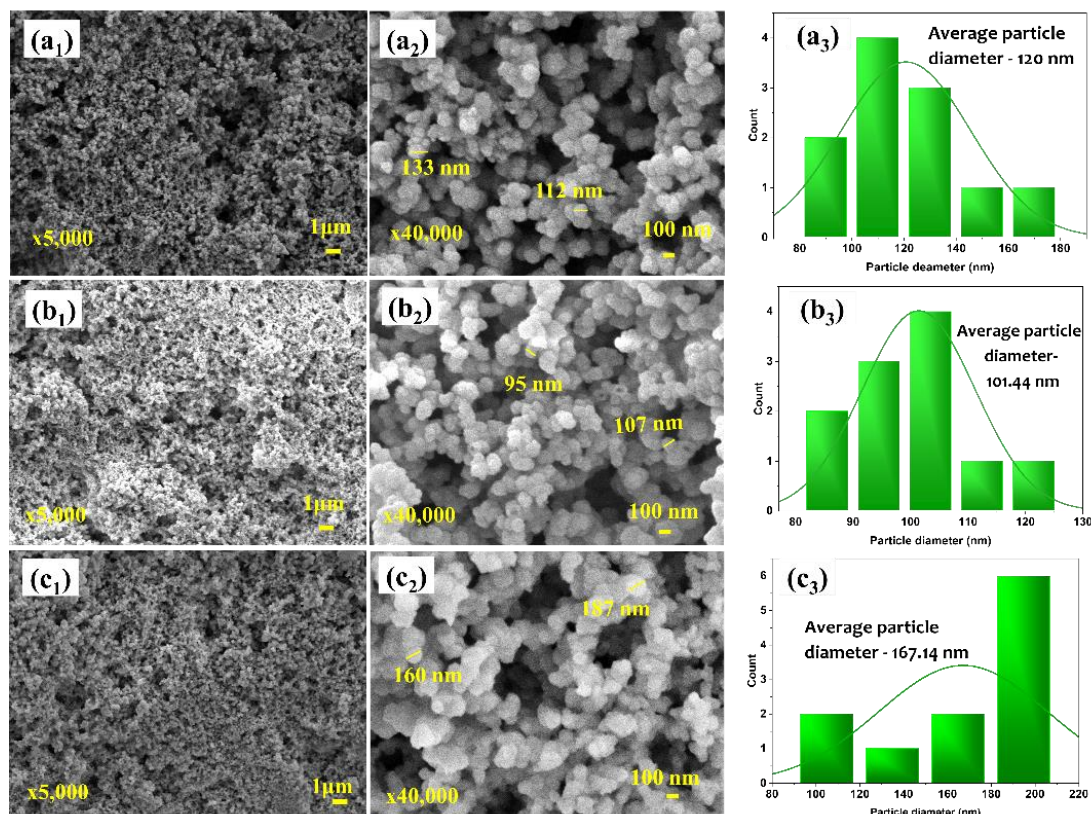


**Figure 4.7:** FE-SEM images of sample (a<sub>1</sub>, a<sub>2</sub>) S-NV1, (b<sub>1</sub>, b<sub>2</sub>) S-NV2, and (c<sub>1</sub>, c<sub>2</sub>) S-NV3 at the magnification of X5K and X40K, respectively, and (a<sub>3</sub>, b<sub>3</sub>, c<sub>3</sub>) histograms of particles size distribution

Moreover, the elemental mapping images displayed in Figure 4.8 demonstrate the uniform distribution of Ni, V, and O elements of NVO thin film over the SS substrate. These EDS mapping results indicate the successful hydrous NVO series thin film electrode preparation.



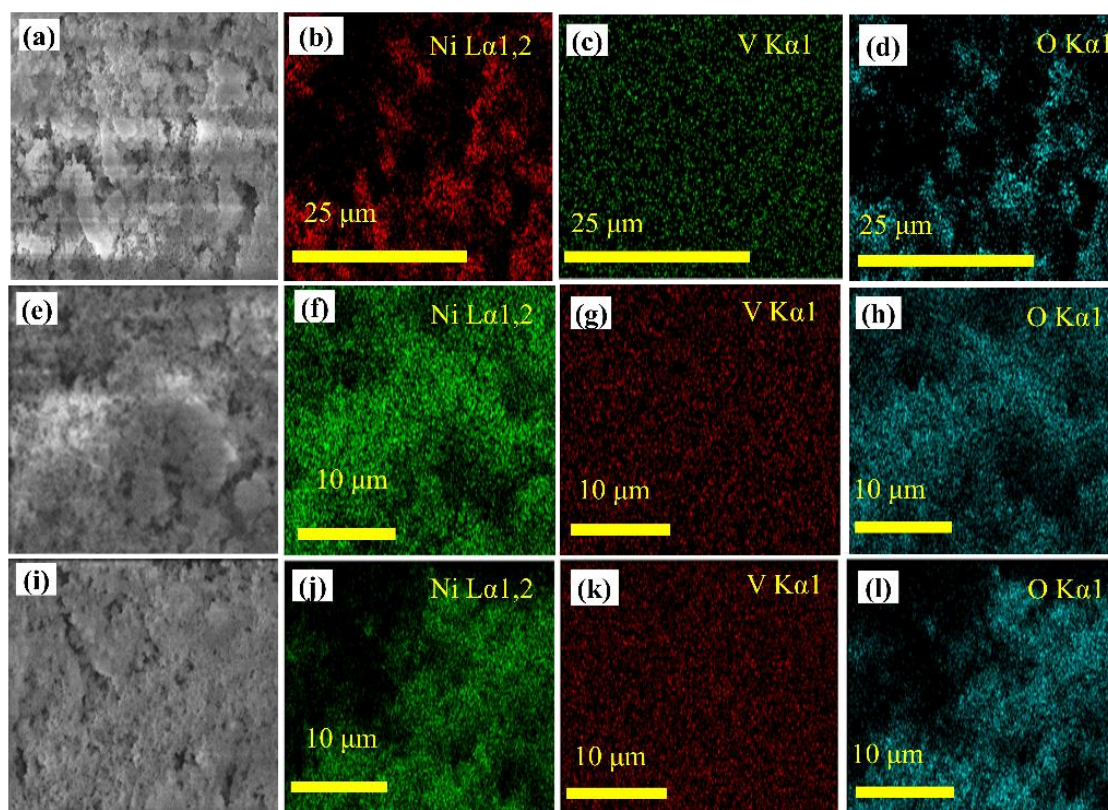


**Figure 4.8:** Elemental mapping of the sample (a-d) S-NV1, (e-h) S-NV2 and (i-l) S-NV3

#### 4.2.A.3.6 HR-TEM analysis

The HR-TEM images of the S-NV2 sample presented in Figure 4.9 (a) reveal agglomerated spherical particles of NVO. Moreover, the HR-TEM image displays interconnected spherical particles with an average size of  $\sim 102.2$  nm, and Figure 4.9 (b) demonstrates that the merged spheres are composed of clusters of quantized particles. The interplanar distance is tailored using the digital microscopy software and determined through the analysis of line profiles observed at higher magnification, as shown in Figure 4.9 (b). The margins of the crystalline fringes are discontinuous (Figure 4.9 (d)), resulting in a significant number of defects, which are more beneficial in increasing the material's conductivity [32]. The observed lattice fringes are depicted in Figure 4.9 (e), and the measured lattice distance is 0.24 nm for the S-NV2 sample, affirming the existence of (122) crystalline planes within respective samples, which is in association with XRD analysis. Furthermore, the SAED patterns are presented in Figure 4.9 (f), showing unclear but ordered rings, confirming the lower crystallinity with polycrystalline characteristics of the material. The obtained rings in the SAED pattern confirm the existence of (122) crystalline planes of NVO [33].

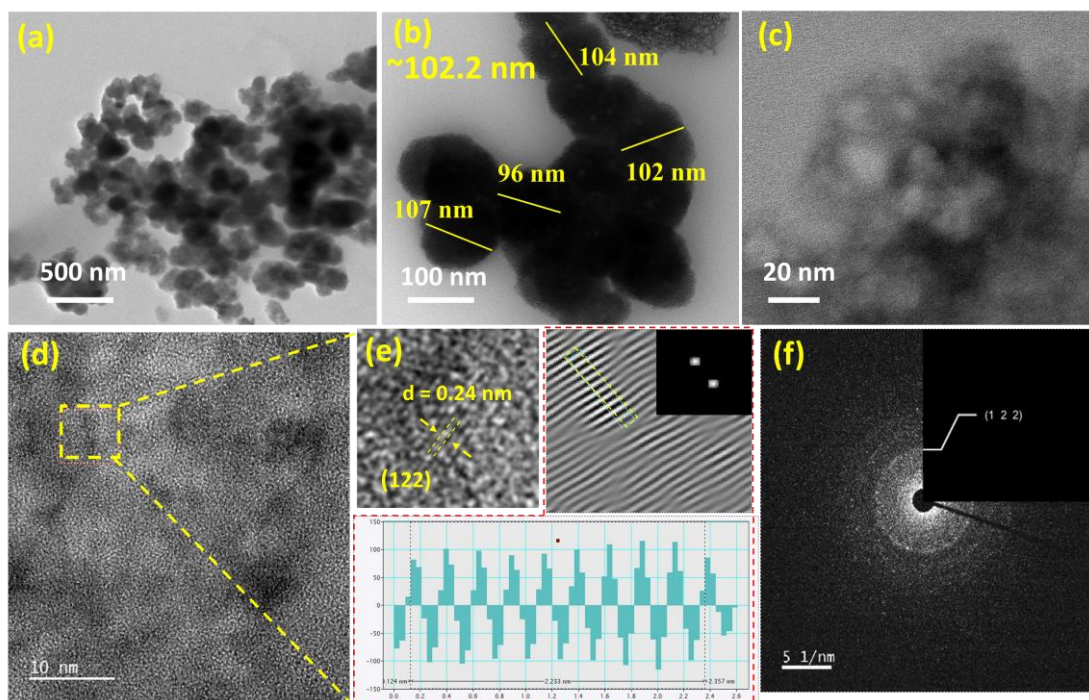


**Figure 4.9:** (a-d) HR-TEM images, (e) Lattice distortion images and interplanar distance calculations from the HR-TEM images, and (f) SAED patterns for the S-NV2 sample

#### 4.2.A.3.7 BET and BJH analysis

The BET and BJH measurements were performed to probe the influence of growth rate variation on the surface area and porosity of deposited S-NV series samples. The plots of  $N_2$  adsorption-desorption isotherms (at 77 K liquid nitrogen) and BJH pore size distribution are displayed in Figure 4.10 (a-c), and obtained  $N_2$  adsorption-desorption isotherms of all S-NV series samples display an H3-type hysteresis loop, endorsing the existence of aggregated particles [34]. The assessment of the specific surface area is found to be 147.1, 167.6, and 117.2  $m^2 g^{-1}$  for S-NV1, S-NV2, and S-NV3 series samples, respectively. The obtained specific surface area of 167.6  $m^2 g^{-1}$  of the S-NV2 sample is higher than ever achieved for NVO materials prepared by different synthetic methods [7, 10–12]. Additionally, the mesoporous structure of NVO samples is confirmed from the pore size distribution BJH analysis, as displayed in the inset of Figure 4.10 (a-c). The BJH plots display the average pore size distribution of 7.6, 6.9, and 9.7 nm for S-NV1, S-NV2, and S-NV3 samples, respectively. The deviations in specific surface area and pore size are observed due to fluctuations in the growth kinetics of the material. Consequently, the obtained change in the surface area agrees with the alteration in the surface morphology of NVO

samples. The relatively higher surface area is attributed to the smaller particle diameter with a pore size of 6.9 nm owing to the slower growth kinetics of S-NV2 thin film. Moreover, the high surface area with the mesoporous structure having shortened pore diameter can introduce hierarchical channels to contact the electrolyte and easy ion diffusion in the deep pore of the particles [35, 36].

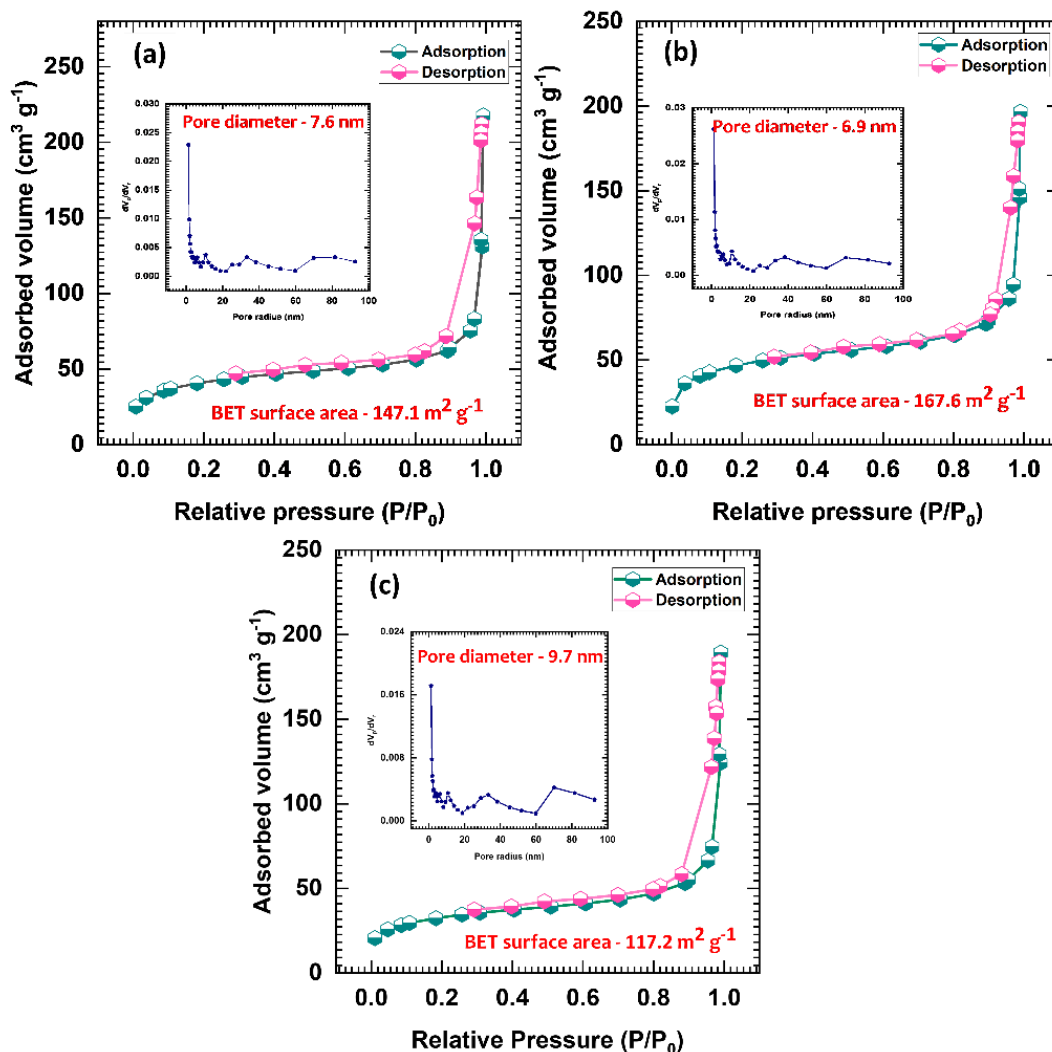


**Figure 4.10:** Nitrogen adsorption/desorption isotherm of (a) S-NV1, (b) S-NV2, and (c) S-NV3 (inset: pore size distribution)

The overall physicochemical analysis concludes that the surface area and porous structure of the NVO samples correspond to changes in surface morphology and average particle size, and varying growth rates can tune it via changing dip time intervals for adsorption/reaction and rinsing in the SILAR method. In this attempt, the dipping interval of the substrate in cationic/anionic precursor and rinsing baths is varied to achieve different growth kinetics as slow (1:2), intermediate (1:1), and fast



(2:1) growth rates. When the rinsing time is twice, the adsorption and reaction time (S-NV2) and ion-by-ion growth kinetics are slow, where particle size reduces since a sufficiently excess rinsing time avoids the agglomeration of particles and results in smaller particle size. On the other hand, rapid growth is observed for the larger/equal time to adsorption/reaction than rinsing of S-NV1 and S-NV3 samples, resulting in relatively larger particles than S-NV2 samples. The increasing growth rates of NVO material led to the formation of relatively bigger particles due to the SILAR synthesis approach; the dipping time variation primarily results in the controlled growth and size of the particles, which aids in tuning the surface area of the material and consequently may electrochemical performance.

#### 4.2.A.3.8 Electrochemical performance

The influence of dipping time on the structure and morphology and its consequent impact is further scrutinized for electrochemical measurements. The three-electrode electrochemical cell system is applied (as described in section Chapter III, subsection 3.2.A.3.7) to examine the electrochemical performance of as-deposited NVO thin film as a working electrode. More details about the required formulae for capacitive performance calculation are given in Chapter II, section 2.5.

##### (a) CV analysis

The comparative CV curves are displayed in Figure 4.11 (a) for S-NV1, S-NV2, and S-NV3 electrodes in the optimized potential window of 0 to 0.7 V vs Hg/HgO at a 20 mV s<sup>-1</sup> scan rate. The elevated area of the CV curve for the S-NV2 electrode leads to a higher charge-storing capacity than the other two electrodes, implying a good correlation between specific surface area and CV curves. The CV curves of the NVO thin film electrode at various scan rates from 2 to 50 mV s<sup>-1</sup> are shown in Figure 4.11 (b-d). The increasing trend of the area under CV curves with scan rate infers the battery-type behavior of NVO material. In the redox process, a greater scan rate causes ion depletion or saturation in the electrolyte inside the electrode, which mainly raises ionic resistance [37]. The observed CV curves are associated with two different domains; a couple of oxidation-reduction peaks are obtained in the region from 0.35 to 0.7 V, mainly associated with the reversible transition of Ni<sup>2+</sup> to Ni<sup>3+</sup> and the remaining part in region 0 to 0.35 V of the CV curve point toward the transfer of double layer charges. During the intercalation and deintercalation of electrolytic ions,



reversible redox reactions occur according to the reaction provided in Chapter III, section 3.2.A.3.7, equation 3.4.

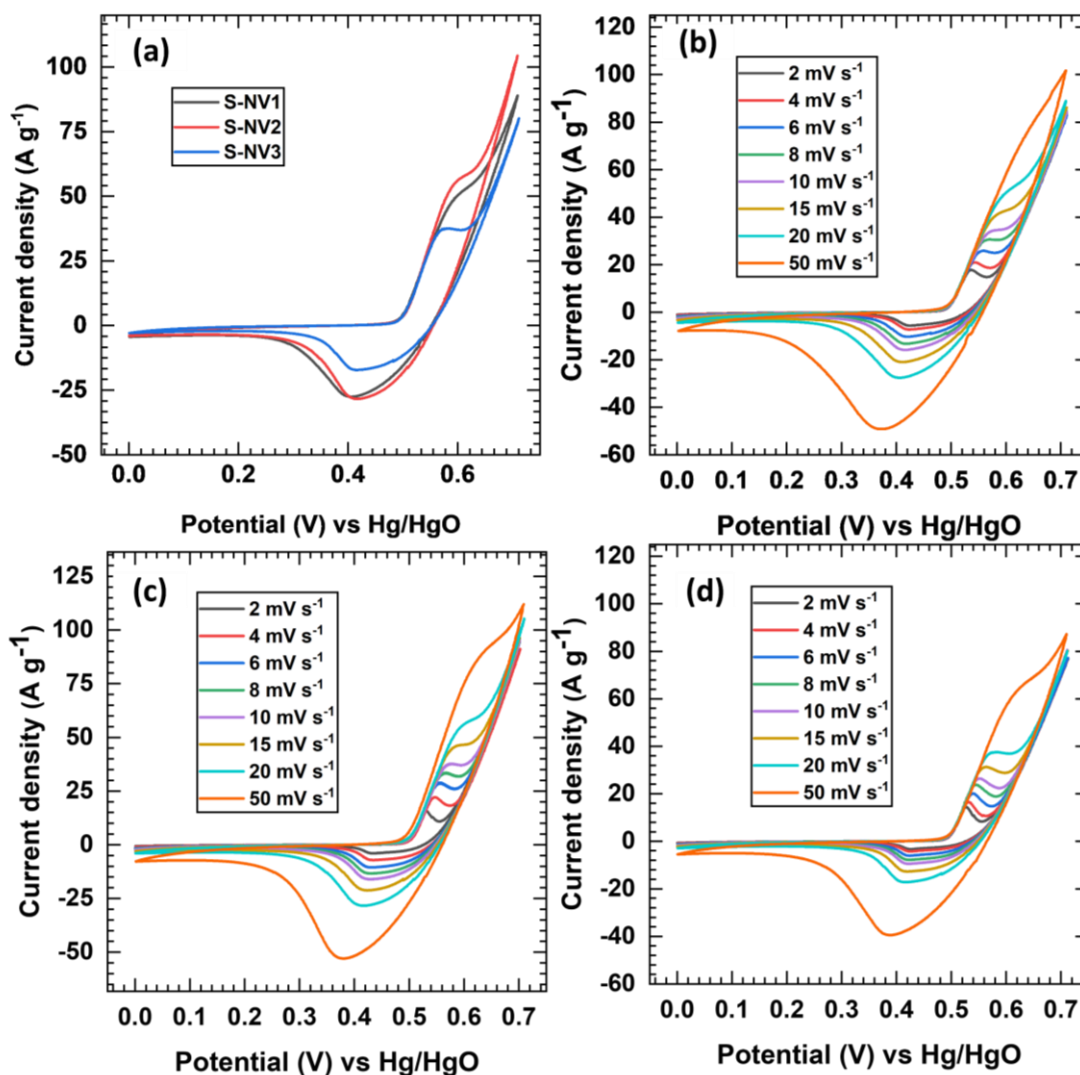


**Figure 4.11:** (a) Comparative CV curves at 20 mV s<sup>-1</sup> scan rate of NV series electrodes, CV curves at various scan rates from 2 to 50 mV s<sup>-1</sup> (a) S-NV1, (b) S-NV2, and (c) S-NV3

The CV curve provides more insights into understanding the charge storage mechanism quantitatively. The 'b' parameter can be determined from the slope of log ( $i_{\text{peak}}$ ) vs. log ( $v$ ) (Figure 4.12) graph. In contrast, S-NV series electrodes exhibited b values of approximately 0.5, suggesting that the battery type diffusive process contributed to store charges.

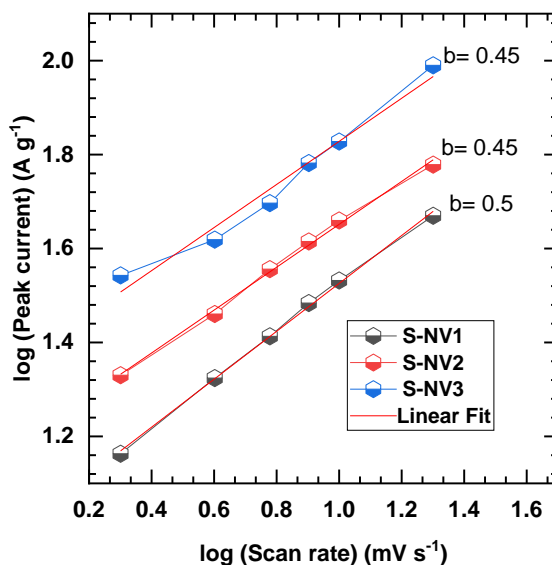


**Figure 4.12:** Plot of  $\log$  (peak current,  $\text{A g}^{-1}$ ) vs  $\log$  (scan rate,  $\text{mV s}^{-1}$ ) for S-NV series electrodes

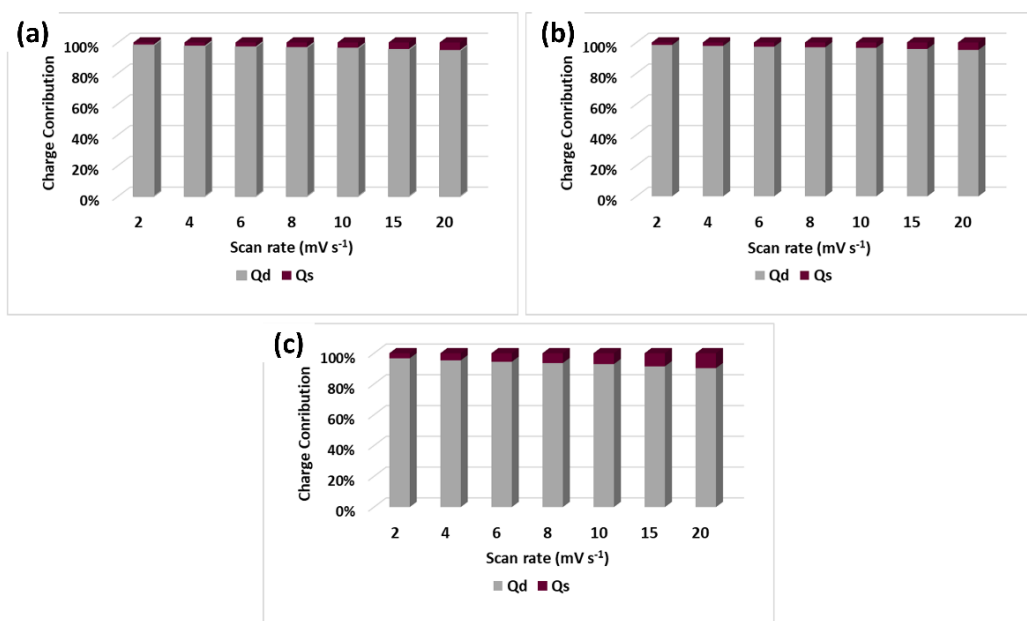


**Figure 4.13:** The plot of surface and diffusive charge contribution with respect to scan rate for (a) S-NV1, (b) S-NV2, and (c) S-NV3 electrodes

Further, total volumetric charge ( $Q_t$ ) differentiates into capacitive ( $Q_s$ ) and diffusive ( $Q_d$ ) behaviors. Figure 4.13 provides a graphic illustration of the scan rate-dependent current response. The charge contribution against the scan rate strikes a similar charge storage mechanism. The overall contribution indicates more diffusive battery-type charge storage; however, increasing the scan rate provides a slight capacitive behavior. Thus, at a scan rate of  $2 \text{ mV s}^{-1}$ , diffusive contribution accounts

for 98%, whereas it is decreased to 95% at  $20 \text{ mV s}^{-1}$  for the S-NV2 electrode. In addition, comparatively more surface contribution charge storage is achieved by the S-NV3 electrode, which decreases from 9% to 4% with scan rate lowering from 20 to  $2 \text{ mV s}^{-1}$ , respectively. From CV analysis it is concluded that the S-NV2 electrode shows superior electrochemical behavior than S-NV1 and S-NV3 electrodes.

#### (b) GCD analysis

GCD analysis provides more insights to evaluate the  $C_{sp}$  of the S-NV series electrodes. Figure 4.14 (a) presented comparative GCD curves measured at a current density of  $1 \text{ A g}^{-1}$  for S-NV series electrodes. It is observed that the obtained GCD profiles for all samples are similar voltage plateaus and are analogues to CV curves.

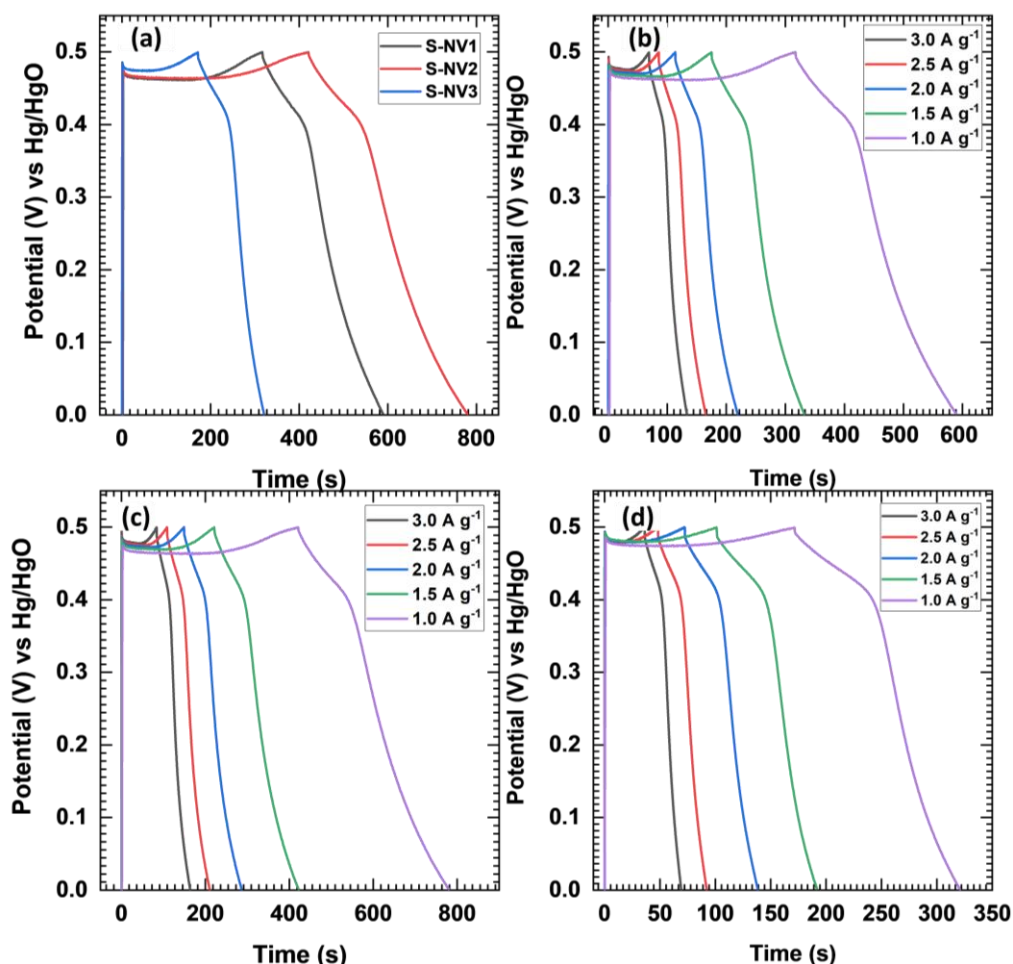


**Figure 4.14:** (a) Comparative GCD curves of S-NV series electrodes at  $1 \text{ A g}^{-1}$  current density, GCD curves at various current densities from 1 to  $3 \text{ A g}^{-1}$  of (b) S-NV1, (c) S-NV2, and (d) S-NV3 electrodes

The battery-type behavior of GCD curves with a minor voltage drop further points out the reversible nature and superior conductivity of the S-NV materials [38].

The GCD profiles at different current densities (1.0-3.0 A g<sup>-1</sup>) obtained for the S-NV series electrode are illustrated graphically in Figure 4.14 (b-d). The maximum  $C_{sp}$  is calculated and found to be 710 F g<sup>-1</sup> at 1 A g<sup>-1</sup> current density for the S-NV2 electrode. Also, calculated values of  $C_{sp}$  for S-NV1 and S-NV3 electrodes are 552 F g<sup>-1</sup> and 300 F g<sup>-1</sup>, at 1 A g<sup>-1</sup> respectively, as shown graphically in Figure 4.15.

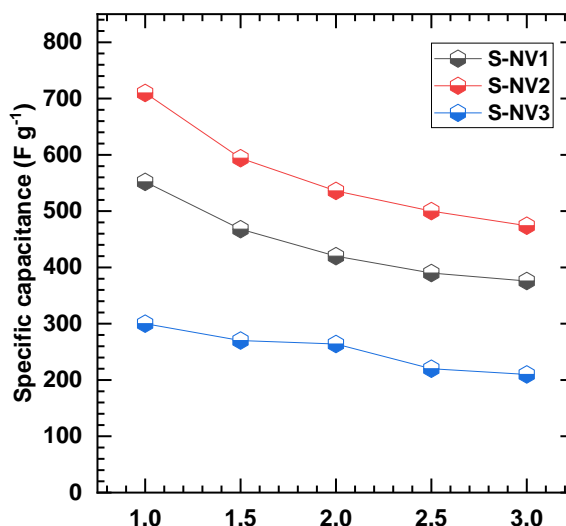


**Figure 4.15:** The plot of current density as a function of  $C_{sp}$  for S-NV1, S-NV2, and S-NV3 electrodes

### (c) EIS analysis

EIS is quantitatively analyzed to extract more information related to the electrical and ionic conductivity of the electrode material and electrolyte. The Nyquist plots for S-NV series samples are shown in Figure 4.16. The experimental data of the Nyquist plot were fitted with a selected equivalent model, and the fitted parameters are provided in Table 4.2. The diameter of the semicircle determines the  $R_{ct}$  values, and these are 0.32, 0.09, and 0.72  $\Omega \text{ cm}^{-2}$  for S-NV1, S-NV2, and S-NV3 electrodes, respectively. Also, a slightly vertical line to the imaginary axis at the lower frequency region with a phase angle of close to 90° suggests capacitive behavior and complete diffusion of ions in the results in W impedance. Also, the low  $R_{ct}$  value of the S-NV2 electrode leads to a high capacitance of the NVO electrode owing to the spontaneous electrochemical reaction among the electrolyte and active electrode material due to its high surface area and mesoporous structure. Furthermore, the smaller  $R_s$  and  $R_{ct}$  values of S-NV series electrodes suggest an excellent attachment (binder-free) of active material with a current collector (SS substrate).

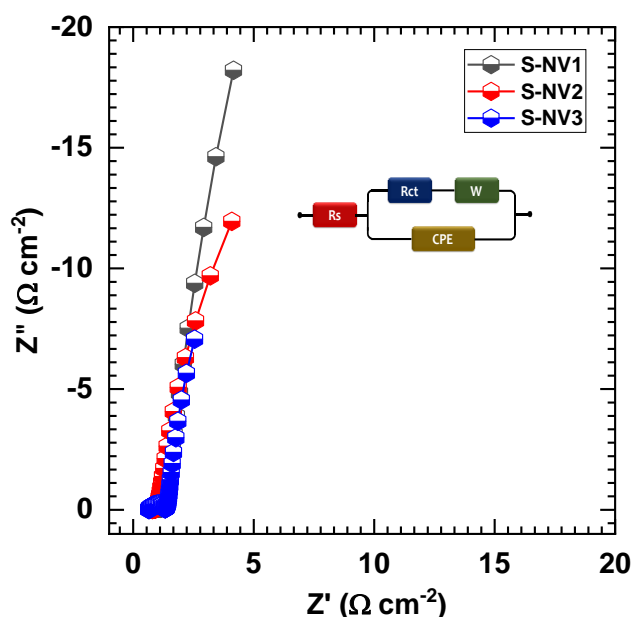


**Figure 4.16:** The Nyquist plots of S-NV1, S-NV2, and S-NV3 electrodes and the fitted equivalent circuit for the EIS data is an inset of figure

**Table 4.2:** Electrochemical impedance spectroscopic fitted circuit parameters for Nyquist plots of S-NV1, S-NV2, and S-NV3 electrodes

Fitted Parameters	S-NV1	S-NV2	S-NV3
$R_s$ ( $\Omega \text{ cm}^{-2}$ )	0.79	0.80	0.64
$R_{ct}$ ( $\Omega \text{ cm}^{-2}$ )	0.32	0.95	0.72
$W$ ( $\Omega \text{ cm}^{-2}$ )	0.45877	0.4491	0.45651
$CPE-T$ ( $\text{mF cm}^{-2}$ )	1.38	0.21	0.51
$CPE-P$ (n)	0.85	0.87	0.71

#### (d) Stability analysis

The cyclic stability and coulombic efficiency of the NVO electrode (S-NV2) for 5000 cycles were carried out at a current density of  $3 \text{ A g}^{-1}$  and provided in Figure 4.17. The S-NV2 electrode exhibits  $\sim 92\%$  capacitive retention with 96% coulombic efficiency over 5000 GCD cycles and an increase of coulombic efficiency and stability after initial cycles attributed to the activation of material by means of opening the pores.

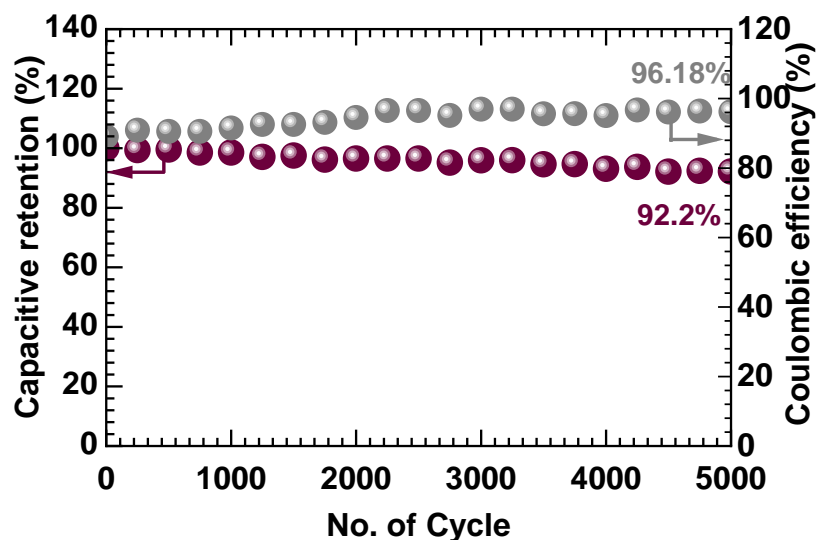


**Figure 4.17:** Plot of capacitive retention and coulombic efficiency versus number of cycles

#### 4.2.A.4 Conclusions

Overall, the mentioned aspects of binder-free, mesoporous, hydrous, nanocrystalline NVO spherical particles prepared through the SILAR method significantly contributed to enhanced electrochemical performance SCs. In the first place, the thin film electrode engineering strategy by the SILAR method with an optimized growth rate possesses a higher surface area ( $167.2 \text{ m}^2 \text{ g}^{-1}$ ) and mesoporous structure due to a reduced average particle size (101.4 nm), provides abundant electroactive sites for charge storage. The S-NV2 sample electrode exhibited a maximum  $C_{sp}$  of  $710 \text{ F g}^{-1}$ . Less EIS values in terms of  $R_s$  and  $R_{ct}$  are attributed to the binder-free synthetic approach and the excellent interface of hydrous NVO material with electrolyte. Moreover, structurally disordered nanocrystalline NVO particles provide more active sites with structural flexibility that increase the electrochemical performance in terms of electrode storage capacity and stability. In conclusion, SILAR is a feasible approach to producing NVO thin films with high electrochemical performance and further rGO can be introduced to the optimized S-NV2 electrode to improve the performance.

### 4.3 Section B

## Nickel Vanadium Oxide/rGO composite by SILAR Method: Synthesis and Characterizations

### 4.3.B.1 Introduction

Graphene and its derivatives represent a highly promising option as a conductive framework for hybrid materials due to their exceptional structure and distinct physical properties. The production process of rGO allows for the development of composite materials using diverse chemical redox pathways [39]. Recently, several publications have highlighted the utilization of rGO in electrochemical ESDs and Numerous hybrid materials have undergone study, including TMOs like CoO, NiO, Co<sub>3</sub>O<sub>4</sub>, NiCo<sub>2</sub>O<sub>4</sub> [40–42], transition metal phosphide such as ZnP, NiP, CoP [43, 44], and transition metal molybdate, MnNiMoO<sub>4</sub> [45]. Interestingly, only a few reports are available on the NVO composite with GO and rGO [46-48] using hydrothermal and solvothermal methods.

In present study, NVO/rGO composite was synthesized using the simple SILAR method. The study focuses on examining the impact of varying concentrations of rGO on the physico-chemical properties and their influence on electrochemical properties. The synthesis involved creating pristine NVO and NVO/rGO composites at different concentrations of rGO (0.025, 0.050, 0.075, 0.1, and 0.125 mg ml<sup>-1</sup>). The electrochemical properties of NVO/rGO materials were thoroughly compared to determine the most effective material for the intended purpose.

### 4.3.B.2 Experimental details

#### 4.3.B.2.1 Synthesis of reduced graphene oxide

The GO was prepared using a modified Hummer's method, and further, it was reduced using hydrazine hydrate. The detailed synthesis of GO and rGO is discussed in Chapter 3, Section B, Subsection 3.3.B.2.1.

#### 4.3.B.2.2 Synthesis of nickel vanadium oxide/reduced graphene oxide composite thin films

The SILAR stands as a cost-effective and facile method for the deposition of composite thin films. The synthesis of NVO/rGO composite thin films developed at room temperature and is depicted schematically in Figure 4.18. The procedure for the



synthesis of pristine NVO thin films has been detailed in section A, subsection 4.2.A.2.2.

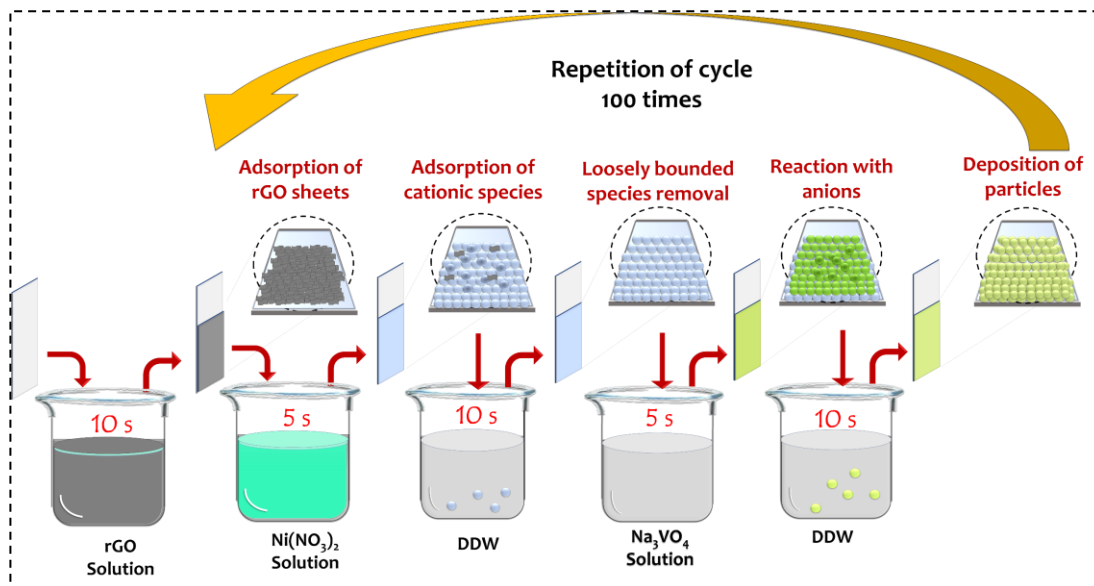


**Figure 4.18:** Schematic representation of SILAR deposition for the NVO/rGO composite thin films

For the synthesis of NVO/rGO, composite five-beaker system is used, starting with the addition of a 50 ml beaker containing rGO prior to the discussed SILAR system for the preparation of S-NV2 thin film. The effect of variation in rGO content was studied by varying the concentration of rGO.

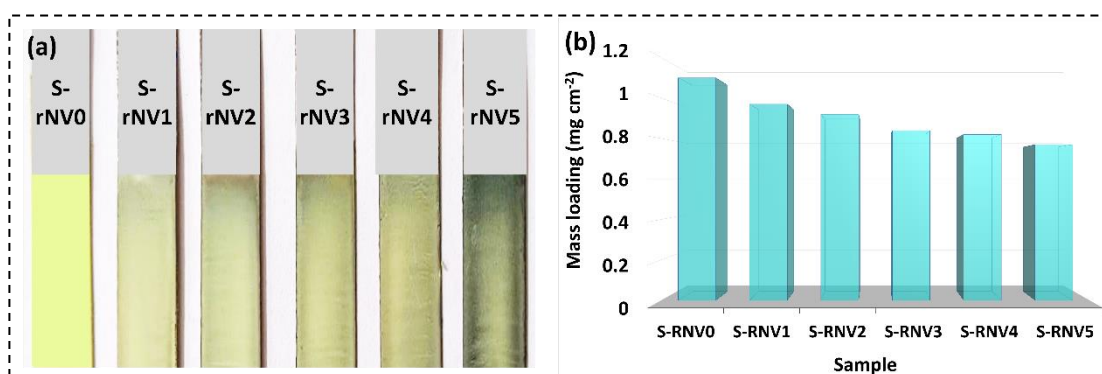


**Figure 4.19:** (a) Photograph of deposited S-rNV series thin films, and (b) Mass loading per unit area of S-rNV series samples

The substrate was dipped in the rGO solution for a fixed time of 10 seconds and previously optimized parameters for S-NV2 were utilized to ensure the production of well-adherent and uniform films. Herein, the concentration of rGO varied as 0, 0.025, 0.05, 0.075, 0.1, and 0.125 mg ml<sup>-1</sup>, and prepared samples were termed S-rNV0, S-rNV1, S-rNV2, S-rNV3, S-rNV4, and S-rNV5, respectively (other

preparative parameters are provided in Table 4.3) and photographs of deposited thin films are illustrated in Figure 4.19 (a). Mass loading per unit area was calculated using the mass difference method and depicted in Figure 4.19 (b). The figure demonstrates that, with the increasing content of rGO the mass loading of material decreases, owing to the lower density of rGO and distinct growth rate of composite material.

**Table 4.3:** Preparative parameters for the synthesis of NVO/rGO thin films and corresponding notations

rGO (mg ml <sup>-1</sup> )	Ni(NO <sub>3</sub> ) <sub>2</sub>	Na <sub>3</sub> VO <sub>4</sub>	Number of cycles	Notation
0	0.05M	0.05M	100	S-rNV0
0.025	0.05M	0.05M	100	S-rNV1
0.050	0.05M	0.05M	100	S-rNV2
0.075	0.05M	0.05M	100	S-rNV3
0.10	0.05M	0.05M	100	S-rNV4
0.125	0.05M	0.05M	100	S-rNV5

#### 4.3.B.2.3 Material Characterizations

The characterization techniques outlined in Chapter III, Subsection 3.2.A.2.4 and 3.4.C.2.3 were utilized to assess the NVO/rGO composite thin film electrodes.

#### 4.3.B.3 Result and discussion

##### 4.3.B.3.1 Thin film formation

To prepare NVO/rGO composite material SILAR method with an LBL approach was utilized. To examine the effect of different rGO concentrations on the pristine sample S-rNV0, a series of NVO/rGO composite materials, termed the S-rNV series, were produced. In the first stage, Ni<sup>2+</sup> ions adhere to the surface of rGO due to electrostatic interactions with the functional groups present. After an initial rinsing, the vanadate (VO<sub>4</sub>)<sup>2-</sup> ions present in the anionic bath solution react to form NVO on the rGO, as represented by the reaction (equation 4.3). Following the establishment of this layer, the next SILAR cycle involves depositing another layer of rGO onto the pre-formed NVO layer. This alternating deposition process of NVO and rGO layers continues for up to 100 SILAR cycles, which is illustrated schematically in Figure

4.18. The S-rNV series electrodes that were synthesized were subsequently subjected to physicochemical analysis.

#### 4.3.B.3.2 XRD analysis

The XRD analyses of NVO/rGO composite featuring various rGO concentrations, as presented in Figure 4.20 (a), earlier findings highlighted in section A, subsection 4.2.A.3.2. Sample S-NV2 displayed a nanocrystalline nature, and no characteristic peak is observed for the NVO. Similarly, all prepared composites (S-rNV0, S-rNV1, S-rNV2, S-rNV3, S-rNV4, and S-rNV5) showcased only peaks for the SS substrate. To further mitigate the potential interference of SS substrate, the XRD patterns of powdered samples were carried out and are plotted in Figure 4.20 (b). The obtained XRD patterns of S-rNV series samples show the three distinct low crystalline peaks at  $2\theta$  values of  $35.6^\circ$ ,  $44.5^\circ$ , and  $62.1^\circ$  corresponding to the indexed planes (122), (042), and (004), respectively, of orthorhombic  $\text{Ni}_3\text{V}_2\text{O}_8$  (JCPDS card No. 01-074-1484). Along with this, the broad hump observed between angles  $2\theta=24^\circ$  signifies the multilayered rGO nanosheets exhibiting (002) plane. The XRD results confirm the successful incorporation of rGO into NVO thin films by the SILAR method.

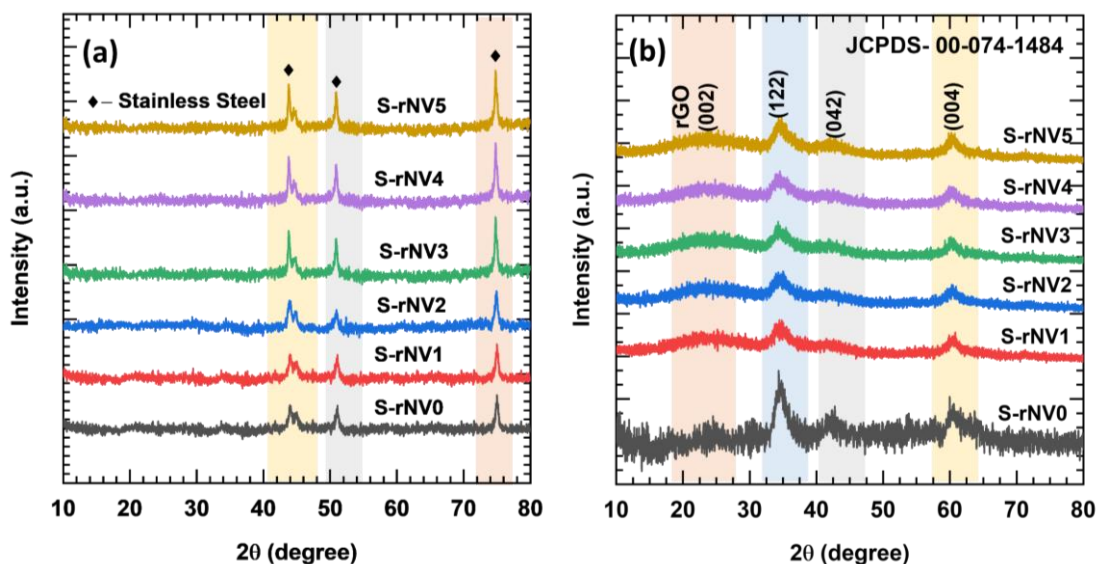


**Figure 4.20:** XRD Patterns (a) on SS substrate, and (b) Powder sample of S-rNV series

#### 4.3.B.3.3 FT-IR analysis

The FT-IR analysis of prepared NVO/rGO composite thin films was carried out within the range of  $400$  to  $4000\text{ cm}^{-1}$  and displayed in Figure 4.21. The composite NVO/rGO showed no significant change with the addition of rGO in NVO, exhibiting

a similar FT-IR spectrum to the pristine material, with the only difference being the appearance of a single additional peak in the composite series. The plotted FT-IR spectra reveal analogous features across all samples, with the band  $\nu_1$  at  $486\text{ cm}^{-1}$  attributed to Ni-O stretching vibrations. Additionally, the appearance of the band  $\nu_2$  in a range of  $659$  to  $890\text{ cm}^{-1}$  aligns with symmetric and antisymmetric stretching vibrations of V-O-V. The peak observed for all samples at  $\nu_3$  ( $1364\text{ cm}^{-1}$ ) corresponds to the trapped nitrate ions present in the precursor. The additional absorption band observed at  $1642\text{ cm}^{-1}$  is attributed to the presence of  $\text{sp}^2$  hybridized carbon atoms (C=C), confirming the rGO present in the S-rNV samples. The FT-IR results confirm the successful preparation of the NVO/rGO composite.

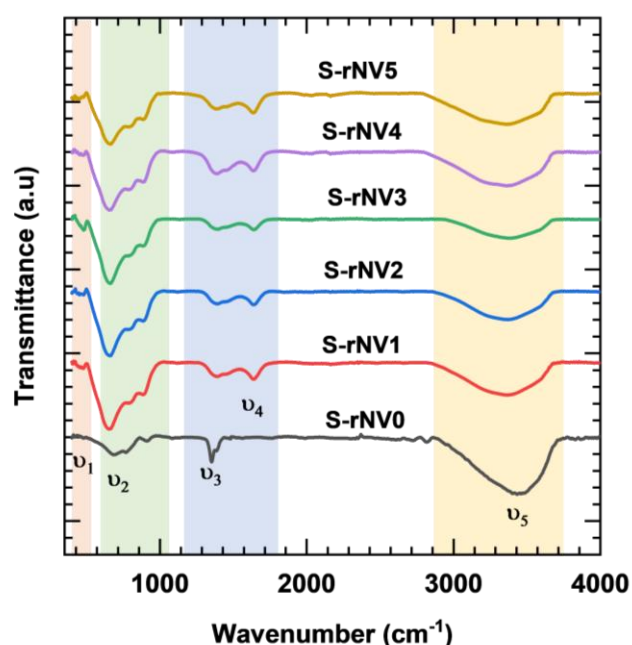


**Figure 4.21:** FT-IR spectra of S-rNV series

#### 4.3.B.3.4 Raman analysis

Raman spectroscopy offers further insights into the structural changes in rGO. Figure 4.22 shows the Raman spectra of S-rNV0 to S-rNV5 samples. The Raman spectra obtained from the S-rNV series sample display two characteristic peaks of NVO. The peak at ( $333\text{ cm}^{-1}$ ) is associated with the asymmetric stretching vibration of V-O-Ni. In contrast, the broad peak noticed at  $\nu_2$  ( $811\text{ cm}^{-1}$ ) is attributed to the symmetric vibration of the V-O band [48]. With the increasing content of rGO, the intensity of D and G bands increases, which lowers the intensity of another characteristic peak of NVO. Additionally, two extra peaks at  $\nu_3$  and  $\nu_4$ , correspond to the 2D and D+G, respectively are observed with the increasing rGO content. The

obtained D and G peaks with a D/G intensity ratio of 1.05, 1.06, 1.07, 1.07, and 1.08 for samples S-rNV1, S-rNV2, S-rNV3, S-rNV4, and S-rNV5 samples, respectively, which indicates the increasing defects owing to the growth of NVO over rGO nanosheets, confirms the successful composite of NVO/rGO

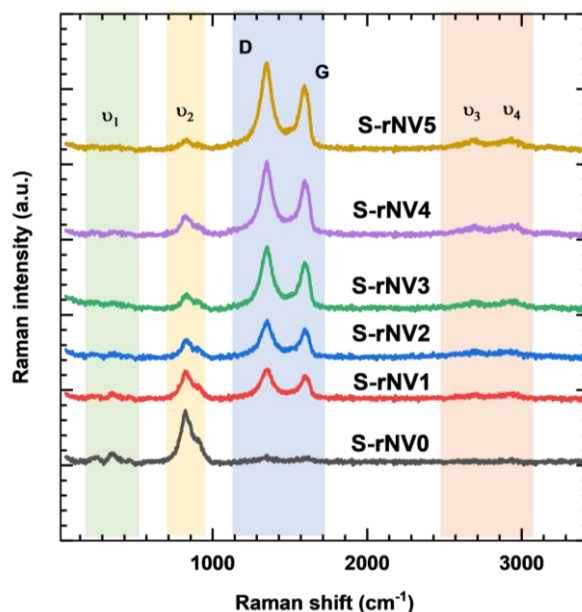


**Figure 4.22:** Raman spectra of S-rNV series

#### 4.3.B.3.5 XPS analysis

The Figure 4.23 shows the comparative XPS spectra for pristine S-rNV0, S-rNV3 and rGO samples. From the survey spectrum plotted in Figure 4.23 (a), the presence of the Ni, V, O, and C elements. The HR spectra of Ni, V, and O for the S-rNV3 sample exhibit a deconvolution pattern comparable to that of the pristine S-rNV0. The HR spectrum in Figure 4.23 (b) displays the deconvolution of the Ni 2p spectrum. The Ni 2p<sub>3/2</sub> deconvoluted into two distinct binding energies, a strong peak at a lower binding energy of 855.3 eV associated with the Ni<sup>2+</sup>, besides a lighter peak at a higher binding energy of 856.7 eV is related to the exterior Ni<sup>3+</sup> [49]. Moreover, a peak at 873.2 eV is associated with Ni 2p<sub>1/2</sub>. Along with these, obtained satellite peaks at 861.3 and 879.2 eV are associated with the octahedral coordination of Ni<sup>2+</sup>. The HR XPS analysis of the V 2p spectrum in Figure 4.23 (c) reveals two prominent peaks, one at 516.6 eV corresponding to V 2p<sub>3/2</sub> and another at 524.4 eV associated with V 2p<sub>1/2</sub> [50]. Specifically, the peak corresponding to V 2p<sub>3/2</sub> further resolves into distinct peaks at 516.2 and 517 eV, linked respectively to V<sup>4+</sup> and V<sup>5+</sup> states [51]. In the oxygen (O 1s) XPS spectrum, depicted in Figure 4.23 (d), three distinct peaks are

observed, each representing different oxygen environments within the samples. The peak at 530.4 eV corresponds to lattice oxygen ( $O_I$ ). The fitted peak at 531.5 eV ( $O_{II}$ ) is indicative of oxygen vacancies, while the peak at 533.1 eV ( $O_{III}$ ) is attributed to water molecules adsorbed on the surface of the sample [52, 53].

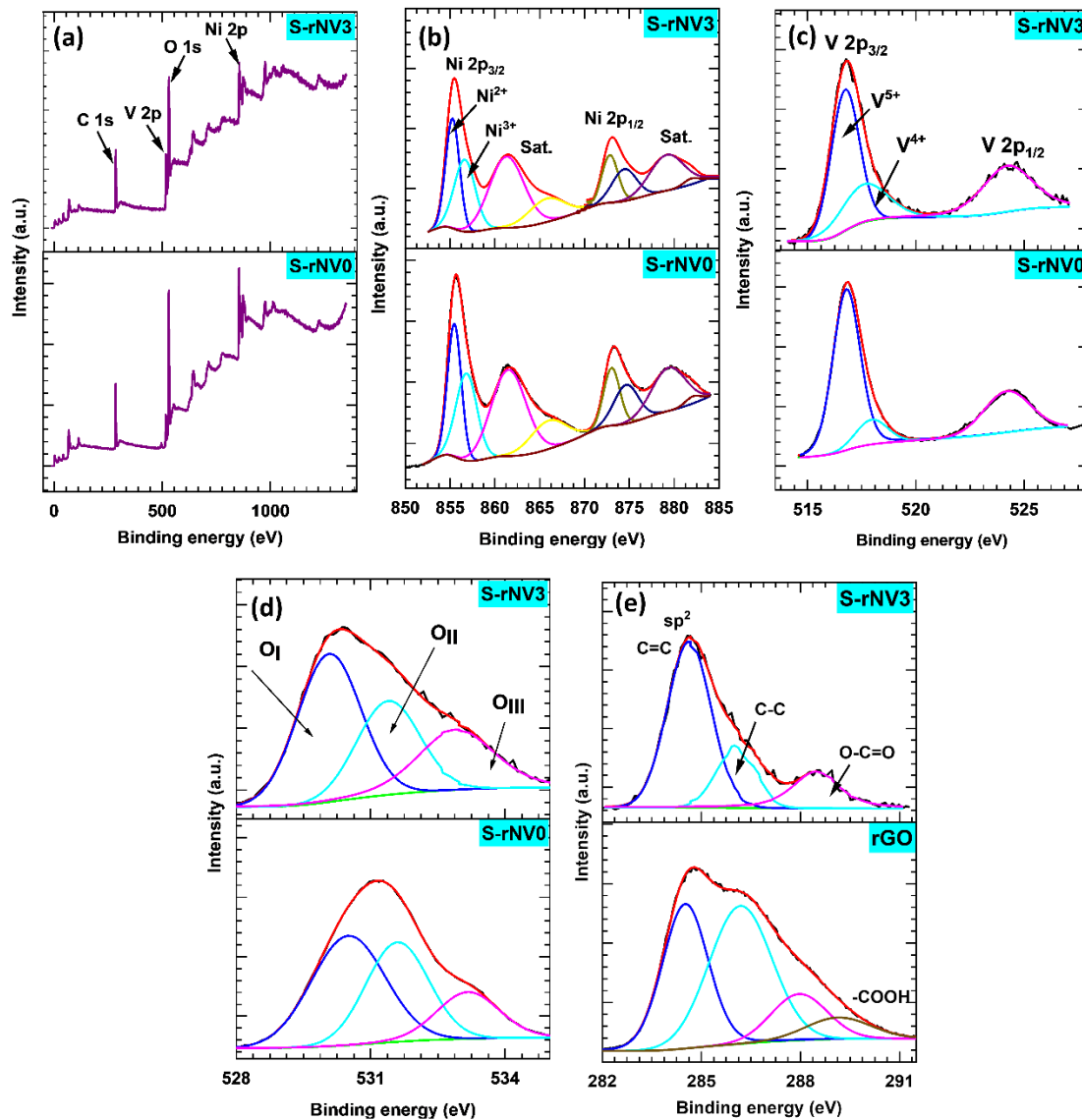


**Figure 4.23:** XPS spectra of S-rNV0 and S-rNV3 samples (a) survey spectrum, HR spectra of (b) Ni 2p, (c) V 2p, (d) O 1s, and (e) C 1s

The prominent peak observed at 284.5 eV corresponds to the C=C in-plane bonding attributed to  $sp^2$  hybridization. In contrast, the out-of-plane bonding of  $sp^3$  hybridized C-C, depicted at 285.9 eV in Figure 4.23 (e), appears notably shorter in comparison to  $sp^2$  hybridization [54], Which suggests that the formation NVO at the expense of rGO functional group.



#### 4.3.B.3.6 TG Analysis

The TG analysis is a powerful technique utilized to examine the thermal stability and quantify the composition of synthesized nanocomposites. Figure 4.24 presents the TG analysis curves for S-rNV series samples. All the TG analysis curves demonstrate a characteristic thermal decomposition process under an air atmosphere. The initial weight loss occurring below 200 °C is ascribed to the evaporation of surface-adsorbed moisture and interlayer water [55].

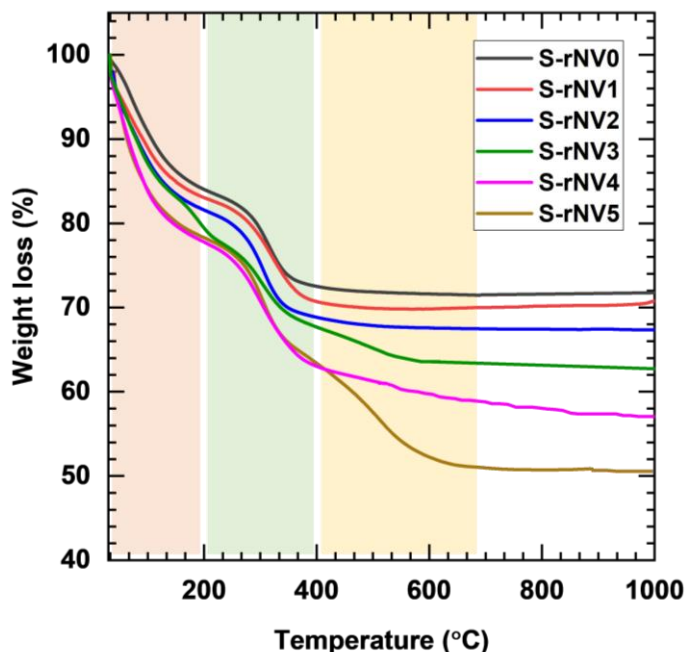


**Figure 4.24:** TG analysis of S-rNV series samples

In the S-rNV series samples, a gradual weight loss was observed within the temperature range of 200 to 400°C. This weight loss is attributed to the removal of labile oxygen-containing functional groups and water vapor [56]. While the TG analysis curve of the pristine S-rNV0 sample stabilizes above 400°C, the S-rNV1 to S-rNV4 samples exhibit substantial weight loss beyond this temperature. This weight loss is indicative of the decomposition of rGO within these samples [57]. The obtained percentage of rGO are of 2.20%, 5.87%, 11.87%, 20.08%, and 29.33% for S-rNV1, S-rNV2, S-rNV3, S-rNV4, and S-rNV5 samples, respectively. TG analysis confirmed the correlation between rGO content and weight loss, demonstrating that higher rGO concentrations resulted in greater weight loss attributed to rGO decomposition. The increased content of rGO observed in TG analysis corresponds to the increasing concentrations of rGO in the synthesis of NVO/rGO.



### 4.3.B.3.7 FE-SEM and elemental analysis

The surface topography of SILAR-synthesized NVO/rGO composite thin films is analyzed by FE-SEM micrographs. Figure 4.25 shows the obtained morphologies of S-rNV series samples at different magnifications (X10K and X40K).

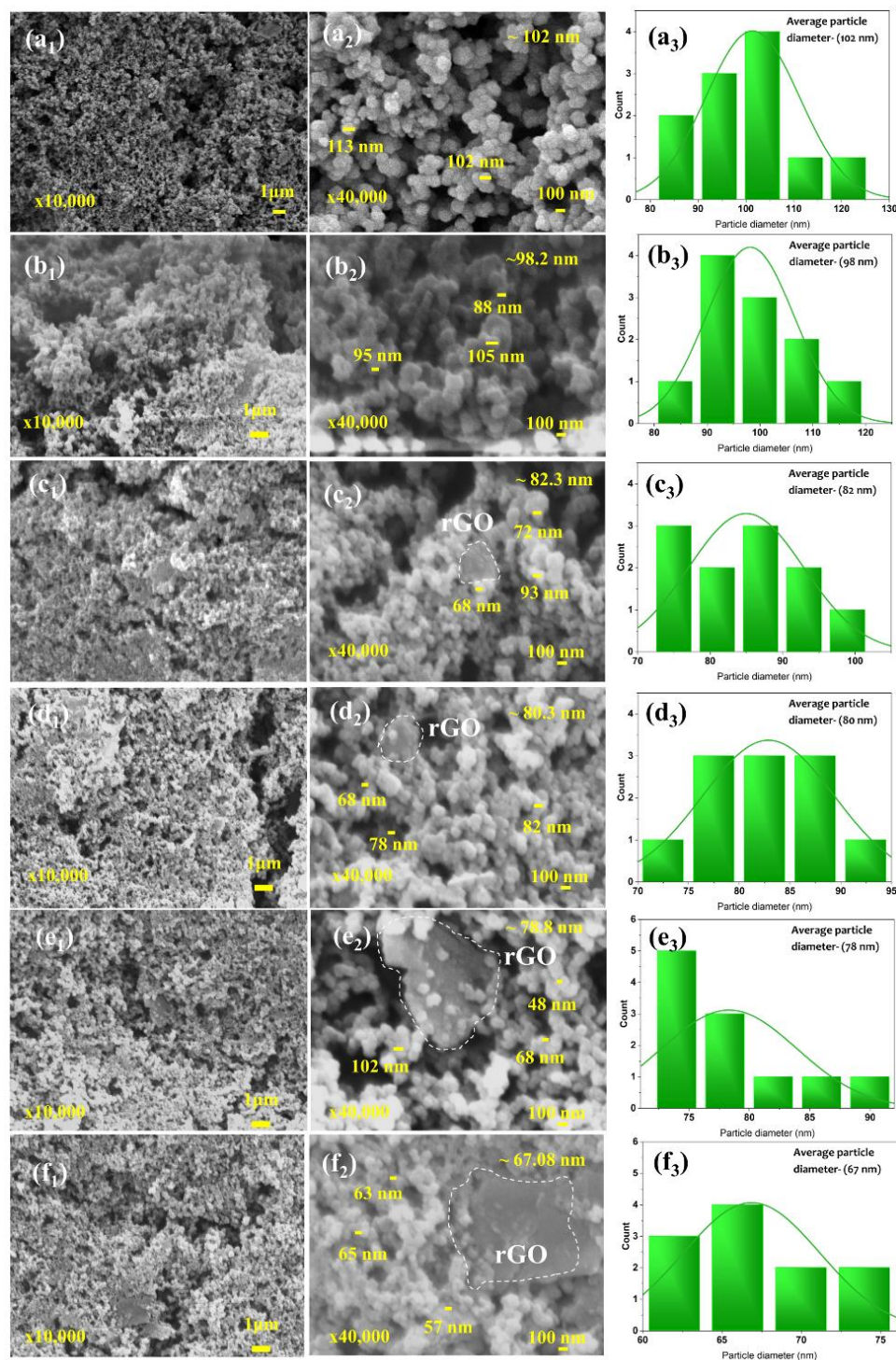


**Figure 4.25:** FE-SEM images of (a<sub>1</sub>-a<sub>2</sub>) S-rNV0, (b<sub>1</sub>-b<sub>2</sub>) S-rNV1, (c<sub>1</sub>-c<sub>2</sub>) S-rNV2, (d<sub>1</sub>-d<sub>2</sub>) S-rNV3, (e<sub>1</sub>-e<sub>2</sub>) S-rNV4, (f<sub>1</sub>-f<sub>2</sub>) S-rNV5, and (a<sub>3</sub>-f<sub>3</sub>) Histograms of average particle size for S-rNV series samples

From Figure 4.25, it is observed that the densely packed, spherical particles are irregularly decorated over the substrate, forming a wide porous thin film. Furthermore, as the concentration of rGO increases, nanosheets of rGO become observable within the structure. The observed average particle diameter for the S-rNV0 sample is  $\sim 102$  nm. Additionally, an inverse correlation is noted between the increase in rGO content within the S-rNV series samples and a decrease in average particle size, transitioning from  $\sim 102$  nm to 68 nm, as illustrated in histograms depicted in Figure 4.25 ( $a_3$ - $f_3$ ). This signifies that NVO nanoparticles decorated over rGO nanosheets could influence the overall properties and electrochemical performance of the material.

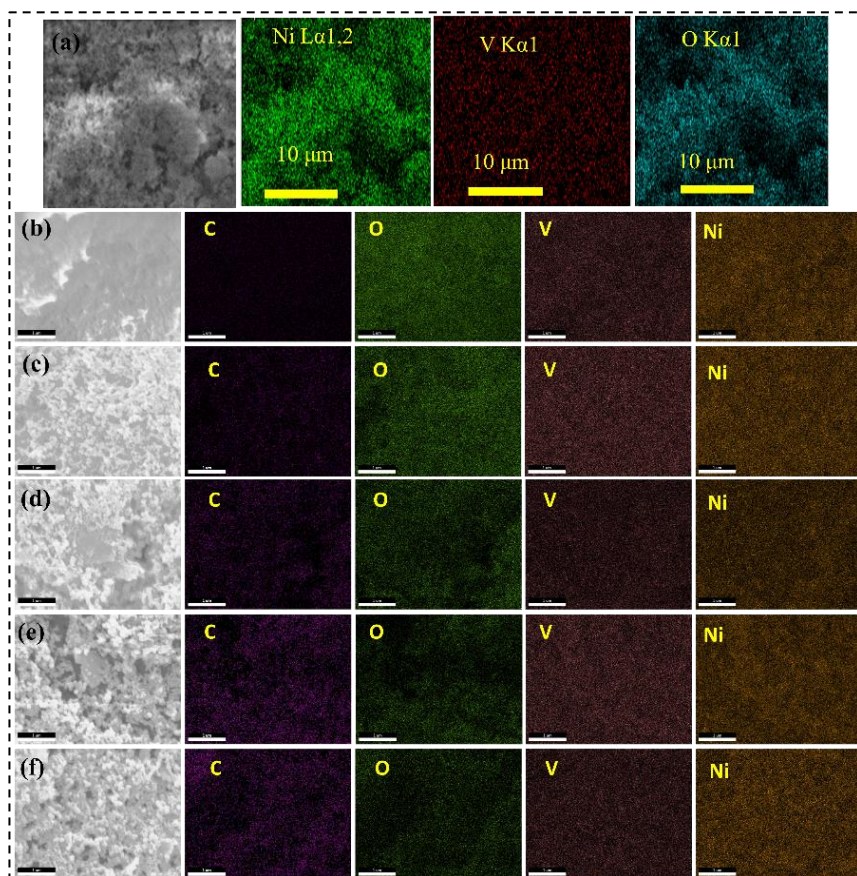


**Figure 4.26:** EDS mapping images of (a) S-rNV0, (b) S-rNV1, (c) S-rNV2, (d) S-rNV3, (e) S-rNV4, and (f) S-rNV5 samples

The EDS elemental mapping analysis was conducted to analyse the composition and distribution of key elements (Ni, V, O, and C) across all S-rNV series samples. Sample S-rNV0 exhibits a uniform distribution of nickel, vanadium, and oxygen while lacking traces of carbon elements, confirming its composition as pure NVO (Figure 4.26 (a)). The uniform distribution of Ni, V, C, and O elements observed



(Figure 4.26 (b-f)) in the remaining samples (S-rNV1 to S-rNV5) confirms the successful preparation of the NVO/rGO composite.

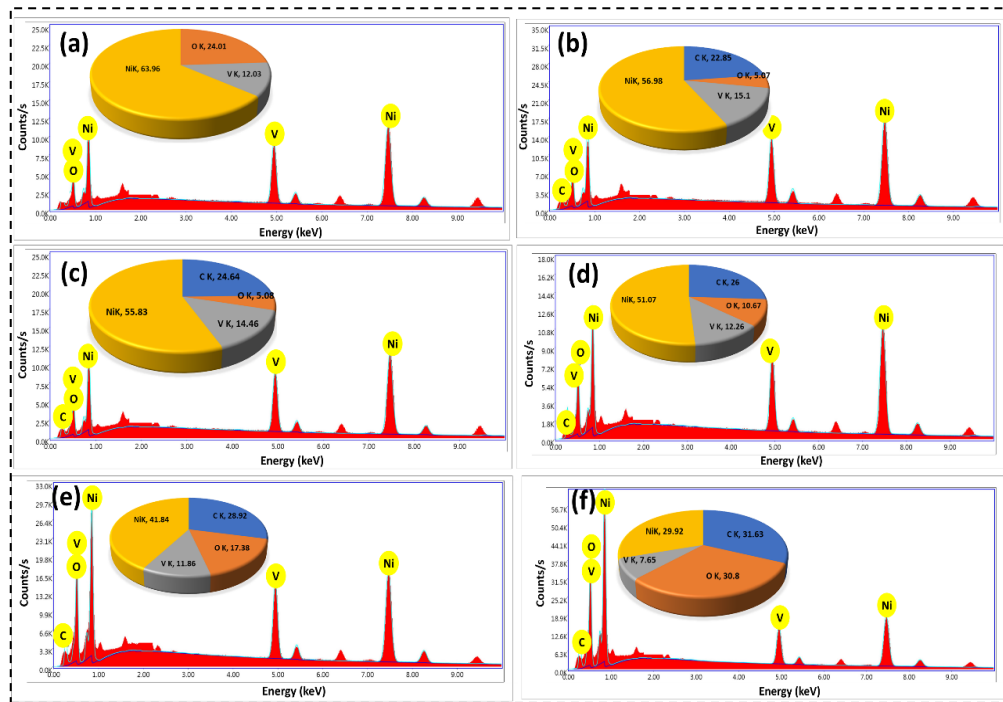


**Figure 4.27:** EDS spectra of (a) S-rNV0, (b) S-rNV1, (c) S-rNV2, (d) S-rNV3, (e) S-rNV4, and (f) S-rNV5 samples

The EDS spectra presented in Figure 4.27 provide insights into the elemental composition of the S-rNV series samples. Analysis confirms the presence of key elements, including nickel, vanadium, oxygen, and carbon within the NVO/rGO composite. The observed atomic percentages (% At.) of carbon in the prepared samples are detailed as follows: 0% for S-rNV0, 22.85% for S-rNV1, 24.64% for S-rNV2, 26.0% for S-rNV3, 28.92% for S-rNV4, and 31.63% for S-rNV5 composite thin films. The EDS analysis serves as conclusive evidence for the successful formation of a composite structure comprising NVO nanoparticles and increasing the content of rGO nanosheets. The progressive increase in the atomic percentage of carbon with increasing rGO content indicates the effective incorporation of rGO into the composite matrix. This integration of rGO within the NVO framework is pivotal for enhancing conductivity and facilitating charge transport pathways within the electrode material.

#### 4.3.B.3.8 HR-TEM analysis

In conjunction with SEM analysis, the HR-TEM images of the S-rNV3 sample (Figure 4.28 (a-c)) reveal particles adorned with rGO sheets. The analysis of line

profiles at higher magnification is provided in Figure 4.28 (e). The observed lattice fringes, exhibit a measured lattice distance of approximately 0.25 nm for the S-rNV3 sample, confirming the presence of (122) crystalline planes within the respective sample. The margins of the crystalline fringes appear discontinuous (Figure 4.29 (e)), indicating a significant presence of defects, which notably enhance the material's conductivity.

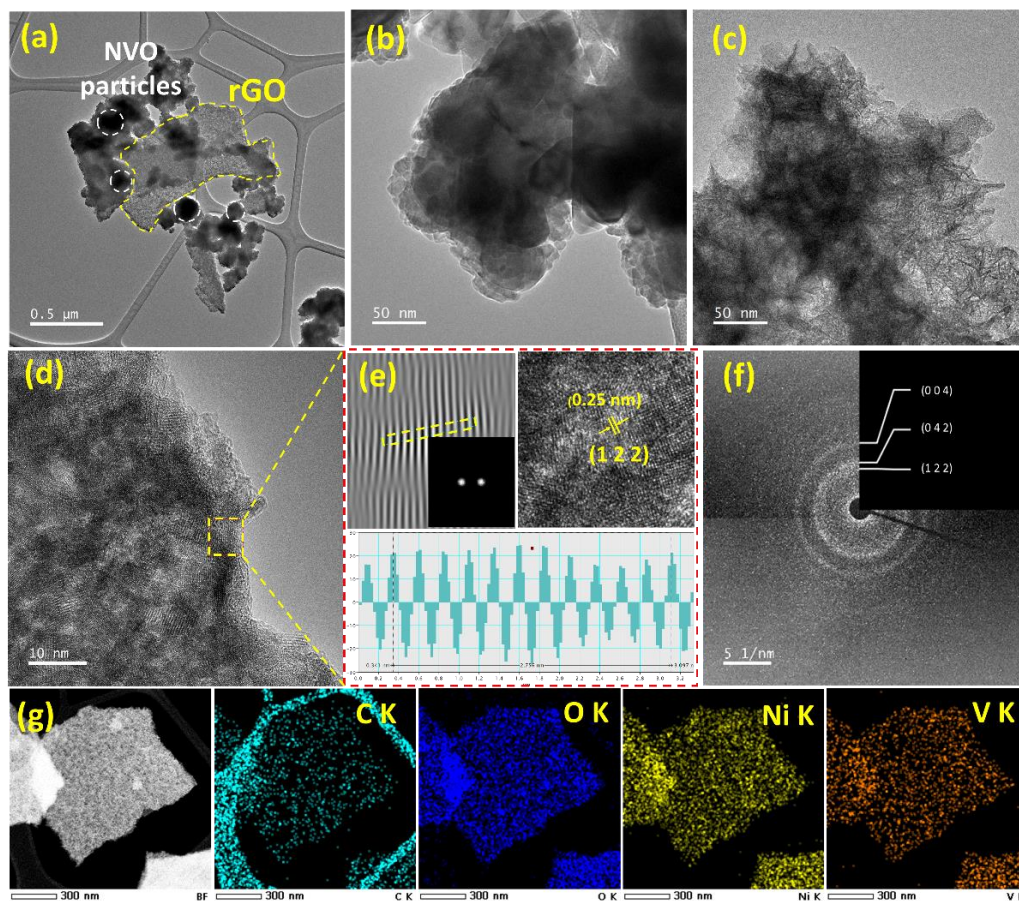


**Figure 4.28:** (a-d) HR-TEM images, (e) Lattice distortion images and interplanar distance calculations from the HR-TEM images, (f) SAED patterns for S-rNV3, and (g) HR-TEM elemental mapping images S-rNV3

Furthermore, the SAED patterns depicted in Figure 4.28 (f) exhibit orderly yet indistinct rings, affirming the material's lower crystallinity and polycrystalline characteristics. The discerned rings in the SAED pattern corroborate the existence of (122), (042), and (004) crystalline planes of NVO, consistent with XRD results. Additionally, Figure 4.28 (g) presents an HR-TEM image along with elemental mapping images, highlighting the presence and uniform distribution of Ni, V, O, and C elements throughout the S-rNV3 sample.

#### 4.3.B.3.9 BET and BJH analysis

The surface area and pore size distribution of the present S-rNV series samples were investigated with  $N_2$  adsorption-desorption isotherm measurements and plotted in Figure 4.29. The curve demonstrates a well-defined loop of hysteresis in the relative pressure range of 0.01-0.99.

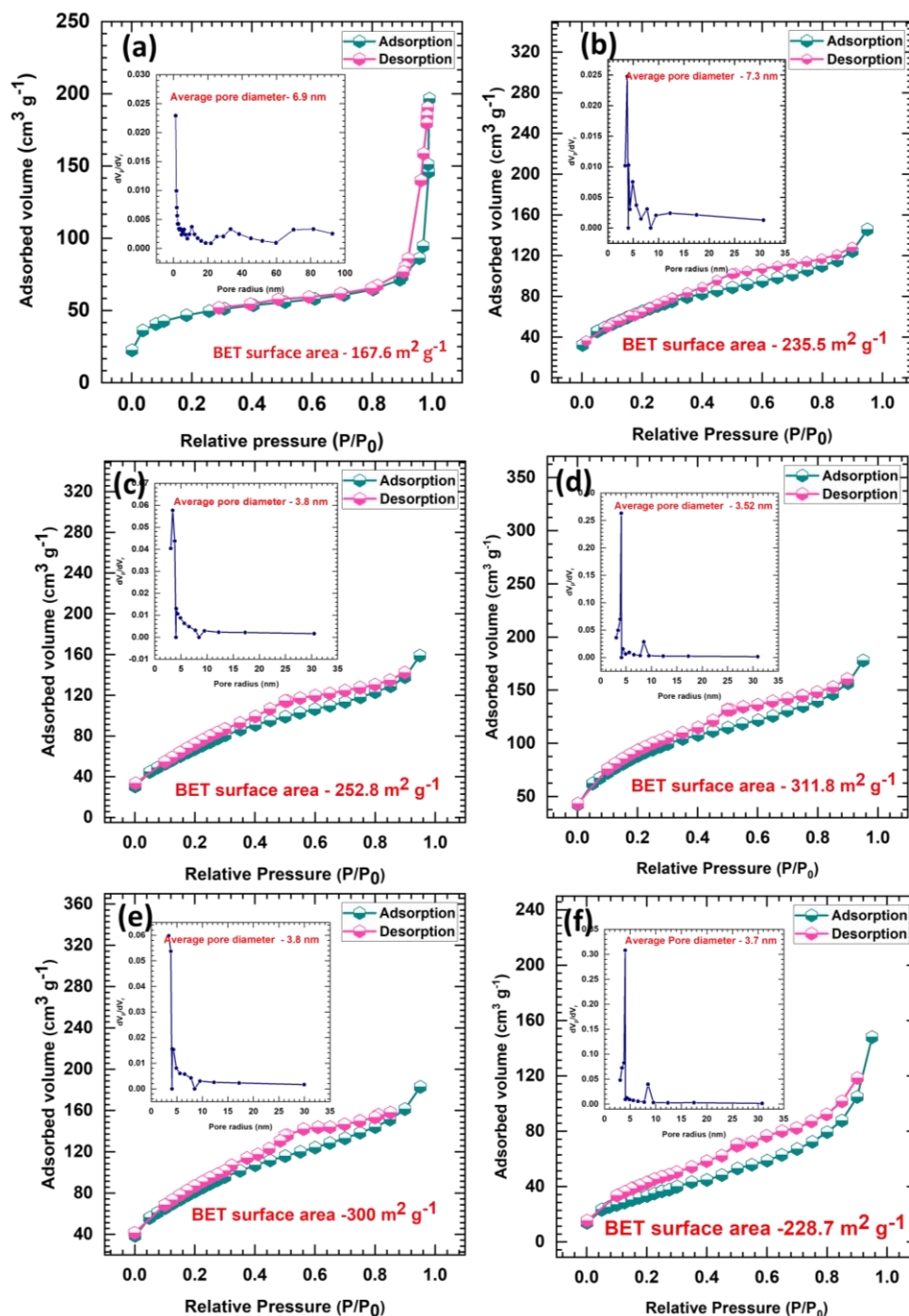


**Figure 4.29:** Nitrogen adsorption-desorption isotherms (BET curves) inset pore size distribution (BJH) curves of (a) S-rNV0, (b) S-rNV1, (c) S-rNV2, (d) S-rNV3, (e) S-rNV4, and (f) S-rNV5 samples

The curve resembles the H3-type hysteresis loop, which mainly underlies the type-II isotherm with high adsorption energy [58]. The obtained value of specific surface area for S-rNV0 sample is  $167.6 \text{ m}^2 \text{ g}^{-1}$  and for the composites, S-rNV1, S-rNV2, S-rNV3, S-rNV4, and S-rNV5, the obtained values are 235.5, 252.8, 311.8, 300.0, and 228.7, respectively. The obtained results highlight that NVO composite with rGO is advantageous for augmenting the specific surface area. Furthermore, the pore size distribution analysis using the BJH method, depicted in the inset of Figure 4.29, confirms the mesoporous structure of the NVO samples. The BJH plots display the average pore size distribution of 6.9, 7.3, 3.8, 3.5, 3.8, and 3.7 nm for S-rNV0, S-rNV1, S-rNV2, S-rNV3, S-rNV4, S-rNV5 samples, respectively. The considerable specific surface area and mesoporous nature of NVO/rGO materials can elevate electrochemical activity by facilitating a multitude of active sites and easy ion transfer through the mesopores.

#### **4.3.B.3.10 Electrochemical analysis**

To further elucidate the influence of the concentration of rGO over the electrochemical performance of S-rNV series samples, CV, GCD, EIS, and stability measurements were carried out utilizing a three-electrode configuration with S-rNV series electrodes as a working electrode as detailed in Chapter-III, subsection 3.2.A.3.7.

##### **(a) CV analysis**

The CV measurements were carried out at a different scan rate of 2 to  $100 \text{ mV s}^{-1}$ . Figure 4.30 relates the CV profiles of S-rNV series thin film electrodes in an optimized potential range of 0 to 0.7 V vs Hg/HgO. Typical CV plots exhibit non-rectangular battery-type curves with a single pair of redox peaks, which are observed in all samples and suggest that faradaic redox reactions occur between  $\text{Ni}^{2+}$  and  $\text{Ni}^{3+}$ , the process of intercalation and deintercalation is discussed in Chapter III, section 3.2.A.3.7, equation 3.4. The area under the CV curves increases with increasing rGO content in the electrode up to the S-rNV3 sample; furthermore, the area under the curve decreases with increasing rGO. The S-rNV3 electrode shows a higher current area in the curve than other electrodes. It is also observed that with increasing concentration of rGO, the region associated with EDLC increases. The b value for S-rNV series electrodes is determined by calculating the slope of the graph depicting  $\log(i)$  versus  $\log(v)$ , as illustrated in Figure 4.30 (h).



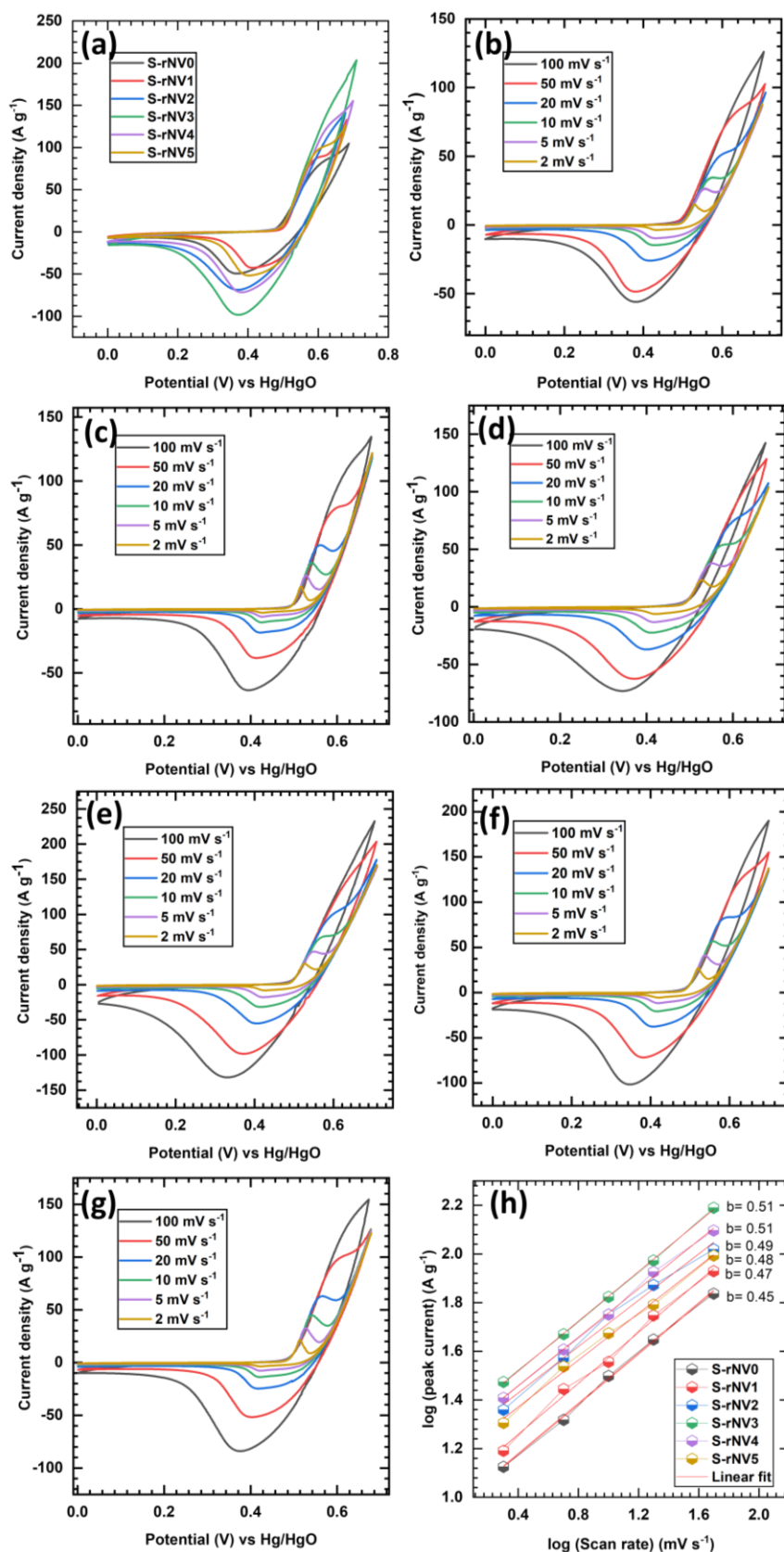


**Figure 4.30:** CV curves of (a) S-rNV0, (b) S-rNV1, (c) S-rNV2, (d) S-rNV3, (e) S-rNV4, (f) S-rNV5 electrodes, (h) Plot of  $\log(\text{current density}, A\ g^{-1})$  vs  $\log(\text{scan rate}, mV\ s^{-1})$



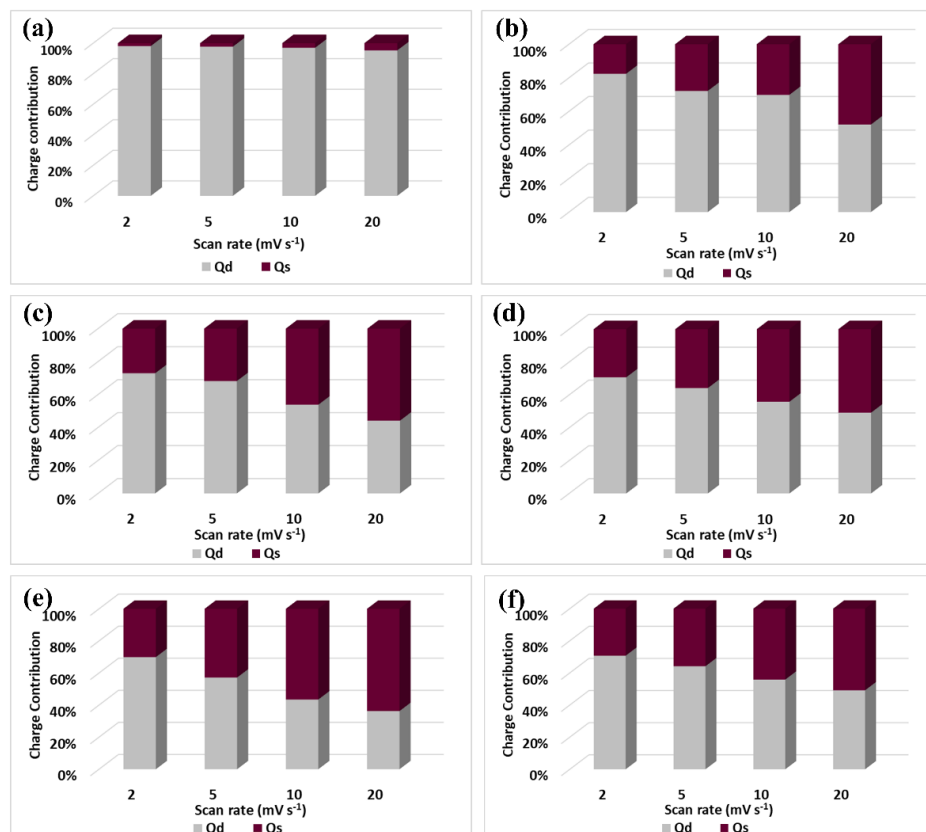


**Figure 4.31:** Charge contribution plots of (a) S-rNV0, (b) S-rNV1, (c) S-rNV2, (d) S-rNV3, (e) S-rNV4, and (f) S-rNV5 electrodes

The obtained ‘b’ values are between the range of 0.47 to 0.52, which confirms the battery-type faradic charge storage mechanism of the NVO/rGO composite. To further elucidate the charge storage kinetics of S-rNV series electrodes, the total capacitance is deconvoluted into the diffusion-controlled and surface-controlled mechanisms. The obtained pseudocapacitive and battery-type current contributions for S-rNV series thin film electrodes are calculated and provided in Figure 4.31. The figure reveals that the surface contribution increases with the increase in the content of rGO in the NVO/rGO. At higher scan rates, the surface pseudocapacitance holds a more significant contribution, while at lower scan rates, the bulk battery type exhibits a more significant contribution. The CV analysis concludes the S-rNV3 electrode shows superior electrochemical behaviour.

#### (b) GCD analysis

The GCD profiles of the S-rNV series electrodes are recorded in an optimized potential window of 0 to 0.5 V (vs Hg/HgO). The GCD curves at various current densities 1 to 3 A g<sup>-1</sup> are displayed in Figure 4.32. The obtained plateau of the charge-discharge curve well matches the associated CV curves, i.e., battery type.

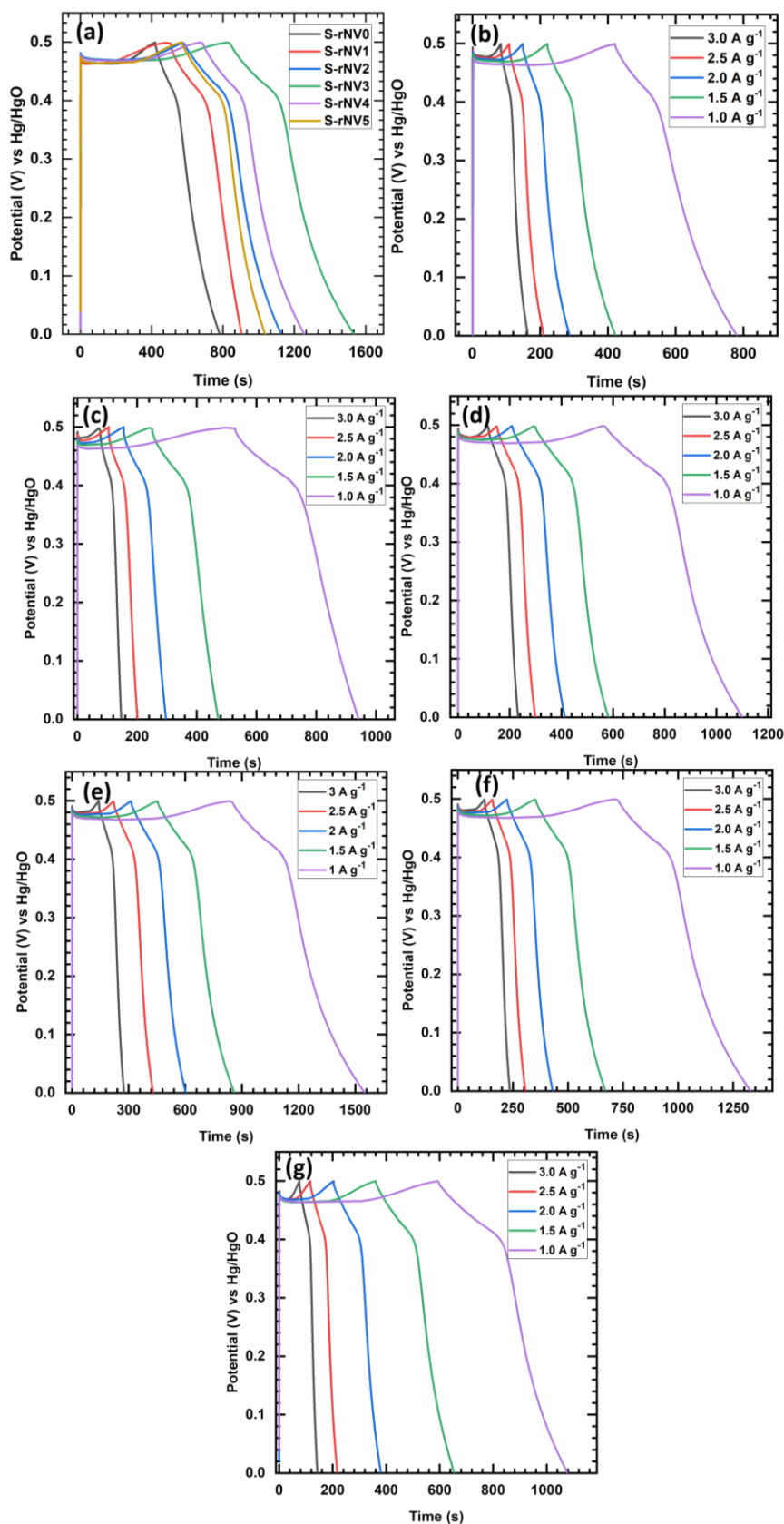


**Figure 4.32:** Comparative GCD plots of S-rNV series and GCD plots of (a) S-rNV0, (b) S-rNV1, (c) S-rNV2, (d) S-rNV3, (e) S-rNV4, and (f) S-rNV5 electrodes at various current densities (1-3 A g<sup>-1</sup>)

The battery-type pseudocapacitors typically display distinctive and gradual voltage changes in the GCD curve because the energy storage mechanism relies on redox reactions that occur near and into the bulk of the electrode material [6]. From the GCD plots, the  $C_{sp}$  values of S-rNV series electrodes are calculated and plotted in Figure 4.33. The S-rNV3 electrode shows a higher discharging time, which is responsible for higher  $C_{sp}$  than other electrodes. The S-rNV3 electrode shows a maximum  $C_{sp}$  of  $1440 \text{ F g}^{-1}$  at  $1 \text{ A g}^{-1}$  current density, and it decreases to  $732 \text{ F g}^{-1}$  at  $3 \text{ A g}^{-1}$  current density.

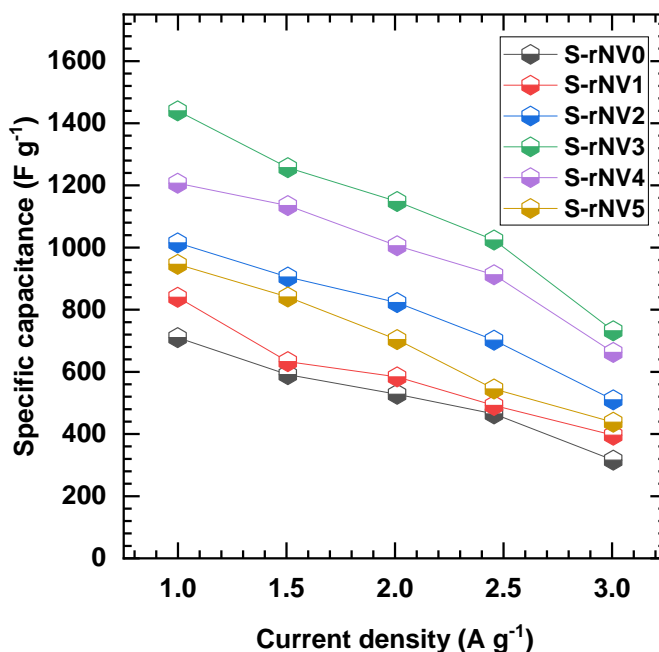


**Figure 4.33:** The plot of  $C_{sp}$  at various current densities for S-rNV series samples

Likewise, the S-rNV0, S-rNV1, S-rNV2, S-rNV4, and S-rNV5 thin film electrodes offer maximum  $C_{sp}$  of 710, 840, 1015, 1206, and 946  $\text{F g}^{-1}$ , respectively at  $1 \text{ A g}^{-1}$  current density. The decrement in capacitance is observed with the increase in current density. Moreover, the capacitance value increases with the rise in the content of rGO up to the S-rNV3 sample; however, further increments in rGO content  $C_{sp}$  decrease.

### (c) EIS analysis

The Nyquist plots depicted in Figure 4.34 illustrate the characteristics of S-rNV series electrodes. The inset of Figure 4.34 presents the fitted equivalent circuit for the EIS data obtained for the S-rNV series electrodes. Within this Figure, the parameters  $R_s$ ,  $R_{ct}$ ,  $W$ , and  $Q$  are illustrated and the values corresponding to each of

these fitted circuit parameters are provided in Table 4.4. The smaller  $R_s$  value of  $0.62 \Omega \text{ cm}^{-2}$  is observed for the S-rNV3 electrode, and overall obtained values of  $R_s$  are between  $0.62$  to  $0.92 \Omega \text{ cm}^{-2}$  for the S-rNV series electrodes. Additionally, the smallest semicircle for the same electrode (S-rNV3) implies that the lower  $R_{ct}$  of  $0.15 \Omega \text{ cm}^{-2}$  is attributed to the LBL incorporation of rGO and binder-free synthesis of the NVO/rGO, which enables the easy intercalation of electrolytic ions and improved conductivity.

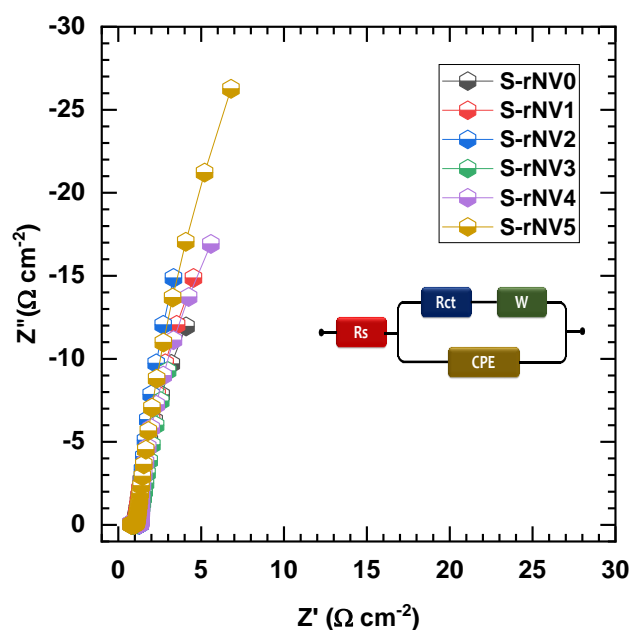


**Figure 4.34:** Nyquist plots for S-rNV series electrodes

**Table 4.4:** EIS fitted circuit parameters for Nyquist plots of S-rNV series electrodes

Fitted Parameters	S-rNV0	S-rNV1	S-rNV2	S-rNV3	S-rNV4	S-rNV5
$R_s (\Omega \text{ cm}^{-2})$	0.80	0.62	0.82	0.64	0.92	0.7
$R_{ct} (\Omega \text{ cm}^{-2})$	0.95	0.36	0.43	0.15	0.80	0.19
$W-P (\Omega \text{ cm}^{-2})$	0.44	0.047	0.47	0.46	0.49	0.47
$CPE-T (\text{mF cm}^{-2})$	0.21	1.6	0.84	0.86	2.4	0.51
$CPE-P (n)$	0.87	0.41	0.73	0.75	0.41	0.72

#### (d) Stability analysis

Moreover, the electrochemical cycling stability of best performed S-rNV3 electrode was carried out for 5000 charge-discharge cycles at  $8 \text{ A g}^{-1}$  current density, and the cyclic stability graph is provided in Figure 4.35. Exploiting the properties of active material and surface structure, the sample S-rNV3 demonstrated good

capacitive retention of 94.5.% even after 5000 cycles, even at a high charge-discharge rate. Moreover, the S-rNV3 electrode maintains an excellent coulombic efficiency of 95.1% after 5000 cycles.

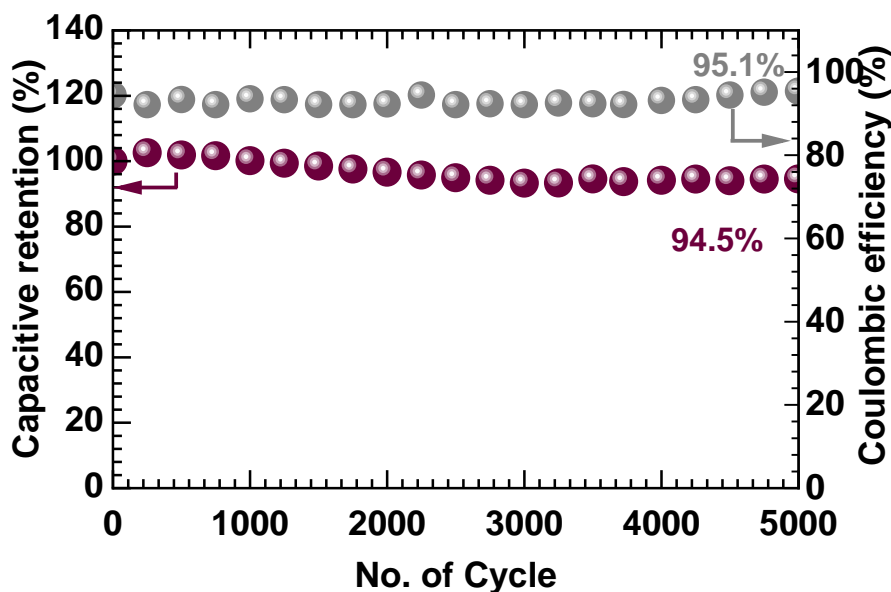


**Figure 4.35:** Stability plots for S-rNV3 samples

#### 4.3.B.4 Conclusions

The thin film electrodes of NVO/rGO nanoparticles were prepared using the SILAR method. The optimal composition/percentage of rGO (11.87%) within the S-rNV3 electrode provides a maximum specific surface area of  $311 \text{ m}^2 \text{ g}^{-1}$ , which further helps to improve the electrochemical performance. The electrochemical performance of the NVO/rGO thin film electrodes was found to be significantly enhanced (twofolds) compared to pristine NVO electrodes. In nutshell, the binder-free, nanocrystalline, mesoporous, hydrous NVO/rGO nanoparticles thin film electrodes synthesized via the SILAR method exhibit enhanced electrochemical performance. The synergistic interaction between rGO and NVO, along with the presence of voids and cavities in the nanoparticle structure, plays a crucial role in improving charge storage capabilities. These findings pave the way for the development of efficient and scalable cathode (S-rNV3) materials for SC application.

#### 4.4 References

- [1] H. Zhao and Z. Yuan, *Catal. Sci. Technol.*, 7 (2017) 330–347.
- [2] I. Dincer, *Renew. Sustain. Energy Rev.*, 4 (2000) 157–175.
- [3] M. Whittingham, *MRS Bull.*, 33 (2008) 411–419.
- [4] M. Thackeray, C. Wolverton, E. Isaacs, *Energy Environ. Sci.*, 5 (2012) 7854–7863.
- [5] Poonam, K. Sharma, A. Arora, S. Tripathi, *J. Energy Storage*, 21 (2019) 801–825.

- [6] Y. Jiang, J. Liu, *Energy Environ. Mater.*, 2 (2019) 30–37.
- [7] Y. Li, H. Sun, Y. Yang, Y. Cao, W. Zhou, H. Chai, *J. Colloid Interface Sci.*, 580 (2020) 298–307.
- [8] J. Singh, J. Kumar, C. Rastogi, B. Mandal, *Mater. Today Proc.* 79 (2023) 231–234.
- [9] D. Nandi, M. Gnanaseelan, F. Simon, J. Pionteck, *New J. Chem.*, 41 (2017) 5620–5627.
- [10] D. Merum, R. Nallapureddy, M. Pallavolu, T. Mandal, R. Gutturu, N. Parvin, A. Banerjee, S. Joo, *ACS Appl. Energy Mater.*, 5 (2021) 5561–5578.
- [11] R. Kumar, P. Rai, A. Sharma, *J. Mater. Chem. A* 4 (2016) 9822–9831.
- [12] S. Sekhar, G. Nagaraju, B. Ramulu, D. Narsimulu, J. Yu, *Inorg. Chem. Front.*, 6 (2019) 1087–1096.
- [13] S. Arasi, R. Ranjithkumar, P. Devendran, M. Krishnakumar, A. Arivarasan, *Ceram. Int.*, 46 (2020) 22709–22717.
- [14] S. Ratnayake, J. Ren, E. Colusso, M. Guglielmi, A. Martucci, E. Gaspera, *Small*, 17 (2021) 2101666.
- [15] V. Shinde, T. Gujar, C. Lokhande, *Sol. Energy Mater. Sol. Cells*, 91 (2007) 1055–1061.
- [16] K. Dastafkan, Q. Meyer, X. Chen, C. Zhao, *Small*, 16 (2020) 1–12.
- [17] C. Chen, N. Zhang, Y. He, B. Liang, R. Ma, X. Liu, *ACS Appl. Mater. Interfaces*, 8 (2016) 23114–23121.
- [18] K. Thiagarajan, J. Theerthagiri, R. Senthil, P. Arunachalam, J. Madhavan, M. Ghanem, *J. Solid State Electrochem.*, 22 (2018) 527–536.
- [19] A. Azharudeen, R. Karthiga, M. Rajarajan, A. Suganthi, *Arab. J. Chem.*, 13 (2020) 4053–4064.
- [20] C. O'Dwyer, V. Lavayen, S. Newcomb, M. Ana, E. Benavente, G. González, C. Torres, *J. Electrochem. Soc.*, 154 (2007) K2.
- [21] J. Gunjekar, A. Inamdar, B. Hou, S. Cha, S. Pawar, A. Abu Talha, H. Chavan, J. Kim, S. Cho, S. Lee, Y. Jo, H. Kim, H. Im, *Nanoscale*, 10 (2018) 8953–8961.
- [22] B. Chang, G. Zhao, Y. Shao, L. Zhang, B. Huang, Y. Wu, X. Hao, *J. Mater. Chem. A*, 5 (2017) 18038–18043.
- [23] X. Liu, J. Wang, G. Yang, *ACS Appl. Mater. Interfaces*, 10 (2018) 20688–2069.
- [24] A. Karmakar and S. Srivastava, *J. Mater. Chem. A*, 7 (2019) 15054–15061.
- [25] K. Halder, R. Biswas, A. Arya, I. Ahmed, S. Tanwar, A. Sharma, *Energy Storage*, 4 (2022) 1–12.
- [26] G. Silversmit, D. Depla, H. Poelman, G. Marin, R. Gryse, *J. Electron Spectros. Relat. Phenomena*, 135 (2004) 167–175.
- [27] S. Zhao, K. Tao, Y. Gong, *Dalt. Trans.*, 48 (2019) 5315–5326.
- [28] M. Can, S. Shah, M. Doty, C. Haughn, T. Frat, *J. Phys. D. Appl. Phys.*, 45 (2012) 195104.
- [29] Y. Teng, Y. Li, D. Yu, Y. Meng, Y. Wu, X. Zhao, X. Liu, *ChemistrySelect*, 4 (2019) 956–962.
- [30] X. Lv, W. Huang, Q. Shi, L. Tang, J. Tang, *J. Power Sources*, 492 (2021) 229623.
- [31] V. Patil, S. Pujari, S. Bhosale, S. Kumbhar, V. Parale, J. Gunjekar, H. Park, C. Lokhande, M. Mali, D. Mhamane, U. Patil, *Energy and Fuels*, 36 (2022) 12791–12806.
- [32] A. Patil, S. Moon, Y. Seo, S. Roy, A. Jadhav, D. Dubal, K. Kang, S. Jun, *Small*, 19 (2023) 2205491.
- [33] M. Klinger, *J. Appl. Crystallogr.*, 50 (2017) 1226–1234.
- [34] D. Dubal, G. Gund, C. Lokhande, R. Holze, *Mater. Res. Bull.*, 48 (2013) 923–928.
- [35] K. Kuratani, T. Kiyobayashi, N. Kuriyama, *J. Power Sources*, 189 (2009) 1284–1291.
- [36] J. Zhao, H. Pang, J. Deng, Y. Ma, B. Yan, X. Li, S. Li, J. Chen, W. Wang, *CrystEngComm*, 15 (2013) 5950–5955.
- [37] M. Mastragostino, F. Soavi, C. Arbizzani, *Advances in Lithium-Ion Batteries*, (2002) 481–505.
- [38] R. Sahoo, T. Lee, D. Pham, T. Luu, Y. Lee, *ACS Nano*, 13 (2019) 10776–10786.
- [39] O. Compton, S. Nguyen, *Small*, 6 (2010) 711–723.
- [40] A. Numan, N. Duraisamy, F. Omar, Y. Mahipal, K. Ramesh, S. Ramesh, *RSC Adv.*, 6



- (2016) 34894–34902.
- [41] C. Sengottaiyan, R. Jayavel, R. Shrestha, J. Hill, K. Ariga, L. Shrestha, J. Inorg. Organomet. Polym. Mater., 27 (2017) 576–585.
- [42] R. Tamilselvi, N. Padmanathan, K. Rahulan, P. Priya, S. Ramachandran, M. Mohandas, J. Mater. Sci. Mater. Electron. 29 (2018) 4869–4880.
- [43] M. Iqbal, M. Faisal, S. Ali, A. Afzal, J. Electroanal. Chem., 871 (2020) 114299.
- [44] S. Zhang, H. Gao, J. Zhou, J. Alloys Compd., 746 (2018) 549–556.
- [45] O. Rabbani, S. Ghasemi, S. Hosseini, J. Alloys Compd., 840 (2020) 155665.
- [46] R. Kumar, P. Gupta, P. Rai, A. Sharma, J. Electrochem. Soc., 3 (2017) 2–6.
- [47] M. Guo, J. Balamurugan, N. Kim, J. Lee, Appl. Catal. B Environ., 239 (2018) 290–299.
- [48] W. Low, P. Khiew, S. Lim, C. Siong, E. Ezeigwe, J. Alloys Compd., 768 (2018) 995–1005.
- [49] S. Marje, V. Patil, V. Parale, H. Park, P. Shinde, J. Gunjekar, C. Lokhande, U. Patil, Chem. Eng. J., 429 (2022) 132184.
- [50] L. Aissani, M. Fellah, A. Chadli, M. Samad, A. Cheriet, F. Salhi, C. Nouveau, S. Weiß, A. Obrosof, A. Alhussein, J. Mater. Sci., 56 (2021) 17319–17336.
- [51] A. Held, J. Kowalska-Kuś, E. Janiszewska, A. Jankowska, K. Nowińska, J. Catal., 404 (2021) 231–243.
- [52] S. Kumbhar, S.B Bhosale, S. Pujari, V. Patil, N. Kumar, R. Salunkhe, C. Lokhande, U. Patil, Energy Technol., 11 (2023) 1–16.
- [53] S. Bhosale, S. Kumbhar, S. Pujari, V. Patil, N. Kumar, R. Salunkhe, C. Lokhande, J. Gunjekar, U. Patil, J. Energy Storage, 72 (2023) 108417.
- [54] J. Zhang, Y. Xu, Z. Liu, W. Yang, J. Liu, RSC Adv., 5 (2015) 54275–54282.
- [55] J. Fuente, M. Ruiz-Bermejo, C. Menor-Salván, S. Osuna-Esteban, Polym. Degrad. Stab., 96 (2011) 943–948.
- [56] F. Farivar, P. Yap, K. Hassan, T. Tung, D. Tran, A. Pollard, D. Losic, Carbon, 179 (2021) 505–513.
- [57] Y. Wang, Q. He, H. Qu, X. Zhang, J. Guo, J. Zhu, G. Zhao, H. Colorado, J. Yu, L. Sun, S. Bhana, M. Khan, X. Huang, D. Young, H. Wang, X. Wang, S. Wei, Z. Guo, J. Mater. Chem. C, 2 (2014) 9478–9488.
- [58] K. Cychosz and M. Thommes, Engineering, 4 (2018) 559–566.



# CHAPTER-V

---

## Hybrid Supercapacitor Devices: Fabrication and Performance Evaluation

---

## Chapter-V

### Hybrid Supercapacitor Devices: Fabrication and Performance Evaluation

Sr. No.	Title	Page No.
5.1	Introduction	155
5.2	<b>Section A</b> <b>Fabrication of Hybrid Supercapacitor Devices</b>	
5.2.A.1	Introduction	155
5.2.A.2	Experimental details	156
	5.2.A.2.1 Electrode preparation	156
	5.2.A.2.2 Fabrication of hybrid aqueous supercapacitor device	156
	5.2.A.2.3 Preparation of gel electrolyte	157
	5.2.A.2.4 Fabrication of hybrid solid-state supercapacitor device	158
5.3	<b>Section B</b> <b>Electrochemical Performance Evaluation of Hybrid Aqueous and Solid-State Devices using CBS Synthesized C-rNV3 Cathodes (C-rNV3//rGO)</b>	
5.3.B.1	Electrochemical performance of C-rNV3//KOH//rGO hybrid aqueous supercapacitor (C-HASc) device:	159
5.3.B.2	Electrochemical performance of C-rNV3//PVA-KOH//rGO hybrid solid-state supercapacitor (C-HSSc) device	162
5.4	<b>Section C</b> <b>Electrochemical Performance Evaluation of Hybrid Aqueous and Solid-State Devices using SILAR Synthesized S-rNV3 Cathodes (S-rNV3//rGO)</b>	
5.4.C.1	Electrochemical performance of S-rNV3//KOH//rGO hybrid aqueous supercapacitor (S-HASc) device	165
5.4.C.2	Electrochemical performance of S-rNV3//PVA-KOH//rGO hybrid aqueous supercapacitor (S-HSSc) device	167
5.5	Conclusions	171
5.6	References	171

## 5.1 Introduction

The SC devices have garnered significant attention in the realm of electrochemical energy storage systems owing to their potential to address the limitations of traditional SCs while offering enhanced performance and safety features [1, 2]. The pursuit of higher SE and expanded potential windows without compromising other essential characteristics has fueled extensive research in this field. Efforts are underway to explore hybrid ESSc that integrate solid-state SCs with other energy storage technologies, such as lithium-ion batteries or fuel cells [3, 4]. These hybrid systems aim to synergize the high PD of SCs with the high ED of batteries, offering a balanced solution for diverse applications ranging from portable electronics to electric vehicles. Moreover, the advancement of solid-state SCs holds great promise for meeting the growing demand for efficient and durable energy storage solutions [5, 6].

The study focuses on the development of HSCs employing NVO/rGO composite electrodes as the cathode and rGO as the anode material to optimize performance. The chapter is structured into three main sections (A, B, and C). Section 'A' outlines the fabrication process of these HSDs. Section 'B' delves into the electrochemical characteristics of the CBS prepared NVO/rGO composite electrode-based hybrid devices. Lastly, Section 'C' addresses the electrochemical performance of SILAR deposited NVO/rGO composite electrode based hybrid devices.

## 5.2 Section A

### Fabrication of Hybrid Supercapacitor Devices

#### 5.2.A.1 Introduction

In the pursuit of high-performance HSCs, both electrode and electrolyte materials play pivotal roles [7, 8]. Parameters such as the pore size and surface area of electrodes, alongside the ionic conductivity and potential working window of electrolytes, exert considerable influence on the capacitance and overall electrochemical performance of the devices [9]. Both aqueous and solid-state SC devices were constructed. The hybrid aqueous supercapacitor (HASc) device was constructed by assembling the NVO/rGO as a cathode in a configuration with the rGO electrode as the anode. HASc offer several advantages, such as high ionic conductivity and low cost of electrolyte materials, which results in high supercapacitive performance [10, 11]. On the other hand, the solid SC device is

constructed by incorporating a polymer gel electrolyte in between the cathode and anode [12, 13]. Hybrid solid-state supercapacitors (HSSc) offer advantages such as improved stability, enhanced safety, leakage-free packaging, and the possibility of miniaturization. Although the  $C_{sp}$  of the solid device was slightly lower compared to the aqueous device, it still demonstrated significant energy storage capability [14]. Overall, both the aqueous and solid supercapacitor devices showed promise in terms of energy storage performance. While the aqueous device exhibited slightly higher  $C_{sp}$ , the solid device offered the advantages of solid-state construction, which may be more suitable for certain applications that require stability and safety [15]. The choice between the two types of devices would depend on the specific requirements and constraints of the intended application.

### **5.2.A.2 Experimental Details**

#### **5.2.A.2.1 Electrode preparation**

Based on the findings from Chapters III and IV, the optimal NVO/rGO composite electrodes are selected for the fabrication of the devices. These selected NVO/rGO composite (cathode) electrodes are synthesized employing CBS and SILAR methods, following the preparative conditions explained in the aforementioned chapters. While fabrication of solid-state devices large area deposition is required so these methods are applied to a large SS substrate, covering an area of  $4 \times 4 \text{ cm}^2$ . Furthermore, in accordance with section B, subsection 3.3.B.2.2 of chapter III, the anode composed of rGO is also prepared over a large area of  $4 \times 4 \text{ cm}^2$ . Additionally, the primary crucial step prior to fabricating the hybrid device involves ensuring the equilibrium of charges on both electrodes to optimize electrochemical performance [16, 17]. Subsequently, the mass loading of each electrode was calculated using the following formula,

$$\frac{m_+}{m_-} = \frac{C_{sp-} \times \Delta V_-}{C_{sp+} \times \Delta V_+} \quad (5.1)$$

Where,  $m_{(+/-)}$  is the mass of active material,  $C_{sp (+/-)}$  is the specific capacitance, and  $\Delta V_{(+/-)}$  is the potential window of cathode and anode materials. The adjustments were made to balance charges due to differing  $C_{sp}$  and operating potential windows for both electrodes.

#### **5.2.A.2.2 Fabrication of hybrid aqueous supercapacitor devices**



In the fabrication of HASc device, a fundamental prerequisite is that the electrodes have dissimilar charge storage mechanisms (Pseudocapacitive and EDLC) within both the cathode and anodes [18]. Therefore, in this study, a HASc device was constructed utilizing best-performed CBS and SILAR synthesized NVO/rGO composite electrodes (C-rNV3 and S-rNV3) as the cathode, and anode schematically shown in Figure 5.1. These electrodes were immersed in a 1 M potassium hydroxide (KOH) electrolyte solution. Subsequent testing encompassed various electrochemical parameters to evaluate device performance thoroughly.

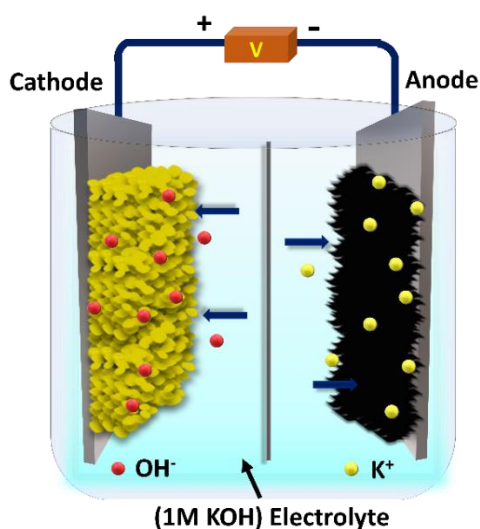


**Figure 5.1:** Schematic representation of HASc device

#### 5.2.A.2.3 Preparation of gel electrolyte

Considerable endeavors have been dedicated to enhancing the utilization of hybrid devices through the use of polyvinyl alcohol-potassium hydroxide (PVA-KOH) solid-state gel electrolyte, which enables operation at elevated voltage [19]. Polymer gel electrolytes represent a unique state of matter, exhibiting characteristics that bridge the properties of liquids and solids. Specifically, they manifest both cohesive and diffusive attributes, facilitating ion transport while maintaining structural integrity [20]. This distinctive property profile renders polymer gel electrolytes particularly advantageous in hybrid device configurations, allowing for enhanced capacitance and expanded operational parameters [21].

The preparation of the PVA-KOH gel proceeded as follows: Initially, 3 grams of PVA were dissolved in 30 mL of DDW under heat, maintaining a temperature of 90°C while ensuring continuous stirring until the solution achieved clarity and transparency. Subsequently, a separate solution of 1 M KOH was prepared. This

KOH solution was then combined with the aforementioned transparent solution of PVA and water, and the resulting mixture was stirred continuously until it exhibited a viscous consistency at ambient conditions [22]. The transparent and viscous gel obtained, known as PVA-KOH, serves the dual function of a separator and an electrolyte in the fabrication of solid-state devices.

#### 5.2.A.2.4 Fabrication of hybrid solid-state supercapacitor devices

To fabricate the hybrid device, NVO/rGO composite electrodes are prepared through CBS and SILAR methods as the cathode, and the rGO electrode is utilized as the anode, alongside a PVA-KOH gel electrolyte, as depicted in schematic 5.2. A HSSc device was assembled employing large-area ( $4 \times 4 \text{ cm}^2$ ) NVO/rGO composite and rGO electrodes.

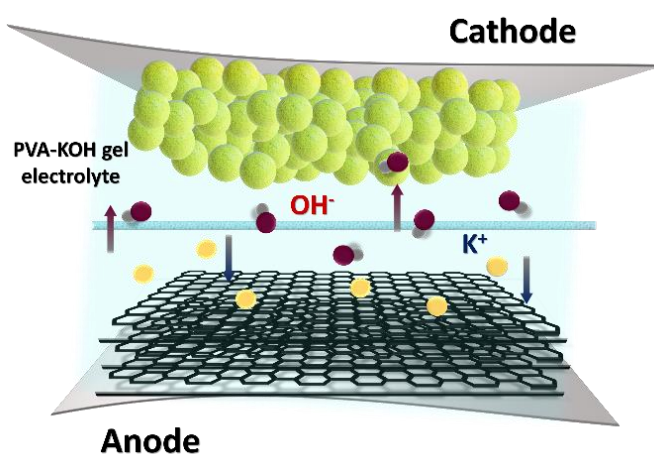


**Figure 5.2:** (a) Schematic representation of a HSSc device

The electrodes were coated with gel electrolyte to form a thin layer and subsequently air-dried at ambient conditions. Insulating tape was employed to seal the edges of the electrodes to prevent any lateral electrical shorting. Following this, the electrodes were combined to form the solid-state device with gel electrolyte, and the assembly was further encased with plastic tape. Finally, the fabricated device underwent a pressing process under 0.5-ton pressure for 2 hours to enhance the interfacial contact between the gel electrolyte and the active electrode materials, resulting in the successful fabrication of the solid-state device.

### 5.3 Section B

## Electrochemical Performance Evaluation of Hybrid Aqueous and Solid-State Devices using CBS Synthesized C-rNV3 Cathodes (C-rNV3//rGO)

### 5.3.B.1 Electrochemical performance of C-rNV3//KOH//rGO hybrid aqueous supercapacitor (C-HASc) device

The development of the C-HASc device, the best-performed C-rNV3 electrode (as discussed in chapter III, section C, subsection 3.4.C.2.2) is used as a cathode, and rGO coated SS substrate is utilized as an anode in 1 M KOH electrolyte. The structural and electrochemical analysis of the capacitive type rGO electrode is carried out and provided in chapter III, section B. To achieve the maximum energy-storing capacity of the C-rNV3//KOH//rGO HASc device, both electrodes are coupled with an appropriate mass ratio derived using the mass balancing equation (equation 5.1). The optimum voltage of the prepared C-rNV3//PVA-KOH//rGO HASc device was determined by measuring CV curves at  $50 \text{ mV s}^{-1}$  and GCD curves at  $3 \text{ A g}^{-1}$  within different upper cutoff voltages in the 1.2 to 1.7 V range, as shown in Figure 5.3. The maximum cell voltage is extended up to 1.6 V; afterward, the oxygen evolution mechanism causes a dramatic spike in current.

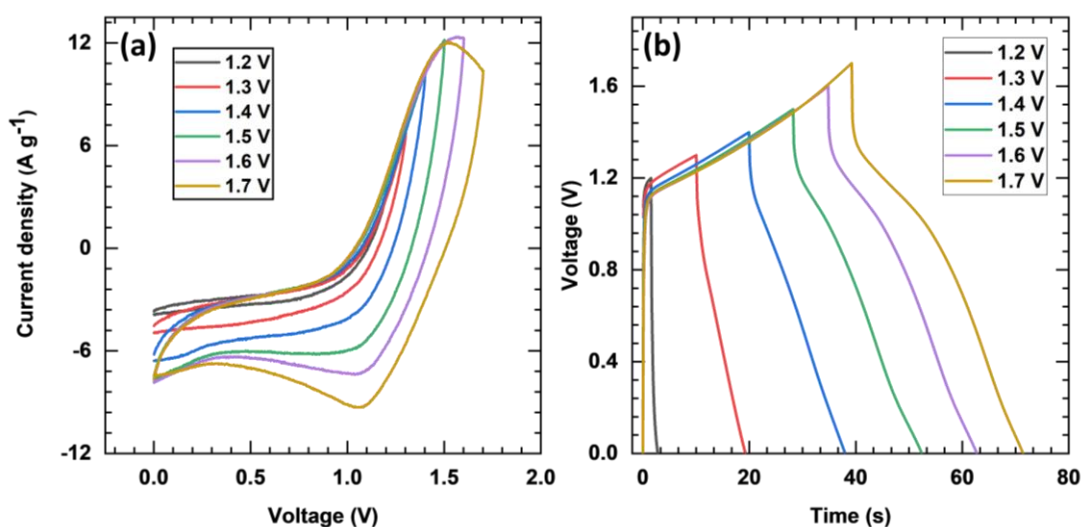


**Figure 5.3:** (a) CV and (b) GCD curves of C-HASc device at different voltages

The CV plots for the C-HASc device were recorded in a 0-1.6 V voltage window at various scan rates of 5 to  $100 \text{ mV s}^{-1}$ , as shown in Figure 5.4 (a). The

similar trend of CV curves at higher scan rates implies that the device can withstand higher scan rates. Also, it can be seen that the current response under CV increases with the increasing scanning rate. Figure 5.4 (b) depicts GCD curves for the C-HASc device at distinct current densities from 3 to 7 A g<sup>-1</sup>. The nearly similar and non-linear trend of GCD curves was observed for the C-HASc device, confirming the hybrid charge storage mechanisms of the prepared C-HASc device.

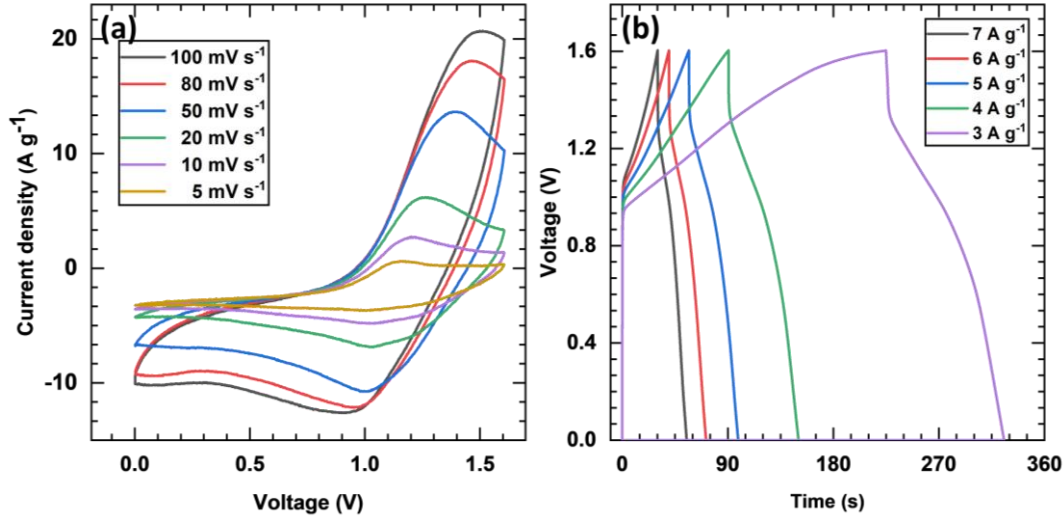


**Figure 5.4:** (a) CV curves at different scan rates and (b) GCD curves at different current densities for C-HASc device.

The following equation was used to calculate the total  $C_{sp}$  of the device from charge-discharge curves:

$$C_{sp} = \frac{I \times \Delta t}{M \times \Delta V} \quad (5.2)$$

All notations were considered the same as used for equation (2.10), excluding ‘M’, which symbolizes the total mass of the device (sum of the mass of both cathode and anode). The C-HASc device reaches  $C_{sp}$  as high as 122 F g<sup>-1</sup> at 3 A g<sup>-1</sup> current density and retains up to 69 F g<sup>-1</sup> for 7 A g<sup>-1</sup> current density. The calculated  $C_{sp}$  values from GCD curves are plotted against the current densities in Figure 5.5 (a).

The SE (Wh kg<sup>-1</sup>) and SP (kW kg<sup>-1</sup>) of the devices were calculated by using the following equations:

$$SE = \frac{1}{2} \times \frac{1}{3600} C_{sp} \times V^2 \quad (5.3)$$

$$SP = 3.6 \times \frac{E}{\Delta t} \quad (5.4)$$

Where,  $C_{sp}$  is the specific capacitance,  $V$  signifies the potential window, and  $\Delta t$  denotes the discharging time. The C-HASc device can achieve a maximum SE of  $43.4 \text{ Wh kg}^{-1}$  at an SP of  $1.57 \text{ kW kg}^{-1}$  and retaining SE of  $24.5 \text{ Wh kg}^{-1}$  at an SP of  $3.68 \text{ kW kg}^{-1}$ , as revealed in Ragone plot (Figure 5.5 (b)).

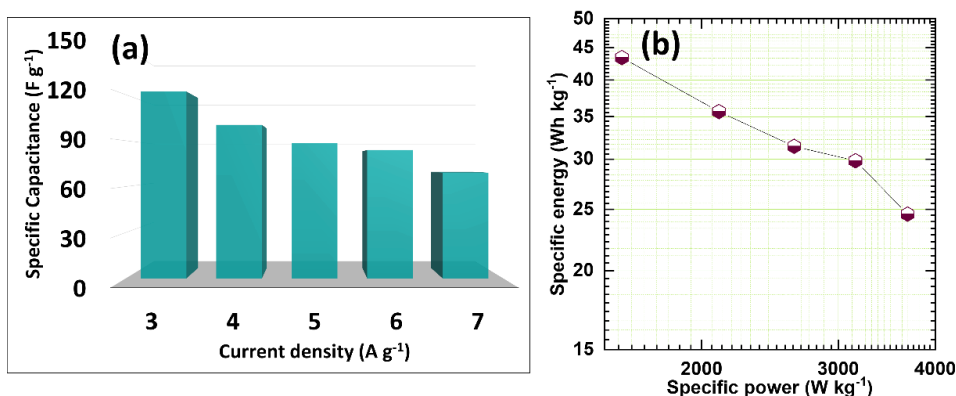


**Figure 5.5:** (a) Plot of  $C_{sp}$  as a function of current density and (b) Ragone plot for C-HASc device

The EIS study further provides more information about the charge transfer kinetics in C-HASc device. The Nyquist plot for C-HASc device shown in Figure 5.6 (a) demonstrated good electrical/ionic conductivity and interface between material and electrolyte as displayed in terms of lower  $R_s$  ( $3.01 \Omega \text{ cm}^{-2}$ ) and  $R_{ct}$  ( $111.03 \Omega \text{ cm}^{-2}$ ) values. Additionally, the C-HASc device cycled up to 5000 cycles at  $4.5 \text{ A g}^{-1}$  to check the cyclic stability, and it was found that the C-HASc device sustained  $\sim 85\%$  of its initial capacitance (Figure 5.6 (b)). Also, the device maintained  $\sim 82.7\%$  coulombic efficiency after 5000 GCD cycles.

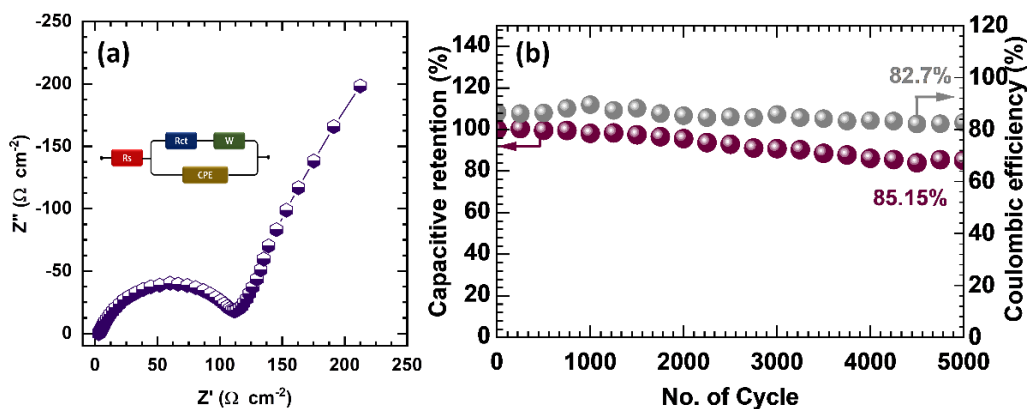


**Figure 5.6:** (a) Nyquist plot of C-HASc device and (b) plot of capacitive retention and coulombic efficiency vs number of cycles

### 5.3.B.2 Electrochemical performance of C-rNV3//PVA-KOH//rGO hybrid solid-state supercapacitor (C-HSSc) device

The C-HSSc device was fabricated using a C-rNV3 electrode as a cathode, rGO as an anode, and a prepared gel of PVA-KOH utilized as a quasi-solid electrolyte, as illustrated in Figure 5.7.

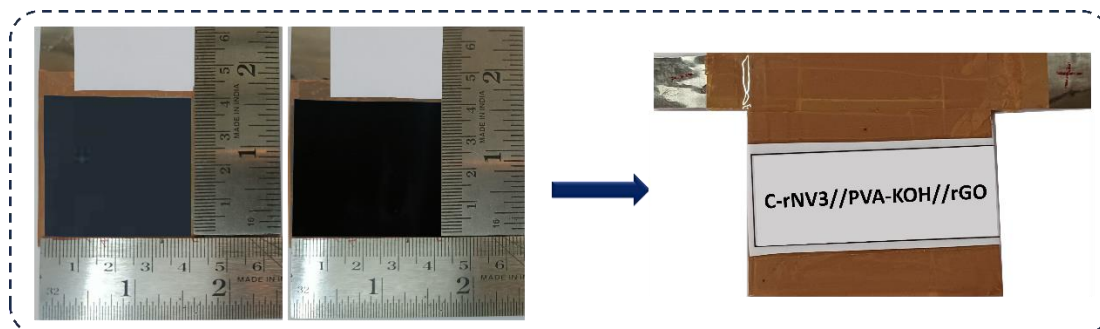


**Figure 5.7** Photograph of solid-state device fabrication

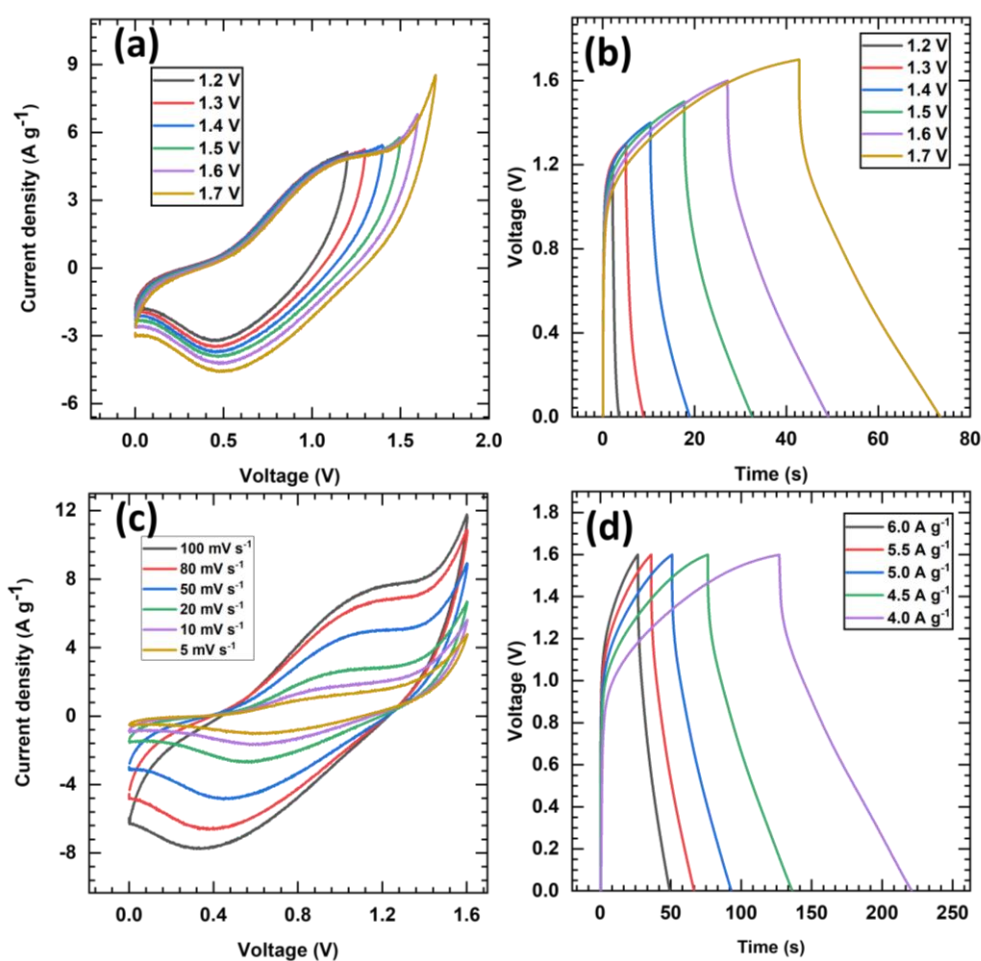


**Figure 5.8:** (a) CV and (b) GCD curves at different voltage windows (c) CV curves at different scan rates and (d) GCD curves at different current densities for C-HSSc device



The CV and GCD profiles in various voltage windows from 0 to 1.2-1.7 V for the C-HSSc device are shown in Figure 5.8 (a and b). The equal potential of both electrodes initiates the discharging process, taking into account that the oxidation potential of C-rNV reaches up to 0.6 V, and the full reduction potential of rGO requires 1 V; hence, it takes 1.6 V to charge the C-HSSc device completely. So, further electrochemical study of the C-HSSc device is carried out in the optimized voltage window of 0 to 1.6 V. The quasi-rectangular CV curves of the C-HSSc at various sweep rates within the 0 to 1.6 V window are recorded and depicted in Figure 5.8 (c). The GCD curves were plotted in the range of current densities 4 to 6 A g<sup>-1</sup> and are shown in Figure 5.8 (d).

The calculated maximum  $C_{sp}$  of the C-HSSc is found to be 98.3 F g<sup>-1</sup> at 4 A g<sup>-1</sup> current density, and it decreases up to 34 F g<sup>-1</sup> at high current density of 6 A g<sup>-1</sup> as shown in Figure 5.9 (a). Furthermore, SE and SP are the most critical factors for assessing the practical performance of HSDs. In this context, calculated SE and SP at an operating voltage of 1.6 V are plotted in the Ragone plot (Figure (5.9 (b)). The estimated maximum SE is 34.9 Wh kg<sup>-1</sup> at an SP of 1.15 kW kg<sup>-1</sup>. Moreover, the SE still sustains up to 13.8 Wh kg<sup>-1</sup> and provides a maximum SP of 2.26 kW kg<sup>-1</sup>.

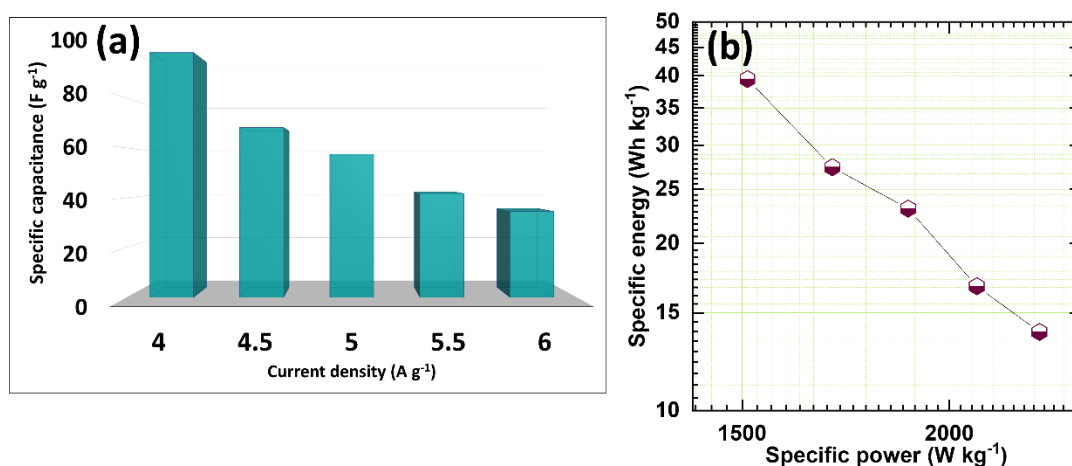


**Figure 5.9:** (a) Plot of  $C_{sp}$  as a function of current density and (b) Ragone plot for C-HSSc device

The complex plane EIS spectrum of the C-HSSc is plotted in Figure 5.10 (a), and the fitted equivalent model for experimental data is provided in the inset of the figure. The obtained Nyquist plot for the C-rNV3//PVA-KOH//rGO HSSc device revealed good material and electrolyte interface and electrical/ionic conductivity, which was confirmed by the lower  $R_s$  (1.72  $\Omega$  cm<sup>-2</sup>) and  $R_{ct}$  (104  $\Omega$  cm<sup>-2</sup>) values.



In addition, the cycling stability of C-HSSc device was investigated for 5000 GCD cycles at a current density of  $8 \text{ A g}^{-1}$ . After completing 5000 charge-discharge cycles, the C-rNV3//PVA-KOH//rGO HSSc device retained 69.2% of its initial capacitance along with the excellent coulombic efficiency of 89.3%, as provided in Figure 5.10 (b). The excellent supercapacitive performance of fabricated C-HSSc device leads us to consider its possible commercial prospect by glowing the white light emitting diode (LED) lamp, and two series-connected devices lightened white LED lamp up to  $\sim 60 \text{ s}$  after charging for 30 s, as depicted in Figure 5.10 (c).

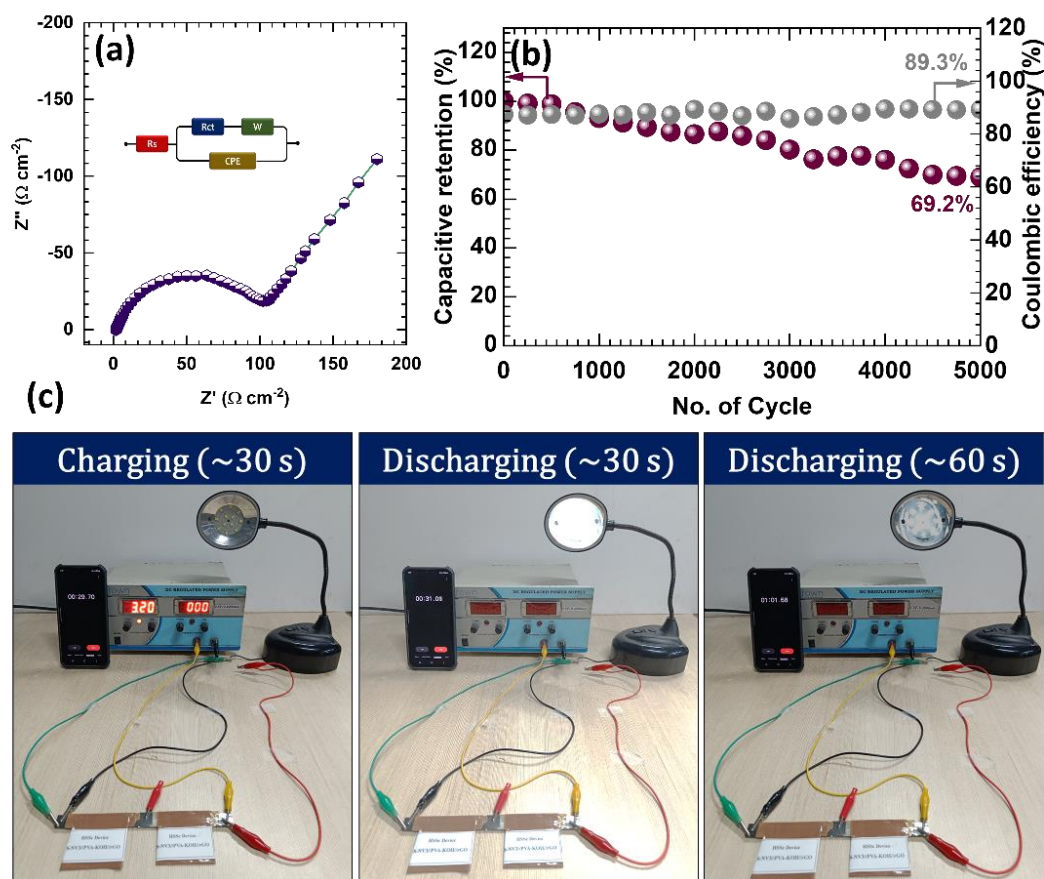


**Figure 5.10:** (a) Nyquist plot of C-HSSc device, (b) plot of capacitive retention and coulombic efficiency vs cycle number, (c) demonstration of glowing LED table lamp using serially connected C-HSSc devices

## 5.4 Section C

### Electrochemical Performance Evaluation of Hybrid Aqueous and Solid-State Devices using SILAR Synthesized S-rNV3 Cathodes (S-rNV3//rGO)

#### 5.4.C.1. Electrochemical performance of S-rNV3//KOH//rGO hybrid aqueous supercapacitor (S-HASc) device

The best-performing S-rNV3 electrode (as discussed in Chapter IV, section B, subsection 4.3.B.2.2) was used as the cathode, and the rGO (Chapter III, section B) electrode was used as an anode in a 1 M KOH electrolyte to construct S-HASc. To investigate the optimum voltage window of as assembled S-HASc device, the CV curves were recorded at different voltage ranges from 1.2 to 1.8 V at  $50 \text{ mV s}^{-1}$  as presented in Figure 5.11 (a).

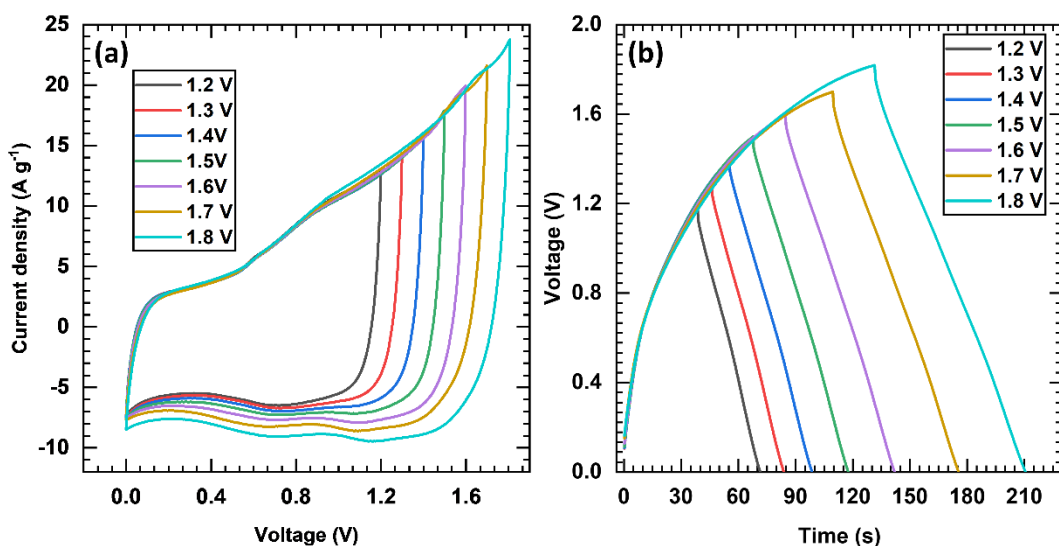


**Figure 5.11:** (a) CV and (b) GCD curves of S-HASc device at different voltage windows

From Figure 5.11 (a), it is observed that the extension of voltage ranges from 1.2 to 1.8 V, gradually increasing the area under the CV curve. However, deviation from the actual CV curve is observed after 1.7 V, possibly due to water-splitting reactions. Similar results are also noticed while recording the GCD curves (Figure 5.11 (b)) at different potential windows. Hence, for further analysis of the S-HASc device, the optimal potential window of 0-1.7 V is considered.

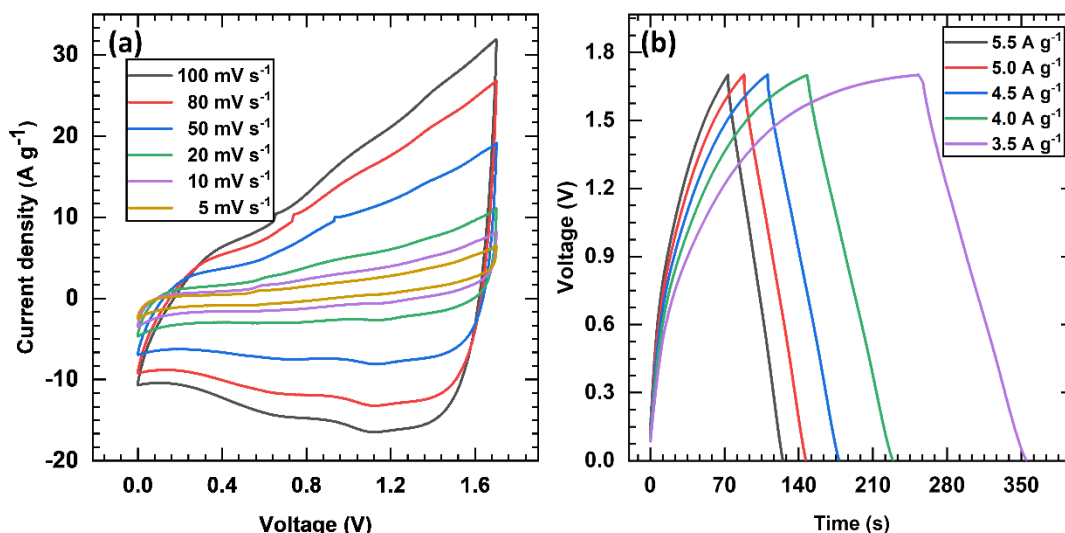


**Figure 5.12:** (a) CV curves at different scan rates and (b) GCD curves at different current densities for S-HASc device

The CV curves of the S-HASc device are recorded at different scan rates (5–100 mV s<sup>-1</sup>), as presented in Figure 5.12 (a). It can be observed from the CV curves that the current density response increases with the scan rate and maintains the quasi-rectangular shape even at higher scan rates. Moreover, GCD curves recorded at various current densities of 3.5 to 5.5 A g<sup>-1</sup> presented in Figure 5.12 for the S-HASc device show a similar and non-linear trend, indicating the hybrid charge storage mechanisms of the S-HASc device.

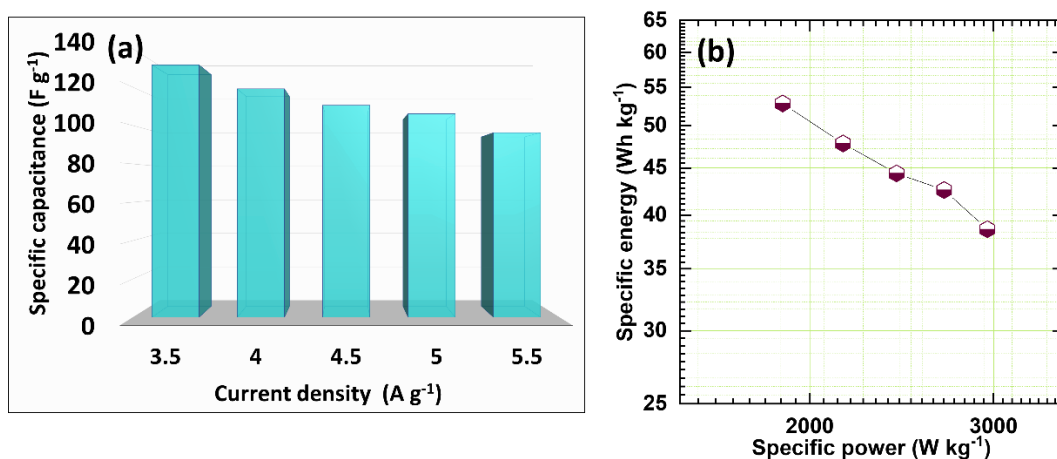


**Figure 5.13:** (a) Plot of  $C_{sp}$  as a function of current density and (b) Ragone plot for S-HASc device

The  $C_{sp}$  is calculated using Equation 5.2, and the obtained values are plotted as a function of current densities in Figure 5.13 (a), where the obtained maximum  $C_{sp}$

value for the S-HASc device is  $131.6 \text{ F g}^{-1}$  at  $3.5 \text{ A g}^{-1}$  current density. Moreover, SE and SP for the S-HASc device are calculated using Equations 5.3 and 5.4. The fabricated S-HASc device exhibited a maximum SE of  $52.8 \text{ Wh kg}^{-1}$  at an SP of  $1.88 \text{ kW kg}^{-1}$  and maintained  $38.6 \text{ Wh kg}^{-1}$  SE even at a high SP of  $2.95 \text{ kW kg}^{-1}$  as shown in the Ragone plot in Figure 5.13 (b).

Furthermore, the ion transfer properties in the S-HASc device are investigated using EIS analysis. The Nyquist plot of the prepared S-HASc device is shown in Figure 5.14, and the corresponding fitted Randel's circuit is shown in the inset. The lower values of  $R_s$  ( $2.6 \Omega \text{ cm}^{-2}$ ) and  $R_{ct}$  ( $39.8 \Omega \text{ cm}^{-2}$ ) confirmed the excellent material and electrolyte interface and electrical/ionic conductivity. In addition, the cycling stability of the HASc device was investigated for 5000 charge-discharge cycles at a current density of  $8 \text{ A g}^{-1}$ . After successfully completing 5000 charge-discharge cycles, the HASc device retained  $\sim 87.7\%$  of its initial capacitance along with the excellent coulombic efficiency of  $\sim 84.2\%$ , as provided in Figure 5.14 (b).

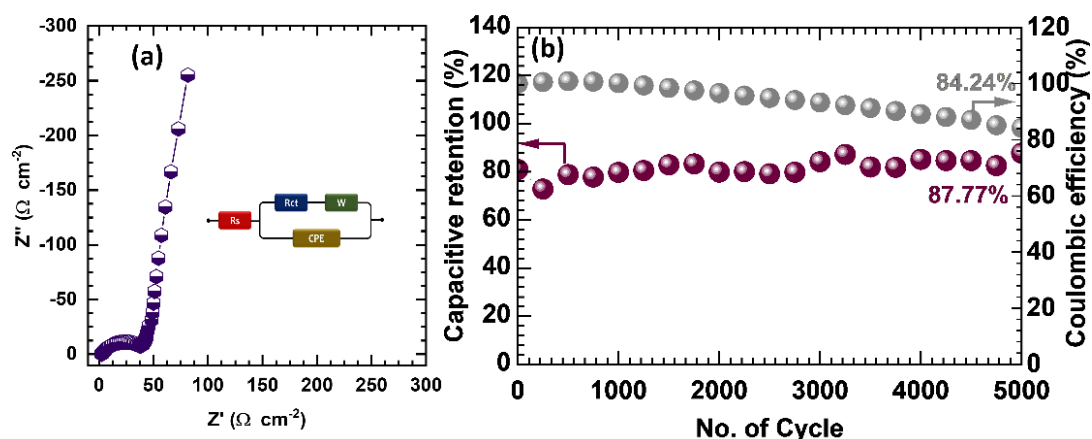


**Figure 5.14:** (a) Nyquist plot of S-HASc device and (b) Plot of capacitive retention and coulombic efficiency vs number of cycles

#### 5.4.C.2. Electrochemical performance of S-rNV3//PVA-KOH//rGO hybrid solid-state supercapacitor (S-HSSc) device

In addition to aqueous devices, S-HSSc has drawn a lot of interest as a promising field for research and development due to their many benefits, including their leakage-free properties and lightweight design that make them easy to handle. The S-HSSc device was fabricated using an S-rNV3 ( $4 \times 4 \text{ cm}^2$ ) electrode as the cathode and rGO as an anode, as illustrated in Figure 5.15.

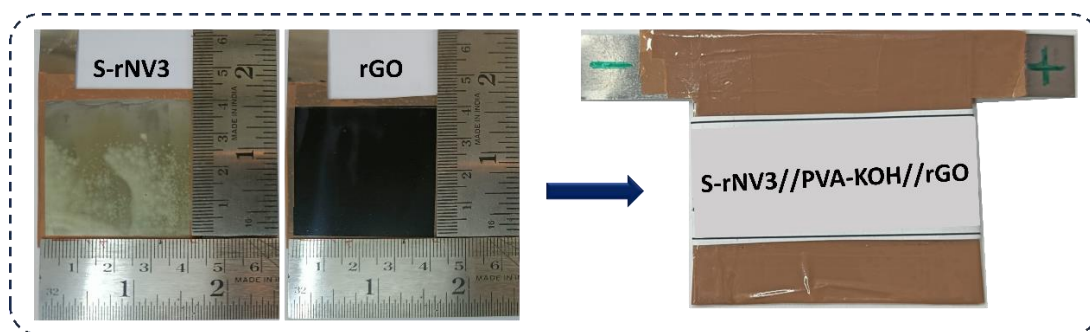


**Figure 5.15** Photograph of solid-state device fabrication

Like the S-HASSc device, the S-HSSc device also maintained a voltage windows of 0 to 1-1.7 V without suffering from electrolysis, as shown in Figure 5.16 (a and b). Hence, the CV measurements at various scan rates (5-100  $\text{mV s}^{-1}$ ) were recorded at a similar voltage range. The CV curves for the S-HSSc device in Figure 5.16 (c) show a quasi-rectangular shape even at the highest scan rate of 100  $\text{mV s}^{-1}$ .

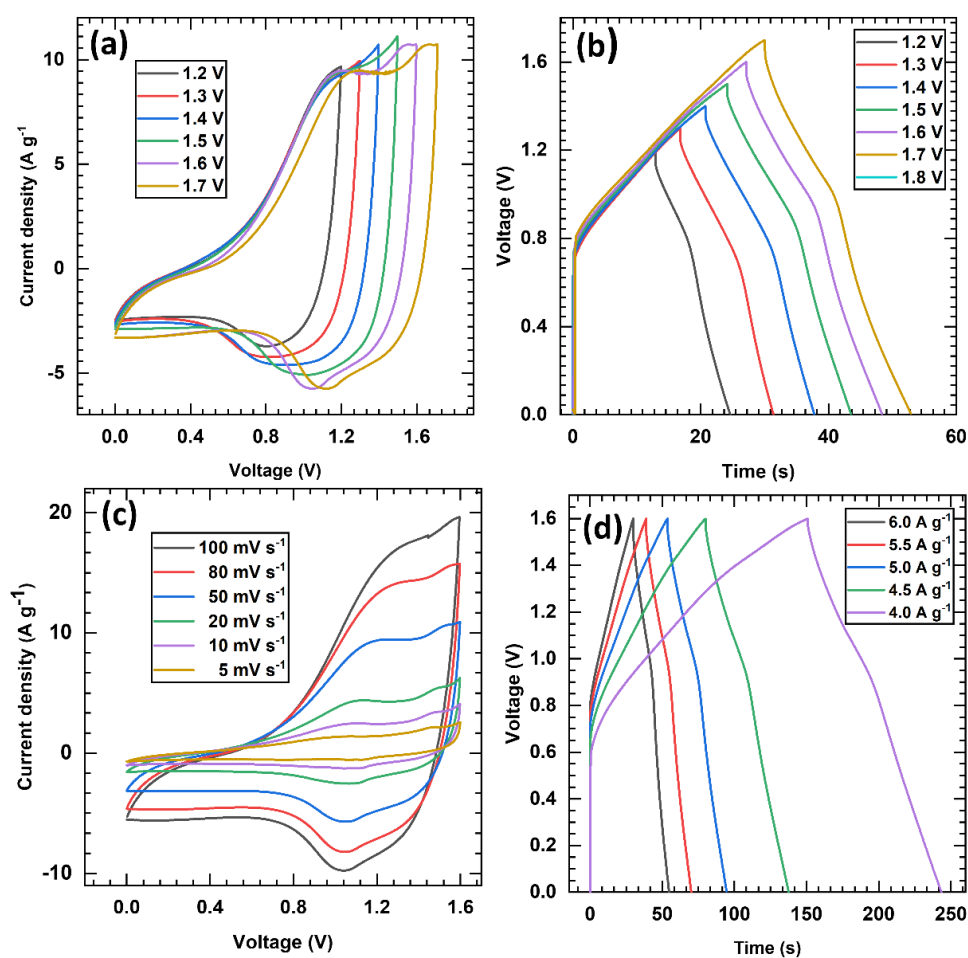


**Figure 5.16** (a) CV and (b) GCD curves at different voltage windows, (c) CV curves at different scan rates, and (d) GCD curves at different current densities for S-HSSc device

Furthermore, the GCD curves for the S-HSSc device at various current densities (4.0-6.0 A g<sup>-1</sup>) are shown in Figure 5.16 (d). The calculated  $C_{sp}$  values vs the current density is shown in Figure 5.17 (a); the  $C_{sp}$  values for the HSSc device were 111 F g<sup>-1</sup> at a current density of 4 A g<sup>-1</sup> and 66 F g<sup>-1</sup> at the maximum current density of 6 A g<sup>-1</sup>. Apart from  $C_{sp}$ , SE and SP are also calculated and displayed in the Ragone plot (Figure 5.17 (b)), where the fabricated S-HSSc device achieves SE of 46 Wh kg<sup>-1</sup> at an SP of 1.184 kW kg<sup>-1</sup> and sustains the SE of 26 Wh kg<sup>-1</sup> at a maximum SP of 2.3 kW kg<sup>-1</sup>.

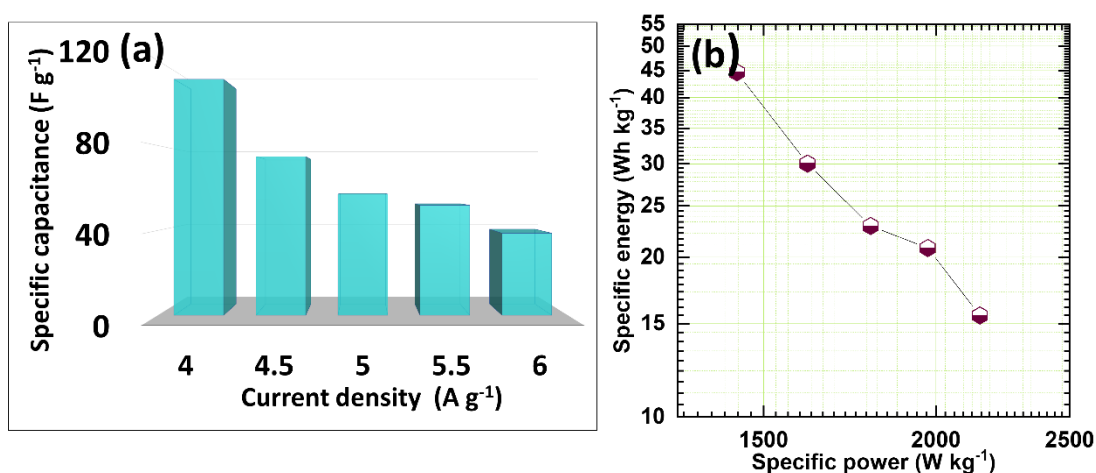


**Figure 5.17:** (a) Plot of  $C_{sp}$  as a function of current density and (b) Ragone plot for S-HSSc device

The EIS study also provides more details regarding the charge transfer kinetics in S-HSSc device. The obtained Nyquist plot is provided in Figure 5.18 (a), and it is fitted with Randel's circuit, which is provided in the inset of the figure. The obtained value for  $R_s$  is 0.16  $\Omega$  cm<sup>-2</sup>, along with a lower  $R_{ct}$  of 126.7  $\Omega$  cm<sup>-2</sup>. The lower values of  $R_s$  and  $R_{ct}$  suggest a quick charge transfer response and good electrical conductivity. The durability of the device is an essential parameter when it comes to practical application. Hence, the cycling stability of the prepared S-HSSc device was investigated at a constant current density of 7 A g<sup>-1</sup> for 5000 GCD cycles, as shown in Figure 5.18 (b). Acquiring benefits from the S-rNV3 (cathode), which provides high electroactivity with reversible battery-type behavior and capacitive nature of rGO (anode), the prepared S-HSSc device yielded 89.5% retention of its initial capacitance along with excellent coulombic efficiency of ~89.1% after 5000 GCD cycles.



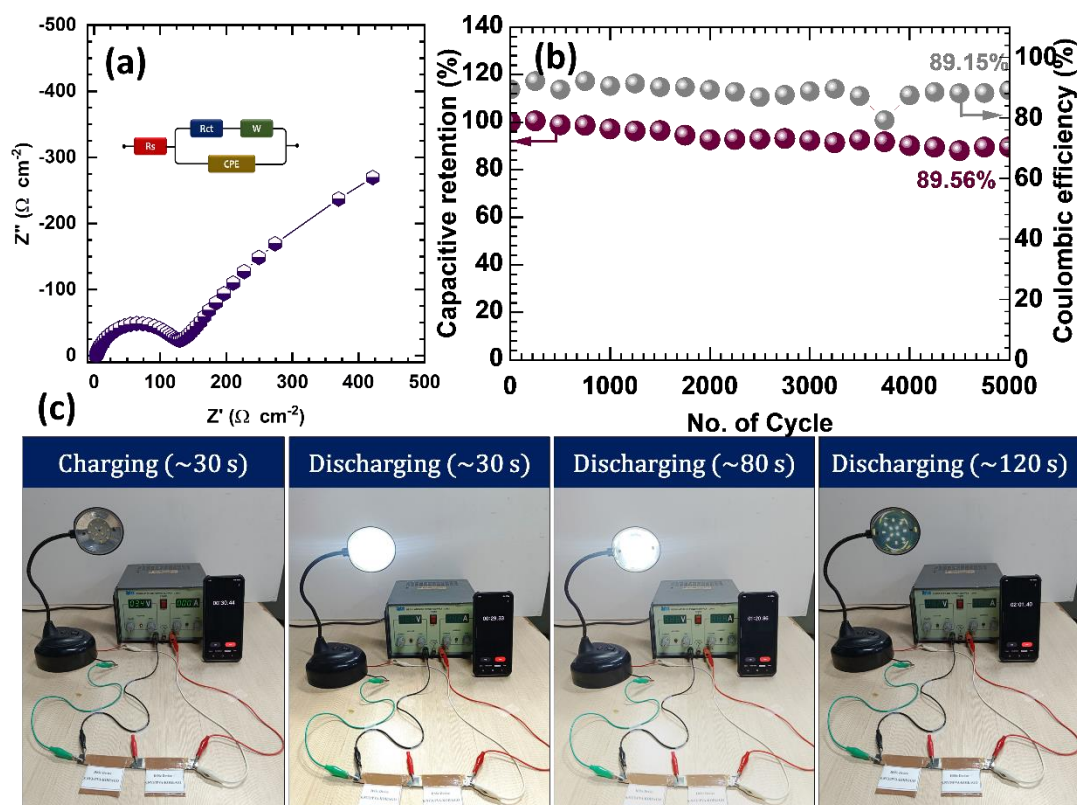


**Figure 5.18:** (a) Nyquist plot of S-HSSc device (b) plot of capacitive retention and coulombic efficiency vs number of cycles, and (c) demonstration of powering an LED table lamp using two serially connected S-HSSc devices

The collective findings highlight that the fabricated S-HSSc device is a viable option for real-world energy storage applications. A white LED lamp was examined to confirm its power capacity. In this endeavor, two S-HSSc devices were connected in series and charged for 30 seconds at a constant voltage of 3.4 V, then discharged through the white LED lamp. As shown in Figure 5.18 (c), the charged S-HSSc devices could light up the white LED lamp for approximately 120 seconds.

The SILAR synthesized NVO/rGO composite electrode exhibits superior performance as a cathode in HSC devices than the cathodes prepared by the CBS method. Moreover, the S-HASc device demonstrates competitive energy storage performance than the SC devices fabricated using NVO-based electrodes in the literature provided in Chapter I Table No. 1.3. Among several reports [23-33], only a few devices achieved higher performance than the present study such as Sahoo et al. [25] prepared  $\text{Ni}_3\text{V}_2\text{O}_8\text{@MWCNT//}\beta\text{FeOOH@rGO}$ , Guo et al. [27] prepared  $\text{Ni}_3\text{V}_2\text{O}_8\text{/NG//Fe}_2\text{VO}_4\text{/NG}$ , Hou et al. [30] prepared  $\text{Ni}_3\text{V}_2\text{O}_8\text{@Co-B//AC}$  and Magadum et al. [33] prepared  $\text{Ni}_2\text{V}_2\text{O}_7\text{/NF//AC/NF}$ , which could be because they



used NF and MWCNT as a current collector, which may contribute to enhance the capacitance of the electrode by contributing their self-charge storing capacity. In contrast, the SE values achieved for the S-HASc and S-HSSc devices in the current study were solely due to the NVO/rGO electrodes. The collective findings highlight that the fabricated S-HSSc device is a viable option for real-world energy storage applications.

## 5.5 Conclusions

Hybrid aqueous and solid-state devices are successfully fabricated using NVO/rGO composite electrodes, which are prepared using both CBS and SILAR methods. The prepared NVO/rGO composite electrodes were utilized as a cathode and rGO as an anode. The CBS NVO/rGO composite based aqueous device C-HASc exhibited a maximum  $C_{sp}$  of  $122 \text{ F g}^{-1}$  along with an SE of  $43.4 \text{ Wh kg}^{-1}$  at an SP of  $1.57 \text{ kW kg}^{-1}$ . Also, the prepared solid-state device C-HSSc comprising the C-rNV3 electrode achieves a maximum  $C_{sp}$  of  $98.3 \text{ F g}^{-1}$  with an SE and SP of  $34.9 \text{ Wh kg}^{-1}$  and  $1.15 \text{ kW kg}^{-1}$ , respectively. Additionally, the SILAR-deposited NVO/rGO composite-based aqueous S-HASc device delivers a maximum  $C_{sp}$  of  $131.6 \text{ F g}^{-1}$  along with a SE of  $52.8 \text{ Wh kg}^{-1}$  at a SP of  $1.88 \text{ kW kg}^{-1}$ . Moreover, the fabricated S-HSSc device exhibited a maximum  $C_{sp}$  of  $111 \text{ F g}^{-1}$  along with SE of  $44.5 \text{ Wh kg}^{-1}$  at an SP of  $1.43 \text{ kW kg}^{-1}$ . The S-rNV3 electrode showed remarkable electrochemical activity in S-HASc and S-HSSc devices, demonstrating the potential for use in various electronic devices. The SILAR deposited NVO/rGO based both aqueous and solid-state devices exhibited excellent electrochemical performance in terms of  $C_{sp}$ , SE, and SP along with superior cyclic stability, suggesting the prepared S-rNV3 material is a prominent candidate as a cathode in hybrid devices.

## 5.6 References

- [1] J. Zhang, M. Gu, X. Chen, *Micro Nano Eng.*, 21 (2023) 100229.
- [2] Poonam, K. Sharma, A. Arora, S. Tripathi, *J. Energy Storage*, 21 (2019) 801–825.
- [3] M. Yaseen, M. Khattak, M. Humayun, M. Usman, S. Shah, S. Bibi, B. Hasnain, S. Ahmad, A. Khan, N. Shah, A. Tahir, H. Ullah, *Energies*, 14 (2021) 1–40.
- [4] M. Amir, R. Deshmukh, H. Khalid, Z. Said, A. Raza, S. Muyeen, A. Nizami, R. Elavarasan, R. Saidur, K. Sopian, *J. Energy Storage*, 72 (2023) 108694.
- [5] M. Iqbal, M. Faisal, S. Ali, *Int. J. Energy Res.*, 45 (2021) 1449–1479.
- [6] N. Choudhary, C. Li, J. Moore, N. Nagaiah, L. Zhai, Y. Jung, J. Thomas, *Adv. Mater.*, 29 (2017) 605336.
- [7] B. Pal, S. Yang, S. Ramesh, V. Thangadurai, R. Jose, *Nanoscale, Adv.* 1 (2019) 3807–3835.
- [8] Z. Iro, C. Subramani, S. Dash, *Int. J. Electrochem. Sci.*, 11 (2016) 10628–10643.
- [9] A. Muzaffar, M. Ahamed, K. Deshmukh, J. Thirumalai, *Renew. Sustain. Energy Rev.*,

- 101 (2019) 123–145.
- [10] A. Mendhe and H. Panda, *Discov. Mater.*, 3 (2023) 29-55.
- [11] S. Zhang, B. Yin, X. Liu, D. Gu, H. Gong, Z. Wang, *Nano Energy*, 59 (2019) 41–49.
- [12] A. Obeidat, M. Gharaibeh, M. Obaidat, *J. Energy Storage*, 13 (2017) 123–128.
- [13] S. Kumbhar, S. Bhosale, S. Pujari, V. Patil, N. Kumar, R. Salunkhe, C. Lokhande, U. Patil, *Energy Technol.*, 11 (2023) 1–16.
- [14] S. Bhosale, S. Kumbhar, S. Pujari, V. Patil, N. Kumar, R. Salunkhe, C. Lokhande, J. Gunjekar, U. Patil, *J. Energy Storage*, 72 (2023) 108417.
- [15] M. Han, X. Wang, C. Chen, M. Zou, Z. Niu, Q.H. Yang, A. Cao, L. Song, J. Chen, S. Xie, *Energy Storage Mater.*, 13 (2018) 119–126.
- [16] J. Feng, N. Chernova, F. Omenya, L. Tong, A. Rastogi, M. Whittingham, *J. Solid State Electrochem.*, 22 (2018) 1063–1078.
- [17] S. Marje, S. Pujari, S. Khalate, V. Patil, V. Parale, T. Kim, H. Park, J. Gunjekar, C. Lokhande, U. Patil, *J. Mater. Chem. A*, 10 (2022) 11225–11237.
- [18] D. Dubal, O. Ayyad, V. Ruiz, P. Gómez-Romero, *Chem. Soc. Rev.*, 44 (2015) 1777–1790.
- [19] G. Ma, J. Li, K. Sun, H. Peng, J. Mu, Z. Lei, *J. Power Sources*, 256 (2014) 281–287.
- [20] K. Aruchamy, S. Ramasundaram, S. Divya, M. Chandran, K. Yun, T. Oh, *Gels*, 7 (2023) 585-623.
- [21] S. Alipoori, S. Mazinani, S. Aboutalebi, F. Sharif, *J. Energy Storage*, 27 (2020) 101072.
- [22] P. Katkar, S. Marje, V. Parale, C. Lokhande, J. Gunjekar, H. Park, U. Patil, *Langmuir*, 37 (2021) 5260–5274.
- [23] Y. Li, H. Sun, Y. Yang, Y. Cao, W. Zhou, H. Chai, *J. Colloid Interface Sci.*, 580 (2020) 298–307.
- [24] D. Merum, R. Nallapureddy, M. Pallavolu, T. Mandal, R. Gutturu, N. Parvin, A. Banerjee, S. Joo, *ACS Appl. Energy Mater.*, 5 (2022) 5561-5578.
- [25] R. Sahoo, A. Pal, T. Pal, *J. Mater. Chem. A*, 4 (2016) 17440–17454.
- [26] R. Kumar, P. Rai, A. Sharma, *J. Mater. Chem. A*, 4 (2016) 9822–9831.
- [27] M. Guo, J. Balamurugan, N. Kim, J. Lee, *Appl. Catal. B Environ.*, 239 (2018) 290–299.
- [28] Q. Zhou, Y. Gong, J. Lin, *J. Electroanal. Chem.*, 823 (2018) 80–91.
- [29] S. Zhao, K. Tao, Y. Gong, *Dalt. Trans.*, 48 (2019) 5315–5326.
- [30] J. Hou, J. Gao, L. Kong, *Electrochim. Acta*, 377 (2021) 138086.
- [31] X. Liu, J. Wang, G. Yang, *ACS Appl. Mater. Interfaces*, 10 (2018) 20688–20695.
- [32] K. Halder, R. Biswas, A. Arya, I. Ahmed, S. Tanwar, A. Sharma, *Energy Storage*, 4 (2022) 1–12.
- [33] M. Magadum, U. Shembade, T. Bhosale, N. Chougale, P. Pawar, T. Dongale, A. Moholkar, *J. Solid State Chem.*, 335 (2024) 124697.

# CHAPTER-VI

---

## Summary and Conclusions

---

Advancements in integrated, wearable, and multifunctional electronics have led to the development of reliable and scalable ESDs, such as rechargeable metal-ion batteries (MIBs) and SCs. However, rechargeable MIBs suffer from slow rate performance and low SP, and the most popular, Li-ion batteries, are challenging to develop, handle, and employ in modern electronics due to their flammability. Conversely, SCs, known for their extended cycle lifespan, safety endurance, high SP, and excellent rate performance, are proficient ESDs. However, conventional surface capacitive charge storage mechanisms limit the feasibility of SCs for practical applications due to their low SE. To make SCs more practicable for real-world applications, extensive research is underway to develop next-generation SCs with superior performance capabilities over the current ones while increasing their energy storage without compromising the power output. There are two ways to increase the amount of SE stored in SCs: improve the cell voltage or increase the capacitance of the energy storage materials. Ideally, both of them should be enhanced since the amount of stored SE in SCs is governed by the relationship  $0.5 CV^2$ . The HSCs are a useful tool for improving both the SE and SP in order to address this problem. They work by combining a capacitive-type anode, which is usually an EDLC electrode that compensates for the high SP and gives a device exceptional rate capability and cyclic durability, with a pseudocapacitive-type cathode that can store charge through reversible faradic reactions to increase energy storage capability.

The electrochemical performance of HSCs is heavily influenced by the physical and electrochemical characteristics of both electrode materials, so rational designing of electrode materials with finely tuned intrinsic properties is essential. Nanostructured cathode materials not only shorten the transportation distance of ions or charges and yield faster diffusion but also provide more active sites for multifarious redox reactions compared to their bulk counterparts. Thus, controlling factors such as the morphology and size of the architecture, as well as the porosity and surface area of the cathode, can improve the electrode performance. The primary objective of this research was to NVO/rGO composite electrodes through simple chemical methods and to develop HSDs. To achieve this, the NVO/rGO composite electrodes were synthesized on conductive SS substrates using CBS and SILAR methods. Additionally, the prepared NVO/rGO electrodes underwent thorough characterization using various physico-chemical analysis techniques. The best-performed electrodes were selected for the fabrication of hybrid aqueous devices

utilizing a 1 M KOH electrolyte, as well as hybrid solid-state devices incorporating a PVA-KOH gel electrolyte. The present thesis comprises six chapters detailing the overview of the literature, methodology, synthesis, characterization, performance evaluation of the prepared electrodes and HSDs, and conclusions.

**Chapter I** initiates with a comprehensive introduction, elucidating the imperative role of SCs in contemporary applications alongside an overview of ongoing advancements and the fundamental operating principles underlying SCs. Moreover, the chapter delves into the classification of SCs based on their distinct charge storage mechanisms. Detailed specifications for a SC utilizing a diverse range of active electrode materials are thoroughly outlined. Moreover, extensive information on the various phases and structures of NVO is provided. Furthermore, the chapter encompasses a detailed literature survey elucidating the utilization of NVO, as well as their composites in SC applications. Concluding this segment, the chapter outlines the main objectives and scope of the theses, establishing the framework for subsequent chapters.

**Chapter II** provides an introduction to nanomaterials and thin films, encompassing various deposition techniques. Theoretical foundations of CBS and SILAR methods are elucidated, covering preparative parameters and advantages. The chapter delves into the operational principles of characterization techniques employed for the analysis of the material, including XRD for structural analysis and FT-IR to study the chemical bonding in the material. Raman analysis for materials chemical structure, XPS for elemental analysis, FE-SEM and HR-TEM for surface morphological investigation, and EDS for elemental mapping. BET for surface area and pore size distribution, and TG analysis to investigate the composition of materials. Moreover, electrochemical techniques for evaluating the electrochemical performance of electrode materials, such as CV, GCD, and EIS, are extensively discussed, elucidating their features in detail.

**Chapter III** focuses on the synthesis, characterization, and electrochemical performance evolution of chemical bath deposited NVO/rGO composite electrodes, segmented into three sections: 'A' 'B', and 'C'. **Section 'A'** entails the synthesis of NVO thin films via a simple and cost-effective CBS method. A conducting and highly stable SS substrates are chosen for deposition, facilitating the direct growth of NVO. The study investigates the influence of varying molar ratios of hydrolyzing agents on the structure and surface morphology of the NVO thin film. XRD and FT-IR analysis

confirms the successful synthesis of  $\text{Ni}_3\text{V}_2\text{O}_8 \cdot n\text{H}_2\text{O}$  material in thin film form; particles like structure are observed in a morphological study, where a reduction in particle size is observed with varying molar concentrations of hydrolyzing agent (urea). Furthermore, the influence of the altered morphology and surface area of synthesized S-NV series electrodes on electrochemical performance was studied. Three electrodes system was used for the supercapacitive performance evaluation. The highest  $C_{\text{sp}}$  of  $692 \text{ F g}^{-1}$  is achieved at  $1 \text{ A g}^{-1}$  current density with 73.3% capacitive retention over 5000 cycles for the C-NV3 electrode. The good electrochemical results concluded that the nanoparticle structure of NVO offers a large number of channels for easy ion intercalation and charge transportation.

**Section ‘B’** delves into the synthesis, preparation of the electrode, and structural characterization, as well as the electrochemical performance evaluation of the rGO electrode. Utilizing XRD and Raman spectroscopy techniques, the rGO electrode's properties are thoroughly examined. The XRD analysis verifies the reduction of GO via a hydrazine hydrate, resulting in the formation of rGO. Furthermore, Raman spectroscopy offers valuable insights into defect analysis determination of graphene layer count and orientation, with the calculated D/G intensity ratio (ID/IG) for rGO being 1.01. Additionally, the supercapacitive performance of the rGO electrode is investigated within a three-electrode electrochemical cell employing a 1 M KOH electrolyte. Notably, the rGO electrode exhibits a remarkable  $C_{\text{sp}}$  of  $180 \text{ F g}^{-1}$  at a current density of  $1 \text{ A g}^{-1}$ .

**Section ‘C’** consists of the preparation of NVO/rGO composite electrodes via the CBS method. The concentration of rGO varied within the pre-optimized C-NV3. The NVO/rGO composite electrodes were analyzed using various physicochemical characterizations. The XRD, FT-IR, Raman, and XPS analysis confirms the successful preparation of the NVO/rGO composite. Morphological study through FE-SEM and HR-TEM shows the particles of NVO deposited over rGO nanosheets. Also, the BET surface area analysis shows an improved specific surface area than the pristine NVO. Furthermore, the optimum composition (percentage) of rGO (20.08%) in NVO by TG analysis within the C-rNV3 electrode provides a maximum specific surface area of  $144 \text{ m}^2 \text{ g}^{-1}$ , which further helps to improve the electrochemical performance. The optimal NVO/rGO composite electrode (C-rNV3) shows a maximum  $C_{\text{sp}}$  of  $854 \text{ F g}^{-1}$  at  $1 \text{ A g}^{-1}$  current density, along with 88.8% capacitive

retention. The NVO/rGO composite has impressive electrochemical performance, indicating its potential as a suitable cathode material for HSDs.

**Chapter IV** encompasses the characterization and evaluation of supercapacitive performance for NVO thin films prepared via the SILAR method. This chapter is structured into two distinct sections: Section 'A' and Section 'B'. **Section 'A'** focuses on the binder-free synthesis of NVO thin films on SS substrates using the SILAR method, followed by comprehensive analyses of their structural, compositional, and morphological properties. In addition to varying precursor concentrations, number of cycles, pH of the cationic and anionic solutions, and bath temperature, this study underscores the influence of rinsing, adsorption/reaction time interval on the growth kinetics, and consequent physicochemical properties of NVO thin film electrodes. The XRD, FT-IR, and XPS study confirms the successful preparation of orthorhombic  $\text{Ni}_3\text{V}_2\text{O}_8 \cdot n\text{H}_2\text{O}$ . The morphological study reveals the spherical nanoparticles-like structure. Furthermore, the optimized growth rate (S-NV2) possesses a higher surface area ( $167.2 \text{ m}^2 \text{ g}^{-1}$ ) and mesoporous structure of NVO. The influence of dipping time on the structure and morphology and its consequent impact is further scrutinized for electrochemical measurements using a three-electrode electrochemical cell system. The optimized S-NV2 sample shows a maximum  $C_{\text{sp}}$  of  $710 \text{ F g}^{-1}$  at  $1 \text{ A g}^{-1}$ , along with 92.2% capacitive retention. Structurally disordered nanocrystalline NVO nanoparticles provide more active sites with structural flexibility that increase the electrochemical performance in terms of electrode storage capacity and stability.

Moreover, **Section 'B'** deals with the preparation of NVO/rGO composite electrodes and their physicochemical characterizations. The synthesis involved pristine NVO and NVO/rGO hybrids at different concentrations of rGO (0.025, 0.050, 0.075, 0.1, and  $0.125 \text{ mg ml}^{-1}$ ). The XRD, FT-IR, and Raman analysis shows the successful preparation of  $\text{Ni}_3\text{V}_2\text{O}_8/\text{rGO}$  composite. FE-SEM and HR-TEM studies show nanoparticles of NVO decorated over nanosheets of rGO. The BET and BJH results highlight that NVO composite with rGO is valuable for augmenting the specific surface area. The optimal composition of rGO (11.87%) within the S-rNV3 electrode provides a maximum specific surface area of  $311 \text{ m}^2 \text{ g}^{-1}$ , with a pore diameter of 3.5 nm, confirming the mesoporous nature of the material, which helps to improve the electrochemical performance. To further elucidate the influence of the content of rGO in NVO over the electrochemical performance of S-rNV series



samples, CV, GCD, EIS, and stability measurements were carried out in 1 M KOH aqueous electrolyte. Moreover, the S-rNV3 electrode shows a maximum  $C_{sp}$  of 1440  $F\ g^{-1}$  at 1  $A\ g^{-1}$  current density along with 94.5% capacitive retention after 5000 GCD cycles. The synergistic interaction between NVO and rGO at the optimal composition of (88.13% NVO and 11.87% rGO), along with the high surface area and mesoporous nature of the composite, play an essential role in enhancing charge storage capacity.

**Chapter V** covers the fabrication of both aqueous and solid-state hybrid devices. The electrochemical performance evaluation is also covered in this chapter. The chapter is divided into three sections ‘A’, ‘B’, and ‘C’. **Section ‘A’** deals with the preparation of electrodes, the fabrication process of hybrid aqueous devices, the preparation of gel electrolytes, and the fabrication of solid-state devices.

**Section ‘B’** involves the electrochemical performance evolution of fabricated hybrid aqueous and solid-state devices based on C-rNV3 composite electrode as a cathode and rGO as an anode. This section is divided into two segments. The initial part pertains to the fabrication and performance assessment of the C-HASc (C-rNV3//KOH//rGO) device using 1 M aqueous KOH electrolyte. The C-HASc device demonstrated a potential window ranging from 0 to 1.6 V and exhibited a  $C_{sp}$  of 122  $F\ g^{-1}$  at a current density of 3  $A\ g^{-1}$ . Moreover, it attained the highest SE of 43.4  $Wh\ kg^{-1}$  at an SP of 1.57  $kW\ kg^{-1}$  while retaining 85.15% of its capacitance after 5000 cycles. The second part covers the fabrication and performance evolution of a C-HSSc device consisting of C-rNV3 as a cathode and rGO as an anode and gel electrolyte. The gel electrolyte, consisting of PVA-KOH, was carefully layered between the NVO/rGO and rGO electrodes, and the assembly was securely sealed using transparent tape. The calculated maximum  $C_{sp}$  of the C-HSSc is found to be 98.3  $F\ g^{-1}$  at 4  $A\ g^{-1}$  current density along with a maximum SE of 34.9  $Wh\ kg^{-1}$  at an SP of 1.15  $kW\ kg^{-1}$ . Also, the fabricated device C-HSSc retained 69.2% of its initial capacitance. The practical effectiveness of the solid-state device was evaluated by conducting a test where two devices connected in series were charged for 30 seconds and then discharged through a lamp containing 12 white LEDs. Remarkably, despite the brief charging duration, the lamp illuminated for ~60 seconds, as depicted in Figure 6.1.

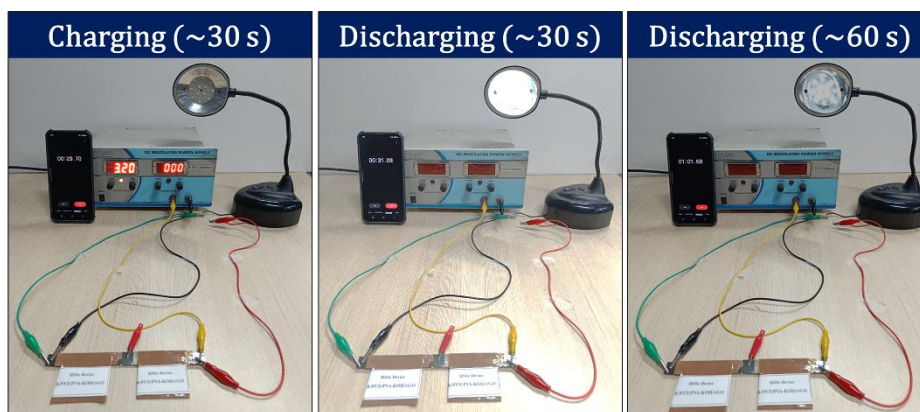


**Figure 6.1:** Demonstration of glowing LED table lamp using serially connected C-HSSc devices

**Section ‘C’** comprises the electrochemical performance of fabricated hybrid aqueous and solid-state devices based on SILAR deposited NVO/rGO composite electrode (S-rNV3) as a cathode and rGO as an anode. The section is subdivided into two parts like section ‘B’. The first part is related to the fabrication and electrochemical performance of an aqueous device consisting of S-rNV3 and rGO in 1 M KOH electrolyte. The prepared device (S-rNV3//KOH//rGO) achieved an operational voltage window of 0 to 1.7 V. Within this potential window, the S-HASc device exhibited a maximum  $C_{sp}$  of  $131.6 \text{ F g}^{-1}$  at  $3.5 \text{ A g}^{-1}$  along with maximum SE of  $52.8 \text{ Wh kg}^{-1}$  at an SP of  $1.88 \text{ kW kg}^{-1}$ . Also, the device sustains up to ~87% even after 5000 charge-discharge cycles.

Moreover, the second part of section ‘C’ is related to the solid-state hybrid device consisting of SILAR-deposited S-rNV3 electrodes as cathode and rGO as an anode with an area of  $4 \times 4 \text{ cm}^2$ . The S-HSSC device also maintained a voltage window of 0-1.7 V without suffering from electrolysis and exhibited a maximum  $C_{sp}$  of  $119 \text{ F g}^{-1}$  at a current density of  $1.5 \text{ A g}^{-1}$ . Additionally, the fabricated S-HSSC device achieves an SE of  $46 \text{ Wh kg}^{-1}$  at an SP of  $1.184 \text{ kW kg}^{-1}$  and yielded 89.5% of its initial  $C_{sp}$  even after 5000 charge-discharge cycles. The comprehensive results underscore the suitability of the fabricated S-HSSc device for practical energy storage applications. Two S-HSSc devices were connected in series and charged for 30 seconds at a constant potential of 3.4 V, followed by discharging through the white LED lamp. As depicted in Figure 6.2, the charged S-HSSc devices illuminated the white LED lamp for approximately ~120 seconds.

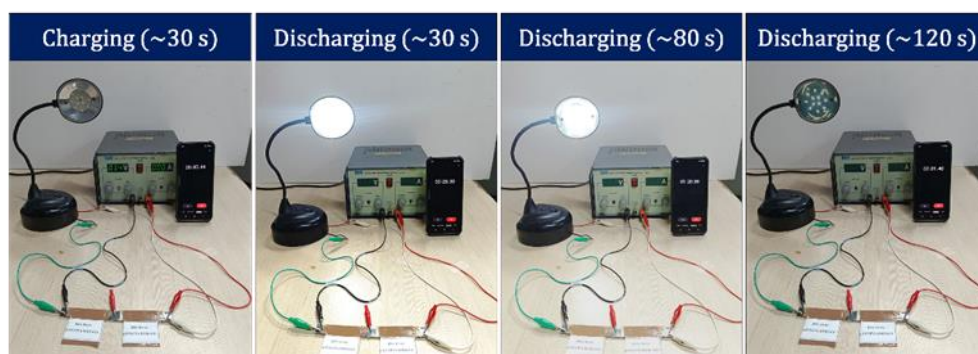


**Figure 6.2:** Demonstration of glowing LED table lamp using serially connected S-HSSc devices

**Chapter VI** presents the extracts from all preceding chapters, serving as a summary and conclusion. In this study, NVO/rGO composites with varying compositions of rGO were effectively prepared using CBS and SILAR methods. Various characterization techniques were employed to analyze and validate the prepared NVO and its composite with rGO.

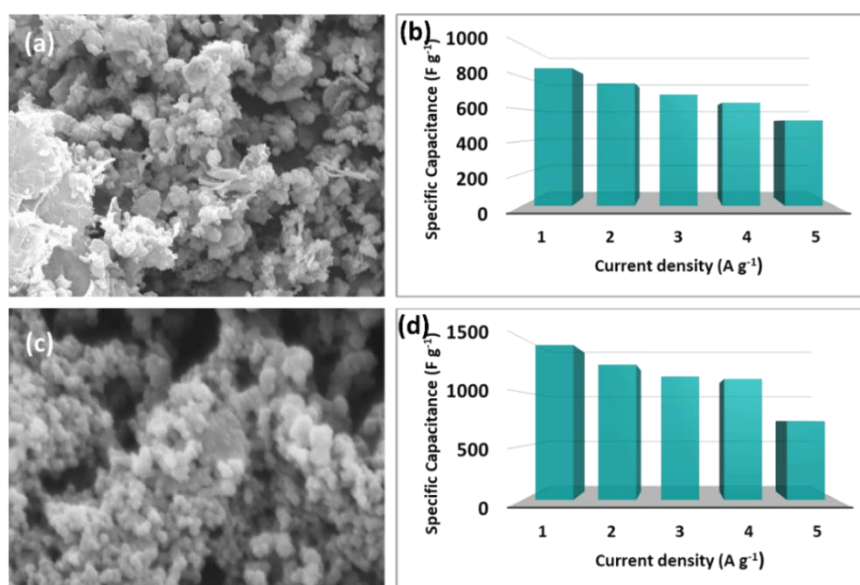


**Figure 6.3:** FE-SEM images for (a) C-rNV3 and (c) S-rNV3 samples, the plots of  $C_{sp}$  vs current densities for (b) C-rNV3 and (d) S-rNV3 electrodes

The supercapacitive performances of these electrodes are investigated in terms of  $C_{sp}$  and stability. The microstructures of best-performing electrodes C-rNV3 and S-rNV3 prepared by CBS and SILAR methods, respectively are shown in Figure 6.3 with their respective supercapacitive performance. Chapters III and IV propose that rGO content of 20.08% and 11.87% in NVO/rGO composites prepared by the CBS

and SILAR methods, respectively, using  $\sim 0.075 \text{ mg ml}^{-1}$  rGO concentration, exhibit higher electrochemical performance than other compositions.

Furthermore, the well-performed electrodes, deposited by CBS (C-rNV3) and SILAR (S-rNV3) methods were applied as cathodes in HSDs. Both aqueous and solid-state devices were fabricated using prepared NVO/rGO electrodes as a cathode and rGO as an anode and their respective performances at similar current density (4 are provided in Table 6.1.

**Table 6.1** Electrochemical performance of fabricated hybrid devices

Device Name	Device Type	$C_{sp}$ at 4 A $\text{g}^{-1}$ (F $\text{g}^{-1}$ )	SE (Wh $\text{kg}^{-1}$ )	SP (W $\text{kg}^{-1}$ )	Stability after 5000 cycles
<b>C-rNV3//rGO</b>	C-HASc	100.3	35.6	2105	85.1 %
	C-HSSc	98.3	34.9	1150	69.2%
<b>S-rNV3//rGO</b>	S-HASc	119.2	47.8	2151	87.7%
	S-HSSc	111	44.5	1184	89.5%

The aqueous hybrid device utilizing SILAR-deposited NVO/rGO (S-rNV3//KOH//rGO) demonstrates superior SE and SP compared to other prepared aqueous and flexible solid-state devices. However, the commercial application of aqueous devices faces limitations that can be addressed by developing solid-state alternatives. Therefore, fabricated HSSc device based on SILAR deposited NVO/rGO (S-rNV3//PVA-KOH//rGO) electrodes, boasting a comparable SE of  $44.5 \text{ Wh kg}^{-1}$  at an SP of  $1.43 \text{ kW kg}^{-1}$ , holds promise for widespread adoption in portable electronic devices.

# CHAPTER-VII

---

## 80\_Recommendation

---

### 7.1 80\_Recommendation

The NVO has garnered significant attention as an electroactive material for SCs due to its multistep redox processes and easy electron transfer. Additionally, NVO possesses numerous advantages, including its abundance in nature, cost-effectiveness, and environmentally friendly nature. In the scope of this research endeavor, thin films composed of NVO were synthesized employing the CBS and SILAR methods. The efficacy of these thin films in charge storage was augmented through the enhancement of their surface area and it was achieved by compositing it with rGO. The concentration of rGO varied to attain superior outcomes through synergistic interactions among them. The primary objective underlying the preparation of the composite electrode was to elevate both the specific capacitance and the stability of the material beyond those attainable with pristine constituents. Ultimately, it is recommended that the SILAR method is appropriate for NVO/rGO composite thin film synthesis which exhibits remarkably superior electrochemical performance than that prepared via the CBS method. To attain the best electrochemical performance, of NVO/rGO composites a concentration of 0.075 mg ml<sup>-1</sup> of rGO is essential during SILAR synthesis. The facile and scalable SILAR deposition method suggests the potential for smooth industrial integration with minimal modifications.

The outcomes derived from the current research endeavor are outlined as follows:

1. Both CBS and SILAR methods are feasible for the preparation of NVO/rGO composite electrodes with desired compositions.
2. The optimum concentration of rGO in NVO plays a crucial role in improving the surface area of the material and charge storage capabilities.
3. Prepared NVO/rGO composite thin films synthesized via the binder-free SILAR method demonstrated significantly superior performance compared to those prepared via the CBS method.
4. The SILAR approach enables the binder-free synthesis of NVO/rGO electrodes and demonstrates favourable characteristics, including high electrical conductivity, and rapid electron, and ion transport rate.
5. The SILAR synthesized S-rNV3 electrodes are promising candidates as a cathode for the fabrication of both aqueous and solid-state devices to achieve excellent electrochemical performance.

## 7.2 Future findings

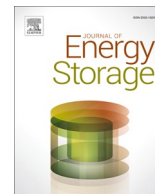
In this research work, NVO/rGO composite thin films were successfully deposited using CBS and SILAR methods and applied as a cathode in both aqueous and solid-state devices. Introducing rGO enhances the specific surface area, electrical conductivity, and overall electrochemical performance of the pristine NVO material. Furthermore, the following measures can be taken to improve and investigate the electrochemical performance of NVO materials,

1. Alternatively, other carbon allotropes like fullerene, carbon nanotubes (CNTs), carbon aerogel, and carbon foam can serve as effective substitutes for rGO in the composite.
2. Additionally, incorporating other transition metals, such as cobalt, iron, etc., to create bimetallic compounds further boosts the electrochemical energy storage properties of the electrode material.
3. Furthermore, the future of TMVOs-based research lies at the intersection of material synthesis, real-time characterizations, and computational simulations.
4. Moreover, the performance of hybrid devices can be further enhanced by utilizing different types of anodes, different electrolyte non-aqueous, and leak-proof packaging.



# **PUBLICATIONS**

---



## Research papers

# Development of binder-free, amorphous nickel vanadate cathodes by SILAR method for hybrid supercapacitors: Exploiting surface area by monitoring growth rate

Shraddha B. Bhosale<sup>a</sup>, Sambhaji S. Kumbhar<sup>a</sup>, Sachin S. Pujari<sup>a</sup>, Vinod V. Patil<sup>a,b</sup>, Nitish Kumar<sup>c</sup>, Rahul R. Salunkhe<sup>c</sup>, Chandrakant D. Lokhande<sup>a</sup>, Jayavant L. Gunjekar<sup>a</sup>, Umakant M. Patil<sup>a,d,\*</sup>

<sup>a</sup> Centre for Interdisciplinary Research, D. Y. Patil Education Society, Kasaba Bawada, Kolhapur 416006, India

<sup>b</sup> School of Chemical Sciences, Purnyashlok Ahilyadevi Holkar Solapur University, Solapur 413255, India

<sup>c</sup> Department of Physics, Indian Institute of Technology Jammu, Jagti, Jammu, J & K 181221, India

<sup>d</sup> Department of Materials Science and Engineering, Yonsei University, 50 Yonsei-ro, Seodaemun-gu, Seoul 03722, Republic of Korea



## ARTICLE INFO

## Keywords:

Growth rate variation  
Nickel vanadate  
SILAR  
Surface area  
Supercapacitor  
Thin film

## ABSTRACT

Developing self-supported electrode material in the absence of electro-inert binders considering the effortless transfer of charges and manipulating physicochemical properties of electrodes in energy storage devices is essential. Hence, the present attempt emphasizes the facile synthetic strategy of successive ionic layer adsorption and reaction (SILAR) for controlled nickel vanadate (NV) growth over the conducting plate. In SILAR synthesis, the growth rate is monitored by rinsing and adsorption/adsorption time variation to tune the surface area, mesoporous structure, and surface morphology of NV thin films. As a result, the formation of mesoporous, amorphous, hydrous nanoparticles of NV over the stainless-steel substrate is affirmed by structural analysis. Furthermore, alteration in specific surface area with variation in growth rate is observed in BET analysis. As a result, the optimal NV(1:2) thin film electrode exhibited the highest specific capacity (capacitance) of  $355 \text{ C g}^{-1}$  ( $710 \text{ F g}^{-1}$ ) at  $1 \text{ A g}^{-1}$  current density. Moreover, the fabricated aqueous hybrid supercapacitor device (NV (1:2)/rGO) delivered  $109 \text{ F g}^{-1}$  specific capacitance at  $1.3 \text{ A g}^{-1}$  current density, and the device exhibited a maximum specific energy (SE) of  $44 \text{ Wh kg}^{-1}$  at a particular specific power (SP) of  $1.14 \text{ kW kg}^{-1}$ . Furthermore, the solid-state hybrid supercapacitor (NV(1:2)/PVA-KOH/rGO) device conferred a specific capacitance of  $89 \text{ F g}^{-1}$  at  $0.5 \text{ A g}^{-1}$  current density and an SE of  $36 \text{ Wh kg}^{-1}$  at  $0.482 \text{ kW kg}^{-1}$  SP. This research paved an avenue to the binder-free, scalable synthesis of NV electrodes and employed them as a cathode in practical applications of hybrid energy storage devices.

## 1. Introduction

Increasing concern over the depletion of fossil fuels turned the attention of this generation toward environmentally friendly energy generation and conversion systems. On the other hand, the fluctuations, intermittency, and less continuity of conventional energy generation have urged researchers toward sources of electrical energy devices (EEDs) [1,2]. Hence, efforts toward a highly efficient, sustainable, low-cost, and environmentally friendly energy storage system are still in progress. Among the various energy storage systems, electrochemical energy storage devices (EESDs), such as supercapacitors, batteries, fuel

cells, etc., are highly desirable and environmentally friendly [3,4]. Among the consortium of clean energy storage systems, 'supercapacitors' are the most common alternative to batteries in many applications and have been extensively studied for many decades because of their high specific power (SP), rapid discharge-recharge rate, and exceptional cyclic stability. But less specific energy (SE) sometimes limits the practical use of supercapacitors compared to battery systems. Hence, it is necessary to contribute more significant potential for developing high-energy supercapacitors without sacrificing the SP. Efforts toward enhancing the SE of supercapacitors by fabricating a hybrid device that emphasizes cathode materials superiority, exhibits high

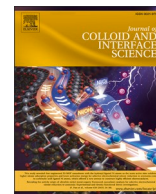
\* Corresponding author at: Centre for Interdisciplinary Research, D. Y. Patil Education Society, Kasaba Bawada, Kolhapur 416006, India.

E-mail address: [umakant.physics84@gmail.com](mailto:umakant.physics84@gmail.com) (U.M. Patil).

<https://doi.org/10.1016/j.est.2023.108417>

Received 6 April 2023; Received in revised form 27 June 2023; Accepted 16 July 2023

2352-152X/© 2023 Elsevier Ltd. All rights reserved.



## Regular Article

# Harnessing morphological alteration from microflowers to nanoparticles and cations synergy (Co:Ni) in binder-free cobalt nickel vanadate thin film cathodes synthesized via SILAR method for hybrid supercapacitor devices

Shraddha B. Bhosale<sup>a</sup>, Sambhaji S. Kumbhar<sup>a</sup>, Sumita S. Patil<sup>a</sup>, Akshay Ransing<sup>b</sup>,  
Vinayak G. Parale<sup>b</sup>, Chandrakant D. Lokhande<sup>a</sup>, Jayavant L. Gunjekar<sup>a</sup>, Hyung-Ho Park<sup>b,\*</sup>,  
Umakant M. Patil<sup>a,b,\*</sup>

<sup>a</sup> Centre for Interdisciplinary Research, D. Y. Patil Education Society, Kasaba Bawada, Kolhapur 416006, India

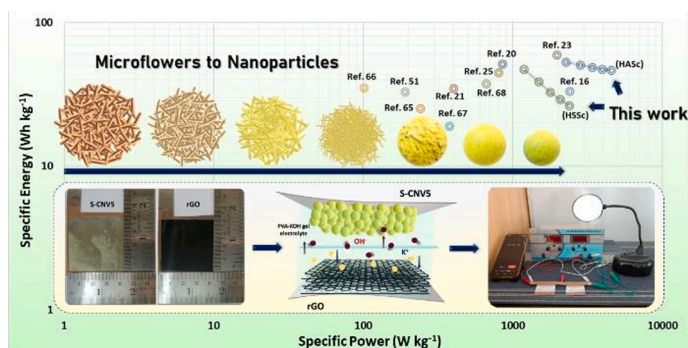
<sup>b</sup> Department of Materials Science and Engineering, Yonsei University, 50 Yonsei-ro, Seodaemun-gu, Seoul 03722, Korea



## HIGHLIGHTS:

- Novel chemical synthesis of binder-free cobalt nickel vanadate (CNV) by SILAR method.
- Change in cation concentrations in CNV led to morphological alteration: microflower to nanoparticles.
- Maximum specific capacitance (1382 F g<sup>-1</sup> at 1 A g<sup>-1</sup>) is achieved by optimizing the Co:Ni ratio (0.4:0.6) in the CNV electrode.
- Remarkable electrochemical capacitive performance of CNV cathode-based aqueous and solid devices.

## GRAPHICAL ABSTRACT



## ARTICLE INFO

## Keywords:

Cation variation  
Hybrid supercapacitor device  
Morphology alteration  
Nickel cobalt vanadate  
SILAR

## ABSTRACT

Electrode materials must be rationally designed with morphologies and electroactive sites manipulated through cations' synergy in bimetal compounds in order to maximize the performance of energy storage devices. Therefore, the present study emphasizes binder-free scalable preparation of cobalt nickel vanadate (CNV) thin films by a facile successive ionic layer adsorption and reaction (SILAR) approach with specific cations (Co:Ni) alternation. Increasing the Ni cation content in the CNV notably transforms its microflower structure comprising nanoflakes (252 nm) into nanoparticles (74 nm). An optimized S-CNV5 thin film cathode with Co:Ni molar ratio of ~ 0.4:0.6 and a high specific surface area of 340 m<sup>2</sup> g<sup>-1</sup>, provided the excellent specific capacitance ( $C_{sp}$ ) and capacity ( $C_{sc}$ ) of 1382 F g<sup>-1</sup> and 691 C g<sup>-1</sup>, respectively at 1 A g<sup>-1</sup> current density. A hybrid aqueous supercapacitor (HASC) device with positive and negative electrodes comprising optimized CNV and reduced graphene oxide (rGO), respectively, in a 1 M KOH electrolyte delivered a  $C_{sp}$  of 133 F g<sup>-1</sup> and a specific energy (SE) of 53 Wh kg<sup>-1</sup> at a specific power (SP) of 2261 kW kg<sup>-1</sup>. Additionally, a fabricated hybrid solid-state supercapacitor (HSSC) device with the same electrodes applying PVA-KOH gel electrolyte displayed a  $C_{sp}$  of 119 F g<sup>-1</sup>, and SE of

\* Corresponding authors at: D. Y. Patil Education Society, Kasaba Bawada, Kolhapur 416006, India (U. Patil); Yonsei University, 50 Yonsei-ro, Seodaemun-gu, Seoul 03722, Korea (H-H. Park).

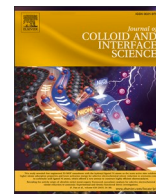
E-mail addresses: [hhpark@yonsei.ac.kr](mailto:hhpark@yonsei.ac.kr) (H.-H. Park), [umakant.physics84@gmail.com](mailto:umakant.physics84@gmail.com) (U.M. Patil).

<https://doi.org/10.1016/j.jcis.2024.04.004>

Received 16 December 2023; Received in revised form 30 March 2024; Accepted 1 April 2024

Available online 2 April 2024

0021-9797/© 2024 Elsevier Inc. All rights reserved.



## Regular Article

# Harnessing morphological alteration from microflowers to nanoparticles and cations synergy (Co:Ni) in binder-free cobalt nickel vanadate thin film cathodes synthesized via SILAR method for hybrid supercapacitor devices

Shraddha B. Bhosale<sup>a</sup>, Sambhaji S. Kumbhar<sup>a</sup>, Sumita S. Patil<sup>a</sup>, Akshay Ransing<sup>b</sup>,  
Vinayak G. Parale<sup>b</sup>, Chandrakant D. Lokhande<sup>a</sup>, Jayavant L. Gunjekar<sup>a</sup>, Hyung-Ho Park<sup>b,\*</sup>,  
Umakant M. Patil<sup>a,b,\*</sup>

<sup>a</sup> Centre for Interdisciplinary Research, D. Y. Patil Education Society, Kasaba Bawada, Kolhapur 416006, India

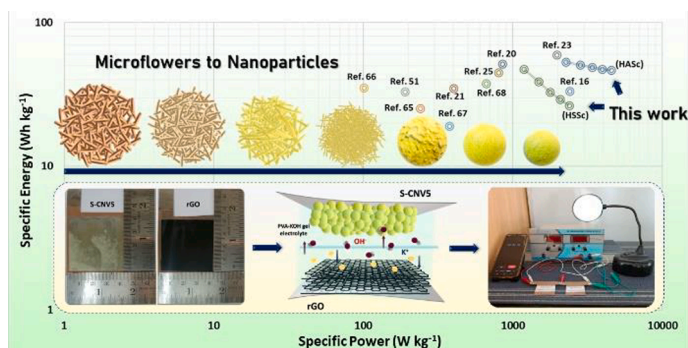
<sup>b</sup> Department of Materials Science and Engineering, Yonsei University, 50 Yonsei-ro, Seodaemun-gu, Seoul 03722, Korea



## HIGHLIGHTS:

- Novel chemical synthesis of binder-free cobalt nickel vanadate (CNV) by SILAR method.
- Change in cation concentrations in CNV led to morphological alteration: microflower to nanoparticles.
- Maximum specific capacitance (1382 F g<sup>-1</sup> at 1 A g<sup>-1</sup>) is achieved by optimizing the Co:Ni ratio (0.4:0.6) in the CNV electrode.
- Remarkable electrochemical capacitive performance of CNV cathode-based aqueous and solid devices.

## GRAPHICAL ABSTRACT



## ARTICLE INFO

## Keywords:

Cation variation  
Hybrid supercapacitor device  
Morphology alteration  
Nickel cobalt vanadate  
SILAR

## ABSTRACT

Electrode materials must be rationally designed with morphologies and electroactive sites manipulated through cations' synergy in bimetal compounds in order to maximize the performance of energy storage devices. Therefore, the present study emphasizes binder-free scalable preparation of cobalt nickel vanadate (CNV) thin films by a facile successive ionic layer adsorption and reaction (SILAR) approach with specific cations (Co:Ni) alternation. Increasing the Ni cation content in the CNV notably transforms its microflower structure comprising nanoflakes (252 nm) into nanoparticles (74 nm). An optimized S-CNV5 thin film cathode with Co:Ni molar ratio of ~ 0.4:0.6 and a high specific surface area of 340 m<sup>2</sup> g<sup>-1</sup>, provided the excellent specific capacitance (C<sub>sp</sub>) and capacity (C<sub>sc</sub>) of 1382 F g<sup>-1</sup> and 691 C g<sup>-1</sup>, respectively at 1 A g<sup>-1</sup> current density. A hybrid aqueous supercapacitor (HASC) device with positive and negative electrodes comprising optimized CNV and reduced graphene oxide (rGO), respectively, in a 1 M KOH electrolyte delivered a C<sub>sp</sub> of 133 F g<sup>-1</sup> and a specific energy (SE) of 53 Wh kg<sup>-1</sup> at a specific power (SP) of 2261 kW kg<sup>-1</sup>. Additionally, a fabricated hybrid solid-state supercapacitor (HSSC) device with the same electrodes applying PVA-KOH gel electrolyte displayed a C<sub>sp</sub> of 119 F g<sup>-1</sup>, and SE of

\* Corresponding authors at: D. Y. Patil Education Society, Kasaba Bawada, Kolhapur 416006, India (U. Patil); Yonsei University, 50 Yonsei-ro, Seodaemun-gu, Seoul 03722, Korea (H-H. Park).

E-mail addresses: [hhpark@yonsei.ac.kr](mailto:hhpark@yonsei.ac.kr) (H.-H. Park), [umakant.physics84@gmail.com](mailto:umakant.physics84@gmail.com) (U.M. Patil).

<https://doi.org/10.1016/j.jcis.2024.04.004>

Received 16 December 2023; Received in revised form 30 March 2024; Accepted 1 April 2024

Available online 2 April 2024

0021-9797/© 2024 Elsevier Inc. All rights reserved.

## Research Article

# SILAR Synthesized Binder-Free, Hydrous Cobalt Phosphate Thin Film Electrocatalysts for OER Application: Annealing Effect on the Electrocatalytic Activity

Vinod V. Patil <sup>1,2</sup>, Sachin S. Pujari <sup>1,3</sup>, Shraddha B. Bhosale <sup>1</sup>,  
Sambhaji S. Kumbhar <sup>1</sup>, Vinayak G. Parale <sup>4</sup>, Chandrakant D. Lokhande <sup>1</sup>,  
Jayavant L. Gunjekar <sup>1</sup>, Mukund G. Mali <sup>2</sup>, Dattakumar S. Mhamane <sup>2,5</sup>,  
Hyung-Ho Park <sup>4</sup> and Umakant M. Patil <sup>1,4</sup>

<sup>1</sup>Centre for Interdisciplinary Research, D. Y. Patil Education Society (Deemed to be University), Kolhapur 416006, India

<sup>2</sup>School of Chemical Sciences, Punyashlok Ahilyadevi Holkar Solapur University, Solapur 413255, India

<sup>3</sup>Department of Physics, Yashwantrao Chavan Warana Mahavidyalaya, Warananagar, Kolhapur-416113, India

<sup>4</sup>Department of Materials Science and Engineering, Yonsei University, 50 Yonsei-ro, Seodaemun-gu, Seoul 03722, Republic of Korea

<sup>5</sup>Department of Chemistry, Sangameshwar College (Autonomous), Solapur 413001, India

Correspondence should be addressed to Dattakumar S. Mhamane; [dkumar.mhamane@gmail.com](mailto:dkumar.mhamane@gmail.com),  
Hyung-Ho Park; [hhpark@yonsei.ac.kr](mailto:hhpark@yonsei.ac.kr), and Umakant M. Patil; [umakant.physics84@gmail.com](mailto:umakant.physics84@gmail.com)

Received 7 July 2023; Revised 14 October 2023; Accepted 18 October 2023; Published 14 November 2023

Academic Editor: Kisan Chhetri

Copyright © 2023 Vinod V. Patil et al. This is an open access article distributed under the Creative Commons Attribution License, which permits unrestricted use, distribution, and reproduction in any medium, provided the original work is properly cited.

Highly efficient and robust electrocatalysts intended for the oxygen evolution reaction (OER) are essential for energy conversion devices; the structural and morphological fractions of the electrocatalyst can also greatly influence the OER performance. Therefore, developing a high-performing electrocatalyst with desired properties is crucial through a simple and cost-effective chemical process. So, the binder-free, hydrous cobalt phosphate ( $\text{Co}_3(\text{PO}_4)_2 \cdot n\text{H}_2\text{O}$ ) thin film electrocatalysts are prepared via the successive ionic layer adsorption and reaction (SILAR) method onto stainless steel (SS) substrates at ambient temperature. Additionally, the impact of annealing on the OER efficiency of thin film electrodes made of hydrous cobalt phosphate was observed by subjecting the electrocatalysts to different temperatures (200°C and 400°C). The SILAR synthesized hydrous  $\text{Co}_3(\text{PO}_4)_2 \cdot n\text{H}_2\text{O}$  with the short-range ordered agglomerated particles transformed into discrete nanoparticles with an annealing temperature. The as-prepared hydrous cobalt phosphate (CP) demonstrated outstanding OER performance with the least overpotential ( $\eta$ ) of 265 mV at 10 mA cm<sup>-2</sup> current density and the lowest Tafel slope of 37 mV dec<sup>-1</sup>, and the overpotential ( $\eta_{10}$ ) increased upon the annealing of catalysts (CP 200 and CP 400). Moreover, the as-prepared electrocatalyst demonstrated overall water splitting at the lowest potential of 1.56 V (@10 mA cm<sup>-2</sup>) in the alkaline electrolysis system (CP//Pt). The present study reveals that the electrocatalytic performance of the as-prepared cobalt phosphate thin film catalyst is significantly associated with the hydrous content present in catalysts and demonstrates the practical applicability of SILAR-synthesized binder-free cobalt phosphate thin film electrocatalysts.

## 1. Introduction

The potential of hydrogen gas ( $\text{H}_2$ ) as a green and sustainable energy source is widely recognized within the industry, with an anticipated significant contribution to the expanding renewable energy sector [1, 2]. Among various hydrogen production

processes, electrochemical water splitting ( $2\text{H}_2\text{O} \rightarrow 2\text{H}_2 + \text{O}_2$ ) is one of the attractive paths to produce hydrogen ( $\text{H}_2$ ); however, electrochemical water splitting at a large scale is significantly hindered by the sluggish oxygen evolution reaction (OER) at the anode [3, 4]. Within the OER, multiple surface-adsorbed intermediates result from four proton-coupled



# Growth Dynamics-Dependent Chemical Approach to Accomplish Nanostructured Cobalt Vanadium Oxide Thin Film Electrodes with Controlled Surface Area for High-Performance Solid-State Hybrid Supercapacitor Devices

Sambhaji S. Kumbhar, Shraddha B. Bhosale, Sachin S. Pujari, Vinod V. Patil, Nitish Kumar, Rahul R. Salunkhe, Chandrakant D. Lokhande, and Umakant M. Patil\*

Rational designing of electrode materials having high surface area can accomplish the enhanced charge-storing ability of the electrochemical energy storage devices. Therefore, the surface area of cobalt vanadium oxide (CVO) material is controlled by changing growth dynamics in successive ionic layer adsorption and reaction methods. Structural analysis confirms the formation of hydrous cobalt vanadium oxide nanoparticles ( $\text{Co}_3\text{V}_2\text{O}_8 \cdot n\text{H}_2\text{O}$ ) thin film electrodes, and alteration in the surface area with change in growth dynamics is observed in Brunauer–Emmett–Teller analysis. The CVO1:1 thin film electrode prepared at optimal growth dynamics illustrates high specific capacitance ( $C_s$ ) (capacity) of  $793 \text{ F g}^{-1}$  ( $396.7 \text{ C g}^{-1}$ ) at  $0.5 \text{ A g}^{-1}$ , respectively. Moreover, aqueous hybrid supercapacitor devices constructed using CVO1:1 as cathode exhibit high  $C_s$  of  $133.5 \text{ F g}^{-1}$  at  $1.1 \text{ A g}^{-1}$ , specific energy (SE) of  $47.7 \text{ Wh kg}^{-1}$  with specific power (SP) of  $0.90 \text{ kW kg}^{-1}$ . The solid-state hybrid supercapacitor devices also offer high  $C_s$  of  $102.9 \text{ F g}^{-1}$  at  $0.3 \text{ A g}^{-1}$ , SE of  $36.6 \text{ Wh kg}^{-1}$  at SP of  $0.30 \text{ kW kg}^{-1}$ . In the SILAR approach, the dipping time plays a critical role in improving the surface area of the material and, consequently, electrochemical performance, as the current work amply indicates.

of researchers has been focused on new energy storage applications like batteries, supercapacitors, etc. Among available electrochemical energy storage devices (EESDs), aqueous electrochemical energy storage devices (AEESDs) systems are considered a promising alternative to batteries owing to their nontoxic nature, low cost, and superior safety.<sup>[3]</sup> Furthermore, in AEESDs, the combination of capacitive and battery features in hybrid supercapacitors (HSCs) are promising AEES systems and offer features such as high energy, power, and stability simultaneously.<sup>[4,5]</sup> Moreover, an additional highly anticipated tactic to enhance the energy density of HSCs is to refine the storage capacity of electrodes by controlling the physical (e.g., crystallinity, hydrous nature, conductivity) and morphological (e.g., surface area, porosity, particle size) characteristics of storing materials.


Therefore, in HSCs, several metal hydroxides, oxides, phosphates, and sulfides have been assessed as cathode materials. Based on charge storage mechanisms, most ever-used pseudocapacitive materials can be categorized into intrinsic, intercalation, and extrinsic (battery-type) pseudocapacitive.<sup>[6]</sup> Moreover, decreasing the size or crystallinity (nanomaterials) of battery-type materials can illustrate pseudocapacitive activities and are referred to as extrinsic pseudocapacitive

## 1. Introduction

Energy storage devices (ESDs) are an essential component for the daily operation of nearly all technological necessities, such as electric vehicles, mobile phones, and laptops. Hence, ESDs with extensive cycle life, high energy, and power density, with cost-effectiveness, are in high demand.<sup>[1,2]</sup> Therefore, the attention

S. S. Kumbhar, S. B. Bhosale, S. S. Pujari, V. V. Patil, C. D. Lokhande, U. M. Patil  
Centre for Interdisciplinary Research  
D. Y. Patil Education Society  
Kasaba Bawada, Kolhapur 416006, India  
E-mail: umakant.physics84@gmail.com

S. S. Pujari  
Department of Physics  
Yashwantrao Chavan Warana Mahavidyalaya  
Warananagar, Kolhapur 416113, India

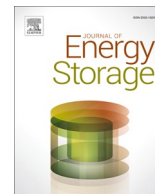
 The ORCID identification number(s) for the author(s) of this article can be found under <https://doi.org/10.1002/ente.202300400>.

V. V. Patil  
School of Chemical Sciences  
Punyashlok Ahilyadevi Holkar Solapur University  
Solapur 413255, India

N. Kumar, R. R. Salunkhe  
Department of Physics  
Indian Institute of Technology Jammu  
Jagti, Jammu, J & K 181221, India

U. M. Patil  
Department of Materials Science and Engineering  
Yonsei University  
Seodaemun-gu, Seoul 03722, Korea

DOI: 10.1002/ente.202300400



## Research Papers

# Hydrothermally synthesized nickel copper phosphate thin film cathodes for high-performance hybrid supercapacitor devices

Sachin S. Pujari<sup>a</sup>, Sujit A. Kadam<sup>b</sup>, Yuan-Ron Ma<sup>b</sup>, Satish B. Jadhav<sup>a</sup>, Sambhaji S. Kumbhar<sup>a</sup>, Shraddha B. Bhosale<sup>a</sup>, Jayavant L. Gunjekar<sup>a</sup>, Chandrakant D. Lokhande<sup>a</sup>, Umakant M. Patil<sup>a,\*</sup>

<sup>a</sup> Centre for Interdisciplinary Research, D. Y. Patil Education Society, Kasaba Bawada, Kolhapur 416 006, India

<sup>b</sup> Department of Physics, National Dong Hwa University, Hualien 97401, Taiwan



## ARTICLE INFO

## Keywords:

Concentration variation

Microplates

Microrods

Nickel copper phosphate

Hydrothermal method

Hybrid energy storage devices

Thin film electrode

## ABSTRACT

Transition metal phosphate (TMP) based materials are developing as advanced type electrode materials for hybrid supercapacitors (SCs) due to their unprecedented conductivity, and rich redox activity. Attracted by these fabulous physicochemical characteristics of metal phosphates, binder-free nickel copper (Ni-Cu) phosphate thin films directly grown on stainless steel (SS) substrate by hydrothermal method. The morphological alteration from microplates like nickel phosphate to microrods like copper phosphate is detected with increasing copper content in Ni-Cu phosphate thin films. The optimal 1:1 ratio of nickel and copper in Ni-Cu phosphate ( $\text{Ni}_{1.62}\text{Cu}_{1.35}(\text{PO}_4)_2 \cdot \text{H}_2\text{O}$ ) thin film illustrates high specific capacitance ( $C_s$ ) (capacity ( $C_c$ )) of  $711 \text{ F g}^{-1}$  ( $355.5 \text{ C g}^{-1}$ ) at  $1.5 \text{ A g}^{-1}$ . More significantly, a hybrid aqueous SC (HASC) and all-solid-state SC (HASSC) electrochemical energy storage devices (ESDs) have been fabricated. The HASC device showed superior  $C_s$  ( $85 \text{ F g}^{-1}$  at  $0.8 \text{ A g}^{-1}$ ) with specific energy (SE) of  $30 \text{ Wh kg}^{-1}$  at  $1.27 \text{ kW kg}^{-1}$  specific power (SP). Additionally, HASSC device offers a higher  $C_s$  ( $52 \text{ F g}^{-1}$  at  $0.6 \text{ A g}^{-1}$ ) with  $18.53 \text{ Wh kg}^{-1}$  SE at  $1.64 \text{ kW kg}^{-1}$  SP. Also, both HASC and HASSC devices exhibit excellent long-term durability of 84.81 and 80.83 %, respectively, after 5000 GCD cycles. Moreover, HASSC device brightens a panel of 201 red light-emitting diodes (LEDs) illustrating its commercial practicability to next-generation hybrid energy storage devices.

## 1. Introduction

High-performance electrochemical energy storage devices (ESDs) (e. g., supercapacitors (SCs) and batteries) are acquiring increasing focus from researchers in the industrial field as well as fundamental scientific research [1]. The SC as steady and reversible ESDs has become the most favourable commercial device [2]. Unlike batteries, SCs possess high specific power (SP) and long cycle lifespan that make them promising candidates where (a) peak power demands and (b) maintenance-free ESDs are necessary [3]. A unique scheme to improve the specific energy (SE) of a SC is the usage of electrolytes with a wide working voltage window and a high specific capacitance ( $C_s$ ) electrode (since  $E = 0.5 \text{ CV}^2$ ) [1,4]. Remarkably, hybrid SC can offer both high SE and excellent SP, ideally suitable for many emerging applications such as smart grids, portable electronics, and electric vehicles [5]. The electrochemical behaviours of hybrid devices depends characteristics of the electrode materials (porosity, surface area and conductivity) and sensitively on

the structures, particularly with the negative electrode materials (carbon based materials) [6,7]. Hence, the design and construction of novel advanced electrode materials along with unique functionalities and structural properties are critical to attaining breakthroughs in the improvement of high-performance hybrid devices [8].

Till today, the various types of cathode materials have been examined for SCs including conducting polymers (polypyrrole, polyaniline, etc.) and transition metal oxides/sulfides/hydroxide. Out of these electrode materials, currently, TMPs have been fascinating enormous attention for several applications including energy conversion, sensors, magnetic devices, and ESDs owing to their metalloid characteristics [9]. Especially, TMPs with the qualities of outstanding redox activity, high conductivity, environmental compatibility, earth abundance, sustainability is more advantageous for ESDs and have been recognized as competitive alternates for conventional metal oxide and hydroxide along with conducting polymers-based electrodes [10]. Basically,  $\text{PO}_4^{3-}$  polyhedral anions along with a zeolite structure are much more

\* Corresponding author.

E-mail address: [umakant.physics84@gmail.com](mailto:umakant.physics84@gmail.com) (U.M. Patil).

<https://doi.org/10.1016/j.est.2022.105037>

Received 3 March 2022; Received in revised form 18 May 2022; Accepted 1 June 2022

2352-152X/© 2022 Elsevier Ltd. All rights reserved.





Cite this: DOI: 10.1039/d2se00978a

# A binder-free facile synthetic approach for amorphous, hydrous nickel copper phosphate thin film electrode preparation and its application as a highly stable cathode for hybrid asymmetric supercapacitors†

Sachin S. Pujari,<sup>a</sup> Sujit A. Kadam,<sup>b</sup> Yuan-Ron Ma,<sup>b</sup> Satish B. Jadhav,<sup>a</sup> Sambhaji S. Kumbhar,<sup>a</sup> Shraddha B. Bhosale,<sup>a</sup> Vinod V. Patil,<sup>ac</sup> Jayavant L. Gunjekar,<sup>b</sup> Chandrakant D. Lokhande<sup>a</sup> and Umakant M. Patil<sup>b,\*a</sup>

Currently, amorphous, hydrous compounds are receiving much attention as electrodes in hybrid supercapacitors (S.C.s) as they offer extraordinary electrochemical efficiency because of disorder in their structure and an excellent electrochemical interface. In this study, a simple, cost-effective and binder-free synthetic SILAR method is used for preparing amorphous, hydrous nickel copper phosphate (NCP-S) thin film on a stainless steel substrate (S.S.). The amorphous, hydrous NCP-S thin films exhibit mesoporous, clustered spherical particle-like morphology. The optimal ratio (1 : 1) of nickel and copper in the NCP-S ( $\text{Ni}_{1.56}\text{Cu}_{1.44}(\text{PO}_4)_2 \cdot \text{H}_2\text{O}$ ) material gives a high specific capacitance ( $C_s$ ) (capacity) of  $750 \text{ F g}^{-1}$  ( $412.50 \text{ C g}^{-1}$ ) at  $1.0 \text{ A g}^{-1}$ . More significantly, hybrid asymmetric aqueous S.C. (HAASC) and hybrid all-solid-state asymmetric S.C. (HASASC) electrochemical energy storage devices (ESDs) have been fabricated using NCP-S as a cathode and rGO as an anode. The HAASC device showed a superior  $C_s$  ( $95.62 \text{ F g}^{-1}$  at  $3.0 \text{ A g}^{-1}$ ) with specific energy (S.E.) of  $34 \text{ W h kg}^{-1}$  at  $2.40 \text{ kW kg}^{-1}$  specific power (S.P.). Additionally, the HASASC device offers higher  $C_s$  ( $37.62 \text{ F g}^{-1}$  at  $0.7 \text{ A g}^{-1}$ ) with  $13.51 \text{ W h kg}^{-1}$  S.E. at  $0.55 \text{ kW kg}^{-1}$  S.P. Also, both devices exhibit excellent long-term durability (94.11 and 93.81%, respectively, after 5000 GCD cycles). The amorphous, hydrous structures clearly indicate excellent accessibility of ions and stability of electrodes, which is favourable for the hybrid S.C.s. These remarkable supercapacitive results promise the application of amorphous NCP-S as a cathode in commercialized hybrid energy storage systems.

Received 17th July 2022  
Accepted 10th November 2022

DOI: 10.1039/d2se00978a

rsc.li/sustainable-energy

## 1. Introduction

Supercapacitors (S.C.s) have attracted extensive attention among all energy storage devices (ESDs) due to their unique properties, which include long cycling durability, high-power capability, ease of operation and wide working temperature

range. Owing to such excellent properties, they are found to be more favourable ESDs for modern electronic applications in energy regeneration and hybrid electric vehicles, weight leveling, and aerospace industries.<sup>1–3</sup> Nevertheless, the surface-controlled electrochemical reactions of S.C.s restrict the charge transfer process near and on the electrode surface,

<sup>a</sup>Centre for Interdisciplinary Research, D. Y. Patil Education Society, (Deemed to be University), Kasaba Bawada, Kolhapur-416 006, M.S., India. E-mail: Umakant.physics84@gmail.com

<sup>b</sup>Department of Physics, National Dong Hwa University, Hualien-97401, Taiwan

<sup>c</sup>School of Chemical Sciences, Punyashlok Ahilyadevi Holkar Solapur University, Solapur 413255, India

† Electronic supplementary information (ESI) available: Formulae for calculation, mass deposition graph, pore size distribution curves of the NCP-S series samples, EDS spectra of the NCP-S series samples, the CV graphs of NCP-S1, NCP-S2, NCP-S4 and NCP-S5 electrodes, pseudocapacitive (surface current) and battery type (bulk current) current density contribution graph at various scan rates for NCP-S1, NCP-S2, NCP-S4 and NCP-S5 electrodes, the GCD curves of NCP-S1, NCP-S2, NCP-S4 and NCP-S5 electrodes, the specific

capacitance of the NCP-S series electrodes at various current densities, XPS study of the NCP-S3 sample before and after stability testing, the structural and electrochemical study of the rGO electrode, the CV and GCD curves of the HAASC device in different potential windows, schematic of HASASC device fabrication, the CV and GCD curves of the HASASC device in different potential windows, compositions of nickel and copper precursors, experimental and observed nickel and copper atomic ratios in NCP-S series thin films, comparison of various amorphous nickel copper phosphate/pyrophosphate based electrodes, EIS fitted circuit parameters of the NCP-S series electrodes, and comparison of electrochemical performance for HAASC and HASASC devices with previous metal phosphate based devices. See DOI: <https://doi.org/10.1039/d2se00978a>

# Hydrous and Amorphous Cobalt Phosphate Thin-Film Electrodes Synthesized by the SILAR Method for High-Performing Flexible Hybrid Energy Storage Devices

Vinod V. Patil, Sachin S. Pujari, Shraddha B. Bhosale, Sambhaji S. Kumbhar, Vinayak G. Parale, Jayavant L. Gunjekar, Hyung-Ho Park, Chandrakant D. Lokhande, Mukund G. Mali, Dattakumar S. Mhamane,\* and Umakant M. Patil\*



Cite This: <https://doi.org/10.1021/acs.energyfuels.2c02202>



Read Online

ACCESS |



Metrics & More

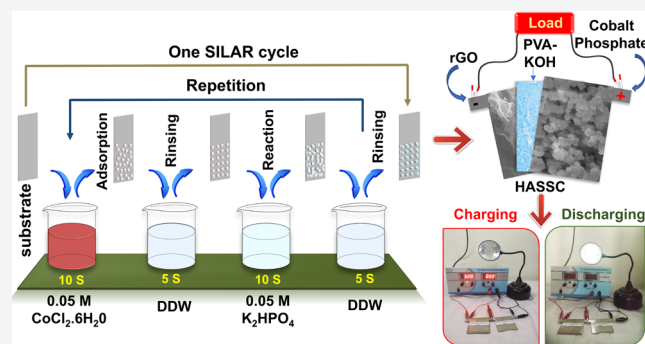


Article Recommendations



Supporting Information

**ABSTRACT:** Recently, excellent electrochemical performance and good conductivity of transition metal phosphates (TMPs) have been obtained, assuring their potential as a cathode in hybrid supercapacitors. Also, amorphous, hydrous materials are supposed to be exemplary active materials for high-performing supercapacitors because of their unique porous structure, structural flexibility, and rich defects. Therefore, the present investigation describes a simple synthesis method for hydrous and amorphous cobalt phosphate thin-film preparation by the simple successive ionic layer adsorption and reaction (SILAR) method on flexible stainless steel (SS) substrate for supercapacitor application. The structural and morphological analyses reveal mesoporous, agglomerated nanoparticle-like, hydrous, and amorphous cobalt phosphate over the SS substrate. The mesoporous nanoparticles of cobalt phosphate material possess the uppermost specific capacitance of  $1147 \text{ F g}^{-1}$  and  $630.7 \text{ C g}^{-1}$  specific capacity at a  $1 \text{ mA cm}^{-2}$  current density. To demonstrate practical relevance, hybrid supercapacitor devices were assembled with cobalt phosphate and rGO (reduced graphene oxide) as cathode and anode electrodes, respectively. Furthermore, the assembled hybrid aqueous supercapacitor device (S-CP4//KOH//rGO) delivers  $44.8 \text{ Wh kg}^{-1}$  specific energy (SE) at a specific power (SP) of  $4.8 \text{ kW kg}^{-1}$  with  $126 \text{ F g}^{-1}$  specific capacitance. The accumulated all-solid-state hybrid supercapacitor device (S-CP4//PVA-KOH//rGO) achieved the uppermost  $77 \text{ F g}^{-1}$  specific capacitance and SE of  $27.37 \text{ Wh kg}^{-1}$  at SP of  $1.5 \text{ kW kg}^{-1}$  with an outstanding 94% capacitive retention over 5000 cycles. Such remarkable supercapacitive performance results demonstrate that the SILAR method is an easy synthesis process for the binder-free preparation of cathode based on hydrous, amorphous cobalt phosphate thin films for hybrid supercapacitor devices.



## 1. INTRODUCTION

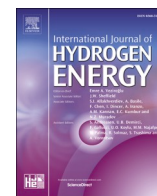
There has been a recent surge in energy demand for escalating electronic appliances and limitations of existing energy storage systems as the traditional energy storage system does not meet the development trend, which instantly demands efficient and clean energy.<sup>1–3</sup> Therefore, supercapacitor devices are in high demand and are considered an upcoming generation of energy storage devices based on benefits such as excellent energy storage capability and long cycle life.<sup>4–6</sup> Nevertheless, their low specific energy confines supercapacitor application in devices that require high energy.<sup>7,8</sup> Therefore, to improve specific energy and power, hybrid asymmetric capacitor devices have been developed, which consist of two dissimilar electrodes: one as an energy source (cathode), where battery-type or pseudocapacitive material is used, and another as a power source (anode), which consists of capacitor-type or electro-

chemical double-layer capacitor (EDLC) electrode materials.<sup>9–12</sup>

In general, existing pseudocapacitive materials are categorized into intrinsic, intercalation, and extrinsic types, and they exhibit higher specific energy than EDLC materials. Interestingly, battery-type materials can exhibit pseudocapacitive behavior upon changing their crystallite size or morphology (nanocrystalline) and are referred to as extrinsic pseudocapacitive materials.<sup>13–16</sup> Therefore, recent research interest has been growing in developing and miniaturizing battery-type

Received: July 1, 2022

Revised: September 18, 2022



# Impact of Co:Fe cations composition in amorphous and mesoporous cobalt iron phosphate electrocatalysts synthesized by SILAR method on durable electrochemical water splitting

Suraj A. Khalate<sup>a</sup>, Sujit A. Kadam<sup>b</sup>, Yuan-Ron Ma<sup>b</sup>, Sambhaji S. Kumbhar<sup>a</sup>, Shraddha B. Bhosale<sup>a</sup>, Vinod V. Patil<sup>a</sup>, Vinayak G. Parale<sup>d</sup>, Sachin B. Kulkarni<sup>c</sup>, Chandrakant D. Lokhande<sup>a</sup>, Hyung-Ho Park<sup>d,\*\*</sup>, Umakant M. Patil<sup>a,d,\*</sup>

<sup>a</sup> Centre for Interdisciplinary Research (CIR), D. Y. Patil Education Society, Kolhapur, 416 006, India

<sup>b</sup> Department of Physics, National Dong Hwa University, Hualien, 97401, Taiwan

<sup>c</sup> Department of Physics, Tuljaram Chaturchand College, Baramati, 413 102, India

<sup>d</sup> Department of Materials Science and Engineering, Yonsei University, 50 Yonsei-ro, Seodaemun-gu, Seoul, 03722, South Korea

## ARTICLE INFO

Handling Editor: Dr J Ortiz

### Keywords:

Amorphous thin film electrocatalyst  
Cations composition variation  
SILAR method  
Electrochemical water splitting

## ABSTRACT

Efficient and durable electrocatalysts are crucial for energy conversion devices that perform the oxygen evolution reaction (OER) and hydrogen evolution reaction (HER). The structural and morphological characteristics of the electrocatalyst can significantly impact the HER/OER performance. Therefore, it is essential to develop a high-performing electrocatalyst with desired properties using a simple and cost-effective chemical process. So, herein, successive ionic layer adsorption and reaction (SILAR) deposited amorphous, hydrous cobalt iron phosphate (CFP) thin film electrocatalysts are implemented toward electrochemical water splitting. Moreover, in the present work, the molar proportions of cobalt and iron were streamlined to study their synergistic effect on electrochemical HER and OER performance. The electrode of best-performing (CFP-S2) requires the lowest overpotentials of 242 mV for OER and 67.9 mV for HER at a current density of 10 mA/cm<sup>2</sup>, which maintains its activity after 24 h. The alkaline water splitting into a similar electrolytic bath using two electrode systems was demonstrated for 100 h with the lowest overpotential of 1.72 V. The remarkable electrochemical performance and postmortem analysis unambiguously demonstrate that CFP electrodes are a highly promising and robust option for long-duration water-splitting devices, and the facile SILAR method for scalable CFP electrode synthesis indicates enormous potential for commercial applications.

## 1. Introduction

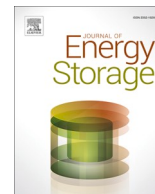
Hydrogen is a prospective energy source that is profitable to grab the market in the renewable energy sector [1,2]. A primary source of renewable energy has been suggested: hydrogen and has been termed ‘transitioning to a hydrogen society’ [3–5]. Various methods are used to produce hydrogen from different sources, such as reforming steam of natural gas, coal gasification, oxidation of methane, carbon/hydrocarbon assisted water electrolysis, radiolysis, thermolysis, photocatalytic water splitting, fermentative hydrogen production, photobiological water splitting, biocatalysts electrolysis, enzymatic hydrogen generation, etc. [6–8]. Among them, the most practical and

cost-efficient method of producing water splitting is electrochemical for generating oxygen and hydrogen [1,2]. Two half-reactions, specifically the hydrogen evolution reaction (HER) and the oxygen evolution reaction (OER), form the electrochemical process of splitting water, and it requires 1.23 V a theoretical potential to initiate water splitting [9,10]. To split water, excess energy or overpotential is necessary to overcome the barrier of activation energy caused by kinetic effects. Therefore, researchers have been making significant efforts to develop excellent catalysts to decrease the overpotential of water splitting. However, thermodynamics does not favor the direct dissociation of water into hydrogen and oxygen under normal pressure and temperature. Even though the HER process is much more promising in an acidic electrolytic

\* Corresponding author. Centre for Interdisciplinary Research (CIR), D. Y. Patil Education Society, Kolhapur, 416 006, India.

\*\* Corresponding author. Department of Materials Science and Engineering, Yonsei University, 50 Yonsei-ro, Seodaemun-gu, Seoul, 03722, South Korea.

E-mail addresses: [hypark@yonsei.ac.kr](mailto:hypark@yonsei.ac.kr) (H.-H. Park), [umakant.physics84@gmail.com](mailto:umakant.physics84@gmail.com) (U.M. Patil).



## Research Papers

Morphology modulation of  $\text{MnFe}_2\text{O}_4$  thin film electrode for enhanced performance of hybrid supercapacitor

Rushiraj P. Bhosale<sup>a</sup>, Sambhaji S. Kumbhar<sup>b</sup>, Shraddha B. Bhosale<sup>b</sup>, Rahul R. Salunkhe<sup>c</sup>,  
Vinita A. Kadam<sup>d</sup>, Sagar P. Pardhi<sup>e</sup>, Sandeep S. Gholap<sup>f</sup>, Chandrakant D. Lokhande<sup>b,\*</sup>, Vinayak  
S. Jamadade<sup>a,\*</sup>

<sup>a</sup> Department of Physics, D.P. Bhosale College, Koregaon, Satara 415516, India

<sup>b</sup> Centre for Interdisciplinary Research, D. Y. Patil Education Society, Kolhapur 416 006, India

<sup>c</sup> Department of Physics, Indian Institute of Technology Jammu Jagti, Jammu, J & K 181221, India

<sup>d</sup> Department of Physics, Yashwantrao Chavan Institute of Science Satara (Autonomous), Karmaveer Bhaurao Patil University, Satara 415001, India

<sup>e</sup> Department of Physics, Karmaveer Bhaurao Patil College, Urur Islampur 415409, India

<sup>f</sup> Agency for Science, Technology and Research (A-STAR), Singapore 138634, Singapore

## ARTICLE INFO

## Keywords:

Electrodeposition

Hybrid supercapacitor

Manganese ferrite

Morphology modulation

Thin film

## ABSTRACT

The preparation of binder-free manganese ferrite electrodes has garnered significant interest in hybrid energy storage devices. This interest stems from their notable electrochemical activity, which is primarily attributed to morphological modulation. Therefore, this study outlines an uncomplicated and scalable synthetic method utilizing electrodeposition (ED) to synthesize manganese ferrite electrodes. These electrodes were synthesized with varying deposition time. By structural analysis, the  $\text{MnFe}_2\text{O}_4$  phase of synthesized thin films is confirmed. With an increase in the deposition time, the modulation in the morphology of manganese ferrite thin films is evident, progressing from nanoflakes to nanorods. The most favorable deposition time for the manganese ferrite electrode, featuring a worm-like morphology, achieved the highest specific capacitance of  $227 \text{ F g}^{-1}$  at a current density of  $2 \text{ A g}^{-1}$ . Additionally, the hybrid solid-state supercapacitor device (HSSD) demonstrated a maximum specific capacitance of  $70.1 \text{ F g}^{-1}$  with specific energy (SE) of  $35.1 \text{ Wh kg}^{-1}$  at a specific power (SP) of  $3.1 \text{ kW kg}^{-1}$ , while retaining 81.1 % of its capacitive performance over 5000 cycles. This research introduces a scalable method for preparing manganese ferrite electrodes without binders, which can serve as cathode in hybrid energy storage devices suitable for real-world applications.

## 1. Introduction

Global energy consumption is increasing exponentially as a result of the rising population and fast industrialization. As a result, energy has been given top priority in addressing the needs of our modern civilization [1]. Fossil fuels currently serve as the primary source of energy and provide the diverse spectrum of energy needs in various industries. Unfortunately, the availability of fossil fuels is steadily decreasing, and our planet is constantly in danger as a result of the massive environmental degradation these sources produce. According to some studies, by the middle of the century, the world's energy needs would have doubled, and by 2100, they would have tripled [2]. In addition, the widespread use of electronic gadgets, such as wearable technology, digital cameras, laptops, and mobile phones, as well as hybrid electric

cars, has prompted the development of transportable forms of energy. In the report, Bosch's (2007–2022 current state of affairs and expenditure prospects of supercapacitor market in China), the worldwide market of supercapacitors has extended US dollars up to  $\$16 \times 10^9$  in 2015, and evaluators look for the market of the supercapacitor to outrun in 2020 up to  $\$92.3 \times 10^9$ , with a 39 % multiple yearly growth rates. From this view, the progress of the supercapacitor market in the whole world is rising [3]. The development of extremely effective energy conversion as well as storage technologies has been a continuous endeavor in this context. Due to their high energy/power densities, prolonged lives, and quick charging-discharging capabilities, energy storage technologies including supercapacitors, fuel cells, and rechargeable batteries are regarded as viable options for meeting a variety of energy demands [4].

Supercapacitors, also known as ultra-capacitors, are among the most

\* Corresponding authors.

E-mail addresses: [l.chandrakant@yahoo.com](mailto:l.chandrakant@yahoo.com) (C.D. Lokhande), [vinayakjamadade@gmail.com](mailto:vinayakjamadade@gmail.com) (V.S. Jamadade).

<https://doi.org/10.1016/j.est.2024.111146>

Received 18 November 2023; Received in revised form 14 February 2024; Accepted 28 February 2024

2352-152X/© 2024 Elsevier Ltd. All rights reserved.

## PAPER

## Chemical synthesis of binder-free nanosheet-like cobalt vanadium oxide thin film electrodes for hybrid supercapacitor devices†

Cite this: DOI: 10.1039/d4se00932k

Sambhaji S. Kumbhar,<sup>a</sup> Shraddha B. Bhosale,<sup>a</sup> Sumita S. Patil,<sup>a</sup> Akshay Ransing,<sup>b</sup> Vinayak G. Parale,<sup>b</sup> Chandrakant D. Lokhande,<sup>a</sup> Hyung-Ho Park<sup>b</sup> and Umakant M. Patil<sup>\*ab</sup>

To enhance the performance of energy storage devices, electrode materials must be designed with a strategic alteration of morphology and electroactive sites, utilizing synergy in bimetallic oxides. Therefore, the present study comprehensively demonstrates that variations in cobalt and vanadate precursor concentrations during chemical bath deposition (CBD) of cobalt vanadium oxide (C-CV) electrode materials significantly impact their physicochemical (structural, morphological and surface area) and electrochemical properties. An increase in vanadium content in the C-CV electrodes induces a notable morphological transformation, from nanoflakes to nanosheets with altered size and surface area. With a nanosheet-like morphology and a surface area of 87.5 m<sup>2</sup> g<sup>-1</sup>, the binder-free C-CV4 electrode synthesized with an optimal precursor composition of cobalt and vanadium (1 : 2) exhibits an outstanding specific capacitance ( $C_s$ ) of 845.3 F g<sup>-1</sup> (a specific capacity of 422.6 C g<sup>-1</sup>) at 1 A g<sup>-1</sup>. Moreover, an aqueous hybrid supercapacitor device (AHSD) and a solid-state hybrid flexible supercapacitor device (SH-FSD) fabricated employing C-CV4 (cathode) and reduced graphene oxide (rGO) (anode) exhibit noteworthy  $C_s$  values of 115 F g<sup>-1</sup> and 105.2 F g<sup>-1</sup>, respectively. Furthermore, the AHSD attains a specific energy (SE) of 40.9 W h kg<sup>-1</sup> at a specific power (SP) of 1.8 kW kg<sup>-1</sup>, while the SH-FSD demonstrates an SE of 37.4 W h kg<sup>-1</sup> at a SP of 0.86 kW kg<sup>-1</sup>. To prepare large-scale binder-free cobalt vanadium oxide with tunable morphology as the cathode material in hybrid energy storage devices, a feasible CBD method is adequate, as demonstrated by the electrochemical performance of hybrid supercapacitor devices.

Received 12th July 2024  
Accepted 9th October 2024  
DOI: 10.1039/d4se00932k  
rsc.li/sustainable-energy

## 1. Introduction

Over the past few decades, the demand for applications in consumer electronics, medicine, clean energy, and environmental sectors has increased, making wearable and flexible energy storage systems increasingly significant. Although flexible energy storage systems have numerous advantages, their commercialization faces new challenges.<sup>1–4</sup> Finding highly efficient energy storage devices for storing and dispensing large amounts of specific energy (SE) is one of the significant challenges.<sup>5</sup> Therefore, flexible hybrid supercapacitors have been developed to achieve higher energy density, faster kinetics, longer cycle life, and enhanced safety with reduced costs.<sup>6–8</sup> The primary goal of flexible hybrid supercapacitors is to develop

electrode materials with higher energy densities, similar to batteries, while maintaining high power densities and long cycling lifetimes.<sup>9,10</sup> Consequently, a variety of materials with various morphologies and structures have been investigated as electrodes; nevertheless, transition metal hydroxides and oxides (TMHs/TMOs) are the most remarkable materials for flexible hybrid supercapacitors owing to their high theoretical capacitance with notable energy density.<sup>1,6</sup> Although significant progress has been made in developing TMOs and TMHs for flexible hybrid supercapacitor electrodes, problems persist when relying solely on a single electrode material with limitations stemming from lower capacitance, limited energy density, and compromised rate capability owing to poor conductivity.<sup>6</sup> Therefore, modifying intrinsic features by rationally designing structural and morphological features through cation synergy in binary compounds becomes crucial to overcoming the restrictions associated with pristine TMO materials.

Vanadium oxides (V<sub>x</sub>O<sub>y</sub>) have been extensively researched over the last few decades as potential host materials for electrolyte cations, enabling multi-electron transfer reactions in energy storage applications.<sup>11</sup> Moreover, V<sub>x</sub>O<sub>y</sub> demonstrates a wide

<sup>a</sup>Centre for Interdisciplinary Research, D. Y. Patil Education Society, Kasaba Bawada, Kolhapur-416006, India. E-mail: umakant.physics84@gmail.com

<sup>b</sup>Department of Materials Science and Engineering, Yonsei University, 50 Yonsei-ro, Seodaemun-gu, Seoul-03722, Korea. E-mail: hhpark@yonsei.ac.kr

† Electronic supplementary information (ESI) available. See DOI: <https://doi.org/10.1039/d4se00932k>



# 1D, 2D, and 3D Structured Metal Chalcogenides for Supercapacitor Application



S. S. Kumbhar, S. J. Marje, V. V. Patil, S. B. Bhosale, S. S. Pujari, J. L. Gunjekar, C. D. Lokhande, and U. M. Patil

## Abbreviations

1D	One dimensional
2D	Two dimensional
3D	Three dimensional
AB	Acetylene black
CBD	Chemical bath deposition
CC	Carbon cloth
CV	Cyclic voltammetry
EDLC	Electric double-layer capacitor
EIS	Electrochemical impedance spectroscopy
FESEM	Field emission scanning electron microscopy
GCD	Galvanostatic charge-discharge
GO	Graphene oxide
NG	N-doped graphene
NMC	Nitrogen-doped mesoporous carbon
NWs	Nanowires
PANI	Polyaniline
Pt	Platinum
rGO	Reduced graphene oxide
TEM	Transmission electron microscopy

---

S. S. Kumbhar · S. J. Marje · V. V. Patil · S. B. Bhosale · S. S. Pujari · J. L. Gunjekar  
C. D. Lokhande · U. M. Patil (✉)  
Centre for Interdisciplinary Research, D. Y. Patil Education Society, Kolhapur, India

Fabian I. Ezema  
Chandrakant D. Lokhande  
Abhishek C. Lokhande *Editors*

# Chemically Deposited Metal Chalcogenide-based Carbon Composites for Versatile Applications



Springer



# PATENTS

---





पेटेंट कार्यालय, भारत सरकार

The Patent Office, Government Of India

पेटेंट प्रमाण पत्र

Patent Certificate

(पेटेंट नियमावली का नियम 74)

(Rule 74 of The Patents Rules)

पेटेंट सं. / Patent No.

529322

आवेदन सं. / Application No.

202221020648

फाइल करने की तारीख / Date of Filing

06/04/2022

पेटेंटी / Patentee

D.Y. PATIL EDUCATION SOCIETY (DEEMED TO BE UNIVERSITY), KASABA BAWADA, KOLHAPUR

आविष्कारकों का नाम / Name of Inventor(s)

1.DR.UMAKANT MAHADEV PATIL 2.MR.SAMBHAJI SHIVAJI KUMBHAR 3.MS.SHRADDHA BANDOPANT BHOSALE 4.MR.VINOD VASANT PATIL 5.PROF.CHANDRAKANT DNYANDEV LOKHANDE 6.DR.RAHUL RAGHUNATH SALUNKHE

प्रमाणित किया जाता है कि पेटेंटी को, उपरोक्त आवेदन में यथाप्रकरित **COBALT VANADIUM OXIDE, PREPARATION METHOD FOR THE SAME, AND SUPERCAPACITOR COMPARISING THE SAME** नामक आविष्कार के लिए, पेटेंट अधिनियम, 1970 के उपबंधों के अनुसार आज तारीख अप्रैल 2022 के छठे दिन से बीस वर्ष की अवधि के लिए पेटेंट अनुदत्त किया गया है।

It is hereby certified that a patent has been granted to the patentee for an invention entitled **COBALT VANADIUM OXIDE, PREPARATION METHOD FOR THE SAME, AND SUPERCAPACITOR COMPARISING THE SAME** as disclosed in the above mentioned application for the term of 20 years from the 6<sup>th</sup> day of April 2022 in accordance with the provisions of the Patents Act, 1970.



इकात की संज्ञा

अनुदान की तारीख : 20/03/2024

Date of Grant :

Controller of Patents

टिप्पणी - इस पेटेंट के नवीकरण के लिए फीस, यदि इसे बनाए रखा जाना है, अप्रैल 2024 के छठे दिन को और उसके पश्चात प्रत्येक वर्ष में उसी दिन देय होगी।

Note. - The fees for renewal of this patent, if it is to be maintained, will fall / has fallen due on 6<sup>th</sup> day of April 2024 and on the same day in every year thereafter.





INTELLECTUAL  
PROPERTY INDIA  
PATENTS | DESIGNS | TRADE MARKS  
GEOGRAPHICAL INDICATIONS



सत्यमेव जयते

क्रम सं/SL No :022129010



पेटेंट कार्यालय, भारत सरकार

The Patent Office, Government Of India

पेटेंट प्रमाण पत्र

Patent Certificate

(पेटेंट नियमावली का नियम 74)

(Rule 74 of The Patents Rules)

पेटेंट सं. / Patent No.

459219

आवेदन सं. / Application No.

202221020670

फाइल करने की तारीख / Date of Filing

06/04/2022

पेटेंटी / Patentee

D.Y. PATIL EDUCATION SOCIETY (DEEMED TO BE  
UNIVERSITY), KASABA BAWADA, KOLHAPUR

आविष्कारकों का नाम / Name of Inventor(s)

1.DR.UMAKANT MAHADEV PATIL 2.MR.SAMBHAJI SHIVAJI  
KUMBHAR 3.MS.SHRADDHA BANDOPANT BHOSALE  
4.MR.VINOD VASANT PATIL 5.PROF.CHANDRAKANT  
DNYANDEV LOKHANDE 6.DR.PRASHANT RAVASAHEB  
DESHMUKH

प्रमाणित किया जाता है कि पेटेंटी को, उपरोक्त आवेदन में यथाप्रकटित **CHEMICAL METHOD FOR GROWING A COBALT VANADIUM OXIDE THIN FILM ON SOLID SUBSTRATE** नामक आविष्कार के लिए, पेटेंट अधिनियम,

1970 के उपबंधों के अनुसार आज तारीख अप्रैल 2022 के छठे दिन से बीस वर्ष की अवधि के लिए पेटेंट अनुदत्त किया गया है।

It is hereby certified that a patent has been granted to the patentee for an invention entitled **CHEMICAL METHOD FOR GROWING A COBALT VANADIUM OXIDE THIN FILM ON SOLID SUBSTRATE** as disclosed in the above mentioned application for the term of 20 years from the 6<sup>th</sup> day of April 2022 in accordance with the provisions of the Patents Act, 1970.



अनुदान की तारीख : 16/10/2023

Date of Grant : 16/10/2023

पेटेंट नियंत्रक  
Controller of Patents

**टिप्पणी** - इस पेटेंट के नवीकरण के लिए फीस, यदि इसे बनाए रखा जाना है, अप्रैल 2024 के छठे दिन को और उसके पश्चात प्रत्येक वर्ष में उसी दिन देय होगी।

**Note** - The fees for renewal of this patent, if it is to be maintained, will fall / has fallen due on 6<sup>th</sup> day of April 2024 and on the same day in every year thereafter.





INTELLECTUAL  
PROPERTY INDIA

PATENTS | DESIGNS | TRADE MARKS  
GEOGRAPHICAL INDICATIONS



सत्यमेव जयते

क्रमांक : 022124439  
SL No :



भारत सरकार  
GOVERNMENT OF INDIA

पेटेंट कार्यालय  
THE PATENT OFFICE

पेटेंट प्रमाणपत्र  
PATENT CERTIFICATE  
(Rule 74 of The Patents Rules)

पेटेंट सं. / Patent No. : 432303  
आवेदन सं. / Application No. : 202221020644  
फाइल करने की तारीख / Date of Filing : 06/04/2022  
पेटेंटी / Patentee : D.Y. PATIL EDUCATION SOCIETY (DEEMED TO BE UNIVERSITY), KASABA BAWADA, KOLHAPUR  
आविष्कारक (जहां लागू हो) / Inventor(s) : 1.DR.UMAKANT MAHADEV PATIL 2.MR.VINOD VASANT PATIL 3.MR.SAMBHAJI SHIVAJI KUMBHAR 4.MS.SHRADDHA BANDOPANT BHOSALE 5.PROF.CHANDRAKANT DNYANDEV LOKHANDE

प्रमाणित किया जाता है कि पेटेंटी को, उपरोक्त आवेदन में यथाप्रकटित NICKEL COBALT PHOSPHATE THIN-FILM ELECTRODES : CHEMICAL METHOD FOR PREPARATION OF THE SAME APPLICATION FOR SUPERCAPACITOR AND ELECTROCATALYSIS USING THE SAME. नामक आविष्कार के लिए, पेटेंट अधिनियम, 1970 के उपबंधों के अनुसार आज तारीख अप्रैल 2022 के छठे दिन से बीस वर्ष की अवधि के लिए पेटेंट अनुदत्त किया गया है।

It is hereby certified that a patent has been granted to the patentee for an invention entitled NICKEL COBALT PHOSPHATE THIN-FILM ELECTRODES : CHEMICAL METHOD FOR PREPARATION OF THE SAME APPLICATION FOR SUPERCAPACITOR AND ELECTROCATALYSIS USING THE SAME. as disclosed in the above mentioned application for the term of 20 years from the 6<sup>th</sup> day of April 2022 in accordance with the provisions of the Patents Act, 1970.



अनुदान की तारीख : 19/05/2023  
Date of Grant :

पेटेंट नियंत्रक  
Controller of Patent

**टिप्पणी** - इस पेटेंट के नवीकरण के लिए फीस, यदि इसे बनाए रखा जाना है, अप्रैल 2024 के छठे दिन को और उसके पश्चात प्रत्येक वर्ष में उसी दिन देय होगी।

**Note.** - The fees for renewal of this patent, if it is to be maintained will fall / has fallen due on 6<sup>th</sup> day of April 2024 and on the same day in every year thereafter.



# CONFERENCES

---

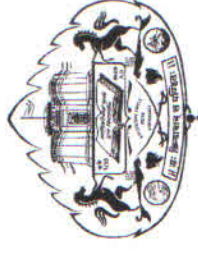
International Conference

on

**"Advanced Materials Synthesis, Characterization and Applications - 2023"**

**(AMSCA - 2023)**

DEPARTMENT OF  
**PHYSICS**



## CERTIFICATE OF PARTICIPATION

This is to certify that,

**Ms. Shraddha Bhosale, D. Y. Patil Education Society, Kolhapur** has presented

**Poster** on the topic **Layer-by-layer binder-free development of mesoporous nickel vanadate thin films for hybrid supercapacitor device** in the **International Conference on AMSCA - 2023** held at the **Department of Physics, Savitribai Phule Pune University, Pune, Maharashtra, INDIA** during **21<sup>st</sup> to 24<sup>th</sup> November, 2023**.

Convener  
AMSCA - 2023

Co-Convener  
AMSCA - 2023

Head  
Department of Physics,  
SPPU, Pune



**D. Y. PATIL EDUCATION SOCIETY**  
(Deemed to be University), KOLHAPUR  
NAAC 'A' Grade in 3<sup>rd</sup> Cycle

# *Certificate*

This is to certify that **Mr. /Ms. Bhosale Shraddha Bandopant** of Centre for Interdisciplinary Research, DYPES, Kolhapur has delivered invited talk/ chaired the session/ presented oral/ presented poster/ participated in the **International Conference on Nanotechnology Addressing the Convergence of Materials Science, Biotechnology and Medical Science (IC-NACMBM-2024)** held at the Centre for Interdisciplinary Research, D. Y. Patil Education Society (Deemed to be University), Kolhapur, Maharashtra, India during 12<sup>th</sup> to 14<sup>th</sup> February 2024. His/ Her contribution to the conference is highly appreciated.

**Dr. Jayavant L. Gunjekar**

Convener

**Prof. Meghnad G. Joshi**

Convener

**Prof. Chandrakant D. Lokhande**

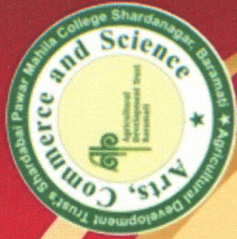
Chairman





*Agricultural Development Trust's*

**Shardabai Pawar Mahila Arts, Commerce & Science College,  
Shardanagar, Malegaon Bk., Tal- Baramati, Dist. - Pune, 413115**



**National Conference**

on

# **Recent Trends in Functional Materials and Their Applications (RTFMA - 2024)**

## *Award Certificate*

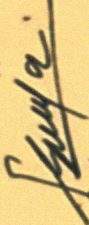
Presented to Dr./Mr./Mrs./Miss. \_\_\_\_\_

**Bhosale Shraddha Bandopant** from \_\_\_\_\_

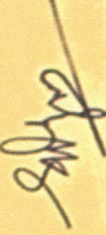
**D. Y. Patil Education Society (Deemed to be University), Kolhapur**, has received **Best Oral / Poster** presentation award in SERB sponsored National conference organized by Department of Physics on 13<sup>th</sup> - 14<sup>th</sup> March 2024.

  
Dr. V. R. Shinde & Ms. S. J. Shinde

Organising Secretary

  
Dr. T. P. Gujar

Coordinator & Head



Prof. Dr. S.V. Mahamuni  
Convener & Principal





# SHIVAJI UNIVERSITY, KOLHAPUR

## SOPHISTICATED ANALYTICAL INSTRUMENT FACILITY (SAIF) – COMMON FACILITY CENTRE (CFC)

### WORKSHOP & HANDS-ON TRAINING ON XRD ORGANISED

### BY SAIF-CFC UNDER STRIDE PROGRAMME

### Certificate of Participation

This is certify that Miss Bhosale Shraddha B. has successfully participated in the workshop & hands-on training on XRD organised by SAIF (CFC), Shivaji University, Kolhapur held during 11-12 Nov, 2021 under the STRIDE (Scheme for Trans-disciplinary Research for India's Developing Economy) programme.

Prof. R. G. Sonkawade  
Co-ordinator : SAIF, Head (i/c) : CFC  
Shivaji University, Kolhapur.  
Chairman



SCHEME FOR TRANS-DISCIPLINARY RESEARCH  
FOR INDIA'S DEVELOPING ECONOMY

Synergistic Training program Utilizing the scientific and Technological Infrastructure

# STUTI-2022

## ONE WEEK TRAINING PROGRAM

Hands-on Training on Sophisticated Instruments for Materials Science

September 14-20, 2022

## CERTIFICATE

This is to certify that Prof./Dr./Mr./Ms. *Shraddha Bandopant Bhasale*  
from *D.Y. Patil Education Society, Kolhapur* participated / delivered an Invited Lecture / given

Hands-on Training on.....~~.....~~.....~~.....~~.....~~.....~~.....

in the DST-STUTI funded One Week Hands-on Training on Sophisticated Instruments for Materials Science  
organized by Bundelkhand University, Jhansi in association with Banasthali Vidyapith, Rajasthan  
during September 14-20, 2022



*Anupam Vyas*  
Dr Anupam Vyas  
Co-Convenor

*Lavkush Dwivedi*  
Dr Lavkush Dwivedi  
Co-Convenor

*Dr Parvej Ahmad Alvi*  
Dr Parvej Ahmad Alvi  
PMU Coordinator

*Dr Sanjeev Kumar Shrivastava*  
Dr Sanjeev Kumar Shrivastava  
Convener





**SANJAY GHODAWAT UNIVERSITY Kolhapur**

Empowering Lives Globally !

(Approved by UGC & Govt. of Maharashtra)

# Certificate

This is to certify that

Prof. / Dr. / Mr. / Ms. Shraddha Bandopant Bhosale, Ph.D. Scholar

of D. Y. Patil Education Society, Kolhapur has participated in National Seminar on

***“Emerging Nano Materials for Renewable Energy”***

held on Monday, 26<sup>th</sup> December, 2022 and organized by Sanjay Ghodawat University, Kolhapur.

**Dr. Sambhaji M. Pawar**  
Convener

**Dr. Pallavi D. Bhangre**  
Convener

**Dr. Sarita P. Patil**  
Co-ordinator

**Prof. Dr. Arun S. Patil**  
Vice-Chancellor